The Molecular Interstellar Medium in Distant Galaxies

A PhD Thesis in Astronomy put forward by

Melanie Kaasinen

Cover design: Montage created by the author.

Cover images: At the bottom of the montage is an image of the Atacama Large Millimeter/submillimeter Array (ALMA) at twilight *(Credit: ESO/B. Tafreshi (twanight.org), obtained from https://www.eso.org/public/images/potw1402a/)*. The background layer is an image of the temperature anisotropies of the Cosmic Microwave Background (CMB) as observed by Planck *(Copyright: ESA/Planck Collaboration, available at https://sci.esa.int/s/WLdlLVW)*. Although this thesis is not occupied with the anisotropies, it *is* occupied with observing cold gas against this background. In front of the CMB is a composite colour image of the eXtremely Deep Field (XDF), obtained by assigning monochromatic (red, green and blue) hues to separate exposures with *the Hubble Space Telescope's* ACS and WFC3/IR instruments, with the filters grouped as follows: Blue: ACS/WFC F435W (B) + F606W (V) Green: ACS/WFC F775W (I) + F814W (I) + F850LP (z) Red: WFC3/IR F105W (Y) + F125W (J) + F160W (H) *(Credit: G. Illingworth, D. Magee, and P. Oesch, R. Bouwens, and the HUDF09 Team)*. The smaller images that are overlaid on the XDF are some of the key figures in this thesis. The two zoom-in images of the XDF galaxy circled at the top left depict the dust-continuum emission (red) and carbon monoxide emission (CO; blue) analysed herein. The zoom-in on the CO emission of this distant galaxy, shows the H_2 column density of one of the simulated clouds used to investigate the CMB's impact on high-redshift observations of the line emission from CO and atomic carbon.

DISSERTATION
SUBMITTED TO THE
COMBINED FACULTY OF NATURAL SCIENCES AND MATHEMATICS
OF HEIDELBERG UNIVERSITY, GERMANY
FOR THE DEGREE OF
DOCTOR OF NATURAL SCIENCES

PUT FORWARD BY
Melanie Kaasinen

BORN IN: Lauf a.d. Pegnitz

ORAL EXAMINATION: 23.07.2021

Printed by:

Title:	*The Molecular Interstellar Medium in Distant Galaxies* *(Das Molekulare Interstellare Medium in Weit-entfernten Galaxien)*
Supervisors:	apl. Prof. Dr. Simon Glover and Dr. Fabian Walter
Oral examination:	23.07.2021
Examiners:	apl. Prof. Dr. Simon Glover, Prof. Dr. Hans-Walter Rix Prof. Dr. Ralf Klessen, Prof. Dr. Björn Malte-Schäfer

Dedicated to my dear friend, Nassib Jabbour.
Your optimism and curiosity will always inspire me.

1993 – 2018

ABSTRACT

With the increased capabilities of sub-/millimeter facilities over the last decade it has become possible to observe the medium out of which most of the stars in today's Universe formed, the molecular interstellar medium in distant galaxies. In this thesis, I have tested what can be learnt from such observations, particularly of dust-continuum and CO emission. I compared the molecular gas masses inferred from observations of the ground transition of CO to those inferred from dust-continuum emission, finding that dust-continuum emission can be used to reliably infer the molecular gas content of massive star-forming galaxies at the peak epoch of star formation. However, by comparing the dust and CO emission at resolutions of a few kiloparsec, I found that dust-continuum emission is a poor tracer of molecular gas in the outskirts of typical star-forming galaxies at the same epoch. I also found that at least some distant star-forming galaxies host large, centrally-concentrated molecular gas reservoirs. Finally, I simulated molecular clouds with the aim of testing the impact of the Cosmic Microwave Background on observations of the emission from CO and atomic carbon in distant galaxies, highlighting the dominance of this background in the distant Universe.

ZUSAMMENFASSUNG

Aufgrund der gestiegenen Leistungsfähigkeit von Sub-/Millimeter-Teleskopen ist es innerhalb des letzten Jahrzehntes möglich geworden die Emission des molekularen interstellaren Mediums in fernen Galaxien zu beobachten, aus dem die meisten Sterne im heutigen Universum entstanden sind. In dieser Dissertation habe ich getestet, was man aus solchen Beobachtungen lernen kann, insbesondere aus der Emission des Staub-Kontinuums und CO-Übergängen. Ich habe die molekularen Gasmassen, die aus Beobachtungen des Grundübergangs von CO abgeleitet wurden, mit denen verglichen, die aus der Staub-Kontinuum-Emission abgeleitet wurden, und festgestellt, dass Letzteres verwendet werden kann, um zuverlässig auf den molekularen Gasgehalt massereicher sternbildender Galaxien in der Hochphase der Sternentstehung zu schließen. Durch den Vergleich der Staub- und CO-Emission bei Auflösungen von einigen Kiloparsec fand ich jedoch heraus, dass die Emission des Staub-Kontinuums ein schlechter Indikator für das molekulare Gas in den Außenbereichen typischer weit-entfernter Galaxien ist. Durch die Analyse dieser Beobachtungen fand ich auch heraus, dass zumindest einige entfernte sternbildende Galaxien große, zentrale molekulare Gasreservoirs aufweisen. Schließlich simulierte ich Molekülwolken mit dem Ziel, den Einfluss des kosmischen Mikrowellenhintergrunds auf die Beobachtungen der Emissionen von CO und atomaren Kohlenstoff von fernen Galaxien zu testen. Diese verdeutlichten die Dominanz dieses Hintergrunds im fernen Universum.

ACKNOWLEDGEMENTS

Over the course of the last four years, many people have helped shape me both as a researcher and as a human being. I will endeavour to thank them all here, but these words cannot capture my true gratitude to everyone who has been part of my PhD experience.

First and foremost, many thanks to my supervisors, Fabian Walter and Simon Glover. I am very grateful to have had the opportunity to benefit from two such experienced and enthusiastic researchers, in different fields and with different supervision styles. Thank you for providing advice and support when I needed it but leaving me to explore rabbit holes when necessary. This balance has helped me become a more independent researcher. You have been the best science role models I could have asked for and I look forward to working with you for many years to come.

I have also been very fortunate to have supportive mentors, who provided career advice and with whom I discussed science (mine, theirs and others). Thank you in particular to Gergö Popping, for taking an interest in my work, wellbeing and development. Working with you has been a joy and I am delighted to continue working closely with you and benefit from your mentorship. Special thanks also go to Elisabete da Cunha for the fruitful science discussions, support and career advice.

During my PhD, I have been part of two supportive research groups, Fabian Walter's research group (MPIA) and the Glover and Klessen star formation group (ITA). The interactions I have had with members of these groups are what conducting science is all about. Particular thanks go to the following people. Thank you Mladen Novak, my interferometry guru, for teaching me that reducing interferometric data requires a little magic. I will keep practising this black magic so that one day I may master it as you did. I also hugely enjoyed indulging in healthy cynicism with Marcel Neeleman. Thanks for showing me the intricacies of kinematic modelling and for always taking time to answer my questions. Thank you to Alex Hygate for calmly working through problems that were "bugging" me and for many interesting non-astronomy discussions. Thank you to Nico Krieger for helping me with all things technical, from producing nice channel maps to navigating the German taxation system. To my simulation gurus at the ITA, Mattis Magg and Robin Tress, thank you for answering all my "stupid" questions without making me feel stupid. Special thanks also go to Ralf Klessen for your boundless enthusiasm for science. I hope that like you, I will have this energy for many decades to come.

I have also benefitted greatly from working as part of collaborations, in particular the ASPECS collaboration. I would particularly like to thank Leindert Boogaard and Roberto Decarli for your great insights, support and enthusiasm. In addition to the ASPECS team, I wish to thank all those who invited me to be part of their research plans or who were excited to join mine, particularly Irene Shivaei, Dominik Riechers, Jaqueline Hodge and Matus Rybak.

Thank you to my colleagues at the MPIA. It was a joy to interact with you all. Special thanks go to Hans-Walter Rix for enabling us, myself included, to focus on science even during a global pandemic. Although I have done my best to be involved in non-science-related endeavours at the institute, I truly appreciate your leadership in this regard. Thank you also to my fellow members of the sustainability group. You have given me hope that we can conduct astronomy more sustainably and thereby continue this fascinating work for many years to come. Thanks also to the Galaxy and Cosmology department in general. I got a great buzz from the department retreats and daily interactions.

Sharing science with the wider public is something dear to my heart, so I want to extend a special thanks to my outreach colleagues. To Markus Pössel, thanks for taking me on as an outreach fellow and for your compliments on each occasion that I worked with you. I hope to work together again in future. I also hugely enjoyed working with my fellow fellows, especially Felix Bosco, Victor Marian, Paul Heeren and Alina Böcker. Thanks for sharing your love and knowledge of astronomy with me as well as our intended audience and for giving your feedback whenever I practiced my German outreach talks. Many thanks also to Sigrid Brümmer, Markus Nielbock and Thomas Müller. I hugely admire the effort you all put in to sharing astronomy with the general public.

The distinction between peers, office mates and friends has often been blurred. To my best friend, office mate and adventure buddy, Neige Frankel - you have been incredible. Thanks for helping me to enjoy adventures, both in nature and in research, and always been patient in discussing topics where I was stuck in my ways. I have learned so much from your attitude to life and work. To Sarah Leslie, whom I followed from Canberra to Heidelberg, thanks for showing me the ropes and for being a mentor throughout my academic career. You are not only a great friend but a real inspiration. To Rebecca McElroy, my fellow gender equality officer - I have learnt so much from you. Thanks for opening my eyes to issues around gender and sexual diversity but also for your support and guidance in other aspects. To my friend and peer Francisco - thank you for dragging me away from the screen for tea breaks, for helping me solve my coding and conceptual issues and for discussing all things life and astronomy. I really missed you when you left halfway through this journey. To Aleksandra Hamanowicz, whom I first met during PhD interviews, thanks for showing me around ESO, encouraging me to talk to the relevant people when I felt too shy and motivating me when I felt incapable. I look forward to scaling more mountains together. To my original office mate, Josha van Houdt - thanks for welcoming me to the office, for cycling up and down mountains with me (Königstuhl included), for sharing lots of laughs and for debating the nature of academia. I hope I will have more office mates like you. To Oliver Völkel, another office mate extraordinaire - thanks for your random and fun interruptions, for checking my German and for keeping it real. To Jacob Isbell - thanks for helping me regain some perspective and for the many mind-clearing walks during the lockdowns. Thank you to Arianna Musso Barcucci and Asmita Bhandare, for helping me navigate student life and enjoying the little things together. To all the current and former students whom I haven't explicitly mentioned - thanks for the many great memories.

There is more to life than work. Sport, art, good food and outdoor adventures have always played a huge role in my life and I thank all the people who shared these experiences with me during my time in Heidelberg. Vielen Dank an meine lieben Mitbewohnerinnen, Elfi Armbrust und Ana Tchokhonelidze - Ihr habt mein Leben sehr bereichert und meine Kuchen und Kunst immer gut geschätzt. Vielen Dank Sebastian Birlin für die gemeinsamen Trainingseinheiten, Rennen, Abenteuer, das ganze leckere Essen und dein Rat. Liebe Marion Stopyra, danke für deine Unterstützung, für das gemeinsame überwinden von Höhenangst und für die gemeinsamen ruhigen Abende. To my adopted big brother, Rob Harris, you have been my rock. Thanks for being there during both the tough times and the best of times. You brought colour to these last few years and have been an incredible role model. To my wonderful partner, Thomas Jackson - thank you for your belief in me, for motivating me and for sharing my ups and downs. You have somehow managed to keep me sane during the final few months of the madness that is a PhD. That has been no mean feat.

Last but certainly not least, thank you to my incredible, supportive parents, Nancy and Rudi Kaasinen. Thank you Papi for going out of your way to support my interest from an early age, for being just as enthusiastic as I was (if not more) and for posing more perplexing astronomy questions than my thesis examiners are likely to. To both of you, thank you so much for providing the encouragement and stability I needed to get to this point. Despite being on the other side of the world during my PhD, you were always right there for me when I needed you.

CONTENTS

LIST OF FIGURES

LIST OF TABLES

ACRONYMS

ACA ALMA Compact Array
ALMA Atacama Large Millimeter/submillimeter Array
AGN active galactic nuclei
ASPECS ALMA Spectroscopic Survey in the Hubble Ultra Deep Field
ATCA Australia Telescope Compact Array
CASA Common Astronomy Software Application
CMB Cosmic Microwave Background
CRIR cosmic ray ionisation rate
ELT Extremely Large Telescope
FIR far-infrared
GMCS giant molecular clouds
HDF-N *Hubble* Deep Field North
HST *Hubble Space Telescope*
HUDF *Hubble* Ultra Deep Field
IR infrared
ISM interstellar medium
ISRF interstellar radiation field
JWST *James Webb Space Telescope*
LTE local thermodynamic equilibrium
LVG large velocity gradient
NOEMA NOrthern Extended Millimeter Array
PDBI Plateau de Bure interferometer
PHANGS Physics at High Angular resolution in Nearby GalaxieS
NIR near-infrared
PAHS Polycyclic Aromatic Hydrocarbons
PDF probability density function
QSOS quasar host galaxies
RMS root mean square
SED spectral energy distribution
SFE star formation efficiency
SKA Square Kilometer Array
SMA Submillimetre Array
SMGS submillimetre(-selected) galaxies
S/N signal-to-noise ratio
TIR total-infrared
ULIRGS ultra-luminous infared galaxies
UV ultraviolet
VLA Karl G. Jansky Very Large Array
XDF *Hubble* eXtremely Ultra Deep Field

1

INTRODUCTION

Science is driven by opportunity.

all of my scientific mentors

New facilities drive astronomical research and the *Hubble Space Telescope* is one prime example. It is now two decades since the iconic image of the *Hubble* Ultra Deep Field was first released by the *Hubble* team (Williams et al., 1996) and in this time much has changed in our perception of the Universe. Within the 2.6 square arcminute speck of sky of the *Hubble* Ultra Deep Field there are $\sim 10,000$ galaxies, exhibiting a range of colours and shapes (see Fig. 1.1). Their apparent colour results from both the distance from us and the relative amount of "young" vs "old" stars, thereby encoding the rate of recent star formation. Their shape is also related to the rate and sites of star formation, with galaxies that are still actively forming stars appearing "disky" rather than elliptical. By studying how such properties vary along the time axis, i.e. the axis going into the page, astronomers have built up an overview of how star formation has shaped galaxies over time. Thus, these kinds of deep field observations have enabled astronomers to conduct a census of the star formation in the Universe, from 1 billion years ago to < 1 billion years after the "Big Bang".

Why should "we", humanity in general, even care about star formation and its effect on galaxies? This is a question I am often posed in some form or another, by members of the general public. From a human-centric point of view, star formation is a key step precluding our own existence here on this little blue dot. So, understanding when and where stars formed is an important part of answering: how did *we* get here? Looking beyond us as a species, star formation plays a key role in the progression of the Universe from a state of hot, near-uniform gas to what now appears to be a vast cosmic web, the densest regions of which are occupied by galaxies, which help regulate the composition of visible matter in today's Universe.

To understand how the content of the Universe evolved, astronomers have consistently pushed for the development of new technologies. On the flipside of "science is driven by opportunities", each generation of observational facilities is driven by the science questions that arose from the previous one. The writing of this thesis comes a decade after the start of operations of the Atacama Large Millimeter/submillimeter Array (ALMA), with which the astronomical community aimed to address some of the key questions that followed from the wealth of science conducted with optical-to-near infared facilities: *Where did stars form? How was the fuel for star formation distributed in galaxies? How efficiently was gas converted into stars?* These are some of the questions that the work in this thesis aimed to help address.

Figure 1.1: The *Hubble* eXtreme Deep Field (XDF) (Illingworth et al., 2013), a deeper, follow-up, zoom-in on the groundbreaking *Hubble* Ultra Deep Field (HUDF) first released in 1996. More than 5000 galaxies are visible in this ~ 2.3 square arcminute patch of the sky, the furthest of which are imaged at only a few hundred million years after the Big Bang. The RGB image is a composite of images of the following filters - Red: F105W+F125W+F160W + Green: F775W+F814W+F850LP + Blue: F435W+F606W *(Credit: NASA; ESA; G. Illingworth, D. Magee, and P. Oesch, R. Bouwens and the HUDF09 Team.)*

1.1 STAR FORMATION AND GALAXIES

In describing the formation and evolution of stars and galaxies, I am faced with a chicken-and-egg problem. What came first, stars or galaxies? As for the chicken and egg this question is ill-posed, but in the posed form has a clear answer; stars (eggs) formed first (e.g. Bromm and Larson, 2004). But, like eggs within chickens, stars continue to form within galaxies, causing their structure and composition to evolve. Throughout this Section, the focus shifts from galaxies to stars via the interstellar medium and back to galaxies. Neither stars nor galaxies can be considered without the other. I will, however, begin with the larger of the two.

1.1.1 An Abridged Summary of Galaxy Formation and Evolution

Nowadays, galaxies are thought of as gravitationally bound systems of stars, gas, dust, and dark matter. Some are found in clusters or groups, whereas others are more isolated from their fellow galaxies; however, even these are not completely cut off. Galaxies appear to occupy the densest clusters and nodes at the intersection of vast cosmic webs of matter and may interact with this

larger structure as well as with other galaxies (e.g. by merging). These interactions alter the composition, size and structure of galaxies. Thus, galaxies form and evolve in a universal context. Yet, the consituents of galaxies do not lie dormant within, e.g. gas is used up during the formation of stars and the deaths of stars expel energy and enriched material back into the galaxy, thereby changing the overall composition and structure of the larger system.

The universal stage on which galaxies form and evolve can be described by cosmological models. Although there are a range of proposed models, the most widely-accepted one, and the one adopted in this thesis, is the Λ Cold Dark Matter (ΛCDM) model. It is characterised by two main assumptions: (1) there exists some property of space (a "dark" vacuum energy) responsible for the accelerated expansion of the Universe, and, (2) most of the matter in the Universe is "dark", i.e. non-baryonic, cold, dissipationless and collisionless. The vacuum energy, parameterised by the constant Λ, makes up $\sim 69\%$ of the energy content of the Universe, with "dark" matter accounting for a further $\sim 26\%$. The component of the Universe that's visible to us, baryonic matter, only accounts for $\sim 5\%$ of total energy content (of which less than a tenth resides in galaxies).

Under the ΛCDM framework, gravity is described by general relativity and the expansion of space is described by combining the Friedmann–Lemaître–Robertson–Walker metric, the Friedmann equations and the cosmological equations of state. Under this framework, the expansion of space is parameterised via the dimensionless scale factor $a(t) = 1/(1+z)$, where t is the cosmic age and z the cosmological *redshift*. The latter is a convenient measure for the distance to a galaxy or the age of the Universe at the time the light was emitted because the wavelength of this light is stretched by a factor of $(1+z)$ with the expansion of the Universe.[(1)].

The events that led to the formation of the first galaxies can be briefly summarised under the ΛCDM model as follows (e.g. Mo et al., 2010). The Universe began with a rapid *inflation* of spacetime, famously called the Big Bang. After ~ 1 second, the Universe consisted of a dense plasma of fundamental particles, at 10^{32}K. These particles combined over the next few minutes to form the nuclei of hydrogen and helium. Several thousand years of exponential expansion followed, during which the Universe consisted of a plasma of coupled photons and particles. Matter started cooling sufficiently for electrons to combine with nuclei (to ~ 3000 K) about 380 000 years after the Big Bang, forming the first neutral hydrogen atoms. With the formation of neutral hydrogen, the Universe finally became transparent to radiation,[(2)] releasing the first detectable light. This afterglow of recombination is still visible at microwave wavelengths today, and is referred to as the Cosmic Microwave Background (CMB).

According to the ΛCDM paradigm, the minuscule temperature fluctuations of the CMB reflect fluctuations in density that later led to the formation of galaxies. While the Universe and matter within it were expanding, gravity was acting on the overdense regions, pulling these together. Above a certain density threshold ($\sim 200\times$ the background density) these regions collapsed. Since the dissipationless cold dark matter could not cool, it stopped collapsing further, forming haloes. In contrast, some of the baryonic gas further cooled and condensed to form the dense visible structures of galaxies. Although galaxies only contain about 10% of the baryons in the Universe, they are responsible for much of the conversion of baryonic matter from one form to another.

Galaxies continued (and still continue) to evolve following the settling of baryonic matter into disks. Internal processes change the composition and structure of the baryonic matter in galaxies, especially the formation of stars from interstellar gas. On the largest physical and temporal scales the process of star formation is regulated by the supply of gas. However, star formation encompasses a wide range of physical scales, linking the larger cosmic stage on which galaxies evolution takes place to small-scale physics and chemistry, as encompassed in the following flowchart.

(1) $a(t_{\rm obs})/a(t_{\rm emit}) = \lambda_{\rm obs}/\lambda_{\rm emit} = (1+z)$

(2) the previously uncombined protons and electrons scattered radiation via Thomson scattering, making the Universe an opaque fog

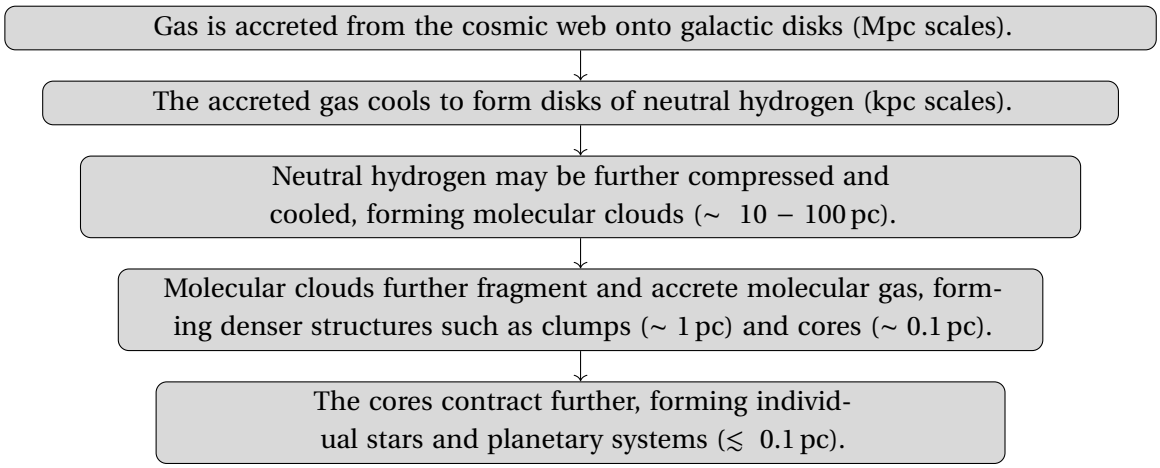

The first step, the accretion of material, takes around $\sim 10^8$ years (Kereš et al., 2005; Dekel and Birnboim, 2006; van de Voort et al., 2011; Pan et al., 2019). It takes a further $\sim 10^7$ years to compress the neutral, atomic gas sufficiently to form clouds of molecular gas (e.g. Glover and Mac Low, 2011; Glover and Clark, 2012b; Walch et al., 2015) and about the same length again to from stars within the molecular medium (e.g. Kawamura et al., 2009; Meidt et al., 2015; Schinnerer et al., 2019b).

1.1.2 A Brief History of Star Formation

Because the various stages of star formation take longer than most human civilisations they cannot be observed from beginning to end. They can, however, be studied by comparing galaxy populations at different time snapshots. This statistical approach was widely adopted at the beginning of this century thanks to observations from ultraviolet-to-infrared space-based facilities, particularly the *Hubble Space Telescope* (HST), the *Galaxy Evolution Explorer (GALEX)*, the *Spitzer Space Telescope* and the *Herschel Space Observatory*. Together, these facilities gathered the unobscured (and dust-obscured) stellar light from galaxies in well-defined fields of the sky, thereby enabling the stellar content and star formation rates of galaxies to be measured per unit cosmic volume, for a range of cosmic epochs. By the early 2010s, these measurements had converged to a consistent picture of the build of up stellar mass, at least from $z \sim 0-4$, as encapsulated in Fig. 1.2. More recent observations, conducted at longer wavelengths, also added in this figure (e.g. Novak et al., 2017) have only confirmed these results.

The left panel of Fig. 1.2 depicts the cosmic star formation rate density (SFRD), i.e. the mass of material converted into stars per year averaged over the cosmic volume in comoving cubic Mpc. The right panel shows the corresponding rise in the stellar mass density. In combination, these figures tell the following story. Early on in the universe *(at cosmic dawn)*, little baryonic mass was in the form of stars. Yet the cosmic SFRD was rising,[3] leading to a steady increase in the density of baryonic material locked up in stars. The cosmic SFRD reached its peak around $z \sim 1-3$ *(cosmic noon)*, after which the increase in the universal stellar mass density slowed. Since then, the cosmic SFRD has declined exponentially by a factor of ~ 8,[4] to the present day *(cosmic tea?)* and thus the stellar mass density appears to be plateauing.

A few fundamental insights into the cosmic matter cycle can be obtained by simply integrating the curves in Fig. 1.2. The integral of the cosmic SFRD, shown as the yellow dashed curve in the right panel, represents the density of stellar mass formed at a given time. This is a factor of 1.4 ± 0.1 times higher than the actual, measured stellar mass density (Walter et al., 2020), because matter (rather unsurprisingly) does not remain entirely locked up in stars. Stars may return gas to the

[3] the slope of the initial, $z > 4$, rise is still uncertain due to the difficulty of measuring the amount of star formation obscured by dust (e.g. Casey et al., 2018b; Bouwens et al., 2020)

[4] Note that physical and comoving densities are related through the scale factor, $a = 1/(1+z)$, via $n_{\rm physical} = n_{\rm comoving}(1+z)^3$. Thus, the trends in this plot would be stretched by $(1+z)^3$ in physical units.

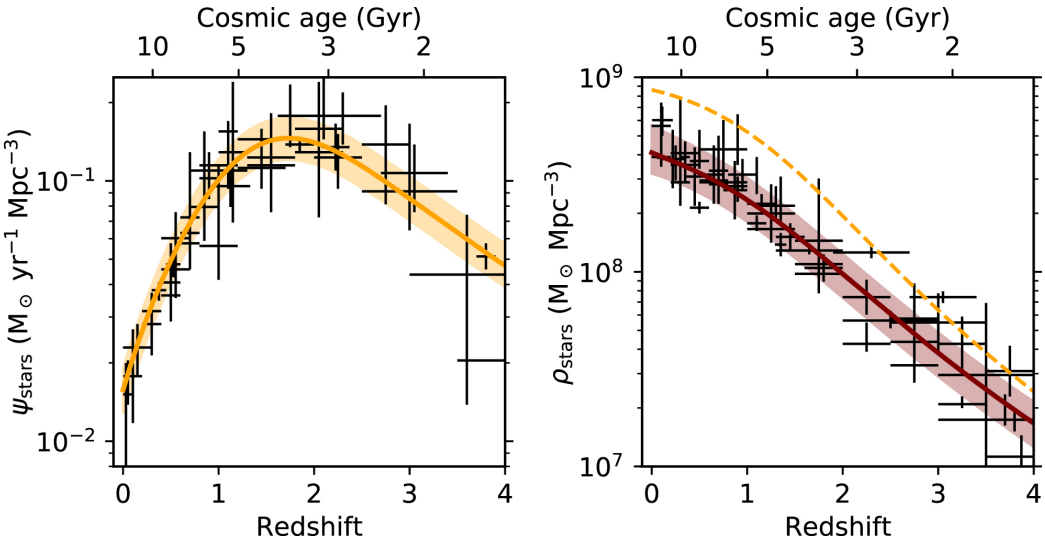

Figure 1.2: The history of star formation on a cosmic scale. The cosmic star formation rate density (SFRD), ψ, and stellar mass density, $\rho_{\rm stars}$, are shown in the left and right panels respectively, as functions of of redshift (bottom axis) and cosmic age (top axis). Both quantities are average per unit comoving volume. The SFRD and stellar mass density measurements are from the compiled set of observations studies in Tables 1 and 2 of (Madau and Dickinson, 2014). The solid curves in each panel denote the best-fit relations, with the shaded regions indicating the 16th to 84th percentile from the Monte Carlo Markov Chain analysis described in Sec. 3.3. of Walter et al. (2020). Integrating the best-fit SFRD in the left panel yields the dashed yellow curve in the right panel, which is higher than the measured stellar mass density due to loss of stellar mass through stellar winds and supernovae. *(Adapted from Fig. 2 of Walter et al. 2020)*

surrounding medium during their lives, through stellar winds, or when they die, in supernova explosions. Accounting for the mass return fraction expected from these two processes leads to a good agreement with the measured stellar mass density (Madau and Dickinson, 2014), implying that very little stellar mass is found outside galaxy disks (as also shown by Behroozi et al., 2013).

Combining the integral of the stellar mass density with the relative abundance and lifetimes of different types of stars, implies that half of the stars in today's Universe formed within the first 5 Gyr (i.e. by $z \sim 1.3$), and of these, most formed at cosmic noon (Madau and Dickinson, 2014). Although this is a neat summary of star formation on a universal scale, it leaves many open questions. *How and where did these stars form? What led to the rapid star formation at $z \sim 2$? Was there simply a greater supply of fuel? Or were stars forming more efficiently than today?* Studies based on computer simulations (e.g. Schaye et al., 2010) have sought to address some of these questions, finding that the build up of stellar mass before $z \gtrsim 4$ can largely be attributed to the increasing number of star-forming galaxies occupying dark matter haloes, whereas the present-day decline is driven more by galaxy-internal processes. However, understanding the interaction between these galaxy-internal processes and the evolution of galaxies on a global scale requires us to fill in the blanks, by observing the *fuel* for star formation.

1.1.3 The Interstellar Medium

Stars are born from the interstellar medium (ISM) and inject enriched matter and energy into the ISM when they die.[(5)] Understanding the physical properties of the ISM is therefore critical to describing how star formation affects galaxies (and vice versa). In general, the ISM consists of gas, dust, cosmic rays, the interstellar radiation field (ISRF) and magnetic fields (e.g. Klessen and Glover, 2016). The dominant component of the gas is hydrogen (H), which makes up 70% of the to-

[(5)] often in a different location to where the stars were born

tal mass. Helium (He) accounts for a further 28% of the gas by mass and the remaining 2% consists of heavier elements, which astronomers crudely lump into the category of "metals". Approximately 1% of the ISM (at least locally) is in solid form, called "dust", consisting primarily of silicates and carbonaceous material. Dust is well-mixed with the gas and acts as a catalyst for the formation of many molecules. Cosmic ray particles also act as catalysts in many chemical reactions and help to regulate the overall energy balance of the gas. Even more importantly, the chemical and thermal states of the gas (and dust) depend on the interaction with the ISRF, which dictates the rates at which molecules are photodissociated and atoms are photoionized. The structure and temperature of the ISM are also regulated to some extent by magnetic fields.

The ISM can be crudely classified into five phases, according to the gas temperature and chemical state of hydrogen (e.g. Ferriére, 2001; Tielens, 2005; Draine, 2011; Kennicutt and Evans, 2012, and references therein).

The hot ionized medium (HIM) typically fills a large portion of the volume of a galaxy ($\lesssim 50\%$) and is characterised by gas at low densities ($n < 0.01$ atoms per cm^{-3}) and temperatures of $T_k \geq 10^5$ K.

The warm ionized medium (WIM) typically fills $\sim 10-30\%$ of a galaxy's volume and consists of gas of $n \lesssim 1\text{cm}^{-3}$ and $T_k \sim 10^4$ K.

The warm neutral medium (WNM) overlaps with the HIM and WIM, filling $\lesssim 40\%$ of the galaxy volume and is comprised of gas with $n \sim 1\text{cm}^{-3}$ and $T_k \sim 0.5-1\times10^4$ K.

The cold neutral medium (CNM) is distributed in filaments or sheets that spread into a disk that is typically co-planar with the stellar disk (in star-forming galaxies) and occupies $\sim 1-4\%$ of a galaxy's volume. It is characterised by gas at $n > 10\text{cm}^{-3}$ and $T_k < 100$ K.

The Molecular Medium (MM) is the coldest and densest region of the ISM, containing as much mass as atomic hydrogen but occupying only $< 1\%$ of the ISM volume (in local galaxies). The molecular ISM is characterised by dense molecular clouds of $n > 100$ cm^{-3} and $T_k \sim 10-20$ K, **which are observed to be the sites of star formation**.

Matter can cycle from one phase to another and be transported within galaxies and their surrounding environment. Inflows from the intergalactic medium supply the galaxy with warm gas. This can cool and settle to become neutral. The neutral atomic gas may move inwards, further cooling and settling into clouds of molecular gas. Conversely, the energy released in stellar winds, supernovae and from black holes may disrupt each phase, ejecting material to the galaxy outskirts or back into the circum- or intergalactic medium.

1.1.4 Star Formation and Molecular Gas

As indicated above, one of the key processes preceding star formation is the formation of molecular gas. Observationally, molecular gas correlates strongly with the star formation rate, from a galactic scale (Kennicutt, 1989; Kennicutt, 1998; Gao and Solomon, 2004; Saintonge et al., 2011), to sub-/kpc-sized regions (Wong and Blitz, 2002; Bigiel et al., 2008; Rahman et al., 2012; Leroy et al., 2013) to the scale of individual giant molecular clouds (GMCs) (Evans et al., 2009; Heiderman et al., 2010; Lada et al., 2010; 2012). The correlation between the gas and SFR surface densities, is typically referred to as the star formation or (Kennicutt-)Schmidt "law" (Schmidt, 1959; Kennicutt, 1998). However, correlation does not imply causation. There is still some debate over whether the presence of molecular gas is necessary to trigger star formation (Krumholz and McKee, 2005; Elmegreen, 2007; Krumholz et al., 2009) or whether molecular gas and star formation are simply co-located due to the ability of the gas to self-shield from intersteller ultraviolet (UV) radiation, thereby allowing it to cool and condense (e.g. Krumholz et al., 2011; Glover and Clark, 2012b).

IMPORTANT NOMENCLATURE

Throughout this thesis, the **star formation rate** of a galaxy is refered to as **SFR** and the stellar mass is denoted by M_*. The relative amount of star formation occuring in different galaxies is commonly defined via the **specific SFR (sSFR)**, i.e. the SFR relative to the stellar mass sSFR = SFR/M_*. The sSFR is also particularly useful in describing the position of a star-forming galaxy in the M_*-SFR plane relative to the main sequence. Symbols with Σ refer to surface densities, e.g. the molecular gas surface density Σ_{mol} (if He is included) and stellar mass surface density, Σ_*. Volume densities are instead denoted by ρ, i.e. ρ_{stars} in this Chapter represent the density of stars averaged over the cosmic volume.

The observed correlation between SFR and H_2 mass defines a **depletion time**,

$$t_{dep} = \frac{M_{mol}}{SFR}, \tag{1.1}$$

which represents the time it would take for the current, measured molecular gas content to be depleted through star formation, assuming that the SFR remains constant at its current value. The inverse of this, from an extragalactic observational standpoint (not the same as the theoretical definition), is the **star formation efficiency, SFE**,

$$SFE = \frac{SFR}{M_{mol}} = \frac{1}{t_{dep}}. \tag{1.2}$$

One convenient way to compare the relative molecular gas and stellar contents of galaxies is via their **molecular gas fraction**,

$$f_{gas} = \frac{M_{mol}}{M_{mol} + M_*} \tag{1.3}$$

although for some situations it is more convenient to express this in terms of the molecular to stellar mass fraction,

$$\frac{M_{mol}}{M_*}. \tag{1.4}$$

Throughout this thesis I also make occasional reference to the infrared (IR), far-infrared (FIR), total-infrared (TIR) luminosity, which is commonly used to derive the SFR via empirical calibrations. Although consistency matters when adopting SFR calibrations, the total IR/FIR luminosity has a number of definitions. In this thesis, I mainly refer to the total bolometric IR or FIR luminosity within 8 – 1000 μm.

This thesis will not enter into the above debate but will simply settle on that the fact that based on observations and simulations *stars form predominantly from molecular gas*, regardless of who triggers what.

The molecular ISM is chemically and dynamically complex, hosting distinct (in terms of density or chemical state) structures called clouds, which contain the denser structures that are the sites of star formation. Molecular clouds appear to constitute the bulk of the molecular ISM in most local galaxies, although for galaxies with high gas surface densities a greater component of molecular gas may be found in a diffuse H_2 component (Papadopoulos et al., 2012a; Papadopoulos et al., 2012b; Pety et al., 2013; Colombo et al., 2014). Molecular clouds also exist in a variety of sizes (and shapes), with a complex hierarchy of filamentary and clumpy structure contained within them. The smallest clouds in the Milky Way have masses of $10^2\,M_*$ and are located in the

outer disk (e.g. Brand and Wouterloot, 1995; Heyer et al., 2001) and at high Galactic latitudes (e.g. Magnani et al., 1985), whereas the largest have masses of $10^7\,M_*$ and are located in the aptly-named Central Molecular Zone (e.g. Oka et al., 2001). Most of the molecular gas in the local Universe is thought to be contained in GMCs (e.g. Casoli et al., 1984; Dame et al., 1986), which have masses of 10^5 to $10^6\,M_\odot$ and extend over a few tens of parsecs. In local galaxies, GMCs appear to be most heavily clustered in the inner disks and spiral arms regions (e.g. Colombo et al., 2014), although massive clouds have also been observed in interarm regions (as in M51; Hughes et al., 2013). Whether the sites and size distribution of molecular clouds differ at high redshift remains unclear as individual clouds have yet to be resolved beyond the local Universe. For now, what is clear is that the amount of star formation occuring in galaxies, from the local to the distant Universe, correlates with their molecular gas content.

1.1.5 "Normal" Star-forming Galaxies

Our understanding of how stars form from the molecular ISM and how this process affects galaxies (and vice versa) is largely driven by studies of particular types of *star-forming galaxies*. But what denotes a star-forming galaxy? Early on, it was recognised that there is a bimodality to the colours of galaxies. Whereas galaxies that are still actively forming stars appear blue, galaxies that have mostly ceased forming stars appear red "and dead" and are dubbed "quiescent" galaxies. Other galaxy properties also appear bimodal, separating star-forming and quiescent galaxies, e.g. star-forming galaxies have disky, spiral structures, whereas quiescent galaxies are elliptical (here I am only referring to the visible structure, i.e. the distribution of gas and stars).

Although star-forming galaxies are blue and disky, they are far from a homogeneous population. They exhibit a range of morphologies, some host actively accreting supermassive black holes, i.e. active galactic nuclei (AGN), in their centres, some are part of denser clusters of galaxies whereas others are isolated, some have winds/outflows, etc. This implies that there is no such thing as a "normal" star-forming galaxy. Despite these differences, however, there appears to be a dominant population of star-forming galaxies, which follows at least one trend. This population[(6)] forms a tight sequence in the stellar mass-SFR plane, now dubbed the "main sequence" (see Fig. 1.3), where galaxies with higher stellar masses have higher SFRs. These "main-sequence galaxies" are responsible for most ($\sim 68\%$ Schreiber et al., 2015) of the stars formed at $z \sim 0-4$. Most of the remaining star formation occurs in the galaxies above the main sequence, dubbed "starbursts", and only very little occurs in the "quiescent" galaxies below the main sequence. Although the exact functional form of the main sequence (e.g. the flattening/turnover at high masses) and normalisation vary for different studies due to the impact of selection biases, galaxy morphology and the wavelength range used to measure the SFR, at least two general statements appear to remain true: (1) the scatter about the best-fit line is quite tight, with a dispersion of ~ 0.3 dex in SFR for a given stellar mass (e.g. Schreiber et al., 2015), and, (2) the main sequence evolves from at least $z \sim 4$ to today, driving the decline in the cosmic SFRD (e.g. Whitaker et al., 2012; Schreiber et al., 2015; Leslie et al., 2020). This makes main-sequence galaxies the most popular targets for understanding cosmic trends.

Irrespective of their position relative to the main sequence, star-forming galaxies may also be classified according to their brightness (or lack of emission) in particular wavelengths, leading to a bewildering host of acronyms, e.g. LBGs, LAEs, BzKs, DRGs, DOGs, LIRGs, ULIRGs and SMGs. The latter two are mentioned on multiple occasions throughout this thesis, as they are bright in a wavelength regime that will later become the focus of this work. ultra-luminous infared galaxies (ULIRGs) are classified according to their high bolometric IR luminosities of $L_{8-1000\mu m} > 10^{12} L_\odot$ (Lonsdale et al., 2006), and were first observed in large numbers by the Infrared Astronomical Satellite. Their bright IR emission is powered by a central starburst or AGN, which heats up a large

[(6)] historically these have been mass-selected galaxies

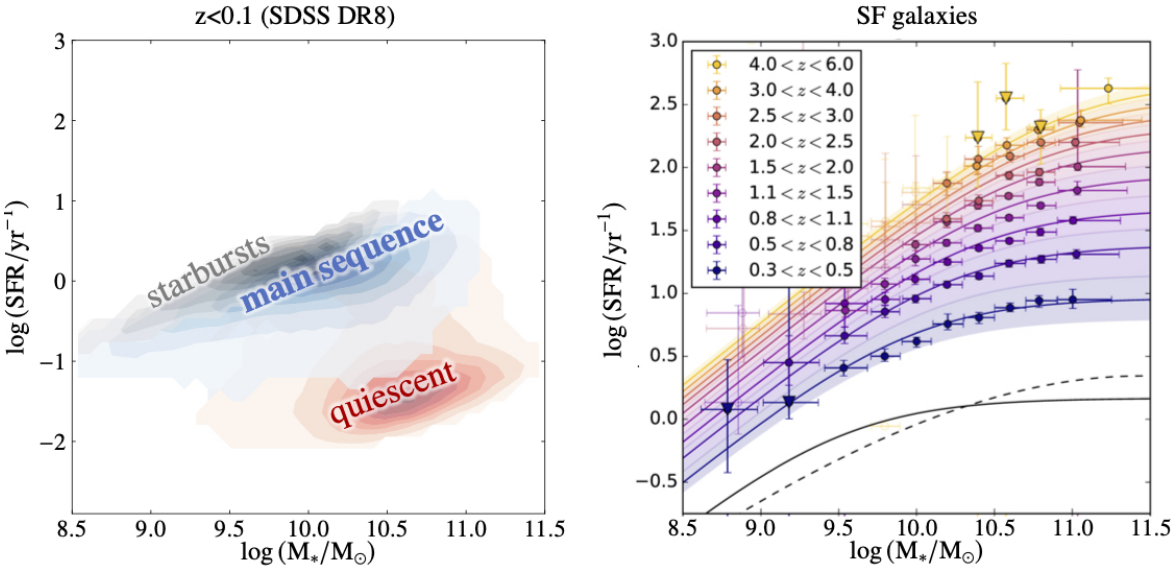

Figure 1.3: The position of star-forming galaxies in the SFR-stellar mass plane. **Left:** Local galaxies from the 8th data release of the Sloan Digital Sky Survey (classifications as in the catalogue Aihara et al., 2011). The majority of galaxies form two sequences; the blue sequence occupied mainly by main-sequence star-forming galaxies and the "red and dead" quiescent population. A smaller fraction of star-forming galaxies, lies above the main sequence. **Right:** The position of star-forming galaxies, binned in stellar mass, at different epochs along with the best-fit main-sequence relations from Leslie et al. (2020) (their Fig. 4). The dashed line is the MS for the SDSS galaxies from Saintonge et al. (2016) whereas the solid black line is the extrapolation of the Leslie et al. (2020) best-fit function to $z = 0.035$.

central dust reservoir. ULIRGs are typically found in major disk mergers and tend to occupy the "starburst" region of the stellar mass-SFR plane. Like ULIRGs, submillimetre(-selected) galaxies (SMGs) have large dust reservoirs. However, SMGs were originally selected from ground-based single-dish submillimetre observations, and are classified as having 850 µm flux densities of > 1 mJy (Blain et al., 2002). They typically also have high stellar masses ($\gtrsim 10^{11}$M$_\odot$) and very high SFRs ($10^2 - 10^3$M$_\odot$yr^{-1} Blain et al., 2002), which mostly places them in the "starburst" category, although some can be classed as main-sequence galaxies. A thorough overview of these and other IR-selected galaxies, which are more generally referred to as dusty star-forming galaxies (DSFGs), can be found in Casey et al. (2014).

1.2 OBSERVING COLD, MOLECULAR GAS

Measuring the total content and distribution of molecular gas in galaxies across cosmic epochs is a crucial step in describing how and where gas is converted into stars. Because the molecular ISM is cold, it is best observed via long-wavelength, i.e. FIR-to-radio emission (Fig. 1.4), but, interpreting these observations is far from trivial. The brightest emission stems from trace components of the ISM and does not scale in a straightforward manner with its total mass. Moreover, the emission that has been painstakingly calibrated in the local Universe becomes difficult to observe at high redshifts, leading astronomers to resort to even more indirect methods.

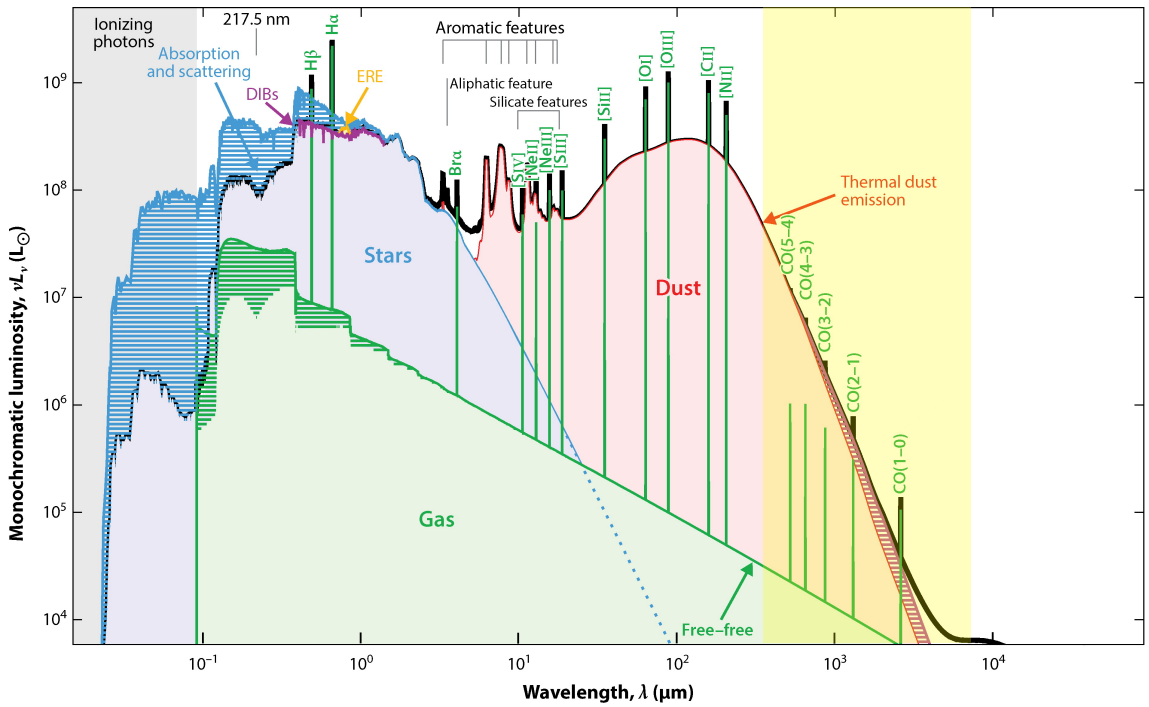

Figure 1.4: Model of the spectral energy distribution (SED) of a typical star-forming galaxy, shown with the monochromatic luminosity as a function of the *rest-frame* wavelength. To trace the cold, molecular gas astronomers rely on FIR-to-radio wavelength observations (light yellow shaded region) of the thermal dust emission (red line) and molecular/atomic lines, particularly the rotational transitions of CO (labeled green lines). The observed SED up to ~ 3000 μm (shown in black) is the sum of the gas emission plus the intrinsic stellar emission (blue) that is reprocessed by dust (red). *(Adapted from Fig. 1 of Galliano et al. (2018).)*

1.2.1 The Need for "Tracers"

At the high densities typical of star-forming regions, hydrogen exists mostly in its molecular form H_2, which nature has conspired to make particularly difficult to observe[7]. H_2 barely emits at the ~ 10s of K typical of star-forming regions, due to the mirror symmetry of its structure[8] and, more importantly, the low mass of hydrogen atoms (e.g. Varsavsky, 1966). As a diatomic molecule, H_2 effectively has three types of excitation: electronic, vibrational and rotational. The rotational excitation states, of which the first four are shown in Figure 1.5, are the lowest in energy. Because of the low mass of the H atoms[9], the first excited state ($J = 1$) is 175 K above the ground state (Fig. 1.5), a temperature so high that almost no molecules in the cold and dense ISM will occupy it. The fact that H_2 is a homonuclear molecule only worsens the situation because the $J = 1 \rightarrow 0$ transition is forbidden for reasons of symmetry. Thus, the first allowed transition is from the $J = 2$ state, at 510 K, to the ground state. For warmer regions of molecular gas, this transition (at 28 μm) may be detected by sensitive infrared instruments on large ground-based and space-based telescopes, especially the *Spitzer Space telescope*, the eternally-upcoming *James Webb Space Telescope* (JWST) and the Extremely Large Telescope (ELT) (Togi and Smith, 2016), but it remains an unviable way of detecting the cold gas in distant galaxies.

Since observations of H_2 are not a viable option, astronomers have instead come to rely upon the emission from rarer components of the cold, molecular ISM to probe the total content and dis-

[7] In contrast, the neutral, atomic form of hydrogen is readily detected for galaxies up to $z \sim 0.3$, through observations of the 21 cm emission that results when the relative spins of the hydrogen atom's electron and nucleus (proton) "flip" from parallel to anti-parallel.

[8] i.e. the lack of a permanent dipole moment

[9] for a quantum oscillator, the level spacing varies with $m^{-1/2}$, where m is the reduced mass

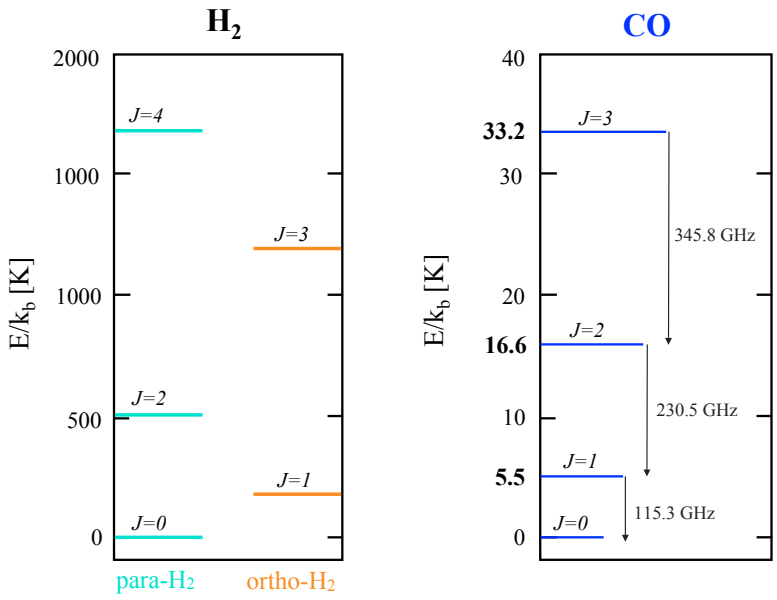

Figure 1.5: Energy level diagrams for the rotational (i.e. lowest energy) transitions for H_2 (left) and CO (right). H_2 level data are taken from `http://www.gemini.edu/sciops/instruments/nir/wavecal/h2lines.dat`, whereas the CO level data are from `https://home.strw.leidenuniv.nl/~moldata/datafiles/co.dat`. The even J state of H_2 is referred to as para-H_2 whereas the odd J state is referred to as ortho-H_2. Transitions with $\Delta J = 1$ (between para- and ortho-states) are forbidden for H_2.

tribution of star-forming gas. For galaxies beyond the local Universe, there are currently two main options: the emission from rotational transitions of carbon monoxide (CO) or thermal dust emission. In the local Universe, it is also possible to observe a host of other atomic and molecular lines or to use dust absorption. However, this thesis focuses on distant galaxies, for which such methods are only relevant as calibrators of the ones described below and will therefore be mentioned in passing, if at all.

1.2.2 CO line emission

From the local to the distant Universe, most of our understanding of the content and distribution of molecular gas comes from observations of carbon monoxide (CO), the second most abundant molecule in the ISM and the primary coolant of molecular gas. Unlike H_2, CO is a heteronuclear diatomic molecule, consisting of nuclei of much greater masses than H. Thus, the lowest rotational transitions of CO have a much lower excitation energy than H_2, beginning at 5.5 K for the ground transition (Fig. 1.5). Even transitions from states with higher rotational quantum numbers, J, have a lower excitation energy than the ground transition of H_2, making them readily detectable for local and high-redshift galaxies.

For local galaxies, and the individual molecular clouds within them, the ground transition of CO, i.e. CO $J = 1 \rightarrow 0$, is the golden standard and the tracer against which other H_2 proxies are most commonly calibrated. For brevity I will use the shorthand notation, CO(1-0), in place of CO $J = 1 \rightarrow 0$ from here onwards. CO(1-0) is easily excited, even in cold molecular clouds, not only due its low excitation energy but also its lower critical density (which is further reduced by radiative trapping) (e.g. Bolatto et al., 2013). Moreover, for local sources, the 2.6 mm emission from CO(1-0) lies in a relatively transparent atmospheric window. Thus, CO(1-0) has been laboriously calibrated as a molecular gas tracer.

1.2.2.1 The CO(1-0)-to-Molecular Gas Mass Conversion Factor

Inferring the molecular gas mass, $M_{\rm mol}$, from the luminosity of the CO(1-0) line, $L'_{\rm CO(1-0)}$, requires the application of the conversion factor, $\alpha_{\rm CO}$, via,

$$M_{\rm mol} = \alpha_{\rm CO} L'_{\rm CO(1-0)} \,. \tag{1.5}$$

Early calibrations of the conversion between CO(1-0) observation and H_2 were performed using observations of individual GMCs. Since individual local GMCs can be spatially resolved, the locally-calibrated conversion factor, $X_{\rm CO}$, is defined as the H_2 column density relative to the velocity-integrated CO(1-0) surface brightness (see Appendix A for the conversion between this and $\alpha_{\rm CO}$). The $X_{\rm CO}$ factor has been calibrated by comparing the brightness of ^{12}CO emission to H_2 column densities estimated via multiple techniques. These include:

a) using the measured CO linewidths of resolved GMCs to infer the cloud masses, assuming the clouds are in dynamic equilibrium (i.e. virialised), and applying the measured sizes to infer the H_2 column densities (e.g. Solomon et al., 1987; Scoville et al., 1987),
b) using observations of optically-thin CO isotopologues (e.g. ^{13}CO) to directly infer their column densities, typically under the assumption that the gas is in local thermodynamic equilibrium, and accounting for the fractional abundance of the isotopologue relative to ^{12}CO and the fractional abundance of ^{12}CO relative to H_2 (e.g. Goldsmith et al., 2008),
c) converting measurements of optically-thin dust-continuum emission or dust extinction to dust column densities and applying an assumed dust-to-gas ratio (e.g. Dame et al., 2001; Goldsmith et al., 2008; Pineda et al., 2008; Planck Collaboration et al., 2011b),
d) converting the emission from > 200-MeV γ-rays, released following collisions between cosmic rays and interstellar matter, to a total nucleon number density which can then be converted to a H_2 column density via a measurement of the neutral hydrogen (HI) column density and an assumed He-to-H abundance ratio (Strong and Mattox, 1996; Grenier et al., 2005).

These methods (and the studies that employed them) are summarised in the review of Bolatto et al. (2013), who conclude that for GMCs in the Milky Way, values of $X_{\rm CO} = 2 \times 10^{20}$ H_2 molecules per cm^{-2} (K km s^{-1})$^{-1}$, equivalent to 4.3 M$_\odot$ (K km s^{-1} pc^2)$^{-1}$ are appropriate.

Unfortunately, $\alpha_{\rm CO}$ is far from a universal constant. Both observation- and simulation-based studies show that $\alpha_{\rm CO}$ varies with physical properties such as the gas temperature and density, metallicity, strength of the local ionising radiation field and the cosmic ray ionisation rate (e.g. Glover and Mac Low, 2011; Ostriker and Shetty, 2011; Feldmann et al., 2012a; b; Shetty et al., 2011; Narayanan et al., 2012; Papadopoulos et al., 2012a; Schruba et al., 2012; Leroy et al., 2013; Narayanan and Hopkins, 2013). Early work showed that the molecular gas masses inferred when assuming a Milky Way $\alpha_{\rm CO}$ factor are close to or indeed exceed the dynamical masses[(10)] in ULIRGs (Downes et al., 1993; Bryant and Scoville, 1996; Bryant and Scoville, 1999; Downes and Solomon, 1998). These low implied $\alpha_{\rm CO}$ values were quantified by Downes and Solomon (1998)[(11)], who found characteristic values of 0.8 M$_\odot$ (K km s^{-1} pc^2)$^{-1}$. Likewise, lower-than-Milky-Way factors have been measured for nearby galactic nuclei (e.g. Meier and Turner, 2004; Meier et al., 2008) and the Milky Way's central region (e.g. Oka et al., 1998). Although such estimates are possible for local galaxies, it remains unfeasible at high redshift. Some studies have attempted to infer $\alpha_{\rm CO}$ by comparing the dynamical mass obtained though observations of line emission to the total CO luminosity, assuming a certain gas-to-total matter fraction (Tacconi et al., 2008; De Breuck et al., 2014), but this approach cannot provide robust constraints, at best indicating a similar range of values to those measured locally.

[(10)] which should represent the total mass of the galaxy
[(11)] who modelled the radiative tranfer and gas dynamics using observations of CO(1-0) and 100 µm dust-continuum obervations

1.2.2.2 Using higher-J CO emission

Ignoring the problem of the α_{CO} conversion factor, there is another obstacle to converting CO observations at high redshift to measurements of molecular gas masses (or surface densities); observing CO(1-0) from galaxies beyond $z \sim 1$ remains technically challenging. Few facilities operate at the long wavelengths needed to observe CO(1-0) beyond $z \sim 1$, and even with the most sensitive radio-wavelength facility, the Karl G. Jansky Very Large Array (VLA), it typically takes tens of hours to observe the unresolved CO(1-0) emission from gas-rich galaxies. Thus, observing the local workhorse, CO(1-0), is impractical for large samples of high-redshift galaxies[12]. Instead, it has become common for higher-redshift studies to target CO transitions with $J > 1$, which are easily accessible with sub-/millimeter facilities, particularly ALMA and the NOrthern Extended Millimeter Array (NOEMA).

Inferring the molecular gas content from higher-J CO lines requires the additional step of down-converting the observed CO line intensity to the CO(1-0) line intensity. This excitation correction may be performed by either; 1) assuming thermalized level populations, for which the line brightness temperature ratios are unity, or, 2) by applying line ratios measured for "similar" galaxies (i.e. with similar selection criteria or inferred physical properties). However, CO excitation ladders have only been observed for a limited number of bright, high-redshift sources, including quasar host galaxies (QSOs) and SMGs. Most of the observed QSOs appear to have near-thermalized level populations, indicating that they are dominated by a warm and/or dense gas component (e.g. Oteo et al., 2017a; Cañameras et al., 2018) but SMGs display a wide range of excitation, with CO(3-2)-to-CO(1-0) luminosity ratios ($r_{31} = L'_{CO(3-2)}/L'_{CO(1-0)}$) spanning from 0.3 to 1.1.

To down-convert the high-J line luminosities of star-forming galaxies, particularly those conforming to the main sequence, most studies assume that high-J lines are subthermally excited, with $r_{31} \sim 0.5$ (e.g. Tacconi et al., 2013; 2018; Genzel et al., 2015; Aravena et al., 2019; Decarli et al., 2019). This appears to be consistent with, and has been motivated by, the first excitation study of star-forming galaxies of moderate IR luminosities, Daddi et al. (2015). For the three sources in their sample with CO(1-0) observations, Daddi et al. (2015) measured a mean line ratio of $r_{32} = 0.42 \pm 0.07$. However, it remains is unclear for what fraction of high-redshift galaxies this subthermal excitation holds true. Indeed for the small sample of main-sequence galaxies in Boogaard et al. (2020), we measured higher line ratios, which are consistent with thermalized level populations. Excitation studies therefore remain an active area of research, as outlined in the final Chapter. Nevertheless, for measurements of the total molecular gas mass of galaxies these uncertainties play no more of a role than the uncertainty on α_{CO}.

1.2.3 Dust Emission

One of the most efficient ways of studying molecular *gas* is to use observations of thermal *dust* emission. Dust is well mixed with the gas in the ISM and acts as a catalyst for the formation of H_2. Moreover, dust absorbs a significant fraction of the UV-to-optical wavelength stellar radiation in the Universe (e.g. ~ 19% in the local Dustpedia galaxy sample; Bianchi et al., 2018), re-emitting this energy in the IR. Thus, the total IR luminosity is one of the most reliable and widely-used tracers of the star formation rate of galaxies. At longer wavelengths, however, the dust emission is optically thin, thereby becoming a "good" tracer of the gas column density and mass. This statement will be dissected further in Chapters 2 and 3, but for now I will start with a brief outline of why and in what regime dust is a "good" tracer of molecular gas.

Dust emission is comprised of at least three distinct components, the sum of which is shown in red as the full dust spectral energy distribution (SED) in Fig. 1.4. The characteristic emission features at $\sim 3-20\,\mu$m arise from the molecular bands of Polycyclic Aromatic Hydrocarbons (PAHs),

[12] This will soon change as Bands 1 and 2 of ALMA come online

whereas at longer wavelengths, the effects of the main dust grain population dominate. The emission at $\sim 20 \rightarrow 60\,\mu$m stems mainly from small grains (with sizes of $\lesssim 0.01\,\mu$m) that are stochastically heated by the intense radiation fields near star-forming regions. Conversely, at longer wavelengths ($\gtrsim 60\,\mu$m) the emission stems mainly from larger grains (with sizes of $0.01 \rightarrow 0.25\,\mu$m), which are in thermal equilibrium with the radiation field (Draine, 2003). The overall shape of the dust SED is therefore determined by the relative sizes of different dust grain populations, the temperature of the grains and the dust opacity as a function of wavelength/frequency.

Since the large dust grains are in thermal equilibrium with the radiation field, the long-wavelength tail of the dust emission tends tends to be optically thin and is well described by the Rayleigh Jeans approximation. A uniform population of dust grains, with a temperature $T_{\rm d}$ will radiate as a blackbody, with the intensity of the thermal emission (in W sr^{-1} m^{-2} Hz^{-1}) described by Planck's Law,

$$B_\nu(T_{\rm d}) = \frac{2h\nu^3}{c^2}\frac{1}{e^{\frac{h\nu}{k_{\rm B}T}}-1}\,, \tag{1.6}$$

where c is the speed of light, h is the Planck constant, ν the frequency of the emission and $k_{\rm B}$ is the Boltzmann constant. At long wavelengths, this may be approximated by the Rayleigh-Jean's law,

$$B_\nu(T_{\rm d}) = \frac{2\nu^2 k_{\rm B} T}{c^2}\,. \tag{1.7}$$

The observed dust-continuum flux density of a source, S_ν, at a distance, d_L, from the observer is described by,

$$S_\nu = \frac{(1-e^{-\tau(\nu)})B_\nu(T_{\rm d})(1+z)}{d_L^2} \tag{1.8}$$

where the dust optical depth, τ may be expressed in terms of the opacity coefficient κ,

$$\tau_{\rm d} = \kappa_{\rm g}(\nu) M_{\rm g} = \kappa_{\rm d}(\nu) M_{\rm d}\,. \tag{1.9}$$

Note that κ can either be expressed per unit dust mass κ_d or per unit gas mass, $\kappa_{\rm g}$, depending on the methodology of the calibration. Thus, in the optically-thin, Rayleigh Jeans limit, the observed flux density is directly proportional to the dust mass, the opacity coefficient, the dust temperature, and the square of the emitted frequency,

$$S_\nu \propto \frac{\kappa_{\rm d}(\nu) T_{\rm d} \nu^2 M_d}{d_L^2}\,. \tag{1.10}$$

This expression implies that long-wavelength continuum emission is a good tracer of the molecular gas mass, $\rm M_{mol}$, provided one has good constraints on the dust opacity, the average dust temperature and the dust-to-molecular gas mass ratio, $M_d/\rm M_{mol}$. However, as outlined below, the assumptions on the dust opacity, dust temperature and DGR, can each introduce a factor of a few uncertainty, which combines to a similar level of uncertainty as that on the $\alpha_{\rm CO}$ factor (more on this in Chapter 2).

1.2.3.1 Dust Opacity

From observations of the ISM in our own and in nearby galaxies, it is possible to calibrate the dust opacity as a function of frequency,

$$\kappa(\nu) = \kappa(\nu_{\rm ref})(\nu/\nu_{\rm ref})^\beta = \kappa_{\rm ref}(\lambda/\lambda_{\rm ref})^{-\beta} \tag{1.11}$$

which involves two aspects: (1) the spectral index β, which relates flux measurements at different wavelengths, and (2) the dust opacity per unit mass at some reference wavelength. Both theoretical models (Draine, 2011) and empirical fits to the observed FIR SEDs of local galaxies (e.g. Dunne

et al., 2000; Clements et al., 2010) imply that $\beta = 1.5-2$. More recently, the Planck collaboration used extensive observations covering the Milky Way, finding $\beta = 1.8 \pm 0.1$ with no significant difference between HI- and H_2-dominated regions (Planck Collaboration et al., 2011a). Whether this value is also representative of high-redshift galaxies is an ongoing matter of debate. A common choice for the reference wavelength is the rest-frame 850 µm ($\nu_{850\mu m}$ = 350 GHz) for which the value of $\kappa_{850\mu m} = 0.77\,g^{-1}\,cm^{-2}$ is commonly adopted (Draine and Lee, 1984).

1.2.3.2 Dust Temperature

To determine the dust mass from a single-band dust-continuum measurement requires an assumption of the temperature that can be considered directly proportional to the dust mass. According to Scoville et al. (2014), 2016 this is best approximated by the mass-weighted dust temperature, $\langle T_d \rangle_M$. They argue that the mass-weighted dust temperature is representative of the bulk of the dust and scales propotionally to the temperature whereas the temperatures typically measured by fitting templates or modified blackbodies to the IR dust SEDs, which they call the "luminosity-weighted" temperatures, are not representative of the bulk of the dust. The simulation-based study of Liang et al. (2019) would appear to support this mass-weighted temperature argument, showing that dust temperatures that are measured based on the peak of the dust SED (not the same as a luminosity-weighted value or template/modified blackbody fit) are systematically higher (by ~ 10 degrees) than the mass-weighted values, increasing with the star formation activity. The simulated $z = 2-6$ star-forming galaxies of Liang et al. (2019) exhibit mass-weighted temperatures spanning $15-40$ K [13]. Similarly, local star-forming galaxies have mean mass-weighted dust temperatures of $\langle T_d \rangle_M \sim 15-35$ K (Scoville et al., 2014). Thus, the representative mean value advocated by Scoville et al. (2014), 2016 is $\langle T_d \rangle_M = 25$ K.

More recently, the issue of temperature definitions has been revisited by Harrington et al. (2021), who test the assertion of Scoville et al. (2014) and 2016 and Liang et al. (2019) that most of the dust mass of high-redshift galaxies can also be described by $\langle T_d \rangle_M = 25$ K. Harrington et al. (2021) also test the actual "luminosity-weighted" temperatures and not the values derived through template/modified blackbody fits. Their results indicate that the mass- and luminosity-weighted temperatures of their sample of $z = 1-3.5$ starbursts are consistent, spanning $\langle T_d \rangle_M = 25-55$ K. Combining these results implies that although there is some debate over temperature definitions, the dust temperatures relevant for inferring dust masses likely vary within a factor of a few.

1.2.3.3 Dust-to-Gas Mass Ratio

For regions of the ISM with roughly solar metallicity, the DGR is ~ 1 : 100. However, the DGR decreases with decreasing metallicity, as shown for nearby and local group galaxies (e.g. Leroy et al., 2011; Sandstrom et al., 2013; Rémy-Ruyer et al., 2014), reaching values of ~ $1 : 10^5$ in local dwarf galaxies. These effects can be calibrated (Leroy et al., 2011; Sandstrom et al., 2013) such that the metallicity can be used to predict the DGR. However, for many high-redshift galaxies, robust metallicity measurements are non-existent and difficult to obtain. To circumvent this issue for main-sequence galaxies one can use the empirically calibrated stellar mass-metallicity relation to infer an approximate metallicity (e.g. Genzel et al., 2015) and thereby guess the correct order of magnitude for the DGR, e.g. $z \sim 2$ main-sequence galaxies of $M_* \sim 10^{10}$ exhibit a mean metallicity consistent with the solar value with a dispersion of ~ 0.2 – 0.4 dex about the mean (e.g. Zahid et al., 2014b; Torrey et al., 2019; Sanders et al., 2020).

[13] (with the minimum temperature increasing slightly with redshift due to the CMB)

1.3 OBSERVATIONS OF THE MOLECULAR GAS IN DISTANT GALAXIES

Prior to the last decade, little was known about the distribution and properties of cold, molecular gas in galaxies beyond $z \sim 1$. To observe the molecular ISM, astronomers relied on:

a) a handful of single-dish submillimetre telescopes, namely the James Clerk Maxwell Telescope (JCMT; Robson et al., 2017), the IRAM 30-metre telescope (Baars et al., 1987), the Atacama Submillimetre Telescope Experiment (ASTE; Ezawa et al., 2004), the Atacama Pathfinder EXperiment (APEX; Güsten et al., 2006), and the South Pole Telescope (SPT; Carlstrom et al., 2011),
b) early submillimeter interferometers, namely the Submillimetre Array (SMA; Ho et al., 2004) and the Plateau de Bure interferometer (PdBI; Guilloteau et al., 1992), which has been succeeded by NOEMA, and,
c) radio-wavelength interferometers, especially the VLA (Thompson et al., 1980; Perley et al., 2011) and to a lesser extent, the Australia Telescope Compact Array (ATCA; Frater et al., 1992).

At $z > 5$, these facilities could only detect the emission from the brightest SMGs or QSOs (as summarised in the compilation of pre-2013 high-redshift detections in Carilli and Walter, 2013). Within the redshift range $z \sim 1-3$ there were multiple detections, but only few observations of molecular gas at sub-galactic scale resolution. The angular resolution of the single-dish facilities (at best 15", corresponding to $\gtrsim 100$ kpc at $z \sim 2$) was often insufficient to distinguish inidividual galaxies, let alone resolve their gas morphology. Moreover, the existing interferometers lacked the sensitivity to resolve the molecular gas in normal galaxies, limiting such studies to a handful of the very brightest sources, particularly GN20 (Younger et al., 2008; Hodge et al., 2012; 2013; 2015), and the most strongly magnified ones, particularly the "Cosmic Eyelash" (Swinbank et al., 2010; 2011). Thus, the content, morphology and dynamics of the cold gas in most $z > 1$ star-forming galaxies were largely unconstrained.

Since 2011, studies of the molecular ISM of distant galaxies have progressed dramatically, becoming ever more "mainstream" at Cosmic Noon and becoming more feasible at higher redshifts. Whereas the molecular gas contents were only known for a few tens of galaxies before 2011, they have now been measured for many hundreds of galaxies. These samples (described in Sec. 1.3.2 and 1.3.4) include not just the bright SMGs and QSOs studied previously but also more commonplace main-sequence galaxies at $z \sim 1-3$. Moreover, cold gas is now routinely being detected up to $z \gtrsim 4$ in lensed star-forming galaxies (e.g. Oteo et al., 2017a; Béthermin et al., 2018; Dong et al., 2019; Apostolovski et al., 2019), unlensed dusty and highly star-forming galaxies (e.g. Williams et al., 2019; Riechers et al., 2021) and QSOs (e.g. Venemans et al., 2017; Feruglio et al., 2018; Wang et al., 2019; Bischetti et al., 2021). This progress has come largely thanks to ALMA (Fig. 1.6), which began operating in 2011, as well as the expanded capabilities of NOEMA.[14].

1.3.1 ALMA

Before summarising the progress made over the last decade, it is worth admiring ALMA, the remarkable observatory that enabled much of this work. ALMA is situated at 5000 m above sea level in one of the driest places on Earth, the Atacama Desert. These high-and-dry conditions are crucial for optimising the amount of light received from the cold Universe, because the water vapour in the Earth's atmosphere absorbs radiation at sub-/millimeter wavelengths. This column of offending water vapour is measured in terms of the "precipitable water vapour" (pwv), the vertical column of water in the atmosphere, from the Earth's surface to the upper edge of the troposphere, that is potentially available for precipitation. During the driest season (winter) the pwv is mostly < 1 mm.[15] In comparison, the average pwv over the winter observing semester at the Plateau de

[14] With the addition of the 7th 15 m antenna in 2014 the Plateau de Bure interferometer (PdBI) became NOEMA At the time of writing NOEMA has ten 15 m antennas

[15] ALMA Cycle 7 Proposer's Guide: https://almascience.org/documents-and-tools/cycle7/alma-proposers-guide

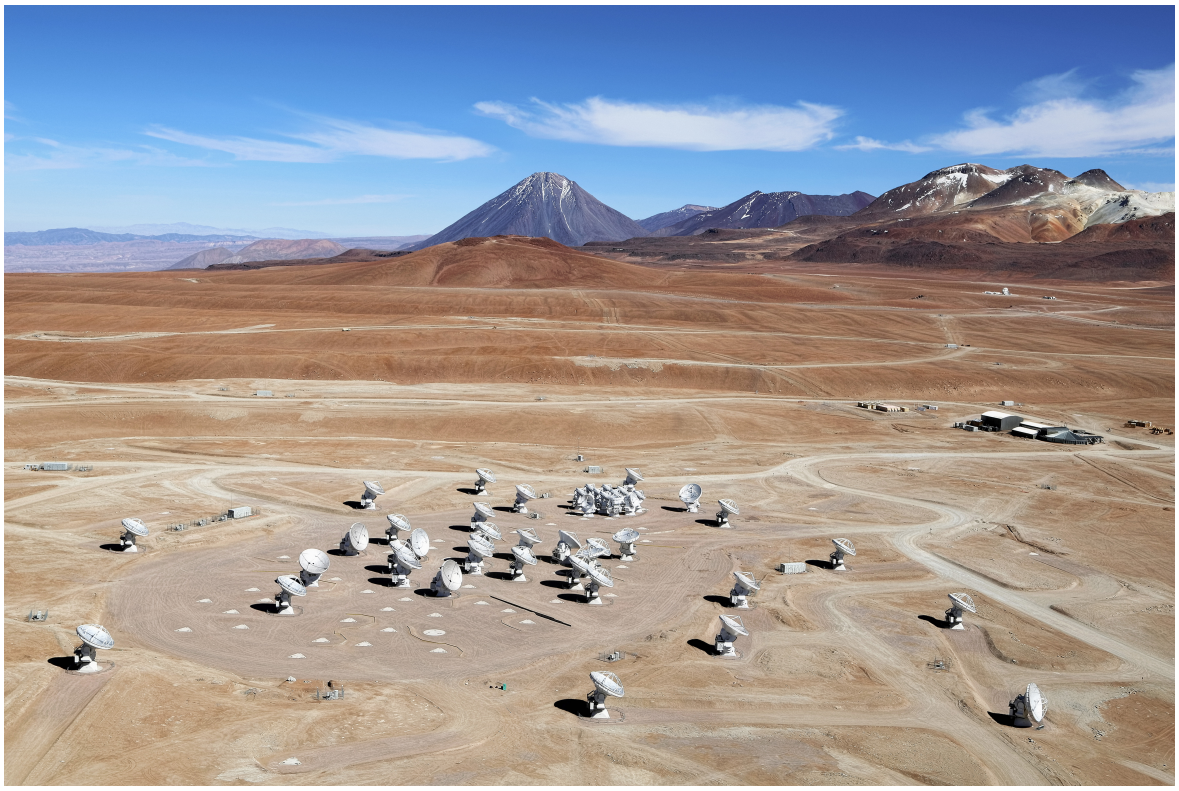

Figure 1.6: An aerial view of ALMA on the Chajnantor Plateau, located at an altitude of 5000 m in the Atacama desert in Chile. The 12 smaller antennas in the centre of the image, each with a diameter of 7 m, make up the ALMA Compact Array (ACA). The larger surrounding antennas have a diameter of 12 m each. On the horizon, the main peaks from right to left are Cerro Chajnantor, Cerro Toco, and Juriques. *Image Credit: Clem & Adri Bacri-Normier, 2012 (wingsforscience.com)/ESO*

Bure (where NOEMA is situated) is ~ 4 mm (Raymond et al., 2021), whereas in Heidelberg (where nobody would dream of building such a telescope) the mean pwv is ~ 20 mm.

ALMA consists of 66 antennas in total; fifty with a diameter of 12 m, comprising the main, configurable array, twelve with a diameter of 7 m, making up the central Atacama Compact Array (ACA), and four more with a diameter of 12 m in the Total Power Array (TPA). These antennas can be arranged in up to ten different configurations, with the maximum distance between two antennas (the maximum baseline) varying from 150 m to 16 km. Changing the maximum baseline provides the interferometric equivalent of a camera's variable "zoom".

The location, configuration and instrument design of ALMA have given it a number of key advantages over previous sub-/millimeter telescopes.

Angular Resolution: In the most extended configuration, the angular resolution probed by ALMA ranges from 20-40 milliarcseconds, for observations at ~ 1.2 – 3 mm respectively, corresponding to physical scales of a few hundred parsec in a $z \sim 2$ galaxy.

Sensitivity: ALMA's point source sensitivity is 10 – 100× better for continuum observations and 10–20× better for spectral lines, compared to previous sub-/millimeter telescopes, allowing it to detect much fainter (i.e. less gas-rich) galaxies. This higher sensitivity is particularly important for resolving the emission from faint sources, since conserving the surface brightness sensitivity when increasing the angular resolution by a factor of x, requires an increase in sensitivity of x^2.

Frequency coverage: The currently-available receiver bands of ALMA, Bands 3-10, offer an almost-continuous frequency coverage from 84-950 GHz (0.4-2.6 mm). With Bands 1 and

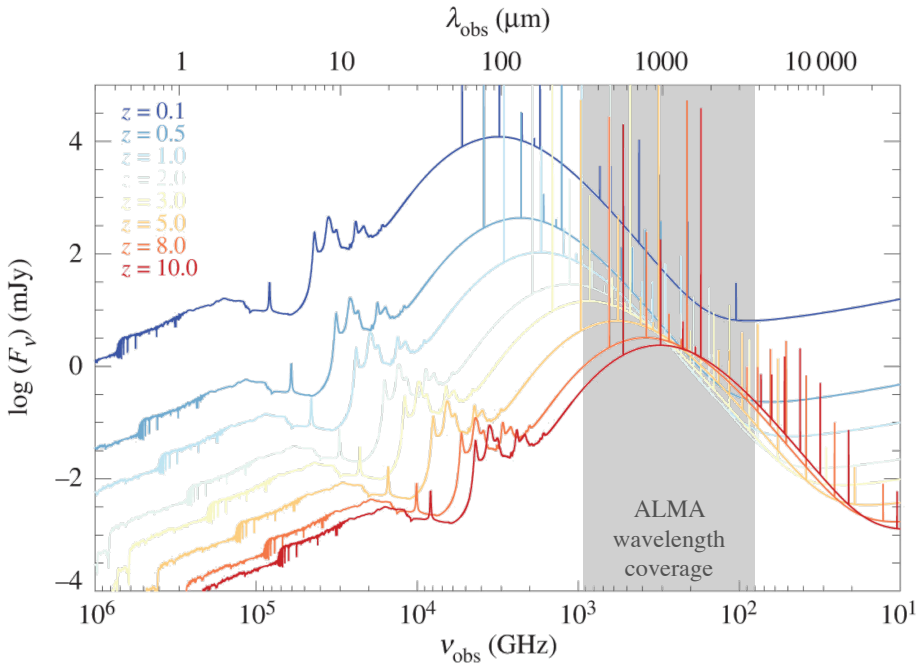

Figure 1.7: An illustration of the part of the galaxy SED sampled by ALMA, from $z = 0 - 10$. The model SED used here is the median SED obtained for the sub-millimetre galaxies studied in da Cunha et al. (2015). The brightest FIR-millimeter wavelength cooling and CO lines are added for illustrative purposes. *(Adapted from Fig.1 of Hodge and da Cunha, 2020)*

2 becoming available in the next few years, this will extend down (up) to 35 GHz (8.5 mm). This extensive frequency range can probe the entirety of the dust SED, from the peak to the Rayleigh-Jeans tail in $z \sim 1 - 5$ galaxies, as well as a range of atomic and molecular lines, particularly the CO and [C I] lines (see Fig. 1.7).

Bandwidth: ALMA's large frequency coverage enables users to conduct spectral scans. In combination with the high sensitivity, this allows for serendipitous line searches for sources in the field of view.

1.3.2 Targeted Surveys of Molecular Gas

To understand how the stellar mass growth of galaxies is regulated by the molecular gas supply, studies of large statistical samples have sought to develop **gas scaling relations** that parameterise the evolution of the molecular gas fraction and depletion time of galaxies as a function of cosmic age (or redshift), stellar mass and sSFR (or offset from the main sequence) (e.g. Genzel et al., 2015; Scoville et al., 2016; 2017; Tacconi et al., 2018; Liu et al., 2019b). These relations aim to address fundamental questions such as: *To what extent is star formation regulated by the size of the molecular gas reservoir? And, does the star formation efficiency (SFE) of galaxies vary with redshift or offset from the main sequence?* Answering these questions requires large sample of galaxies at different epochs. To this end, multiple targeted surveys of CO and/or dust-continuum emission have been conducted over the past decade, particularly focusing on galaxies at the peak of cosmic star formation.

The first studies of the molecular gas contents of galaxies at cosmic noon were based on observations conducted with the PdBI's 1-, 2- and 3-mm receiver bands, which covered the CO(2–1), CO(3–2), and CO(4–3) transitions. The first of these focused on SMGs (e.g. Frayer et al., 1998; Neri et al., 2003; Greve et al., 2005), with subsequent studies selecting galaxies based on their near-infrared (NIR) colours (Daddi et al., 2010a; Genzel et al., 2010; Tacconi et al., 2010). These small

samples of CO observations were followed up by the more-extensive PdBI HIgh-z Blue Sequence Survey (PHIBSS), which targeted the CO(3-2) emission of galaxies at $z \sim 1.0-1.6$ and $z \sim 2.0-3.0$ (PHIBSS 1; Tacconi et al., 2013) and the CO(2-1) emission of galaxies at $z = 0.5-0.8$ (PHIBSS 2; Freundlich et al., 2019). Selected from large UV/optical/IR surveys to have $M_* > 2.5 \times 10^{10} M_\odot$ and SFR $\geq 30\,M_\odot\,yr^{-1}$, the PHIBSS observations greatly increased the number of detection at $z > 1$, adding 38(14) detections at $z \sim 1.2$ ($z \sim 2.2$).

Multiple surveys of dust-continuum emission have also been conducted over the last few years, with ALMA, (e.g. Schinnerer et al., 2016; Scoville et al., 2016; Miettinen et al., 2017). For example, Schinnerer et al. (2016) observed the 1.2 mm (Band 7) continuum emission (rest-frame $\sim 300\,\mu m$) of 45 massive, mostly main-sequence star-forming galaxies at $z \sim 3-4$, selected from the COSMOS field based on their rest-frame UV-to-optical colours. Scoville et al. (2016) also observed the dust-continuum emission of star-forming galaxies in the COSMOS field, selecting a more extensive sample of 145 star-forming galaxies with both well-sampled IR (100-350 μm) photometric data and large stellar masses ($0.2-4 \times 10^{11} M_*$). Their $z \sim 1.15$, 2.2 and 4.4 samples contained galaxies both on and well above the main sequence. In contrast, Miettinen et al. (2017) selected the classical favourite for submillimeter astronomy, observing 129 SMGs at 1.3 mm (Band 6). However, like the sample of Scoville et al. (2016), their sample lies both on and above the main sequence with $\sim 42\%$ of their sample occupying the starburst regime. Many more continuum surveys of SMGs have been conducted over the last decade, as summarised in Table 1 of Hodge and da Cunha (2020), but these mostly lack the complementary multi-wavelength data needed to constrain the SFRs and stellar masses, and thus link these global properties to the molecular gas supply.

Another way of gathering large samples of molecular gas measurements that has only become viable with ALMA is to systematically mine data archives. One of the largest such mining efforts is the Automated mining of the ALMA Archive in COSMOS (A^3COSMOS) project (Liu et al., 2019a). The A^3COSMOS team trawled the public ALMA archives for serenditpitous continuum observations of sources within the COSMOS field with observations at other wavelengths. This resulted in a dataset of over 700 galaxies at $z = 0.3-6$ with continuum detections, occupying a range of positions with respect to the main sequence.

1.3.3 The Derived Gas Scaling Relations

The new, large and targeted surveys of CO/dust-continuum emission have enabled gas scaling relations to be derived for statistically-significant samples (Scoville et al., 2017; Tacconi et al., 2018; Liu et al., 2019b). These studies now mostly agree that the molecular gas fraction increases with redshift for a fixed galaxy stellar mass, i.e. massive galaxies at $z \sim 2$ were significantly more gas-rich than local galaxies of the same mass, implying that they had more fuel available to form new stars. However, there is still some disagreement over how this relationship evolves for galaxies of different stellar masses and whether or not there is a flattening/turnover of the gas mass fraction at $z \gtrsim 4$. Likewise, these large statistical studies qualitatively agree that there is little increase in the SFE with redshift but quantitatively disagree on the exact scaling; Liu et al. (2019b) find an almost constant depletion timescale with redshift for fixed stellar mass, Tacconi et al. (2018) find $t_{dep} \sim (1+z)^{-0.62}$ and Scoville et al. (2017) find $t_{dep} \sim (1+z)^{-1.04}$.

There is a also still some disagreement over how the global SFEs vary with stellar mass and the position of a galaxy relative to the main sequence. In earlier work, Genzel et al. (2010), 2015 found a significant variation of the SFE between main sequence and starburst galaxies of the same stellar mass (with little change in the gas fraction), whereas Scoville et al. (2016) concluded the opposite. However, Scoville et al. (2017), Tacconi et al. (2018) and Liu et al. (2019b) find that galaxies above the main sequence are forming stars more efficiently than those on it, perhaps as a result of the dynamical compression of the molecular gas through infalling gas and minor mergers (Scoville et al., 2017). According to Scoville et al. (2017) and Tacconi et al. (2018), the SFE depends only weakly

on stellar mass, i.e. main-sequence galaxies across a range of stellar masses are converting their gas supply into stars at the same rate. In contrast, Liu et al. (2019b) find a stronger correlation of the SFE with stellar mass, which if true, could be indicative of a downsizing phenomenon whereby where more massive galaxies evolve at earlier times.

While there has been some convergence in these gas scaling relations, the remaining differences make it difficult to gauge just how much galaxy-internal star formation processes have evolved over time. Isolating the main cause/s of these differences has proven difficult. Some may be explained by the assumptions made when converting observations of molecular gas to gas masses, i.e. the assumptions on the dust properties, CO excitation or $\alpha_{\rm CO}$, as explored in this thesis. Other issues, not touched upon here, include the methods used to infer SFRs, the functional form of the main sequence and the functional form of the best-fit gas scaling relations. Disentangling these effects these will require a smarter approach than simply gathering more unresolved CO or dust-continuum data. Instead, further multi-wavelength and more detailed physical modelling of cold, molecular gas are required.

1.3.4 "Blind" Surveys of Molecular Gas

By design, the CO and dust-continuum surveys mentioned previously are biased towards specific types of galaxies, e.g. ones that have high stellar masses or are bright at specific wavelengths. Inferring the density of molecular gas over the entire cosmic volume from these observations is challenging as it is unclear just how much gas is being missed through observations of biased samples within poorly-defined volumes. Establishing a cosmic census of molecular gas therefore requires a different approach. The most straightforward strategy is to uniformly observe a field of large enough area to be "universally representative" at great depth. Surveys conducted in this way are flux-limited, i.e. within a well-defined volume they are complete down to the instrument sensitivity threshold. In the case of CO/dust observations this also means that such surveys can be considered complete down to a given molecular gas/dust mass.

The first "blind" survey of CO emission was conducted with the PdBI for a 1 arcmin^2 region of the *Hubble* Deep Field North (HDF-N) (Decarli et al., 2014). Interestingly, this led to the detection of massive molecular gas reservoirs in galaxies that were not associated with obvious NIR/optical counterparts and which therefore would not have been observed with classical selection techniques. Moreover, it was the first attempt to provide constraints on the cosmic molecular gas density, albeit very loose ones. With the improved capabilities of ALMA it became possible to efficiently probe molecular gas over a wider redshift range, by covering multiple CO lines (and continuum emission). Enter the ALMA Spectroscopic Survey in the Hubble Ultra Deep Field (ASPECS), a survey of the *Hubble* Ultra Deep Field (HUDF) conducted with ALMA's 3 mm (Band 3) and 1.2 mm (Band 6) windows. The ASPECS Pilot program (Walter et al., 2016) was carried out in Cycle 2 of ALMA,[16] covering only 1 arcmin^2 of the HUDF. This program pushed the detection of CO to fainter (less gas-rich) galaxies than previously detected. Moreover, the 1.2 mm continuum data cube provided the deepest map of dust-continuum emission obtained till then at such long wavelengths. Yet the pilot program was limited by the small survey area. The follow-up Large Program (LP), instead covered most of the area ($\lesssim$ 5 arcmin^2) of the *Hubble* eXtremely Ultra Deep Field (XDF), for which the deepeset NIR data are available (Illingworth et al., 2013).

Conducted in Cycle 4,[17] the ASPECS LP consisted of 150 hours of ALMA observing time, split across the two spectral scans. Some of this data is used in Chapter 3 of this thesis (further details are provided there). The ASPECS observational setup naturally divided sources into different redshift bins, with the Band 3 observations picking up CO(2-1) for $z = 1.0 - 1.6$ galaxies and CO(3-2) for $z = 2.0 - 2.7$ galaxies. For most sources, these lines are further complemented by higher-J

[16] June 1st 2014 to Oct. 31th 2015
[17] Sept 30th 2016 to Sep. 28th 2017

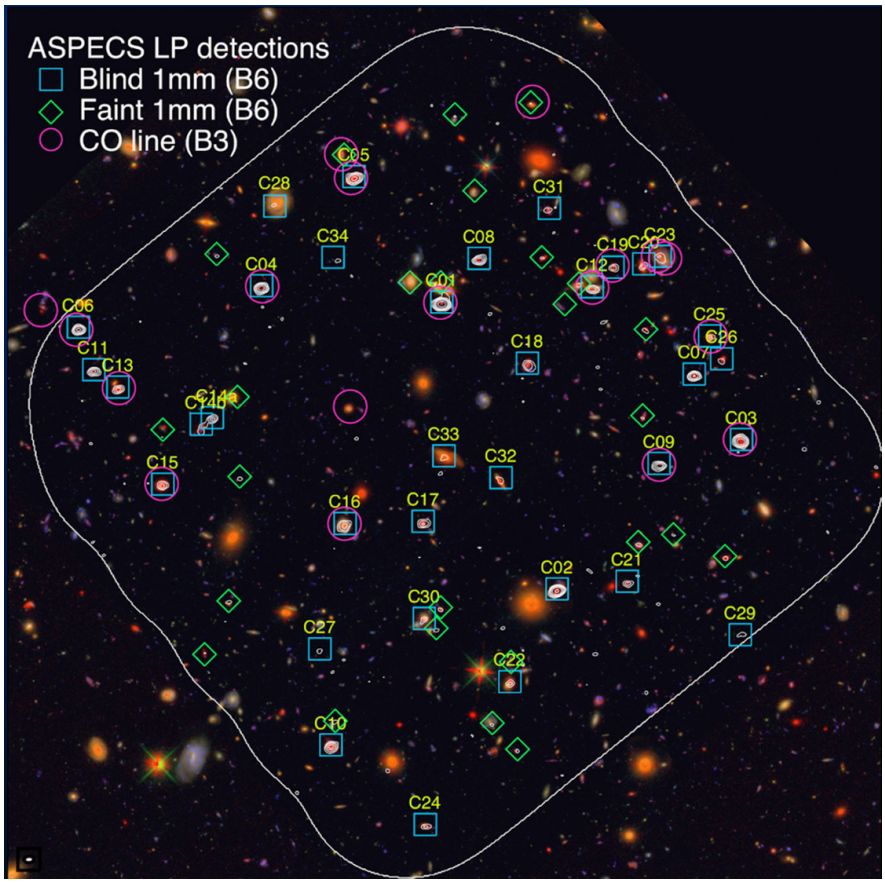

Figure 1.8: Sources detected in dust-continuum emission (blue squares and green diamonds) and/or CO emission (magenta circles) as part of ASPECS, overlaid on the optical/near-infrared HST composite image of the field observed with ALMA. The ASPECS field zooms in on a ~ 5 armin^2 patch of the HUDF (shown in Fig. 1.1). *(Image credits: STScI, Aravena et al., 2020)*

transitions observed in the 1.2 mm window (Boogaard et al., 2020). In combination with the multiwavelength coverage of the XDF and complementary observations of ionized gas emission from the Multi Unit Spectroscopic Explorer (MUSE) (Boogaard et al., 2018) this enabled precise redshift measurements for all line candidates. The 3 mm-window observations of CO led to the detection of 18 sources in total,[18] whereas the 1.2 mm continuum data led to highly-significant detections of 35 sources, of which 32 had clear NIR counterparts (González-López et al., 2020). ASPECS led to a wealth of insights into the molecular gas and dust content of galaxies from $z \sim 1-4$.[19]. Crucially, the majority of the CO emission in the ASPECS field of view appears to have captured by the observations, as implied by the application of stacking (Inami et al., 2020) and intensity mapping techniques (Uzgil et al., 2019). Thus, these CO observations could be used to constrain the cosmic molecular gas density without the fear of missing a large component of molecular gas.

Other large surveys have helped make tremendous progress over the last few years. At the same time as the ASPECS program was being carried out, another large blind survey of CO emission, COLDz, was conducted with the VLA (Pavesi et al., 2018; Riechers et al., 2019). In contrast to other $z > 1$ surveys of molecular gas, the COLDz setup exposed the CO(1-0) emission in $z \approx 2.0-2.8$ galaxies (and CO(2-1) at higher redshifts). COLDz covered a small region of the COSMOS field as well as the entire GOODS-North footprint (Giavalisco et al., 2004) (including the HDF-N) thereby providing tighter constraints on the cosmic molecular gas density and yielding 58 CO line candidates, of which seven were independently verified (Pavesi et al., 2018). Further blind surveys have

[18] two identified with the help of the complemetary MUSE observations
[19] which I will shamelessly advertise further here: https://www.aspecs.info/publications/

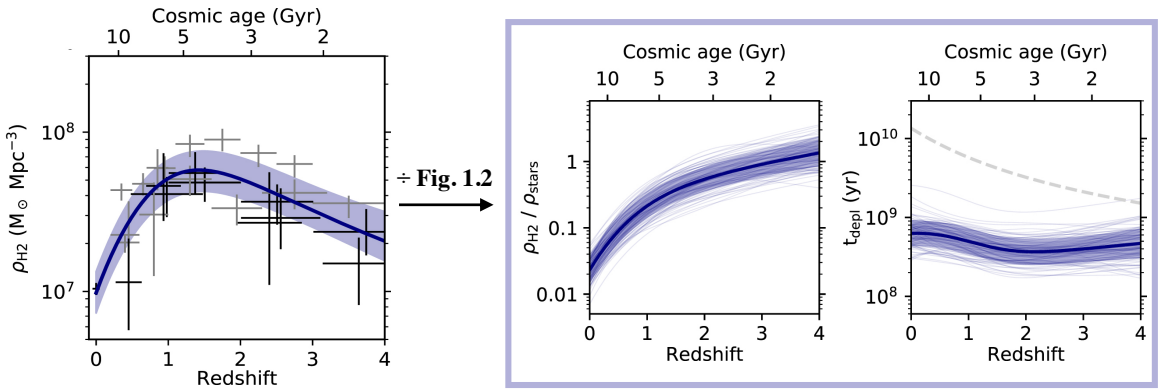

Figure 1.9: Left: The evolution of the cosmic molecular gas density, as derived mainly from blind surveys of CO and dust-continuum emission. Diving the cosmic molecular gas density by the cosmic SFRD and stellar mass density in Fig. 1.2, yields the evolution of the molecular-gas-to-stellar-mass fraction in the middle panel and molecular gas depletion time in the right panel, respectively. The observations are compiled in Appendix B of Walter et al. (2020). *(Adapted from Figures 2 and 4 of Walter et al., 2020)*

also been conducted of the ~ 1 mm dust-continuum emission in frontier fields (summarised in Table 4 of Hodge and da Cunha, 2020). However, most of these sample too small a volume or lack the corresponding redshift measurements needed to constrain the cosmic gas density. More targeted surveys of bright galaxies in specific fields, such as the continuum surveys of (Scoville et al., 2016; 2017) and (Liu et al., 2019a) (described in Section 1.3.2) and the survey of SMGs in the SCUBA-2 Cosmology Legacy Survey UKIDSS/UDS field (Stach et al., 2019) have also been used to estimate the cosmic molecular gas density (e.g. Scoville et al., 2017; Dudzevičiūtė et al., 2020), albeit with larger errors on the completeness.

Other approaches to amassing deep and wide coverage of molecular gas tracers are also beginning to yield results. The ALMA archive mining program ALMACAL was (and is) being used to exploit ALMA CALibrator scans in order to coduct surveys of the: (1) submillimeter continuum emission (Oteo et al., 2016), (2) CO absorption lines in the spectra of background QSOs (Klitsch et al., 2019b) and (3) CO emission (Hamanowicz, 2020). These have helped to further constrain the evolution of the cosmic molecular gas density (Klitsch et al., 2019b; Hamanowicz, 2020) as well as identifying highly star-forming dust galaxies (Oteo et al., 2017b) and enabling a study of the excitation properties of the molecular gas (Klitsch et al., 2019a).

1.3.5 The Cosmic Census of Molecular Gas

As shown in Fig. 1.9, the result of the blind molecular gas surveys conducted over the last decade appears to be that the cosmic molecular gas density evolved in a similar manner to the star formation rate density, decreasing by a factor of 6^{+3}_{-2} from the peak of cosmic star formation, at $z \sim 2$, to the present day (Walter et al., 2020). Tentative evidence also implies that the molecular gas density increased from $z \sim 6 \rightarrow 2$ (Riechers et al., 2019; Decarli et al., 2019; 2020); however, the associated uncertainties beyond $z \sim 4$ remain significant. However, the results from $z \sim 4 \rightarrow 0$ have been used to address to what extent the peak in star formation at $z \sim 2$ and subsequent decline are governed by a change in the quantity of molecular gas, vs the efficiency with which it is converted into stars.

Taking the ratio of the cosmic SFRD and stellar mass density, shown in Fig. 1.2, yields the evolution in the average molecular gas to stellar mass fraction and molecular gas depletion timescale, shown in the enclosed rectangle of 1.9. This indicates that there has been very little, if any, evolution in depletion timescale or star formation efficiency. Instead, the peak and decline in the Universe's star formation activity is mainly driven by the supply of molecular gas.

While these results were being analysed and compiled, this thesis aimed to test the accuracy of the underlying inferences. As for the gas scaling relations, the shape of the cosmic molecular gas density is highly sensitive to the caveats mentioned in Section 1.2. If any of assumed properties, e.g. the gas excitation, dust temperature or dust-to-gas ratio, vary systematically as a function of redshift (or galaxy type), it will change the cosmic molecular gas density in Fig. 1.9. Additionally, the increase in temperature of the CMB with redshift may play a significant role, as is discussed further in the Section 1.4.3.

1.3.6 "Resolved" Observations of Dust and Molecular Gas

As hinted at in the beginning of this introduction, star formation is a multi-scale process. Thus, the galaxy-integrated measurements described in the previous subsections only tell part of the story. Integrated measurements do not address *where* the star-forming gas is located and what its physical properties (kinetic energy, temperature, density etc) are. Addressing such questions requires at least sub-kpc observations of molecular gas, although experts on the small-scale physics would argue that it requires resolutions of 10 – 100 pc, i.e. at least the scale of individual clouds.

High-resolution observations of molecular gas tracers have been gathered for many local star-forming galaxies, the most detailed examples of which are from the Physics at High Angular resolution in Nearby GalaxieS (PHANGS) survey (Leroy et al., 2021). The PHANGS-ALMA large program mapped the CO(2-1) emission of 90 nearby ($\lesssim$ 18 Mpc) galaxies at an angular resolution of 1.″, corresponding to a physical resolution matching the scale of GMCs, $\leq$ 100 pc (Schinnerer et al., 2019b). An example of the exquisite detail reached by the PHANGS observations is shown on the left of Fig. 1.10.

With the extended configurations and high sensitivity of ALMA it has become possible to resolve the molecular gas of galaxies at $z > 1$. Technically, ALMA has the capability to resolve the sub-/millimetre emission from galaxies at $z \sim 2$ at scales down to $\sim$ 350 pc. In practice though, such attempts are limited by the fact that the surface brightness sensitivity is proportional to the inverse square of the resolution, with the integration time proportional to $1/\text{resolution}^4$.[(20)] Thus, to simultaneously conserve the sensitivity of the observations and increase the resolution by a factor of x, would require an increase in the integration time of x^4. Even if one relaxes the sensitivity criteria slightly, increasing the resolution results in a significant increase in integration time.

Because resolved interferometric observations are expensive, even with ALMA, the first attempts at resolving $z > 1$ galaxies have focused on the "low-hanging fruit", i.e. resolving the dust-continuum emission of submillimeter-bright galaxies. The centres of dusty starbursts (Simpson et al., 2015; Hodge et al., 2016; Nelson et al., 2019) and some main-sequence galaxies with small rest-frame optical sizes (Barro et al., 2016; Tadaki et al., 2017a) have been mapped at high resolution ($\lesssim$0.″2, corresponding to physical scales of $\sim$ 2kpc), revealing compact and bright dust emission. For all but a few of the most compact sources, the dust emission appears to be more centrally-concentrated than the rest-frame UV/optical stellar emission. This has mostly been interpreted as evidence for high central SFR densities, under the assumption that the dust emission traces the SFR. Moreover, it has been suggested these galaxies must therefore be undergoing rapid morphological transformation and/or bulge growth. But does it also imply the existence of a centrally-concentrated molecular ISM?

Compared to the abundance of resolved FIR continuum observations, there are still few resolved CO observations of galaxies at $z > 1$. Resolutions of a few 100s of pc have only been reached in studies of lensed galaxies (e.g. Rybak et al., 2020), with CO observations of non-lensed sources mostly limited to resolutions of a few kpc. Moreover, most of this early work has focused on the SMGs for which resolved dust observations had already been obtained. In their pioneering study

[(20)] as was vehemently repeated during my attendance at the 10th IRAM Interferometry Summer School https://www.iram-institute.org/medias/uploads/file/PDFs/IS-2018/gueth-noise.pdf

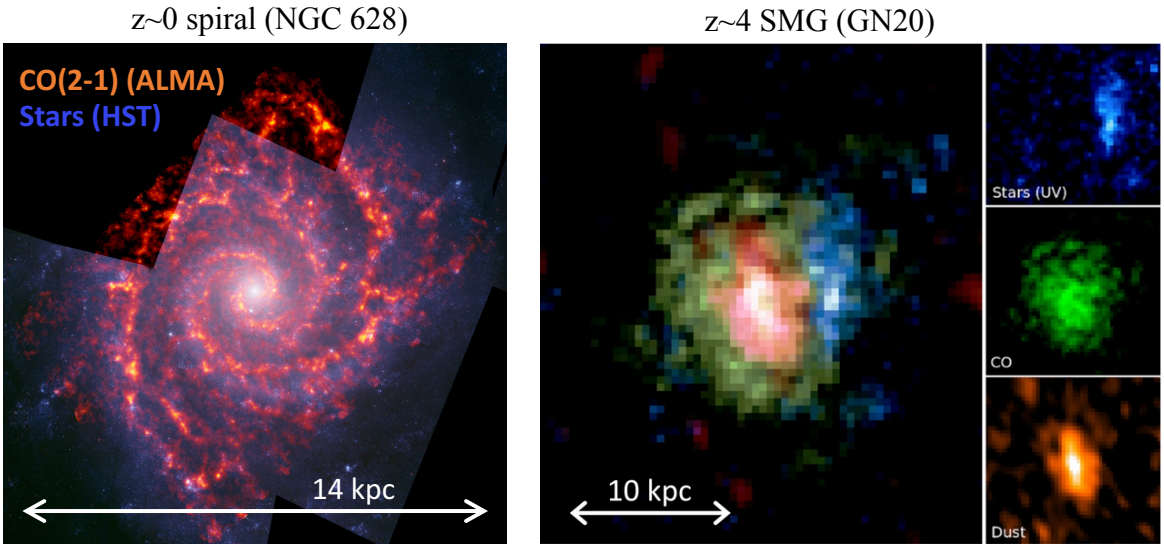

Figure 1.10: Resolved observations of the molecular gas and stas in a local vs. high-redshift galaxy. **Left:** Composite image of the CO(2-1) emission (orange) and stellar emission (blue) obtained with ALMA and the HST as part of the PHANGS survey *(Credit: NRAO/AUI/NSF, B. Saxton: ALMA (ESO/NAOJ/NRAO); NASA/Hubble)*. **Right:** Composite CO(2-1) (green), dust continuum (orange) and rest-frame UV image of the $z \sim 4$ starburst GN20. These dust-continuum and CO images represent some of the highest resolution images taken prior to this thesis. *(Fig. 2 of Hodge et al. (2015))*

of resolved CO emission, Hodge et al. (2015) compared the CO, dust and stellar emission of the luminous starburst GN20, as shown in the right in Fig. 1.10. This comparison appeared to indicate that the dust emission was more centrally concentrated than the CO emission. Similarly, Chen et al. (2017) compared the CO, dust and rest-frame optical emission of a $z = 2.12$ SMG, finding that the dust emission is more compact than the CO emission. The stacking analysis of four SMGs, conducted by Calistro Rivera et al. (2018) further quantified the compactness of the dust emission, relative to that of CO. Moreover, in the only such study of main-sequence galaxies prior to this thesis, Tadaki et al. (2017a) also observed more compact dust vs CO emission, although their two galaxies were specifically selected based on the compactness of the dust emission.

Given the apparent unreliability of dust as a molecular gas tracer at large radii, the sparcity of existing resolved CO observations and their poor resolution and sensitivity it is still unclear how molecular gas is distributed in $z > 1$ star-forming galaxies. In Chapter 3, we investigate this further, comparing the dust and CO emission of three *extended*, main-sequence galaxies at $z \sim 2$. As discussed in the previous section, FIR continuum emission is used to trace the gas content, under the assumption of a certain gas-to-dust ratio. Thus, the immediate but naive interpretation of the compactness of the dust emission relative to that of CO (seen previously) would be that the dust-to-gas ratio varies across high-redshift galaxy disks. Small variations (a factor of a few) have been observed in some local galaxies (e.g. Magrini et al., 2011; Sandstrom et al., 2013; Casasola et al., 2017) but these hardly seem sufficient to explain the high-redshift observations. As discussed in detail in Chapter 3, multiple other effects are likely to play a role as neither CO nor dust emission are straightforward tracers of molecular gas (or dust). Truly unravelling these effects also requires the application of detailed physical models, another field which has gained traction along with the increasing number of sub-/millimeter observations.

1.4 SYNTHETIC OBSERVATIONS OF MOLECULAR GAS

New observations are best interpreted with the aid of detailed physical models, a statement that also holds true for observations of the molecular ISM in distant galaxies. Observations provide in-

formation on projected or volume-averaged quantities and are limited by the resolution and sensitivity. In combination, these effects pose a significant challenge for deriving information about the underlying properties and distribution of the molecular ISM. The expected physical properties can be inferred from theoretical models, but these cannot be directly compared to observations. To do so, the emission of photons from gas and dust, their propagation through matter and the way they are detected must also be accounted for. This step, in addition to the theoretical modelling, produces a *synthetic observation*.

Creating synthetic observations is a computationally-intensive process, and thus relies on many choices in order to simply the models. Simulating the full complexity of the molecular ISM on multi- or even single-galaxy scales is beyond the capabilities of the best modern computational facilities. Thus, simplifying assumptions have to be made, which depend on the source of emission being interpreted, the resolution of the observations and the sample size. Modelling the interaction of photons with the simulated medium is also far from straightforward, involving a further array of choices. In this Section, I briefly summarise some of the methods and assumptions pertinent to studies of the molecular ISM in distant galaxies, but the curious reader can find a more in-depth review of synthetic ISM observations in (Haworth et al., 2018).

1.4.1 Capturing the Complexity of the Molecular ISM

The first step to generating synthetic observations of the molecular ISM is to model the distribution, temperature and density of its key components. There are two possible approaches to doing so (1) via parametric (either analytic or semi-analytic) models or (2) via full dynamical simulations. Parameteric models are quick to compute, allowing for large parameter studies (e.g. Popping et al., 2017a; Lagos et al., 2020), but they lack the details needed to capture the non-linear regime. Conversely, dynamical models involve a greater computational expense, as they solve the (magneto-)hydrodynamical equations of fluid flow on a discretised region of space and can therefore be used to describe three-dimensional, non-homogeneous and non-symmetric regions of the ISM. However, they have been too computationally-expensive to model the full three-dimensional structure of the molecular ISM for samples of galaxies. Thus, a choice has to be made regarding the level of detail required.

Since the focus in this thesis is on accurately modelling the main components of the molecular ISM, rather than performing a large parameter study, we employ the dynamical modelling approach. We therefore require a framework that tracks H_2 and CO and models the fluid flow. Many hydrodynamical codes have been developed for this purpose and it is beyond the scope of this section to list them all here. The curious reader may instead search the public repository of astrophysics software `http://www.ascl.net` for themselves using the search keyword “hydro”. Each of these codes is based on a different set of numerical techniques and has been adapted for different astrophysical purposes, as described in depth in (Springel, 2010b; Teyssier, 2015). The main distinction between these codes is how they solve the equations of hydrodynamics. Most codes fall in one of two categories, employing either Lagrangian smoothed particle hydrodynamics (SPH) technique or Eulerian hydrodynamics on a Cartesian mesh with (optional) adaptive mesh refinement (AMR). Both approaches have their advantages and disadavantages. SPH codes may suppress fluid instabilities whereas AMR codes may lead to overmixing (see Springel, 2010a, in addition to the reviews previously listed).

One code that was developed to overcome the weaknesses of both schemes, while inheriting the strengths of both, is AREPO (Springel, 2010a). AREPO is a massively-parallel code that uses a finite volum eapproach to solve the equations of fluid flow on an unstructured mesh, defined by the Voronoi tessellation of mesh-generating points. The underlying idea is that these points move with the local velocity of the fluid, with the mesh reconstructed at each time step, resulting in a “quasi-lagrangian” code. This quasi-lagrangian nature ensures an adaptive refinement (or dere-

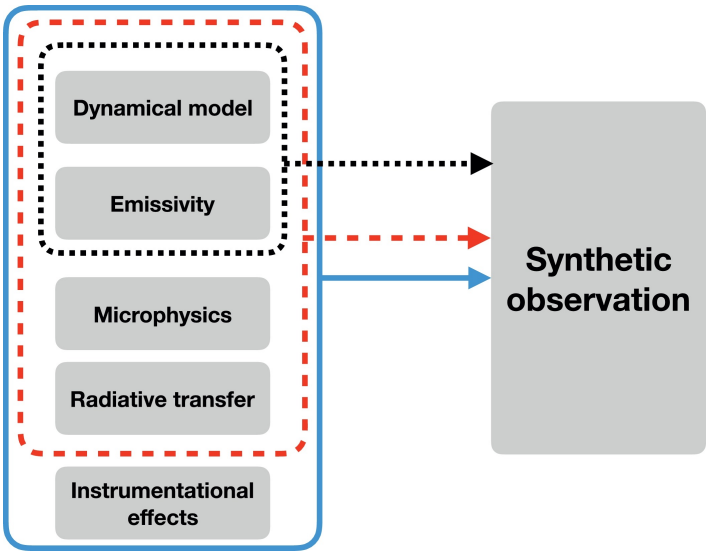

Figure 1.11: A schematic summary of how synthetic observations are created. The first and most fundamental step is to estimate the emissivity from an assumed/calculated density, temperature and velocity structure. Then, the composition and thermal structure are computed with radiative transfer and additional microphysics (e.g. a chemical network) and the synthetic observation is produced via the radiative transfer post-processing. As a final (optional) step the intrumentational effects, e.g. interferometric filtering and beam convolution, may be included. *(Fig. 1 of Haworth et al., 2018)*

finement) with density, but, the mesh can also be further de-/refined at will to focus on regions of interest, thereby allowing the key chemical and physical processes in dense regions of the ISM to be captured accurately. AREPO is therefore highly versatile and can solve problems that connect many orders of magnitude in spatial and density scales. It has therefor been applied in a variety of astrophysical applications, from cosmological simulations of structure formation, e.g. the *Illustris* simulations (Pillepich et al., 2018), to simulations of individual molecular clouds (e.g. Clark et al., 2019). It is also the hydrodynamical code of choice in this thesis.

Modelling the molecular ISM requires more physics than simply hydrodynamics (i.e. the fluid flow of the medium). Gravity, stellar feedback, cosmic rays, magnetic fields and chemistry all affect the structure and composition of the molecular ISM. Thus, *fully* modelling the molecular ISM would require coupling a magneto-hydrodynamic model of cold gas and dust to a complete chemical network (that captures the transition from atomic to molecular gas) and models the interaction of all involved species with the UV radiation. This remains prohibitively expensive. The most complete database of chemical reactions, the UMIST Database for Astrochemistry (McElroy et al., 2013), contains more than 6100 gas-phase, binary reactions among 467 chemical species, involving 13 elements. Attempting to also account for all possible grain surface reactions and all possible isotopic variants of chemical species can easily lead to a tenfold increase in the number of reactions (e.g. Albertsson et al., 2013). Since these chemical reactions take place on different timescales, the ordinary differential equations (ODEs) that describe the evolution of the gas are more efficiently solved implicitly[21], the cost of which scales as the cube of the number of ODEs. This ideal approach is therefore unfeasible for three-dimensional (3D) hydrodynamic simulations of invididual GMCs (let alone entire galaxies).

The computational expense of modelling the molecular ISM forces certain simplifications to be adopted, the choice of which depends on the physical scales of interest and on which chemical species are important for regulating the thermal balance of the ISM. Chemical species that have little impact of the dynamics of the gas can often be modelled in the post-processing step. At the

[21] Implicit numerical methods solve the fluid equations at each time step by involving **both** the current state of the system and the later one.

largest scales, cosmological simulations provide a statistical overview of the baryonic matter cycle, but they lack the resolution and chemistry needed to account for molecular gas. Indeed, the lowest gas temperature of the AREPO-based *Illustris* cosmological simulations is 10^4 K (Vogelsberger et al., 2013). Thus, the molecular gas properties of galaxies from cosmological simulations are accounted for via "sub-grid" treatments, in which e.g. a particular molecular cloud distribution is assumed and the gas within these is assumed to follow some density distribution function (such as a logotropic, Plummer, power-law or constant density profile) (Narayanan et al., 2012; Popping et al., 2014; Tomassetti et al., 2015; Vallini et al., 2018). At the smallest scales, hydrodynamic simulations of individual molecular clouds can be used to follow, in detail, the hyrodynamical, chemical and thermal evolution of the gas. On their own, such simulations do not predict galaxy-integrated observations, but they are instructive in understanding how physical properties such as the turbulence, star formation rate, or metallicity affect the relative abundance of chemical species (e.g. Glover and Mac Low, 2011; Glover and Clark, 2012c; Clark and Glover, 2015).

This thesis is focused towards the modelling at smaller scales, with the aim of accurately constraining the integrated line emission of the *turbulent* molecular ISM. The turbulence circulates gas particles such that they alternate between regions of low and high density density in short times frames. Thus, the main chemical species, particularly H_2, never reach chemical equilibrium. To retain a description of molecular gas that is not in chemical equilibrium there are two options; one can either 1) simplify the chemistry network (e.g. to only include the reactions that directly alter the abundance of chemical species involving hydrogen, carbon and oxygen) or 2) simplify the treatment of the gas dynamics and/or geometry, e.g. as in codes modelling photodissociation regions (PDRs). Option 2) is only valid if the chemical species have characteristic timescales shorter than representative dynamical timescale and is therefore a poor approximation for H_2, the abundance of which is sensitive to the previous dynamical state of the gas. Thus, coupling a hydrodynamic simulation to a simplified chemistry network, is the best option for accurately capturing the H_2 and CO abundances of the molecular ISM.

For the abundance and distribution of both H_2 and CO to be modelled accurately, the applied chemical network must include the main formation and destruction mechanisms of the two molecules. H_2 forms predominantly on dust grains, as the gas-phase reaction pathways are too inefficient to form large quantities of H_2 at typical ISM densities (e.g. Glover, 2003). In contrast, CO forms almost exclusively in the gas phase, via a number of ion-neutral and neutral-neutral reactions. Both molecules are destroyed via photodissociation, absorbing UV photons with energies below the Lyman alpha limit; however, the photodissociation mechanisms differ. H_2 photodissociates via a two-step process known as spontaneous radiative dissociation, whereas CO undergoes a process called predissociation, the main difference being that the lifetimes of the excited states of CO are shorter than those of H_2 and the UV absorption lines are broader. Thus, CO is less effective at self-shielding from UV radiation than H_2 and is less abundant, in regions of low column densities. In addition, dust acts as an effective shield from UV radiation. However, dust shielding declines for regions with low metallicity (where less dust forms), thereby affecting the relative abundance of CO and H_2.

Various implementatations of H_2 and CO chemistry have been developed that can be coupled to hydrodynamics codes. The main difficulty in modelling H_2 is correctly accounting for H_2 self-shielding and dust shielding, but there are now various approaches to do so (see e.g. Glover and Mac Low, 2007a; b; Clark et al., 2012a; b; Hartwig et al., 2015). Modelling the carbon and oxygen chemistry is comparatively more difficult, although again several options have been developed (Nelson and Langer, 1997; Keto and Caselli, 2008; 2010; Glover et al., 2010). The available H_2 and CO chemistry networks are compared in detail in Glover and Clark (2012a). Based on this comparison, we adopt the treatment of hydrogen chemistry described in Glover and Mac Low (2007a), b, which includes the formation of H_2 on dust grains, destruction by photodissociation, collisional dissociation of atomic hydrogen, the recombination of ionized hydrogen in the gas phase and on

grain surfaces as well as cosmic ray ionisation. For the CO chemistry we adopt the Nelson and Langer (1997) network described in Glover and Clark (2012a), which assumes that the formation of CO is limited by an initial radiative association step, and that the CO destruction rate is mainly governed by photodissociation.

Having an accurate description of the chemistry is of little use if the resolution is insufficient for the abundance of the involved species to converge. The resolution of hydrodynamical simulations of molecular gas must be high enough to at least resolve the densities at which (1) the formation and dissociation times of each molecule are equivalent within the grid cell and (2) the formation time and typical cell crossing time are equivalent (Joshi et al., 2019; Borchert et al., 2021). The second criteria is the main one that dictates the choice of resolution for modelling H_2 and CO, with CO requiring an even higher resolution than H_2. Indeed, recent numerical studies find that the resolution required to obtain the convergence of the total content of both molecules is high, even in gas with moderate levels of turbulence. Resolutions of at least 0.1 pc are required for the formation of CO luminosity to converge in hydrodynamical simulations with non-equilibrium chemistry (Seifried et al., 2017; Gong et al., 2018; Joshi et al., 2019; Borchert et al., 2021).

1.4.2 Accounting for Radiation

Making all the decisions described above and evolving the simulation for the appropriate amount of time results in a 3D description of the density, temperature and abundances of main species of the molecular ISM. But, an additional crucial step is required to compare these to observations - the strength of the emission must also be modelled. To predict the emission, hydrodynamic simulations must be coupled to a model of the **radiative transfer**, which accounts for the absorption, emission and scattering of photons within the medium. Various radiative transfer codes have been developed, e.g. DESPOTIC (Krumholz, 2014), SKIRT (Camps and Baes, 2015), POLARIS (Reissl et al., 2016) and RADMC-3D (Dullemond et al., 2012), all of which solve the radiative transfer equation within the medium of choice by adopting various approximations to describe the gas and/or dust.

At their core all of these codes solve the radiative transfer equation,

$$\frac{dI_\nu}{d\tau_\nu} = S_\nu - I_\nu \,. \tag{1.12}$$

where I_ν is the specific intensity at frequency ν, τ_ν is the optical depth and S_ν is the source function. Although this equation appears simple, solving it for a realistic medium is *not*. The complexity is partly due to the multi-dimensional nature of the problem as the radiation field must be computed over three spatial dimensions accounting for the direction, frequency and possibly time dependence of the emitted radiation. Moreover, the properties of the gas and dust (e.g. the density, temperature and composition) are themselves dependent on the strength of the radiation field. Thus, radiative transfer is a coupled problem that usually hsa to be solved iteratively.

The first step to solving the transfer of photons through a medium is to define the medium. Radiative transfer algorithms require a description of the chemical species of interest at a discretised set of points. This information is provided by the simulation output, which would ideally be used directly as an input to the radiative transfer calculation, thereby avoiding the complication of regridding, which, depending on the required geometry, may result in a loss of information. POLARIS is one example of a radiative transfer code that avoids this complication, performing the radiative transfer on a range of grids including the Voronoi grids ouput by AREPO. Based on this, and the fact that the developer is in-house, POLARIS is the radiative transfer code of choice in this thesis.

1.4.2.1 Line Radiative Transfer

The opacity of gas is the result of discrete energy transitions, which are governed by quantum mechanics. Line radiative transfer calculations must account for these transitions, which can be either collisional or radiative. Modelling the optically thick line emission requires calculating the level populations, including the effects of absorption and stimulated emission. This is a tightly coupled problem, requiring a numerical treatment. However, performing the full-scale line transfer modelling is too computationally and memory intensive. Thus, additional approximations must be adopted. The simplest, textbook, assumption would be to treat the gas as being in local thermodynamic equilibrium (LTE), i.e. in a state where the rates of collisional excitation and de-excitation are the same. The high optical depth of CO means that the populations of the first and second levels are often close to what would be expected if the molecules were in LTE. However, at low optical depths (and low densities) this is no longer the case. Moreover, the effective critical density is line-dependent and thus the LTE assumption is less valid for higher-J transitions. To predict the CO level populations one must therefore rely on other means of approximating the line radiative transfer.

In practice, one of the best approximations to calculating level populations is the large velocity gradient (LVG) method (Sobolev, 1957), which assumes that the doppler shift between two neighbouring gas particles, i.e. the velocity gradient, $|dv/dl|$, is larger than the local line width, thereby allowing the photon to escape by "shifting out of the line". The important length scale for the LVG method is set by the ratio of the thermal velocity and velocity gradient, $v_{\rm thermal}/|dv/dl|$. Thus, the LVG approximation may be applied in cases where this length scale is significantly shorter than the typical length scale of variations in the gas density, temperature or velocity, as for the case of CO (e.g. Ossenkopf, 2002). The LVG approximation effectively converts a non-local problem to a local one, allowing the level populations of each fluid element to be solved for separately.

To model the specific intensity using the LVG method, POLARIS describes the mean intensity as,

$$J_{\rm i,j} = (1-\beta)S_{i,j} + \beta J_{ext} \tag{1.13}$$

where $S_{\rm i,j}$ is the source function of the transition, $J_{\rm ext}$ is the intensity of the external radiation field and β is the probability of a photon escaping the cloud. This probability is set by,

$$\beta = \frac{1-\exp(-\tau_{\rm LVG})}{\tau_{\rm LVG}} \tag{1.14}$$

where the optical depth, $\tau_{\rm LVG}$, in a given direction is inversely proportional to the velocity gradient and is given by,

$$\tau_{i,j} = \frac{c^3 n_g A_{i,j}}{8\pi\nu_{ij}^3 |dv/dl|}\left(\frac{g_i}{g_j}n_j - n_i\right) \tag{1.15}$$

where ν_{ij} is the transition frequency, g_i is the statistical weight of the ith level, A characterises the probability for spontaneous emission to occur and $n_{i/j}$ are the fractional occupation numbers. By removing the need to calculate the effect of radiation being absorbed and re-emitted before reaching the observer in this way, the LVG approximation greatly simplifies and speeds up the radiative transfer calculations.

1.4.3 Backgrounds

Another crucial component that needs to be taken into account when interpreting observations of the ISM is the effect of the fore- or background emission. There are many possible sources of fore-/background emission, including: galactic synchroton emission, the CMB, IR emission from

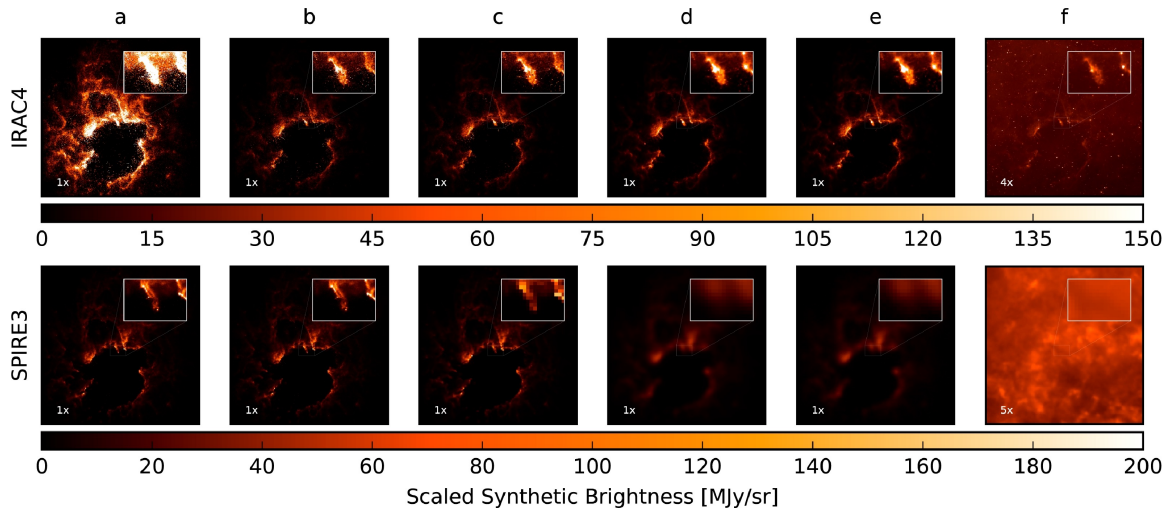

Figure 1.12: Synthetic observations of dust-continuum emission at 8 µm (top row; corresponding the the IRAC4 filter on the *Spitzer Space Telescope*) and 500 µm (bottom row; corresponding to the SPIRE3 filter of *Herschel*. Column (a) shows the ideal emission output after performing the radiative transfer calculations. For each subsequent column an additional effect is taken into account; column (b) includes interstellar reddening, in (c) the images are regridded to the resolution of the detectors, in (d) the images are also convolved with the instrumental point spread function (PSF), thermal noise is added in (e) and a realistic background is taken into account in (f). The images were created with the FLUX-COMPENSATOR tool (Koepferl and Robitaille, 2017) *(Adapted from Fig. 4 of Haworth et al. 2018)*

dust grains, bound-bound, bound-free and free-free emission from ionized plasma, starlight and X-rays from hot plasma. The importance of taking these into account is demonstrated clearly in the synthetic observations of dust emission shown in Fig. 1.12. As indicated by the right-most column, for which the IR background has been included in the radiative transfer calculations, the simulated cloud is too faint to be observed against the background at the longer wavelengths (bottom panel).

In the sub-/millimeter regime, in which the main components of the cold ISM emit, the thermal energy budget is dominated by the CMB. The CMB emission can be described by a near perfect blackbody spectrum, which peaks at 2.726 K in the local Universe (Fixsen, 2009), a temperature that is significantly lower than that of the bulk of molecular gas and dust. Thus, the CMB plays a negligible role in affecting the energy balance of the *local* molecular ISM and is too weak a background to provide much contrast against the gas or dust emission being observed. At high redshift, the energy density and temperature of the CMB are far greater, with the temperature scaling as,

$$T_{\rm CMB}(z) = T_{\rm CMB}^{z=0}(1+z)\,. \tag{1.16}$$

Thus, at $z = 3$, the background temperature is ~ 11 K, i.e. close to the temperature of the bulk of molecular gas in molecular gas clouds (e.g. Glover and Clark, 2012a). This increase in temperature means that the CMB plays a significant role in regulating the thermal evolution of gas and dust at higher redshift, as well as being a stronger background against which this emission must be observed. These effects need to be taken into account when interpreting observations of distant galaxies, but so far they have only been described through one-dimensional, isothermal models of the molecular ISM (da Cunha et al., 2013a; Zhang et al., 2016; Tunnard and Greve, 2017). This is particularly problematic in the case of CO emission, as the ISM temperature helps to dictate the density structure and thereby the relative abundance of carbon species. In Chapter 4 of this thesis, I test how the CMB-driven change in the density and temperature structure of the cold ISM affects the strength of the emission from the main atomic and molecular carbon transitions observed at high redshift.

1.4.4 Instrumentation

The nature of the instrumentation used to perform the observations also has a significant impact on the final data products. Images created from observations conducted with submillimeter-to-radio wavelength interferometers are subject to two main effects; (1) the reconstructed images are smoothed to the "beam size", making it impossible to resolve structures on smaller scales, and (2) large-scale structures may be "filtered out" as they cannot be sampled at the observed resolution.[(22)] Directly computing the intrinsic radiation field from the final data products is impossible. Indeed, reducing interferometric data essentially relies on a complex process of filling in the blanks.

Realistic synthetic observations, that match submillimeter-to-radio wavelength interferometric observations, can be created by modelling the effects of the interferometric response on post-processed simulation outputs. Such algorithms have been developed in the software that is used to reduce interferometric observations, i.e. CASA (for ALMA; McMullin et al., 2007) and GILDAS (for NOEMA). Although I have not adopted these tools for the main studies presented in this thesis, I have relied upon them to test the 2D models fit in Chapter 3 and request further observations following on from the work peresented herein.

[(22)] Because interferometers have a finite number of baselines, not all the fourier space can be sampled, resulting in some scales being filtered out.

1.5 THIS THESIS

Many of the observational studies of $z > 1$ galaxies mentioned in this introduction took place at the same time as this thesis (between 2017 and 2021), highlighting the boom in molecular ISM studies over the last few years. It therefore became increasingly critical to test what physical properties of the molecular ISM of distant galaxies could be reliably inferred from submillimetre observations. Such tests can be performed via at least two different approaches: (1) comparing the outcome from different sets of observations, supposedly tracing the same component of the ISM and/or (2) comparing real observations to synthetic ones, generated via detailed physical models. In this thesis, I have used both approaches to better understand the physical properties of the cold, molecular ISM of distant galaxies. Note that I use *we* in the following Chapters to denote that much of this work was conducted in collaboration with other astronomers, whose contributions are specifically listed at the end of each Chapter.

In **Chapter 2**, I investigate how well the gas masses derived from observations of CO(1-0) and dust-continuum emission agree for the kinds of galaxies where most of the star formation in the Universe took place, i.e. massive star-forming galaxies at $z \sim 2$. This test is particularly timely given the wealth of dust-continuum observations being using to derive gas scaling relations as well as study the cosmic molecular gas density (Sections 1.3.2 and 1.3.4). *Can dust-continuum emission be used to constain the total molecular gas content as reliably as the traditional tracer CO(1-0)?*

In **Chapter 3**, I compare the resolved stellar, dust and CO emission of three, star-forming galaxies in the HUDF. Unlike previous resolved studies of molecular gas at this epoch (of which there are few), these galaxies were not selected based on compact or bright submillimeter continuum emission, but were instead selected based on their large rest-frame optical extents, bright CO emission and the fact that they lie on the Main Sequence. *Do dust-continuum and CO emission paint the same picture of the distribution of molecular gas? What does the combination of these tracers reveal about the sites for star formation? Is the bulk motion of molecular gas on a global galaxy scale ordered or random?*

In **Chapter 4**, I study the effect of the CMB on the emission from CO and atomic carbon, from $z = 0-7$. As discussed in this introduction, such observations are increasingly being used to probe the total molecular gas content of star-forming galaxies, but *are we correctly taking the effects of the CMB into account? To what extent does the increase in CMB temperature with redshift alter the temperature and density structure of the molecular ISM? And how does this affect the strength of the line emission relative to the background emission?*

In **Chapter 5**, I summarise what we learnt from these three studies, what questions remained open, what new questions arose and where the field is headed in the next few years. *What do we still have to learn about the molecular ISM of distant galaxies?*

Taking the Plunge

Novel, ambitious, exciting data!
A huge time investment.
Yet, what magic is this?
The uv plane, a pattern
on the sky, transformed.

Shun the outlying points
Bad baselines, a faulty scan
Flag them! Flag them all!
Where art thou,
bright emission line?
70 hours with the VLA
yet nothing to show?

Nothing? Zip! Zero...
Patience young un. Patience
We are searching for
the faint and distant ones
not the blazing, blaring
monsters of the tutorials
So keep digging young un,
Keep digging.

It's there! it's there!
A line, another, another
Only four evaded us
The needle in the haystack
can be found, if...
you know where to look.
Now clean it, collapse it
Gather those precious moments

Perhaps it was the work
of a genius?
One dust-to-gas ratio,
One average temperature,
One emissivity index...
To rule them all?
And an alpha CO of 6.5!
Quelle horreur!!

Yet, it would not be broken
no matter how it was shaken.
Each measurement, a test
of each others bias.
But in walking the tightrope
of diplomacy and will
a balance was struck.
Unshakeable, robust, solid.

2

THE MOLECULAR GAS RESERVOIRS OF $z \sim 2$ GALAXIES: A COMPARISON OF CO(1-0) AND DUST-BASED MOLECULAR GAS MASSES

This chapter comprises the article of the same title, published in the Astrophysical Journal (Kaasinen, Scoville, Walter, Da Cunha, Popping, Pavesi, Darvish, Casey, Riechers, and Glover, 2019). The published paper has been reformatted to match the style of this thesis. The main coauthor contributions are listed at the end of the Chapter. I conducted the data reduction and analysis, with advice and initial tutoring in some of the software by some coauthors. Likewise, the text is written by me, with suggestions from coauthors.

Abstract

We test the use of long-wavelength dust-continuum emission as a molecular gas tracer at high redshift, via a unique sample of 12, $z \sim 2$ galaxies with observations of both the dust-continuum and CO(1-0) line emission (obtained with the Atacama Large Millimeter Array and Karl G. Jansky Very Large Array, respectively). Our work is motivated by recent, high redshift studies that measure molecular gas masses (M_{mol}) via a calibration of the rest-frame 850μm luminosity ($L_{850\mu m,rest}$) against the CO(1-0)-derived M_{mol} of star-forming galaxies. We hereby test whether this method is valid for the types of high-redshift, star-forming galaxies to which it has been applied. We recover a clear correlation between the rest-frame 850μm luminosity, inferred from the single-band, long-wavelength flux, and the CO(1-0) line luminosity, consistent with the samples used to perform the 850μm calibration. The molecular gas masses, derived from $L_{850\mu m,rest}$, agree to within a factor of two with those derived from CO(1-0). We show that this factor of two uncertainty can arise from the values of the dust emissivity index and temperature that need to be assumed in order to extrapolate from the observed frequency to the rest-frame at 850μm. The extrapolation to 850μm therefore has a smaller effect on the accuracy of M_{mol} derived via single-band dust-continuum observations than the assumed CO(1-0)-to-M_{mol} conversion factor. We therefore conclude that single-band observations of long-wavelength dust emission can be used to reliably constrain the molecular gas masses of massive, star-forming galaxies at $z \gtrsim 2$.

2.1 INTRODUCTION

Most star formation is observed to occur within the molecular phase of the interstellar medium (ISM), with observations demonstrating a strong correlation between the surface density of the star formation rate (SFR) and that of the molecular gas (e.g. Wong and Blitz, 2002; Bigiel et al., 2008; 2011; Leroy et al., 2008). On a cosmic scale, the SFR density peaked at $z \sim 2$, and has since declined exponentially (see Madau and Dickinson, 2014, and references therein). This decline can largely be attributed to the $10-100$ fold decrease in SFR of the dominant population of star-forming galaxies, i.e. those occupying the Main Sequence (MS, linear relation between the SFR, and stellar mass), from $z \sim 2$ to the present day (e.g. Daddi et al., 2007; Elbaz et al., 2011; Speagle et al., 2014; Whitaker et al., 2014). Understanding the physical processes driving the decline in

SFR requires the accurate measurement of the molecular gas content out to high redshift. But, measuring the molecular gas masses (M_{mol}) of galaxies at $z > 1$ remains a challenge.

The emission from H_2, the most abundant component of the cold, dense phase of the ISM relevant to star formation, cannot be observed directly. Thus, M_{mol} is usually measured via the emission from other, less abundant components of the ISM. Studies of local galaxies typically rely on the ground transition of CO ($J = 1 - 0$) to measure M_{mol}, converting the CO(1-0) line luminosity to a molecular gas mass via the application of an empirically-derived, CO-to-M_{mol} conversion factor (see Bolatto et al., 2013, for a review). However, the majority of high-redshift ($z > 1$) observations are of higher-J CO transitions, which are brighter and more readily detected by millimeter interferometers operating in the 1-3mm atmospheric windows, i.e. the Atacama Large Millimeter/submillimeter Array (ALMA) and the NOrthern Extended Millimeter Array (NOEMA). The use of higher-J, CO lines requires an additional correction for the (a priori unknown) excitation of the gas, increasing the uncertainty of the derived gas masses by at least a factor of two (see e.g. the variation in the CO(3-2)-to-CO(1-0) line ratio in Iono et al. 2009; Mao et al. 2010; Harris et al. 2010; Ivison et al. 2011; Riechers et al. 2011; Papadopoulos et al. 2012a; Sharon et al. 2016 and other issues discussed in Carilli and Walter 2013).

To combat the difficulty of relying on faint and/or high excitation lines at high redshift, Scoville (2012), suggested the use of the long-wavelength, Rayleigh-Jeans (RJ) tail of dust emission. Methods of measuring M_{mol} from long-wavelength dust-continuum emission were subsequently developed via empirical calibrations of rest-frame infrared (IR) luminosities against CO-derived molecular gas masses (Eales et al., 2012; Bourne et al., 2013; Groves et al., 2015; Scoville et al., 2014; 2016; 2017; Hughes et al., 2017). The rest-frame 850μm luminosity ($L_{850\mu m,rest}$) was found to exhibit a particularly tight correlation with the CO(1-0) line luminosity (e.g. Scoville et al., 2016; Hughes et al., 2017). For brevity, we henceforth refer to the method calibrated against $L_{850\mu m,rest}$ as the RJ method.

Applying the RJ method requires the conversion of the observed emission to $L_{850\mu m,rest}$, either by fitting the IR portion of the spectral energy distribution (SED) (e.g. Hughes et al., 2017), or, extrapolating from a single-band measurement in the RJ tail, assuming the dust opacity coefficient and mean temperature of dust contributing to the RJ tail (e.g. Scoville et al., 2016). The single-band RJ method is particularly convenient for bright, high-redshift sources, for which the dust-continuum can be detected in only a few minutes with ALMA (Scoville et al., 2016), in contrast to the multiple hours required to observe CO emission (e.g. Tacconi et al., 2013).

The variety of methods used to measure M_{mol} complicate efforts to link the molecular gas contents and SFRs of galaxies. Like the SFR, the molecular gas mass fractions of star-forming galaxies appear to have declined since $z \sim 2$ (e.g. Daddi et al., 2010a; Riechers et al., 2010; Genzel et al., 2010; 2015; Tacconi et al., 2010; 2018; Dessauges-Zavadsky et al., 2015; Decarli et al., 2016; Schinnerer et al., 2016; Scoville et al., 2017; Darvish et al., 2018). But, there remains some tension between the gas scaling relations derived in these studies, especially regarding the contribution of the star formation efficiency to the declining SFRs of MS galaxies.

Most studies find a slight decline in the star formation efficiency of MS galaxies with redshift (Tacconi et al., 2010; Genzel et al., 2010; 2015; Scoville et al., 2016; 2017; Tacconi et al., 2018; Darvish et al., 2018), but the exact scaling varies. Genzel et al. (2015) find that the increased SFRs of high-redshift (high-z), MS galaxies can be mainly attributed to higher gas mass fractions, whereas Scoville et al. (2016) and Darvish et al. (2018) also find a significantly more efficient mode of star formation in high-z galaxies (5× shorter gas depletion times). A similar inconsistency exists regarding the difference between MS and starburst galaxies. Whereas Scoville et al. (2016) and Darvish et al. (2018) conclude that the high SFRs of starburst galaxies relative to the MS are driven by both the higher molecular gas masses and star formation efficiencies of the former, Daddi et al. (2010b) and Genzel et al. (2010), 2015 mainly attribute the offset from the MS to higher star formation efficiencies.

The extent to which the differences between molecular gas scaling relations are affected by the assumptions used to infer molecular gas masses, from CO vs dust-continuum emission, has not yet been quantified in detail. Recent studies have begun to address the need for consistency between dust and CO-based measurements. For example, Hughes et al. (2017) compared the CO(1-0) line luminosities and $L_{850\mu m,rest}$ of local star-forming galaxies, whereas Liang et al. (2018) and Privon et al. (2018) compared the RJ-based M_{mol} with the "true" M_{mol} of a set of simulated star-forming galaxies. Although these studies have investigated the use of $L_{850\mu m,rest}$ as a gas mass tracer, they do not confirm whether the gas masses, already determined for $\gtrsim 600$ high-z galaxies (Scoville et al., 2016; 2017; Schinnerer et al., 2016; Miettinen et al., 2017; Darvish et al., 2018), are equivalent to what would be derived using CO(1-0).

To compare the molecular gas masses, derived from the single-band RJ continuum and CO(1-0), we have assembled a unique sample of 16 unlensed, $z \sim 2$, star-forming galaxies with CO(1-0) observations from the VLA, and, dust-continuum measurements from the ALMA. This sample represents a significant increase in the number of CO(1-0) detections at high redshift with ~ 50 sources at $z > 1$ having been detected previously e.g. supplementary table of Carilli and Walter, 2013, out of which $\lesssim 20$ sources are unlensed (e.g Emonts et al., 2013; Aravena et al., 2014; Bolatto et al., 2015; Huynh et al., 2017; Pavesi et al., 2018). The fact that our sources are unlensed avoids potential complications involving differential lensing. Our sample consists of massive ($> 2\times10^{10}M_{\odot}$) galaxies both on and above the MS. We thereby focus on the galaxy population dominating the peak of the cosmic SFR density.

The remainder of this Chapter is structured as follows. We present our sample and describe the observations and data reduction in Section 2.2. In Section 2.3 we explain how we derive the molecular gas masses, SFRs and stellar masses. We present our results and discussion in Section 2.4, comparing the CO(1-0) line luminosity and $L_{850\mu m,rest}$, as well as the molecular gas masses derived from these luminosities. Our work is summarised in Section 5.1. Throughout this paper we assume a ΛCDM cosmology with $H_0 = 70 km s^{-1} Mpc^{-1}$, $\Omega_M = 0.3$ and $\Omega_\Lambda = 0.7$. All stellar masses and SFRs are based on a Chabrier (2003) IMF. We use a CO-to-M_{mol} conversion factor of $\alpha_{CO} = 6.5 M_{\odot}/(K km s^{-1} pc^2)$ throughout this paper.

2.2 SAMPLE AND OBSERVATIONS

2.2.1 Sample Selection

Our sample is comprised of 16, massive, star-forming galaxies at $z \sim 2$, with long-wavelength (rest-frame $\sim 250\mu m$) dust-continuum measurements from ALMA (ALMA, Wootten and Thompson, 2009). Our sample was selected from the ALMA-detected, IR-bright sample of Scoville et al. (2017). The parent sample of Scoville et al. (2017) was chosen using the Herschel-based catalogue of far-IR sources in the COSMOS field (Lee et al., 2013; 2015). We therefore have photometric measurements of at least two of the five IR Herschel bands: the $100\mu m$ and $160\mu m$ bands from PACS (Lutz et al., 2011) and the $250\mu m$, $350\mu m$, and $500\mu m$ bands from SPIRE (Griffin et al., 2010), for all 16 sources discussed in this paper. Like the parent sample of Scoville et al. (2017), our sample is restricted to objects with $M_* > 2\times10^{10}M_{\odot}$ (based on the COSMOS catalogue described in Laigle et al. 2016).

To maximise the chances of detecting CO(1-0) emission, we selected the 16 galaxies with the highest ALMA Band 7 (343.5 GHz) fluxes. Based on the calibration presented in Scoville et al. (2014), 2016, 2017 we expected CO(1-0) detections of $S_{CO}\Delta v > 100 mJy km s^{-1}$, with the Very Large Array (VLA). Our sample is therefore intentionally biased to the types of high SFR ($SFR > 300 M_{\odot} yr^{-1}$) sources to which the RJ method is applied (Scoville et al., 2016; 2017; Schinnerer et al., 2016; Miettinen et al., 2017; Darvish et al., 2018). Our sample is relevant to the types of high-z, star-forming galaxies targeted by molecular gas surveys, extending from starbursts down to the MS. We discuss our sample with respect to the MS further in Section 2.3.3.2. Because of our

Table 2.1: Source Information

Galaxy ID	Position (J2000)		z_{COSMOS} [a]	z_{flag} [b]	$z_{CO(1-0)}$
	R.A.	Decl.			
1	$10^h00^m35.^s29$	$2°43'53.''2$	2.38	photometric	2.607
			2.608	4 [MOSFIRE] [c]	2.607
2*	$10^h00^m08.^s91$	$2°40'10.''3$	2.284	2 [MOSFIRE] [c]	-
			1.847	photometric	-
3	$9^h58^m40.^s28$	$2°05'14.''7$	2.416	3 [DEIMOS]	2.414
4	$10^h00^m31.^s82$	$2°12'43.''2$	2.104	4 [MOSDEF] [c]	2.104
5	$10^h02^m24.^s77$	$2°32'11.''6$	2.287	4 [MOSFIRE]	2.287
6*	$10^h02^m32.^s09$	$2°34'41.''4$	2.68	photometric	-
			-	[MOSDEF] [c]	-
7	$10^h01^m03.^s55$	$1°48'10.''6$	2.240	4 [MOSFIRE]	2.240
8	$9^h58^m37.^s34$	$2°42'58.''5$	2.11	photometric	2.173
9*	$10^h00^m03.^s89$	$2°47'32.''4$	1.76	photometric	-
			1.958	4 [MOSFIRE]	-
10	$10^h01^m19.^s52$	$2°09'44.''7$	2.934	3 [zDEEP]	2.934
11	$9^h59^m57.^s35$	$2°03'11.''3$	1.942	4 [MOSFIRE] [c]	1.941
12	$10^h01^m16.^s28$	$2°42'59.''4$	2.340	4 [MOSFIRE] [c]	-
13	$10^h01^m58.^s96$	$2°06'58.''6$	2.400	4 [MOSFIRE]	2.400
14*	$10^h01^m01.^s24$	$2°28'00.''6$	2.264	2 [FMOS]	-
15	$10^h00^m56.^s68$	$2°52'22.''5$	1.654	3 [FMOS]	-
16	$9^h59^m04.^s39$	$2°13'12.''5$	1.779	2 [zDEEP]	1.780

[a] Redshift provided in the COSMOS catalogue, as well as, spectroscopic redshifts obtained from our 2019 MOSFIRE observations (sources 1, 2, 4, 9, 11 and 12).
[b] Flag assigned to the quality of the spectroscopic redshift of column 4, where 4 is completely secure, 3 is secure but the classifier(s) recognise at least a remote possibility for error and 2 indicates that a significant possibility remains that the redshift is incorrect (Lilly et al., 2007). We reclassify sources 14 and 15 after inspecting the spectra ourselves.
[c] We use new MOSFIRE spectroscopy, not yet included in the COSMOS catalogue, to analyse the data for sources 1, 2, 4, 6, 9, 11 and 12. No rest-frame optical emission lines were observed for source 6.
Sources marked with * are deemed to have unreliable redshift estimates (insufficient to infer CO(1-0) upper limits or SED-based properties) and are therefore removed from the sample. Note that this includes sources 2 and 9, for which the VLA observations were optimised for the catalogued redshifts, which our 2019 MOSFIRE observations show to be incorrect. Hence, the observations do not encompass the CO(1-0) line for source 2, whereas for source 9 the CO line is expected on the edge of the observed frequency range, where the noise is the greatest.

selection criteria, our sample spans a wide redshift range of $1.6 < z < 2.9$. The coordinates and estimated redshifts of the full sample are provided in Table 2.1.

2.2.2 CO(1-0) Observations and Data Reduction

The VLA observations analysed here were taken during February and March 2017. Of the 16 galaxies in our sample, four were observed in the Q band (40 – 50 GHz) and 12 in the Ka band (26.5 – 40 GHz). Each target was observed for a total of four hours, including the time spent on bandpass, phase and amplitude calibration sources.

The raw VLA data were processed to produce clean images using the Common Astronomy Software Application (CASA; McMullin et al., 2007) [(1)], version 4.7.2. To calibrate the data, we applied the VLA calibration pipeline[(2)] without Hanning smoothing. We created the initial dirty images using Common Astronomy Software Application (CASA)'s `TCLEAN` algorithm. These dirty images are used to visually identify the presence of CO and ensure the source emission is found at the anticipated position. We then create cleaned image cubes for these sources via CASA's `TCLEAN`, applying a natural weighting scheme, a cleaning threshold of twice the root-mean-square (rms) noise level (2σ) and a circular mask with a radius of 5", centred at the position of the source. We optimise the spectral resolution to achieve higher signal-to-noise ratio (S/N). For sources 8 and 16 it was necessary to use the native resolution ($\sim 16\,\mathrm{km\,s^{-1}}$) to extract the spectra (see Figure A.2). We provide the smoothed, extracted spectra of our full sample in Figure A.1 (Appendix A.1).

We detect CO(1-0) emission in 10 of the 16 sources in our sample. To classify a source as a CO detection we require the peak flux of the spectrum, extracted at the source position, and the peak flux in the moment zero map to be detected at $\geq 3\sigma$. For the CO-detected sources, we derive the CO(1-0) flux, central frequency, and spectroscopic redshift by fitting a single Gaussian to the CO(1-0) line emission via `Python`'s `scipy.optimize.curvefit` algorithm. We use a $1/\sigma^2$ weighting scheme, where σ is the rms noise per channel, and take the 1σ errors estimated by our fitting routine as the uncertainties of the measured values. We provide the rms noise of the channel corresponding to the CO(1-0) peak, the peak flux and total line flux in Table 2.2. The spectra and emission-line fits are shown in Figure A.2 (Appendix A.1), with two examples shown in Figure 2.1. Although the spectra of sources 3 and 8 are best fit by double Gaussian profiles (based on the χ^2 values) we provide the single Gaussian fits in this paper. We do not consider the double Gaussian profiles to be physical given the relative strengths of the rms and dip in flux. Our choice of line profile has no impact on our results. The fluxes derived from the double Gaussian line profiles are consistent, within uncertainties, with the single Gaussian fits shown in Figure A.2 of the Appendix.

The CO(1-0) line fluxes, and subsequent luminosities, quoted in this paper are based on our single Gaussian line profile fits. These values are consistent, within uncertainties, with the integrated line fluxes extracted from the moment zero maps, for which we tested two methods: (1) extracting the fluxes at the source position and (2) estimating the line flux via the 2D Gaussian fits of CASA's `imfit`. Our moment zero maps are shown in the central panel of the integrated maps in Figures 2.2 and A.3 (Appendix). We provide three channel maps in order to: (1) show the lack of continuum emission around CO(1-0), and, (2) highlight that we have captured all CO(1-0) emission in the moment zero maps (centre). The velocity widths of the moment zero (and adjacent, integrated) maps, indicated by the yellow shaded regions of Figures 2.1 and A.2 (Appendix), were selected to encompass the range of velocities at which the source emission was visible at $\geq 3\sigma$ in the cleaned data cubes. For most sources, the velocity widths of the integrated, moment zero maps are ~ 1.2 the full width at half maximum (FWHM) of the CO(1-0) line. However, for sources 4 and 5, where the spectra are not as well fit by Gaussian profiles, we create the integrated channel maps based on greater velocity widths.

Our CO-derived redshifts are consistent with the redshifts derived from rest-frame optical lines (flagged 3 or 4 in Table 2.1). As for the rest-frame optical emission lines, the typical uncertainties of our CO-derived redshifts are ~ 0.0002. In contrast, the uncertainty of the photometric redshifts are ~ 0.2, on average, with values of ~ 0.4 for some COSMOS sources (Laigle et al., 2016). For example, source 1 has a secure CO(1-0) detection at $z = 2.607$ but a predicted photometric redshift of 2.38.

We remove four sources from our sample, which have unreliable redshifts (flagged in Table 2.1). Accurate spectroscopic redshifts are required in order to estimate upper limits on the CO(1-0) emission and fit the correct SED models to infer stellar masses and SFRs (see Section 2.3.3). We relied on the COSMOS redshift catalogue to design our VLA observations but reobserved sources

[(1)] https://casa.nrao.edu
[(2)] https://science.nrao.edu/facilities/vla/data-processing/pipeline

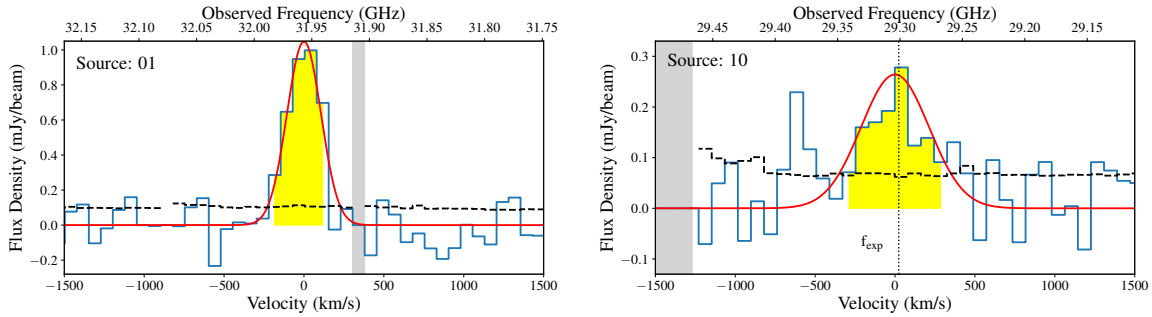

Figure 2.1: Examples of two CO(1-0) spectra (blue). The remaining spectra and line fits are shown in Figure A.2. The Gaussian line fits are shown for comparison (red) with the spectral region used to create the integrated maps in Figure 2.2 shaded in yellow. Flagged channels, not used for the line fits, are shaded in grey. The root-mean-square noise per channel is indicated by the black, dashed histogram.

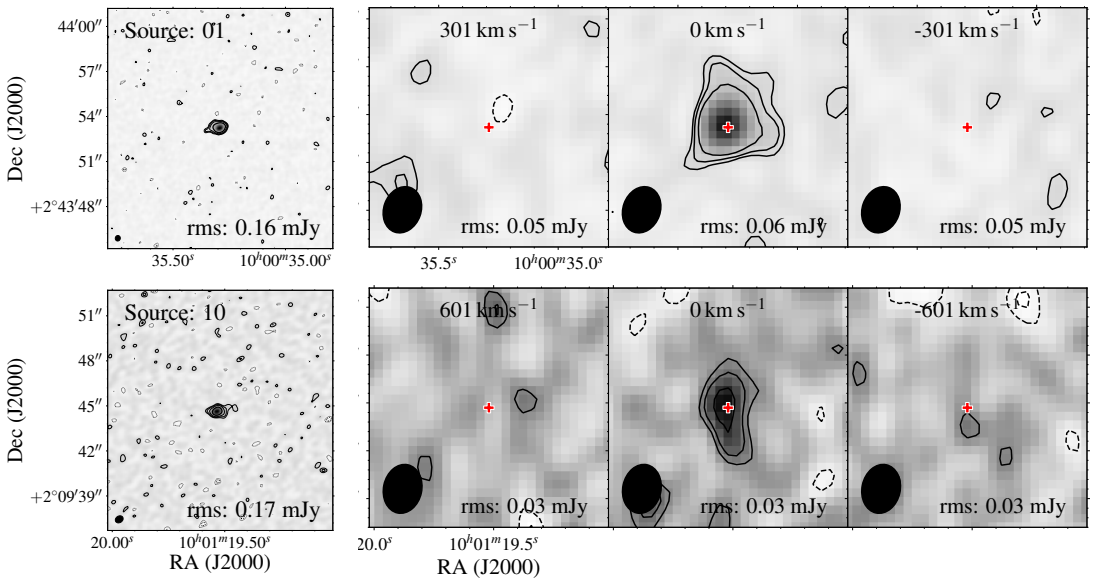

Figure 2.2: Example comparison of the ALMA dust continuum (left map) and integrated VLA CO(1-0) maps for sources with CO(1-0) detections. The integrated maps of the remainder of the sample are shown in Figure A.3 (Appendix). The source number is labeled at the top left of the left hand panel in each row. The rms value is given in the bottom right corner of each map. Left column: ALMA observations at 343.5 GHz. Contours are shown for $\pm 2, 3, 5$ and 10σ (dashed contours for negative values). Right columns: Channel maps around the measured (expected) CO(1-0) line. For each source, the central panel of the VLA channel map represents the moment zero map and is centred at the central velocity of the CO spectrum. The velocity width of the integrated maps is chosen to encompass the full source emission (1.2×FWHM of the CO(1-0) line for sources other than 4 and 5). Contours are shown for $\pm 2, 3$ and 5σ (dashed contours for negative values). The red cross indicates the expected position of the source, at which the CO spectrum was extracted. The color shading indicates the flux density in mJy/beam.

1, 2, 4, 6, 9, 11 and 12 with the Multi-Object Spectrometer For Infra-Red Exploration (MOSFIRE, on Keck I), after our VLA observations were taken. Because we relied upon the catalogued redshifts when taking our VLA data, the observed frequency intervals for sources 2 and 9 are not optimised for the correct redshift (see note below Table 2.1). Thus, the frequency range of the observations for source 2 does not encompass the CO(1-0) line, whereas for source 9, the expected position of CO(1-0) falls at the edge of the observed frequencies, where the spectral noise is greatest. For source 6 we observed neither CO(1-0) emission, nor any rest-frame optical emission lines. Thus, we conclude that the photometric redshift of $z = 2.68$, on which we based both the VLA and MOSFIRE

Table 2.2: CO(1-0) and Dust-Continuum Data

Galaxy	Beam		PA	σ	$S_{peak,CO(1-0)}$	$S_{CO(1-0)}\Delta v$	$S_{343.5GHz,cont}$
	max ($''$)	min ($''$)	($^\circ$)	(mJy/beam)	mJy	(mJy km s^{-1})	(mJy)
1	2.96	2.34	-19.6	0.10	1.05 ± 0.08	279 ± 34	13.02 ± 0.46
3	3.84	2.25	167.9	0.15	0.50 ± 0.07	272 ± 64	9.67 ± 0.47
4	2.75	1.98	-6.35	0.09	0.29 ± 0.06	185 ± 55	8.23 ± 0.37
5	2.49	2.05	-179.0	0.16	0.55 ± 0.13	158 ± 55	6.34 ± 0.35
7	2.67	1.90	0.3	0.20	0.79 ± 0.13	236 ± 59	7.96 ± 0.36
8	2.50	2.23	-22.7	0.13	0.44 ± 0.05	125 ± 22	6.08 ± 0.36
10	2.54	1.19	-12.3	0.07	0.26 ± 0.04	141 ± 31	4.91 ± 0.37
11	2.25	1.77	18.7	0.17	0.58 ± 0.07	368 ± 74	5.39 ± 0.47
12	2.68	2.19	10.8	-	-	≤ 80	4.44 ± 0.40
13	2.87	2.25	23.3	0.15	0.74 ± 0.09	150 ± 28	4.29 ± 0.36
15	2.24	1.81	16.7	-	-	≤ 243	3.34 ± 0.29
16	2.24	1.87	31.0	0.29	1.05 ± 0.16	112 ± 25	3.86 ± 0.81

observations, is not reliable. For source 14, we observe no CO(1-0) emission and the rest-frame optical spectra exhibit only low S/N peaks.

For the two sources without CO(1-0) detections but with reliable spectroscopic redshifts (sources 12 and 15) we estimate upper limits on the CO(1-0) emission based on the moment zero maps, centred on the expected frequency of the CO(1-0) line. We create each map using `TCLEAN`, with a channel width of 500 km s^{-1} (consistent with the broader lines of our CO-detected sample). We measure the rms value in these single channel maps and use the 3σ value as our upper limit, consistent with our detection criteria. It is likely that source 15 is not detected because it is just below the detection limit, i.e. the data here were too noisy to detect the predicted signal. However, the same is not true for source 12, for which we would expect to detect CO based on the predicted CO luminosity and noise limit. We can only speculate that one of the assumptions applied in the RJ method does not apply to this source, e.g. that the dust-to-gas ratio is greater than expected (see Section 2.3.2.1 for the assumptions).

2.2.3 Dust-Continuum Data

We carefully measure the dust-continuum flux of each source, examining the images in the left panels of Figures 2.2 and A.3. We note that the FWHM of the synthesized ALMA beam is at least 6× smaller than that of the VLA beam (Figures 2.2 and A.3). Thus, unlike for the CO(1-0) data, some of our sources (particularly source 16) show resolved structure in the dust-continuum emission. We therefore use CASA's `imfit` to fit elliptical Gaussians to the source emission, focussing on the region of interest within 5" of the source. We fit two Gaussians to the emission of source 16 but fit all other sources with a single Gaussian element. We use the flux error returned by `imfit` as the uncertainty on our derived fluxes. The S/N of the continuum fluxes varies from 4 (Source 16) to 29 (Source 1). Our derived fluxes are mostly consistent with those predicted by the automated procedure of Scoville et al. (2017), except for source 5, for which our measured flux is 20% lower. We provide our measured fluxes in Table 2.2.

2.3 DERIVED QUANTITIES

2.3.1 CO(1-0)-based Molecular Gas Masses

We use our measured CO(1-0) fluxes and upper limits to derive the CO(1-0) line luminosities, $L'_{\rm CO(1-0)}$(K km s^{-1} pc^2). For sources with a CO(1-0) detection we use the CO-derived spectroscopic redshift. For upper limits, we rely on the spectroscopic redshifts from the COSMOS catalogue. We calculate the CO(1-0) line luminosities, via Equation (3) of Solomon et al. (1992),

$$L'_{\rm CO} = 3.25 \times 10^7 S_{\rm CO}\Delta v\, \nu_{\rm obs}^{-2} D_{\rm L}^2 (1+z)^{-3}, \tag{2.1}$$

where the CO(1-0) line flux, $S_{\rm CO}\Delta v$, is in Jy km s^{-1}, the observed frequency $\nu_{\rm obs}$ is in GHz, and the luminosity distance, D_L, is in Mpc.

We derive the total molecular gas mass, based on the CO(1-0) line luminosities, via,

$$M_{\rm mol} = \alpha_{\rm CO} L'_{\rm CO(1-0)}, \tag{2.2}$$

with $\alpha_{\rm CO} = 6.5\,{\rm M}_\odot/({\rm K\,km\,s^{-1}\,pc^2})$. The chosen value of $\alpha_{\rm CO}$ is based on a standard Galactic conversion factor of $X_{\rm CO} = 3 \times 10^{20}\,{\rm cm^{-2}(K\,km\,s^{-1})^{-1}}$ and includes a factor of 1.36 to account for the associated mass of heavy elements (mostly He at 8% by number). We provide the values of $L'_{\rm CO(1-0)}$ and the CO(1-0)-based M$_{\rm mol}$ in Table 2.3.

The CO- and $L_{850\mu{\rm m,rest}}$-based M$_{\rm mol}$ presented in this paper are calculated using the same CO-to-M$_{\rm mol}$ conversion factor, $\alpha_{\rm CO} = 6.5\,{\rm M}_\odot/({\rm K\,km\,s^{-1}pc^2})$. We select this value solely in order to ensure consistency between the molecular gas masses we derive from CO(1-0) and $L_{850\mu{\rm m,rest}}$, because the latter was calibrated against CO(1-0)-derived M$_{\rm mol}$ using this conversion factor (Scoville et al., 2016). Our adopted value is a factor of ~ 1.5 higher than the $4.36\,{\rm M}_\odot/({\rm K\,km\,s^{-1}pc^2})$ typically adopted by other studies, based on the recommendation of Bolatto et al. (2013) (e.g. Tacconi et al., 2013; Genzel et al., 2015; Tacconi et al., 2018). Whereas the typically-adopted Milky Way value (corresponding to $X_{CO} = 2 \times 10^{20}\,{\rm cm^{-2}(K\,km\,s^{-1})^{-1}}$) is based on the compilation of results from gamma-ray observations, extinction measurements, dust emission and CO isotopologues, the value we have adopted here is derived from the correlation of the CO line luminosities and virial masses for resolved Galactic giant molecular clouds (Solomon et al., 1987; Scoville et al., 1987).

2.3.2 RJ-based Molecular Gas Masses

We derive the molecular gas masses from the inferred $L_{850\mu{\rm m,rest}}$, the reference luminosity against which the RJ method is calibrated. We infer $L_{850\mu{\rm m,rest}}$ via two methods: (1) from the single, ALMA band 7 flux only ($L^{\rm single-band}_{850\mu{\rm m,rest}}$), and, (2) from the best-fit model SEDs ($L^{\rm SED}_{850\mu{\rm m,rest}}$). We compare the values of $L_{850\mu{\rm m,rest}}$ derived via these two methods in Section 2.4.1.

2.3.2.1 Single-band Derived $L_{850\mu{\rm m,rest}}$

The first method we use to derive $L_{850\mu{\rm m,rest}}$ follows the prescription described in detail in Appendix A.1 of Scoville et al. (2016), 2017. We briefly their approach again here, for clarity. Note that this follows on from the description of dust-continuum emission as a molecular gas tracer presented in Sec. 1.2.3. Scoville et al. (2016), 2017 assume that the long-wavelength dust-continuum emission can be described by a single modified blackbody, with a flux density given by:

$$S = \frac{{\rm M_{mol}}\kappa(\nu_{\rm rest}) B_{\nu_{\rm rest}}(T_{\rm dust})(1+z)}{d_L^2}, \tag{2.3}$$

where $\kappa(\nu_{\rm rest})$ is the absorption coefficient of dust per unit total mass of molecular gas, $B_{\nu_{\rm rest}}$ is the Planck function and d_L the luminosity distance. The mean, mass-weighted dust temperature,

used to describe the modified blackbody emission, is assumed to be 25 K (discussed in Appendix A.2 of Scoville et al., 2016). This choice is further justified by the recent work of Liang et al. (2019). In the long-wavelength regime, the flux is proportional to ν^2 and Equation (2.3) can be rewritten by including a correction for the departure in the rest frame of the Planck function from RJ approximation, $B_{\rm rest}/RJ_{\rm rest} = \Gamma_{\rm RJ}(\nu_{\rm obs}, z)$. To relate the specific luminosity in the rest frame of the galaxy to $L_{850\mu{\rm m,rest}}$, the long-wavelength dust opacity, κ, is described by a power law,

$$\kappa(\nu_{\rm obs,rest}) = \kappa(\nu_{850\mu{\rm m}})(\lambda/850\mu m)^{-\beta} \tag{2.4}$$

with a dust emissivity index of $\beta = 1.8$ (see Appendix A.3 of Scoville et al., 2016, for details). Note that because the dust opacity is defined relative to the molecular gas mass, there is an implicit assumption here of a constant gas-to-dust ratio. Combining the above assumptions, the reference luminosity can be calulated from the measured, RJ flux via,

$$L^{\rm single-band}_{850\mu{\rm m,rest}} = S\left[\frac{\nu_{850\mu{\rm m}}}{\nu_{\rm rest}}\right]^{3.8} \frac{d_L^2}{1+z}\frac{\Gamma_{\rm RJ}(\nu_{850\mu{\rm m}},0)}{\Gamma_{\rm RJ}(\nu_{\rm obs},z)}, \tag{2.5}$$

where the exponent of 3.8 is the result of the ν^2 dependence of the RJ flux (eq. 1.7) combined with the dust emissivity index. We use Equation 2.5 to derive the values of $L^{\rm single-band}_{850\mu{\rm m,rest}}$ and provide the derived values in Table 2.3.

2.3.2.2 SED-derived $L_{850\mu{\rm m,rest}}$

For our second method, we apply the updated version of the SED-fitting algorithm MAGPHYS high-z, which builds a likelihood distribution for $L_{850\mu{\rm m,rest}}$ by marginalising over a library of models with varying dust emission parameters, such as dust temperatures (see also da Cunha et al., 2013b). MAGPHYS models the dust emission, from the rest-frame mid-infrared to millimeter wavelengths, as the sum of four dust components: (i) a component of polycyclic aromatic hydrocarbons (PAHs); (ii) a mid-infrared continuum that characterizes the emission from hot grains at temperatures in the range 130-250 K; (iii) a warm dust component in thermal equilibrium with temperatures in the range 30-80K; and (iv) and a component of cold grains in thermal equilibrium with adjustable temperature in the range 20-40 K. The emission from the warm and cold dust components are described by modified blackbodies.

We choose not to analyse the SED-derived dust masses or temperatures due to degeneracies between these parameters. Our data do not sample far enough along the RJ tail to break the degeneracy between $T_{\rm dust}$ and β (see e.g. da Cunha et al., 2015). Moreover, the dust temperature relevant to the RJ emission tail is the mass-weighted dust temperature (discussed in Appendix A.2. of Scoville et al., 2016). The total dust mass inferred by MAGPHYS is a sum of the masses of the modeled components, which are free parameters, and is therefore degenerate with the temperatures of the dust components.

To assess what impact variations in β and $T_{\rm dust}$ have on the derived $L_{850\mu{\rm m,rest}}$ we apply MAGPHYS with four sets of assumptions:

1. with $\beta = 1.5$ and 2.0 for the warm and cold components, respectively, and with the cold dust temperature as a free parameter (standard version),
2. with $\beta = 1.8$ for the warm and cold components and with the cold dust temperature as a free parameter,
3. with $\beta = 1.5$ and 2.0 for the warm and cold components, respectively, but with the temperature of the cold component fixed to 25 K, and,
4. with $\beta = 1.8$ for the warm and cold components and the temperature of the cold component fixed to 25 K.

We fit the rest-frame SEDs and build likelihood distributions for $L^{\rm SED}_{850\mu{\rm m,rest}}$ for each of these four cases. The rest-frame SEDs and best fit, based on the standard version of MAGPHYS, are shown

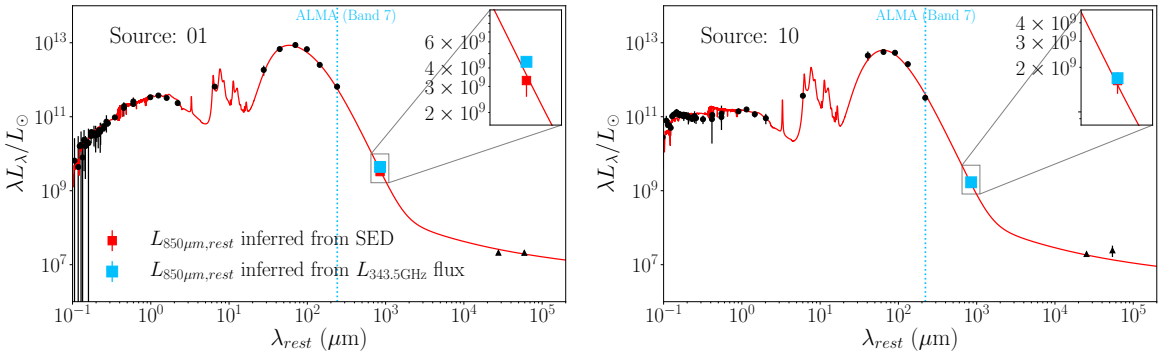

Figure 2.3: Examples of rest-frame SEDs. The inset focuses on the portion of the rest-frame spectrum around 850µm, comparing the single-band (blue) and SED-derived (red) $L_{850\mu m,rest}$, where the single-band derived value is calculated from Equation (2.5). Note that the best-fit SED and value of $L_{850\mu m,rest}$ shown are based on the standard MAGPHYS assumptions of $\beta = 1.5$ and 2.0 for the warm and cold components, respectively, with the temperature of the cold dust component as a free parameter. The black filled circles represent the photometry used to fit the SEDs whereas the black triangles show the radio fluxes, which were not used to fit the SEDs.

in Figures 2.3 and A.4 (Appendix), with the single-band and SED-derived values of $L_{850\mu m,rest}$ compared in the zoom-in panels.

2.3.2.3 Converting $L_{850\mu m,rest}$ to M_{mol}

We convert both the single-band and SED-derived values of $L_{850\mu m,rest}$ to molecular gas masses by applying the conversion factor,

$$\begin{aligned} \alpha_{850\mu m} &= \frac{L_{850\mu m,rest}}{M_{mol}} \\ &= \frac{L_{850\mu m,rest}}{L'_{CO(1-0)}} \frac{1}{\alpha_{CO}}, \end{aligned} \tag{2.6}$$

derived by Scoville et al. (2016). The calibration of $\alpha_{850\mu m}$ is based on the Herschel SPIRE 350 and 500μm data and CO(1-0)-derived M_{mol} of 28 local star-forming galaxies, 12 low-redshift ultraluminous infrared galaxies (ULIRGs), and 30 $z \sim 2$ submillimeter galaxies (SMGs) from the literature (Scoville et al., 2016). Thus, the single-band RJ method is suited to massive ($> 2 \times 10^{10} M_\odot$), star-forming galaxies for which the dust-to-gas ratios are $\sim 1:100$ (see discussion in Scoville et al., 2016).

Applying the single-band method of Equation (2.5), with the constant $\langle \alpha_{850\mu m} \rangle$ we find a range of M_{mol} of $1.7 - 7.1 \times 10^{11} M_\odot$ with a mean uncertainty of $0.9 \times 10^{11} M_\odot$. The uncertainties of these M_{mol} values are derived from the uncertainty of both the measured dust-continuum fluxes and $\langle \alpha_{850\mu m} \rangle$. Applying the standard version of MAGPHYS to derive $L_{850\mu m,rest}$, with the constant $\langle \alpha_{850\mu m} \rangle$, we find a range of M_{mol} of $1.1 - 5.3 \times 10^{11} M_\odot$ with a mean uncertainty of $0.8 \times 10^{11} M_\odot$. The uncertainty of the MAGPHYS-derived M_{mol} is based on the 16th and 84th percentiles of the likelihood distribution of $L_{850\mu m,rest}$ and the uncertainty of $\langle \alpha_{850\mu m} \rangle$.

2.3.3 Stellar Masses and SFRs

We self-consistently derive the stellar masses, SFRs and reference luminosities, $L^{SED}_{850\mu m,rest}$, upon which the RJ method is based (see Section 2.3.2) by fitting the SEDs of our sources. The stellar masses and SFRs of our sample have been previously derived by fitting the optical-to-infrared SEDs via various techniques (see Lee et al., 2013; 2015; Scoville et al., 2017, for details). The stellar masses, determined with the SED-fitting algorithm `LePhare` (Arnouts et al., 1999; Ilbert et al., 2006), are provided as part of the COSMOS catalogue (Laigle et al., 2016). However, for this small

sample we revisit the stellar mass and SFR fits, using the SED-fitting algorithm MAGPHYS, in order to:

1. self-consistently fit the stellar masses, SFRs and $L^{\rm SED}_{850\mu{\rm m,rest}}$,
2. explore the effect of the assumptions used to derive $L^{\rm SED}_{850\mu{\rm m,rest}}$
3. use the CO(1-0)-based redshifts (where these are the most reliable redshifts), and,
4. validate the robustness of the SED-derived properties.

We describe our application of MAGPHYS in the following subsection. Sources with uncertain redshift measurements (starred in Table 2.1) have been excluded from this analysis. The derived stellar masses and SFRs are provided in Table 2.3.

The stellar masses and SFRs presented here are consistent with the previously-derived values. The stellar masses derived via MAGPHYS and `LePhare` are consistent within a factor of two (with no systematic offset) for all but source 15, for which the MAGPHYS derived M_* is a factor of five greater (we trust our SED fit in Figure A.4). Similarly, our MAGPHYS-derived SFRs are consistent to within a factor of two with the values used in Lee et al. (2015) and Scoville et al. (2017), with no systematic offsets. Thus the conclusions we draw with respect to the global properties of our sample are not affected by the choice of SED-fitting algorithm. However, the scatter in values derived via different SED-fitting algorithms indicates an uncertainty of at least a factor of two in both the stellar masses and SFRs.

2.3.3.1 Application of MAGPHYS

We derive the stellar masses, SFRs and $L^{\rm SED}_{850\mu{\rm m,rest}}$ of our sample via an updated version of the SED-fitting algorithm, MAGPHYS, that builds a likelihood distribution for $L^{\rm SED}_{850\mu{\rm m,rest}}$, applying the version optimised for high-z galaxies (da Cunha et al., 2015). We fit the available COSMOS photometry, from the GALEX far-ultraviolet to Herschel PACS 500 μm filters (taken from the 2016 catalogue of Laigle et al. 2016), in addition to the ALMA Band 7 (343.5 GHz) dust-continuum measurements (described in Section 2.2.3). For source 16, no Herschel data is available in the Laigle et al. (2016) catalogue. Instead, we use the Herschel data described in Lee et al. (2013)[3]. The details of the SED-fitting framework, stellar model libraries and treatment of dust are described in da Cunha et al. (2008), 2015. Two example SED fits are shown in Figure 2.3, the rest are shown in Figure A.4 in the Appendix. We choose not to apply the 1.4 and 3 GHz continuum flux measurements, available for the majority of the sample (see overplotted black triangles in both figures) because the radio/FIR correlation (assumed in MAGPHYS da Cunha et al. 2015) is uncertain at these redshifts and may bias the results.

We use the median stellar masses and SFRs inferred via MAGPHYS, and quote errors as the 16th and 84th percentile ranges of the posterior likelihood distributions. These values are based on the spectroscopic redshifts, derived from either CO(1-0), or, infrared emission lines (see Table 2.1 for redshifts). The SFRs inferred by MAGPHYS represent the average of the star formation history (SFH) over the last 100 Myr (da Cunha et al., 2015). The SFH library of MAGPHYS includes a wide range of continuous SFHs as well as accounting for stochasticity on the SFHs by superimposing star formation bursts of random duration and amplitude. Thus, MAGPHYS models the SFHs of starburst-like and more quiescently star-forming galaxies (see da Cunha et al., 2015, for details). We use the SFH-based SFRs, rather than SFRs derived empirically from the IR luminosities here. However, we note that the SFRs derived empirically from the total IR luminosities are consistent to within a factor of 1.5 for the entire sample, with the IR-inferred SFRs a factor of 1.2 higher on average.

[3] provided via private correspondence

Table 2.3: Derived Properties

ID	$L'_{\rm CO(1-0)}$ (10^{10} K km s^{-1} pc^2)	$L^{\rm single-band}_{850\mu{\rm m,rest}}{}^a$ (10^{31} erg s^{-1} Hz^{-1})	$M_{\rm mol,CO}$ ($10^{11}M_\odot$)	$M_{\rm mol,RJ}{}^a$ ($10^{11}M_\odot$)	M_* ($10^{11}M_\odot$)	SFR ($M_\odot$ yr^{-1})	$T_{\rm cold\,dust}$ (K)	$M_{\rm dust}$ ($10^9 M_\odot$)
1	8.7 ± 1.1	4.72 ± 0.16	5.7 ± 0.7	7.1 ± 1.8	$2.6^{+0.6}_{-0.7}$	1028^{+195}_{-250}	$28.6^{+7.2}_{-1.4}$	$1.7^{+0.3}_{-0.4}$
3	7.4 ± 1.8	3.47 ± 0.15	4.8 ± 1.1	5.3 ± 1.4	$1.8^{+0.2}_{-0.2}$	$865^{+230}_{-\ 60}$	$31.3^{+8.0}_{-2.0}$	$1.5^{+0.1}_{-0.6}$
4	4.0 ± 1.2	2.90 ± 0.13	2.6 ± 0.8	4.4 ± 1.1	$2.5^{+0.6}_{-0.3}$	948^{+164}_{-294}	$26.3^{+0.6}_{-4.9}$	$1.6^{+0.1}_{-0.8}$
5	3.9 ± 1.4	2.26 ± 0.13	2.5 ± 0.9	3.4 ± 0.9	$1.1^{+0.1}_{-0.2}$	$1419^{+50}_{-\ 294}$	$25.8^{+7.1}_{-1.6}$	$1.5^{+1.1}_{-0.0}$
7	5.7 ± 1.4	2.83 ± 0.13	3.7 ± 0.9	4.3 ± 1.1	$1.0^{+0.2}_{-0.2}$	1089^{+10}_{-600}	$28.3^{+13.}_{-2.9}$	$1.7^{+0.3}_{-0.5}$
8	2.8 ± 5.0	2.15 ± 0.13	1.8 ± 0.3	3.3 ± 0.9	$4.6^{+0.9}_{-1.2}$	395^{+204}_{-132}	$29.1^{+7.9}_{-7.9}$	$1.1^{+0.2}_{-0.2}$
10	5.4 ± 1.2	1.81 ± 0.14	3.5 ± 0.8	2.7 ± 0.7	$0.47^{+0.01}_{-0.01}$	$558^{+15}_{-\ 13}$	$36.3^{+3.0}_{-2.3}$	$0.8^{+0.2}_{-0.1}$
11	6.9 ± 1.4	1.89 ± 0.16	4.5 ± 0.9	2.9 ± 0.8	$2.0^{+0.6}_{-0.6}$	598^{+268}_{-117}	$30.2^{+7.2}_{-1.6}$	$1.0^{+0.1}_{-0.2}$
12	≤ 2.1	1.58 ± 0.13	≤ 1.3	2.4 ± 0.6	$2.0^{+0.5}_{-0.6}$	264^{+79}_{-61}	$28.9^{+15.1}_{-2.5}$	$0.9^{+0.3}_{-0.3}$
13	4.1 ± 7.7	1.54 ± 0.13	2.6 ± 0.5	2.3 ± 0.6	$2.4^{+0.7}_{-0.7}$	449^{+186}_{-170}	$28.1^{+15.}_{-3.7}$	$0.6^{+0.3}_{-0.1}$
15	≤ 3.4	1.14 ± 0.98	≤ 2.2	1.7 ± 0.5	$1.0^{+0.5}_{-0.4}$	$391^{+\ 90}_{-\ 99}$	$29.7^{+3.7}_{-3.5}$	$0.5^{+0.2}_{-0.1}$
16	1.8 ± 4.1	1.34 ± 0.28	1.2 ± 0.3	2.0 ± 0.7	$1.3^{+0.1}_{-0.6}$	$391^{+\ 5}_{-\ 53}$	$29.2^{+4.9}_{-4.1}$	$0.4^{+0.2}_{-0.3}$

[*] Derived from the dust-continuum flux at 343.5 GHz using Equation (2.5).

2.3.3.2 Main Sequence Offset

To investigate the relationship between the derived gas masses, we derive the offset from the MS, defined as the specific SFR (sSFR) of the source relative to the sSFR expected for a MS galaxy of the given stellar mass and given epoch ($\rm sSFR_{MS}$). We define the MS using the best fit from Speagle et al. (2014):

$$\log \mathrm{SFR}(\mathrm{M}_*, \mathrm{t(z)}) = [0.84 - 0.026\,t(z)] \log \mathrm{M}_* - [6.51 - 0.11\,t(z)]\,, \tag{2.7}$$

where $t(z)$ is the age of the Universe at redshift, z, in Gyr. We show the position of our sample in the MS plane in Figure 1.3. The points are colour-coded by the MS offset, $\rm sSFR/sSFR_{MS}$, based on the Speagle et al. (2014) definition, where the SFRs are derived from the SED. Our sample encompasses both MS and above-MS galaxies, spanning $1 < \rm sSFR/sSFR_{MS} < 7$.

2.4 RESULTS AND DISCUSSION

2.4.1 Comparison of single-band and SED-derived $L_{850\mu\rm m,rest}$

To assess the extent to which the assumed values of β and $T_{\rm dust}$ affect the derived $L_{850\mu\rm m,rest}$, and thereby also $\rm M_{mol}$, we compare the single-band and SED-derived values of $L_{850\mu\rm m,rest}$ via the ratio between the two in Figure 2.4. Our results are based on the mean value, $\langle\alpha_{850\mu\rm m}\rangle = 6.7 \pm 1.7 \times 10^{19} \mathrm{erg\,s^{-1}\,Hz^{-1}\,M_\odot^{-1}}$ derived for the Scoville et al. (2016) calibration sample. Scoville et al. (2016) also provide a fit for the conversion factor that varies with $L_{850\mu\rm m,rest}$, based on the best-fit relation between $L_{850\mu\rm m,rest}$ and $\rm L'_{CO(1-0)}$ (solid line in Figure 2.5). However, the molecular gas masses derived from the mean and best-fit $\alpha_{850\mu\rm m}$ are consistent for our sample. The comparison between the single-band and SED-derived values of $L_{850\mu\rm m,rest}$ is of particular relevance given that there now exist a range of approaches to estimating $L_{850\mu\rm m,rest}$. For example, Harrington et al. (2018) fit their Herschel SPIRE $250-500\mu$m and AzTEC 1.1 mm photometry with a modified blackbody (based on Equation 14 of Yun and Carilli, 2002) whereas Hughes et al. (2017) extrapolate the value of $L_{850\mu\rm m,rest}$ from the best-fit SEDs, modeled with MAGPHYS.

We find that most values of $L_{850\mu m,rest}$ inferred via the SED fit of MAGPHYS are consistent, within errors, with the single-band derived values, once the dust emissivity and temperature of the cold dust are fixed to match the assumptions of the single-band RJ method (see Figures 2.4 and 2.5). The standard version of MAGPHYS, which allows for variable dust temperatures for the hot and cold components, predicts values of $L_{850\mu m,rest}$ that are systematically lower than those inferred via Equation (2.5), i.e. centred at 78% of the single-band values (pink line and filled histogram). Fixing the dust emissivities of both the warm and cold components to $\beta = 1.8$, but allowing the dust temperatures to vary, leads to slightly stronger agreement, with a median $L_{850\mu m,rest}$ ratio of 83% (red line and outlined histogram). Fixing only the temperature of the cold dust component of MAGPHYS leads to stronger agreement with the single-band method (median of 94% that of the single-band method) than when solely fixing the dust emissivities to match (see light blue line and filled histogram). Attempting to replicate the assumptions made in the single-band RJ method (by fixing the temperature of the cold dust component to $T_{\rm cold\,dust} = 25$K, and assuming $\beta = 1.8$ for both dust components), leads to values of $L_{850\mu m,rest}$ that are mostly consistent with those derived from the single-band measurement (blue line and outlined histogram).

We find a significant range in the relative reference luminosities, $L^{\rm SED}_{850\mu m,rest}/L^{\rm single-band}_{850\mu m,rest}$, derived for each set of MAGPHYS assumptions. Even when the assumptions on β and $T_{\rm dust}$ are matched to the single-band method the ratio varies from 0.7 – 1.6 (Figure 2.4). This distribution of values can be attributed mainly to the variation in the relative masses of the warm and cold dust components fit by MAGPHYS, but may also reflect small variations in the intrinsic gas-to-dust ratios of the sample.

We find that mismatches between the assumed β and $T_{\rm dust}$ vs the intrinsic properties of the sources can lead to up to a factor of two uncertainty on $L_{850\mu m,rest}$. The mean variation of values of $L^{\rm SED}_{850\mu m,rest}$ inferred per source, for different sets of MAGPHYS assumptions, was 20%, with differences of up to 70%. Likewise, the values of $L^{\rm SED}_{850\mu m,rest}$, derived from the standard MAGPHYS assumptions, differed from the $L^{\rm single-band}_{850\mu m,rest}$ values by 20% on average, with differences of up to 70%. These results are consistent with the comparison of the inferred and intrinsic $L_{850\mu m,rest}$ for the simulated galaxies of Privon et al. (2018), for which the extrapolation from the observed frequency to the rest frame at 850μm resulted in errors of the order of ~ 20%, with deviations of up to 50% for some snapshots.

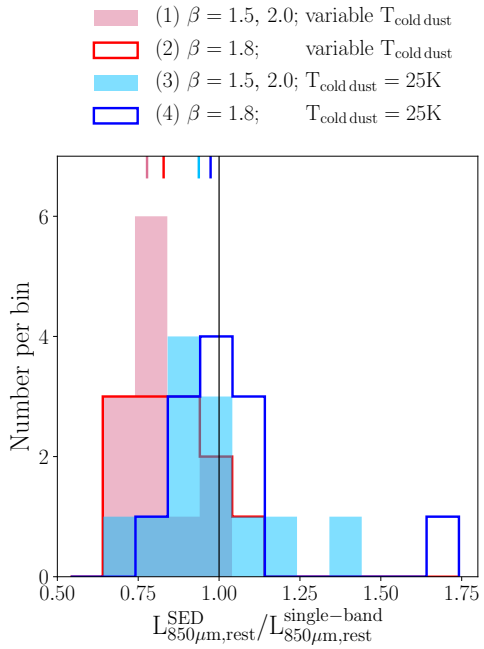

Figure 2.4: Histograms of the ratio of the single-band to SED-inferred $L_{850\mu m,rest}$ for the four sets of MAGPHYS assumptions (labeled at the top): (1) the standard MAGPHYS assumptions (filled pink), (2) $\beta = 1.8$ for both dust components with the $T_{\rm cold\,dust}$ as a free parameter (red outline), (3) $\beta = 1.5$(2) for the warm (cold) components and $T_{\rm cold\,dust}$, and (4) replicating the assumptions of the single-band RJ calibration. The coloured solid lines at the top of the plot indicate the median values of the four distribution, with the colour matching that of the histogram (labeled at top). The black solid line at unity indicates where the SED- and single-band derived values are equivalent.

Our comparison of $L^{\rm SED}_{850\mu{\rm m,rest}}$ indicates that the value of α_{850} derived by calibrating the CO(1-0)-derived $M_{\rm mol}$ against the $L_{850\mu{\rm m,rest}}$, is systematically affected by the assumptions on the dust emissivity index and temperature. For example, Hughes et al. (2017), who apply the standard form of MAGPHYS to derive $L_{850\mu{\rm m,rest}}$ from the SEDs of their sample, find a slightly lower α_{850} than Scoville et al. (2016), based on the single-band conversion of Equation (2.5). The lower values found by Hughes et al. (2017) are consistent with our findings that the $L^{\rm SED}_{850\mu{\rm m,rest}}$ estimated from the standard MAGPHYS SED models are 20% lower, on average, than for the single-band method. However, based on the χ^2 values of the MAGPHYS SED fits, none of the four sets of model assumptions (on β and $T_{\rm cold\,dust}$) that we tested result in a better systematic fit to the photometry.

2.4.2 CO(1-0) vs. Dust-Continuum Luminosity

We compare the luminosities used to derive $M_{\rm mol}$ in Figure 2.5. For the CO-detected sources, the observed-frame luminosity (at 343.5 GHz) correlates strongly (Pearson rank correlation coefficient of 0.78) with the CO(1-0) luminosity (left hand panel). This strong correlation remains even after the 343.5 GHz flux is scaled to $L_{850\mu{\rm m,rest}}$ (blue points, central panel), indicating that the dust continuum traces the same component of molecular gas as the CO(1-0) emission for our sample. The values of $L_{850\mu{\rm m,rest}}$ derived from both the single-band fluxes and SEDs are mostly consistent with the predictions from the $L_{850\mu{\rm m,rest}}$-to-$M_{\rm mol}$ conversion factors derived by Scoville et al. (2016) (solid and dotted lines in Figure 2.5), with all but source 12, consistent to within a factor of two.

We compare the scatter of our sample, around the best-fit line of $L'_{\rm CO(1-0)}$ vs $L_{850\mu{\rm m,rest}}$, with the scatter of the calibration sample of Scoville et al. (2016). To quantify the scatter and the goodness of fit compared to the predictions from the mean and best-fit $\alpha_{850\mu{\rm m}}$, we compute the standardized residuals. By comparing the standardized residuals of the two samples we account for the difference in samples sizes and dynamic ranges.

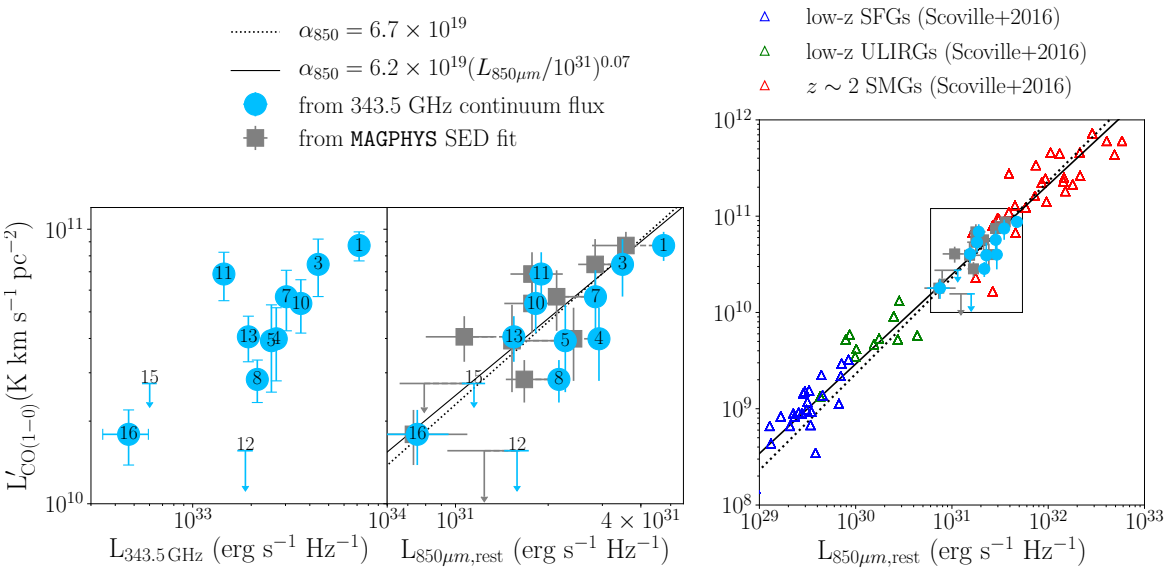

Figure 2.5: Comparison of CO(1-0) and dust-continuum luminosities. Left panel: CO(1-0) luminosity vs. measured 343.5 GHz (ALMA Band 7) luminosity. Central panel: CO(1-0) luminosity vs. rest-frame 850μm luminosity from ALMA band 7 measurements (blue) and rest-frame, SED fits (grey; from the standard, high-z version of MAGPHYS with β = 1.5 and 2, respectively for the warm and cold dust components). Right panel: CO(1-0) luminosity vs. rest-frame 850μm luminosity of our sample (rectangular inset from central panel) compared to the calibration samples of Scoville et al. 2016. The dotted (solid) lines represent the constant (best-fit) $\alpha_{850\mu{\rm m}}$ fit to the calibration sample of Scoville et al. (2016)

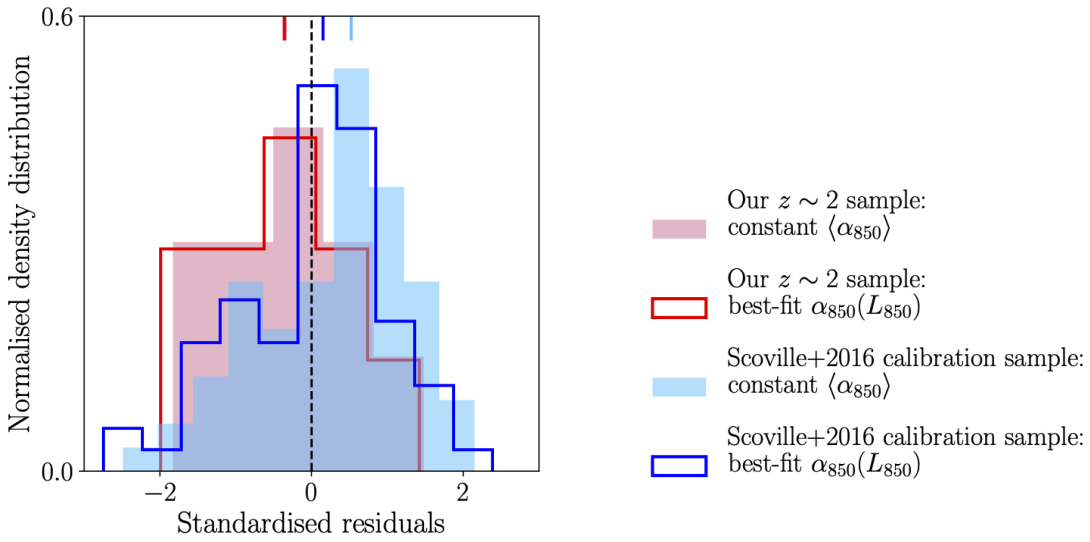

Figure 2.6: Comparison of the standardized residual distributions for our sample (red, solid and filled) and the Scoville et al. (2016) calibration samples (blue, solid and filled). The standardized residuals represent the distance of the measured $L'_{\mathrm{CO(1-0)}}$ from the mean (filled histograms) and best-fit (solid outline) $\alpha_{850\mu\mathrm{m}}$.

We use the residuals, given by,

$$e = L'_{\mathrm{CO(1-0),measured}} - L'_{\mathrm{CO(1-0),predicted}}, \tag{2.8}$$

to calculate the standardized residuals, via,

$$e/\sigma_e, \tag{2.9}$$

where σ_e is the standard deviation of residuals. For each source, $L'_{\mathrm{CO(1-0),predicted}}$ is inferred from the value of $L_{850\mu\mathrm{m,rest}}$ derived from our Band 7 dust-continuum flux measurements (via Equation (2.5)) as well as: (1) the mean, $\alpha_{850\mu\mathrm{m}}$, and (2), the best-fit $\alpha_{850\mu\mathrm{m}}(L_{850\mu\mathrm{m,rest}})$, derived for the Scoville et al. (2016) calibration sample. We compare the distributions of the standardized residuals from our sample against the Scoville et al. (2016) calibration sample in Figure 2.6. Note that for the chosen $\alpha_{850\mu\mathrm{m}}$ to be a good fit, the distribution of standardized residuals should approximate a normal distribution, with 95% between -2 and +2. Because the best-fit $\alpha_{850\mu\mathrm{m}}$ was derived as a fit to the calibration data, the standardized residuals should be centred at 0, and, indeed we find a mean (median) standardized residual of 0.00 (0.15).

Our sample exhibits the same level of scatter as the calibration sample of Scoville et al. (2016) and is well fit by the constant and best-fit $\alpha_{850\mu\mathrm{m}}$, derived using the calibration sample. For both our sample, and the calibration sample, the standard deviation of the distribution of standardized residuals ≈ 1.0, indicating that our sample exhibits the same variation around the line of best fit as the calibration sample. Our sample exhibits a very small (and insignificant) offset from the best fit to the calibration sources, with a mean (median) standardized residual of -0.40 (-0.36). Moreover, the standardized residuals of our sample lie within, $|e/\sigma_e| < 2$, indicating that the line that best fits the calibration data is also suitable for our sample.

We find no significant difference in the goodness of fit when applying the mean vs best-fit $\alpha_{850\mu\mathrm{m}}$ of Scoville et al. (2016), with almost identical distributions of the standardized residuals for both cases (filled red vs solid red outlined histogram, Figure 2.6). Moreover, the mean $\alpha_{850\mu\mathrm{m}}$ of our sample, $7.7 \pm 2.3 \times 10^{19}\,\mathrm{erg\,s^{-1}\,Hz^{-1}\,M_\odot^{-1}}$, is consistent with the mean of the calibration samples. Thus, we conclude that the application of the constant value, $\langle \alpha_{850\mu\mathrm{m}} \rangle = 6.7 \pm 1.7 \times 10^{19}\mathrm{erg\,s^{-1}\,Hz^{-1}\,M_\odot^{-1}}$, is valid for our sample.

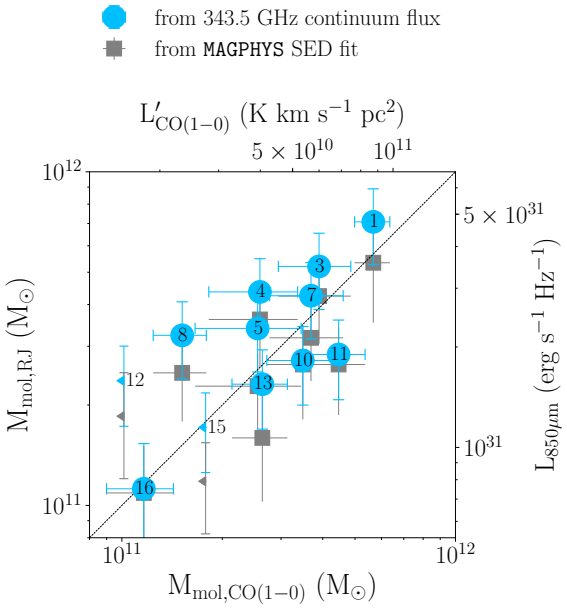

Figure 2.7: Comparison of CO(1-0) and RJ-based molecular gas masses derived from the single ALMA Band 7 flux measurement (filled sky blue circles) and $L_{850\mu m,rest}$ derived from the standard MAGPHYS SED fit (filled grey squares). The dotted black line is the line of equality. Note that the RJ-based molecular gas masses are the right y-axis, $L_{850\mu m,rest}$, divided by $\alpha_{850\mu m} = 6.7 \times 10^{19} erg s^{-1} Hz^{-1} M_\odot^{-1}$ whereas the CO(1-0) based molecular gas masses are the top x-axis, $L'_{CO(1-0)}$, multiplied by $\alpha_{CO} = 6.5 M_\odot / (K km s^{-1} pc^2)$.

2.4.3 The Accuracy of CO(1-0)- and Dust-Continuum-Based Molecular Gas Masses

The molecular gas masses derived from the RJ dust continuum are consistent with those derived from CO(1-0) (Figure 2.7). For six of the 10 CO-detected sources, the values of M_{mol} derived from the single-band RJ method are consistent within the errors, whereas for all CO-detected sources, the values of M_{mol} are consistent to within a factor of 1.7. The main source of uncertainty in measuring M_{mol} from the dust continuum is the conversion to a common rest-frame luminosity. As discussed in Section 2.4.1, the variation of β and $< T_{dust} >$ alone are sufficient to account for the differences in the derived $L_{850\mu m,rest}$ and thus also the differences between the RJ and CO-based M_{mol}.

We investigate whether the scatter about the 1:1 line in Figure 2.7 correlates with any observed galaxy properties (Figure 2.8). To quantify the scatter, we use the relative luminosities, $L_{850\mu m,rest}/L'_{CO(1-0)}$. Note that this is equivalent to the ratio between the value of M_{mol} determined from the single-band RJ method and CO(1-0) ($M_{mol,RJ}/M_{mol,CO(1-0)}$). We find no statistically significant correlation with the stellar mass, SFR or main sequence offset within our sample (Spearman rank coefficients of < 0.3 with p-values of > 0.5), despite our sample spanning an order of magnitude in both M_* and SFR.

The robustness of $L_{850\mu m,rest}$ as a molecular gas tracer for our sample, appears to be consistent with recent studies based on cosmological zoom-in simulations. Privon et al. (2018) and Liang et al. (2018) compared the RJ-derived M_{mol} with the M_{mol} of simulated massive star-forming galaxies, finding that the RJ-based M_{mol} correlates well with "true" M_{mol} of their simulated galaxies. The strong correlation only appeared to break down for sources with $L_{850\mu m,rest} < 10^{28}$ erg s^{-1} or $\log(Z/Z_\odot) < -0.8$ (Privon et al., 2018), which are likely to have significantly higher gas-to-dust ratios than expected for our sample. The fact that we find such strong agreement between the CO-derived M_{mol} and RJ-based M_{mol}, indicates that our sources have similar gas-to-dust ratios to the calibration samples of Scoville et al. (2016).

The assumption of a constant gas-to-dust abundance ratio is implicit in the RJ method, for which the calibration and application has so far been intentionally restricted to galaxies with $M_* > 2 \times 10^{10} M_\odot$ (Scoville et al., 2016; 2017). These massive sources are expected to be high metallicity systems, with gas-to-dust ratios of the order of $\sim 100:1$ and little CO-dark gas (Bolatto et al., 2013). Based on the M_{dust} inferred via MAGPHYS, and the α_{CO} used here, our sample has gas-to-dust ratios of the order of $\sim 300:1$. Although there likely exists some variation in these values, which contributes to the scatter about the 1:1 line in Figure 2.7, it is not sufficient to lead to any

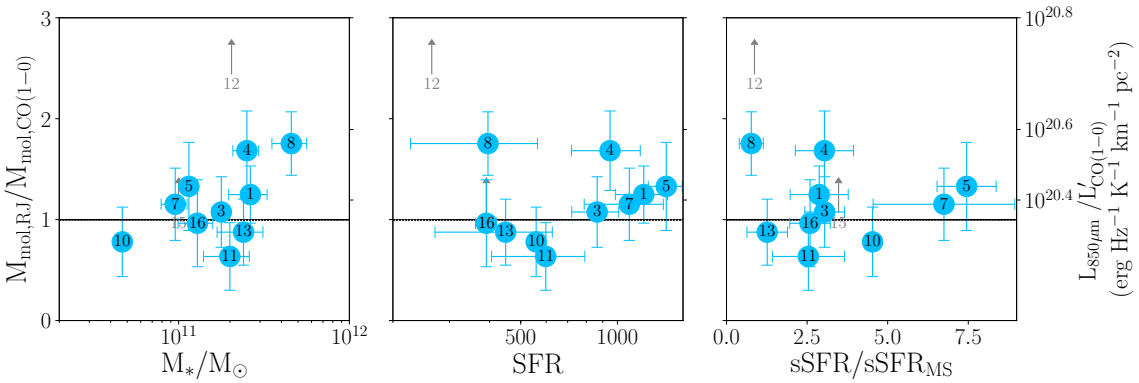

Figure 2.8: Ratio between the CO(1-0)-based to dust-based molecular gas masses as a function of stellar mass (left), SFR (center) and main sequence offset (right).

significant offset in M_{mol}. We note that these results are consistent with the work of Groves et al. (2015), who find that the total gas mass can be constrained to within a factor of two for massive galaxies.

We do not find any major deviations between the CO- and RJ- derived gas masses of our sample. However, significant deviations are to be expected for low metallicity, and low M_*, galaxies. For example, Groves et al. (2015) and Privon et al. (2018) show that for low metallicity (low M_*) galaxies, the calibration based on higher mass sources (such as the one tested here) would underpredict the observed $L'_{CO(1-0)}$, or simulated M_{mol}, respectively. Similarly, Dessauges-Zavadsky et al. (2015) find that low-mass, MS galaxies at $z \sim 2$ show smaller $\alpha_{850\mu m}$ than our sample by ~ 0.4 dex. These low mass galaxies are likely to have significantly higher gas-to-dust ratios, of $\sim 1000:1$, (e.g. Popping et al., 2017a) than the samples to which the RJ method has so far been applied (which have ratios of $\sim 100:1$). Hence, the constant gas-to-dust abundance ratio, implicit in the RJ method, is not applicable to low M_* sources. The underprediction of the CO-derived M_{mol} for low M_* sources would be even more pronounced if one were to account for the expected variation of α_{CO} with metallicity (e.g. Bell et al., 2006; Wolfire et al., 2010; Shetty et al., 2011; Feldmann et al., 2012b; Bolatto et al., 2013).

Our results indicate that for massive, star-forming galaxies, the main source of uncertainty in deriving M_{mol} remains the conversion factor, α_{CO}. The value of α_{CO} we have adopted does not affect the relative comparison of the M_{mol} derived via CO(1-0) and the long-wavelength dust continuum, both of which depend on the same α_{CO}. However, it has a significant impact on the absolute M_{mol} inferred via either method. As argued in previous studies, the value of α_{CO} is likely to vary across the calibration samples, with values of ~ 4, ~ 1.3 and $\sim 0.8 M_\odot/(\mathrm{K\,km\,s^{-1}\,pc^2})$ derived for SFGs, ULIRGs and SMGs, respectively (see list of references in Bolatto et al., 2013). In addition to the α_{CO} adopted here, this variation can lead to a factor of $\lesssim 8$ uncertainty in the derived M_{mol}, far more than the factor of ~ 2 uncertainty introduced by the assumptions of β and $\langle T_{dust} \rangle$ in the RJ method (Section 2.4.1).

2.5 SUMMARY

We have presented a comparison of the molecular gas masses derived from dust-continuum and CO(1-0) observations for a unique sample of 12, $z \sim 2$ star-forming galaxies. This is the first time that the Rayleigh-Jeans method of measuring molecular gas masses from single-band, dust-continuum observations has been tested on the types of high-redshift sources to which it is typically applied (Scoville et al., 2016; 2017; Schinnerer et al., 2016; Miettinen et al., 2017; Darvish et al., 2018). The dust-continuum method we have tested is based on the calibration of the rest-frame 850 µm luminosity ($L_{850\mu m,rest}$) against the CO(1-0)-derived molecular gas masses,

proposed by Scoville et al. (2016). We applied two techniques to derive the rest-frame 850μm luminosity: (1), using the calibration of Scoville et al. (2016), based on the observed dust-continuum emission at 343.5 GHz (ALMA Band 7), and (2) from the model fits to the rest-frame SEDs.

Our findings can be summarised as follows:

1. We find that the molecular gas masses derived from single-band, long-wavelength flux measurements are consistent, within a factor of two, with the molecular gas masses derived from CO(1-0), for $M_* > 2 \times 10^{10} M_\odot$ star-forming galaxies, when the same α_{CO}, is assumed.

2. This factor of < 2 variation between the M_{mol} derived from CO(1-0) vs the single-band dust continuum, can be accounted for by variations in the dust emissivity index and temperature, which are assumed when extrapolating from the observed flux to $L_{850\mu m,rest}$. Small variations in the gas-to-dust ratios are also likely to contribute to this scatter.

3. The main source of uncertainty in deriving M_{mol}, regardless of whether one uses CO(1-0) or the dust continuum, remains the CO-to-M_{mol} conversion factor, α_{CO}, which varies by a factor of up to ~ 8.

We conclude that single-band, dust-continuum observations can be used to constrain the molecular gas masses of massive ($M_* > 2 \times 10^{10} M_\odot$), star-forming galaxies at high redshift as reliably as the CO(1-0) line. Thus, future single-band surveys with ALMA will provide important constraints on the physics of star formation in massive, high-z galaxies.

ACKNOWLEDGEMENTS

This chapter makes use of the VLA data: VLA/17A-251, and, the ALMA data: 2013.1.00034.S, 2015.1.00137.S, 2013.1.00118.S, and 2013.1.00151.S. The Joint ALMA Observatory is operated by ESO, AUI/NRAO, and NAOJ. The National Radio Astronomy Observatory is a facility of the National Science Foundation operated under cooperative agreement by Associated Universities, Inc. The near IR spectroscopy presented herein were obtained at the W. M. Keck Observatory, which is operated as a scientific partnership among the California Institute of Technology, the University of California, and the National Aeronautics and Space Administration. The Observatory was made possible by the generous financial support of the W. M. Keck Foundation. I would like to recognize and acknowledge the very prominent cultural role and reverence that the summit of Mauna Kea has always had within the indigenous Hawaiian community. We are fortunate to have the opportunity to perform observations from this mountain.

Signifiant contributions were made by coauthors to the procurement and analysis of the data and the interpretation of results presented in this Chapter. In particular,

- Nick Scoville, shared the continuum and optical data, described the physics underlyign the calibration and pointed out inconsistencies in the initial analysis,
- Fabian Walter, precured the VLA data and provided guidance throughout the project,
- Elisabete da Cunha, helped perform some of the SED fitting and discussed its limitations.

The work presented in this chapter was greatly improved by the feedback provided from both the coauthors and external contributors. The comments of the anonymous referee improved the clarity and details of this work, Olivier Ilbert provided assistance in cross-checking the fits to the COSMOS photometry using LePHARE and conversations with Alberto Bolatto and Desika Narayanan led to helpful insights.

The Neverending Story

Mosaic, grid, transform, clean
Repeat, test, repeat, test
The uv-plane, it lurks unseen
Many choices, but which is best?

Why not resolve the SFR?
Great idea, I will with glee
Have others done so thus far?
Not with such photometry.

Is it resolved, or is it not?
Repeat, test, repeat, test
Four beams the best of the lot
This matter finally laid to rest.

Now for the blob sizes
Which plane to fit?
The problem arises,
in what we omit.

Yet, does all this matter?
Alone in my room
The world is in crisis
Zoom, zoom, zoom, zoom

"Why don't you try ...?"
Says author x
Is it over? not yet
Repeat, repeat, test

Finally a result!
While the chaos goes on
Simulations, let's consult!
The world woebegone.

3

A COMPARISON OF THE STELLAR, CO AND DUST-CONTINUUM EMISSION FROM THREE, STAR-FORMING GALAXIES AT $z \sim 2$

This Chapter comprises the article titled "A Comparison of the Stellar, CO and Dust-Continuum Emission from Three, Star-Forming HUDF Galaxies at $z \sim 2$", published in the Astrophysical Journal (Kaasinen, Walter, Novak, Neeleman, Smail, Boogaard, Cunha, Weiss, Liu, Decarli, Popping, Diaz-Santos, Cortés, Aravena, Werf, Riechers, Inami, Hodge, Rix, and Cox, 2020). The published paper has been reformatted to match the style of this thesis. Coauthor contributions are listed at the end of the Chapter. The written text, data reduction and analysis are my own work, with advice and suggestions from coauthors.

Abstract

We compare the extent of the dust, molecular gas and stars in three star-forming galaxies, at $z = 1.4, 1.6$ and 2.7, selected from the Hubble Ultra Deep Field based on their bright CO and dust-continuum emission as well as their large rest-frame optical sizes. The galaxies have high stellar masses, $M_* > 10^{11} M_\odot$, and reside on, or slightly below, the main sequence of star-forming galaxies at their respective redshifts. We probe the dust and molecular gas using subarcsecond Atacama Large Millimeter/submillimeter Array observations of the 1.3 mm continuum and CO line emission, respectively, and probe the stellar distribution using *Hubble Space Telescope* observations at 1.6 μm. We find that for all three galaxies the CO emission appears $\gtrsim 30\%$ more compact than the stellar emission. For the $z = 1.4$ and 2.7 galaxies, the dust emission is also more compact, by $\gtrsim 50\%$, than the stellar emission, whereas for the $z = 1.6$ galaxy, the dust and stellar emission have similar spatial extents. This similar spatial extent is consistent with observations of local disk galaxies. However, most high redshift observations show more compact dust emission, likely due to the ubiquity of central starbursts at high redshift and the limited sensitivity of many of these observations. Using the CO emission line, we also investigate the kinematics of the cold interstellar medium in the galaxies, and find that all three have kinematics consistent with a rotation-dominated disk.

3.1 INTRODUCTION

The molecular gas phase of the interstellar medium (ISM) is a crucial component of star-forming galaxies, hosting and providing the fuel for star formation. Constraining the spatial distribution of both stars and molecular gas is therefore critical to understanding the evolutionary state of a galaxy. Whereas the stellar component of a galaxy is best traced via the rest-frame near-infrared emission, molecular gas is most commonly observed via carbon monoxide (CO) line emission or far-infrared (FIR) dust-continuum emission. These stellar and molecular gas tracers have been mapped at high resolution (down to 100 pc scales) for local galaxies (e.g. Leroy et al., 2008; Sandstrom et al., 2013; Schinnerer et al., 2019a), providing fundamental insights into the physics of

star formation and the matter cycle of the ISM. However, such detailed, multi-wavelength comparisons are still lacking for galaxies at the peak epoch of stellar mass assembly, at $z \sim 2$.

The advent of sub/millimeter interferometers, particularly the Atacama Large Millimeter/submillimeter Array (ALMA) and NOrthern Extended Millimeter Array (NOEMA), have led to a growing body of work aimed at characterising the molecular gas properties of $z \gtrsim 2$ galaxies via their CO and/or dust-continuum emission (e.g. surveys described in Walter et al., 2016; Scoville et al., 2017; Tacconi et al., 2018; Pavesi et al., 2018; Decarli et al., 2019; Stach et al., 2019). Based on unresolved measurements, the long-wavelength (observed-frame 850 μm), dust-continuum emission appears to trace the bulk of the cold, molecular gas in massive, star-forming galaxies as accurately as the traditional tracer, CO(1-0) (Scoville et al., 2014; Kaasinen et al., 2019). However, resolved observations indicate that the dust-continuum emission stems from a significantly more compact region than the CO emission (e.g Simpson et al., 2015; Hodge et al., 2015; Chen et al., 2017; Calistro Rivera et al., 2018; Gullberg et al., 2019), calling into question its application as a molecular gas tracer.

To date, the sizes of the rest-frame optical, dust-continuum and CO emitting regions have only been compared for the brightest and most massive high-redshift ($z > 1$) sources. For $z \sim 2-4$ submillimetre(-selected) galaxies (SMGs) , the measured dust-continuum emission appears $2-4\times$ more compact than the CO emission (Simpson et al., 2015; Hodge et al., 2015; Chen et al., 2017; Calistro Rivera et al., 2018). Similarly, for quasar host galaxies at $z \gtrsim 6$ (studied with lower resolution observations) the dust-continuum sizes also appear $z \sim 2-4$ more compact than those of the CO (Feruglio et al., 2018; Wang et al., 2019). The dust-continuum and rest-frame optical (but not CO) sizes, have also been compared in detail for SMGs (Hodge et al., 2016; 2019; Gullberg et al., 2019; Lang et al., 2019), six, massive and compact star-forming galaxies at $z \sim 2.5$ (Barro et al., 2016), a $z \sim 1.25$ starburst (Nelson et al., 2019) and massive, H$_,$-selected galaxies at $z \sim 2.2-2.5$ (Tadaki et al., 2017b). These studies all find that the dust emission is $2-4\times$ more compact than the rest-frame optical emission.

It is still unclear how the spatial extents of the stellar, dust-continuum and CO emission compare for the wider population of star-forming galaxies, including the population conforming to the so-called "main sequence" (MS) of star-forming galaxies (the correlation between the stellar mass and star formation rate of the majority of star-forming galaxies observed for each epoch up to $z \sim 4$, e.g. in Noeske et al., 2007; Salmi et al., 2012; Whitaker et al., 2012; Whitaker et al., 2014; Schreiber et al., 2016). In the first study of MS galaxies, Tadaki et al. (2017a) measure $1.5-2\times$ smaller dust-continuum vs CO half-light radii. However, the two massive ($M_* > 10^{11} M_\odot$) galaxies in their study were selected based on their compact, dusty, star-forming cores. An additional complication to the selection biases, is that most previous observations of the dust-continuum emission of high redshift sources have been conducted at infrared (IR) wavelengths, at which the dust luminosity is highly sensitive to the ISM temperature and thereby traces the star formation rate along with the dust reservoir. Moreover, few studies exist with resolved observations of both the CO and dust-continuum emission in unlensed objects (e.g. Hodge et al., 2015; Chen et al., 2017; Tadaki et al., 2017a; Calistro Rivera et al., 2018), of which only a subset are at a comparable resolution (Hodge et al., 2015; Calistro Rivera et al., 2018).

In this Chapter, we test how the spatial extent (quantified by the half-light radii) of dust continuum, CO and rest-frame optical emission compare for three extended, MS galaxies at $z \sim 2$. To this end, we selected sources in the *Hubble* Ultra Deep Field (HUDF) for which the dust continuum and CO emission have already been detected with ALMA as part of the ALMA Spectroscopic Survey in the Hubble Ultra Deep Field (ASPECS) Large Program (González-López et al., 2019; Decarli et al., 2019; Aravena et al., 2019). To best compare the spatial extents, we study the three sources with the most extended morphologies in the ultraviolet (UV) to near IR images taken with the *Hubble Space Telescope* (HST). We use observations taken as part of the ASPECS Large Program

(LP) as well as our "ALPS" (ASPECS Large Program Source) follow-up, higher resolution ALMA observations. Thus, throughout this paper we refer to our sources as ALPS.1, 2 and 3.

This published article and remainder of this Chapter are structured as follows. In Section 3.2 we describe the observations, data reduction and imaging of the CO and dust-continuum emission. We discuss the global galaxy properties inferred from the multi-wavelength data in Section 3.3. In Section 3.4, we derive and compare the half-light radii of the dust-continuum emission, CO and rest-frame optical. We derive dynamical properties in Section 3.5 via kinematic modeling. We compare our sources to other samples in Section 3.6 and summarise our main findings in Section 3.7. Throughout this paper we assume a ΛCDM cosmology with $H_0 = 70\,\mathrm{km\,s^{-1}Mpc^{-1}}$, $\Omega_M = 0.3$ and $\Omega_\Lambda = 0.7$. Stellar masses and SFRs are based on a Chabrier (2003) IMF. When quoting molecular gas masses we account for a factor of 1.36 to include He.

3.2 SAMPLE SELECTION, OBSERVATION AND DATA REDUCTION

3.2.1 Galaxy Selection

The three galaxies studied here are derived from the ASPECS Large Program (LP), a survey of the sub-mm to mm emission within the HUDF (González-López et al., 2019; Decarli et al., 2019). Because the survey was conducted without preselection, it identified the sources brightest in CO line and dust-continuum emission. Based on the line searches performed by González-López et al. (2019), ASPECS provided 16 highly significant CO detections. From this sample of 16, we selected the three CO- and dust-brightest galaxies, with the most extended rest-frame optical emission. These two criteria were equally important. We required the sources to be CO-bright in order to resolve their emission, at ∼ 0.″5, within five hours of integration time, with ALMA, and select galaxies that are extended in the rest-frame optical to increase the chances of observing extended dust and CO emission. In Figure 3.1, we compare the properties of the three galaxies studied here to the parent sample of ASPECS LP 1.2 mm candidates (listed in Table 1 of González-López et al. 2020) and the full set of galaxies in the HUDF (see Aravena et al., 2020). Our "ALPS" sources have large stel-

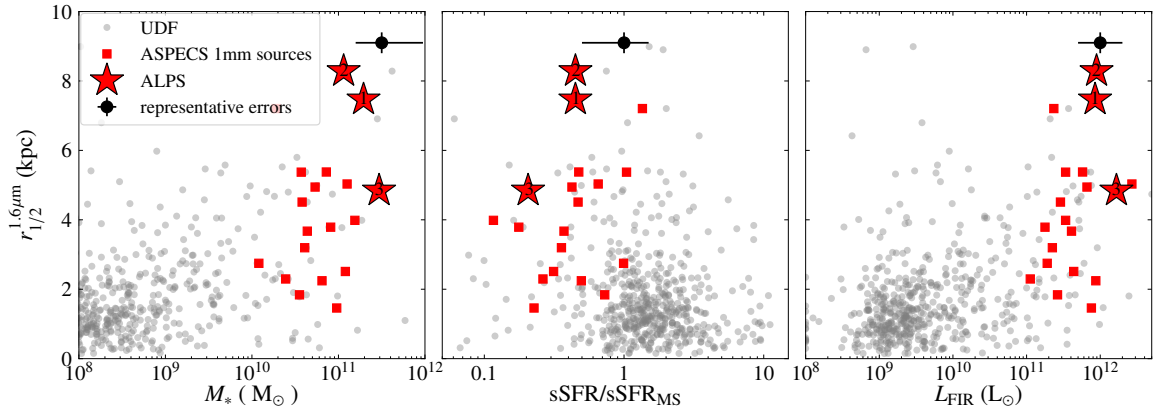

Figure 3.1: Comparison of the ALPS sample properties relative to the parent samples at $1 < z < 3$. The 1.6 µm (stellar) half-light radii are shown as a function of stellar mass, offset from the main sequence and FIR luminosity (within 8-1000µm) in the left, middle and right panels, respectively. The three "ALPS" sources studied in this work (red stars) are compared to the ASPECS 1 mm continuum and line sources (red squares) and the HUDF sample (grey circles), from Aravena et al. (2020). The offset from the main sequence (in the middle panel) is calculated individually, based on the measured redshift, stellar mass and SFR of each source, and, following Aravena et al. (2020), the main sequence is defined by the best-fit relation of Schreiber et al. (2015). The 1.6 µm half-light radii are from Table 2 of van der Wel et al. (2012) and were measured from the F160W maps. The three galaxies studied here were selected to be both extended in the rest-frame optical and be CO- and FIR-bright. They also have large stellar masses and systematically lower sSFRs than the majority of galaxies observed in the HUDF.

lar masses ($\gtrsim 10^{11} M_\odot$) and high FIR luminosities compared to the majority of the sources in the field, due to our selection of CO- and 1 mm-bright targets. Their extended and inclined rest-frame UV-optical morphologies are shown in the first three columns of Figure 3.2.

Compared to most observed SMGs, our galaxies have more extended morphologies in the rest-frame UV and optical emission. However, the interpolated 870 µm flux densities are consistent with the definition of a SMG, i.e. > 1 mJy (see Casey et al., 2014; Hodge and da Cunha, 2020, for discussions on the selection and classification). Assuming that the FIR continuum can be described by a modified blackbody with an average dust temperature of 25 K and a dust emissivity index of 1.8 (see Section 3.3.1), the 1.3 mm flux densities measured by González-López et al. (2020) extrapolate to 1.4 ± 0.1, 1.5 ± 0.1 and 2.8 ± 0.1 mJy for ALPS.1, 2 and 3 respectively. However, the FIR luminosities (bolometric luminosity between 8-1000 µm) of ALPS.1 and 2 are lower than what is typically measured for SMGs. Based on the models fit to the spectral energy distributions, ALPS.1, 2 and 3 have FIR luminosities of $(0.78 \pm 0.04) \times 10^{12}$, $(0.9 \pm 0.1) \times 10^{12}$ and $(1.8 \pm 0.6) \times 10^{12} L_\odot$, respectively. SMGs have FIR luminosities of $L_{\rm FIR} \gtrsim 10^{12} L_\odot$, typically $\sim 3 \times 10^{12} L_\odot$ (e.g. Swinbank et al., 2014). Thus, ALPS.1 and 2 are at the faint end of the SMG population, whereas ALPS.3 is entirely consistent with most observed SMGs.

3.2.2 Dust continuum (Band 6) Observations

We analyse two Band 6 (211-275 GHz; 1.1-1.4 mm) surveys of the HUDF, taken at different depths and resolutions. We use the unresolved observations from the ASPECS LP (project code: 2016.1.00324, described in González-López et al., 2020) and the 1.3 mm observations of Dunlop et al. (2017) (project code: 2012.1.00173.S), which provide a higher spatial resolution. The source IDs from the ASPECS LP and HUDF data of Dunlop et al. (2017) are provided in Table 3.1. In the subsequent analysis (Section 3.2.4), we combine both datasets to achieve high resolution without the loss of large-scale emission. The ASPECS 1.3 mm observations, executed between March 10, 2017 and July 13, 2018, were conducted in the C43-3 configuration with a minimum baseline of 15 m and maximum baseline of 500 m. Our three sources lie towards the edges of the mosaic (where the primary beam reponses are 87%, 65% and 20% of the peak sensitivity, respectively for ALPS.1, 2 and 3). Thus, the data for our sources are not as deep as those in the center of the mosaic. The Dunlop et al. (2017) observations were conducted in ALMA Cycle 2 using a variety of configurations, with maximum baselines between 550 and 1250 m (see Table 2 of Dunlop et al., 2017). The pointings of the ASPECS LP are more closely spaced than for the Dunlop et al. (2017) observations, however the latter sample a larger area. Thus, for ALPS.3, on the edge of the ASPECS field, the majority of the data used here is from Dunlop et al. (2017).

3.2.3 CO Line (Band 3) Observations

To study the CO line emission of our three sources, we use two sets of ALMA Band 3 (84-115 GHz; 2.6-3.6 mm) data. We use the ASPECS LP Band 3 survey (project code: 2016.1.00324.L) and our targeted, follow-up "ALPS" observations, at higher resolution (project code: 2017.1.00270.S). The source IDs from the ASPECS LP are provided in Table 3.1 along with the CO-derived redshifts and observed CO transitions. An additional source was observed at the same redshift as, and at small angular separation to, ALPS.3 (ASPECS ID 3mm.09), but was excluded from the main text work due to the lack of extended emission. We discuss this source further in Appendix A.2.1.

The ASPECS LP Band 3 observations comprised of 17 pointings conducted in the compact, C40-3 configuration (with baselines ranging from 15 to 700 m). Further details are described in Decarli et al. (2019). For our sample, the sensitivity of the observations was the highest for ALPS.2 and lowest for ALPS.3 (with primary beam responses of 70%, 80% and 50% of the peak sensitivity for ALPS.1, 2 and 3, respectively). In addition, we rely on new, supplementary, high-resolution Band 3 data, taken between January 4-11, 2018. These ALMA observations were conducted in the

Table 3.1: Description of ALMA Observations

ALPS ID	ALPS.1	ALPS.2	ALPS.3
ASPECS LP 1 mm ID	1mm.03	1mm.05	1mm.06
ASPECS LP 3 mm ID	3mm.04	3mm.05	3mm.07
Dunlop et al. (2017) ID	UDF.6	UDF.8	UDF.2
RA (J2000)	03:32:34.44	03:32:39.77	03:32:43.53
DEC (J2000)	-27:46:59.8	-27:46:11.8	-27:46:39.2
z_{CO}	1.4140	1.5504	2.6961
CO transition	$2 \rightarrow 1$	$2 \rightarrow 1$	$3 \rightarrow 2$
50 km s^{-1} CO Cube			
Weighting parameter	0.5	2	2
Beam FWHM ($''\times''$)	0.82×0.72	0.71×0.58	0.88×0.61
rms per channel (mJy beam^{-1})	0.14	0.09	0.11
Dust continuum map (211-231 GHz; 1.3mm)			
Weighting parameter	2	2	2
Beam FWHM ($''\times''$)	0.59×0.49	0.56×0.47	0.48×0.40
rms (μJy beam^{-1})	21	22	24

C43-5 configuration (minimum baseline of 15 m and maximum baseline of 2.5 km). The Bandpass, flux and phase calibrators were J0522-3627, J0329-2357 and J0342-3007, respectively.

3.2.4 Data Reduction and Imaging

All sets of raw data were reduced using the standard ALMA calibration scripts for the Common Astronomy Software Application (CASA; McMullin et al., 2007). For all sets of observations, the standard pipeline produced uv-data products of high quality and was therefore used without additional modifications. Following the raw data reduction, we combine the various sets of data for each band. The subsequent concatenating and imaging was carried out using Common Astronomy Software Application (CASA) version 5.4.0.

3.2.4.1 Dust Continuum (Band 6) Imaging

We image the dust continuum using the Band 6 data from the ASPECS LP (González-López et al., 2020) and from Dunlop et al. (2017). These two datasets cover different frequency ranges, i.e. the ASPECS LP data (González-López et al., 2020) spans 212-272 GHz whereas the Dunlop et al. (2017) data spans 211-231 GHz, and were taken with different configurations. In order to probe the extended 1.3 mm emission at high resolution, and ensure that we are probing the same wavelengths at all radii, we select the four (out of 32) spectral windows from the ASPECS LP that match those of Dunlop et al. (2017). By subselecting these spectral windows from the ASPECS LP data, we reduce the depth of our observations relative to the LP. However, this selection is the best compromise between the sensitivity to extended emission and resolution required for our study. In effect this subselection is a form of tapering, which we use to avoid weighting the final maps to the large amount of short baseline measurements from the large program.

We jointly image the two sets of uv-data via CASA's `TCLEAN`, by applying the "mosaic" gridding option. To maximise the signal-to-noise ratio (S/N) of the final images, we image the data using a natural weighting scheme and clean to 2σ, within a circular mask of $3''$ radius. The cleaned maps, for each source, are shown in the 4th column of Figure 3.2 and their properties are summarised in Table 3.1. The comparative size of the synthesized beams reflects the relative contribution of the ASPECS LP versus Dunlop et al. (2017) data, with the beam size decreasing the further a source lies towards the edge of the ASPECS 1 mm mosaic. ALPS.3 (at the very edge of the LP mosaic) has by far the smallest beam size as most of the visibilities are from the Dunlop et al. (2017) data.

3.2.4.2 CO Line (Band 3) Imaging

To image the CO emission, we combine the low- and high-resolution data from the ASPECS LP Band 3 and ALPS programs. We initially attempt to subtract the continuum (via CASA's `uvcontsub`), but recover no significant continuum emission, rendering this step redundant. We image the uv-data using CASA's `TCLEAN` task, mosaicing the pointings from the ASPECS LP and follow-up ALPS program via the "mosaic" gridding option and setting the phase centre to the expected source centre (the pointing of the ALPS data). We apply a circular mask of $3''$ radius to create all cleaned images. We test a variety of robust weighting parameters to find the optimum balance between the resolution and resulting noise level. For the final images of ALPS.2 and 3 we use natural weighting, whereas for ALPS.1 we use robust weighting (see Table 3.1).

To create the moment-0 maps, from which we estimate source sizes, we create a single-channel image over the extent of the line emission, (the 99.99th percentile range, as in Aravena et al. 2019) applying the "multiscale" deconvolver (with a deconvolution scale of up to $2''$) and cleaning down to a threshold of 2σ within a mask of radius $3''$. We compare these moment-0 maps to maps obtained from 50 and 100 $\mathrm{km\,s^{-1}}$ data cubes, ensuring that the extent and morphology of the source emission in all moment-0 maps are consistent, but select the single-channel image for the moment-0 map, to ensure that we have robust noise estimates.

3.3 DERIVED GLOBAL QUANTITIES

3.3.1 Deriving Dust and Gas Masses from the ALMA Maps

We measure the total CO and dust-continuum flux densities from the cleaned, dirty and residual maps by applying the residual scaling method (described in detail in Appendix A of Novak et al., 2019). This involves estimating the unknown, intrinsic flux by rescaling the contribution from the residual map with an estimate of the area of the dirty beam in the region of interest. The rescaling process is necessary to account for the ill-defined beam units of each cleaned interferometric map, which is a combination of the residual component in units of Jy per dirty beam, and a cleaned component in units of Jy per clean beam. For both the CO and dust-continuum emission, we extract the total flux densities from within circular apertures of $1\farcs5$, $2''$ and $1\farcs5$ for ALPS.1, 2 and 3, respectively. We estimate the uncertainties of these flux densities as the local root mean square (rms), σ, (in units of Jy $\mathrm{beam^{-1}}$) scaled by the square root of the number of independent clean beams filling the aperture.

We compare the flux densities measured here (Table 3.2) to those derived using the ASPECS LP data only. Our CO emission line fluxes are consistent, within the uncertainties, with the spectral line fits of the unresolved ASPECS LP data, presented in Boogaard et al. (2020), and are 20% lower, on average, than the values in González-López et al. (2019) (although still consistent within errors). For ALPS.1 and 3, our 1.3 mm continuum flux density measurements are consistent with the measurements of Dunlop et al. (2017), whereas our value for ALPS.2 is $(50 \pm 20)\%$ larger. Conversely, the 1.3 mm flux density measured here for ALPS.1 is $(55 \pm 20)\%$ lower than the continuum flux density meaured based on the ASPECS LP data in González-López et al. (2020), whereas the

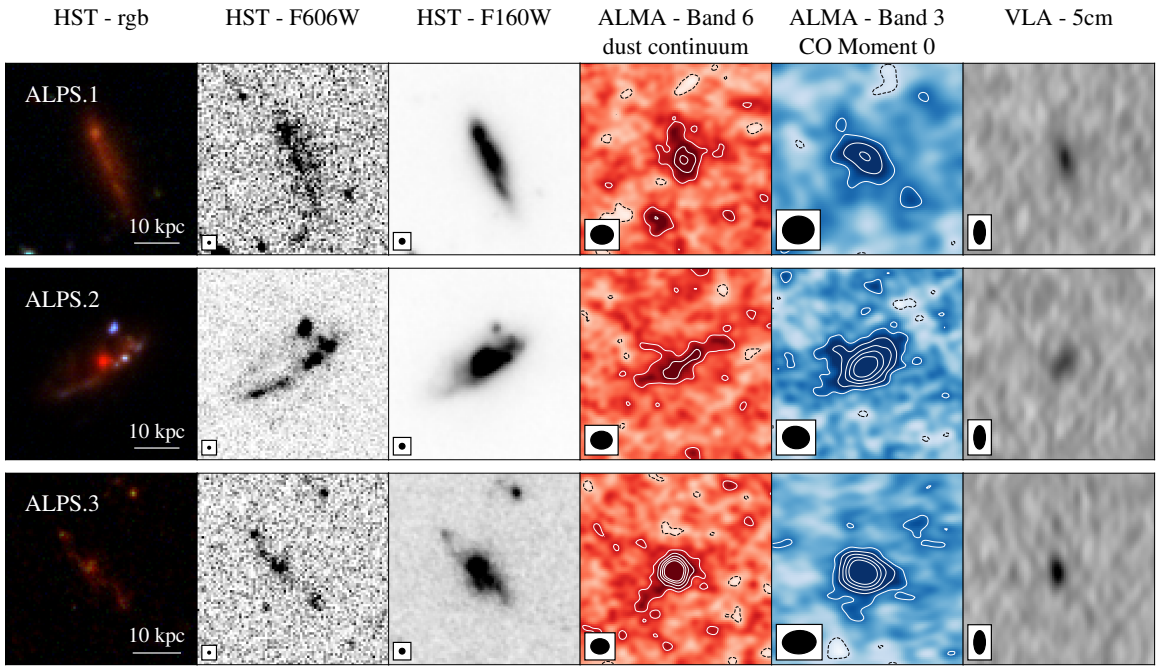

Figure 3.2: Multiwavelength data for the three observed sources (labeled ALPS 1, 2 and 3 at the upper left of the left panel in each row). Each panel depicts a 5" × 5" region centred on the kinematic centre of the source. Columns, from left to right: HST 435-775-105 color composite, HST/F606W, HST/F160W, Band 6 (1.3 mm) dust continuum (combined ASPECS LP and Dunlop et al. 2017 data), CO moment 0 map (from the combined ASPECS LP and ALPS data) and VLA - 5 cm continuum flux. The contours for the Band 6 dust continuum and CO moment 0 start at $\pm 2\sigma$ and change in steps of 2σ. Dashed black (solid white) lines show negative (positive) contours.

flux density measured for ALPS.3 is consistent within the errors. The 1.3 mm flux density measured here for ALPS.2 is consistent with the value in González-López et al. (2020). The difference between the flux densities measured by Dunlop et al. (2017) and González-López et al. (2020) can be mostly attributed to the different spectral setups, with the Dunlop et al. (2017) covering longer wavelengths. Similarly, the smaller flux density measured here for ALPS.1 is, in part, the result of the subselection of spectral setups.

To estimate the molecular gas masses from our CO observations we first convert the line fluxes to luminosities (in $\mathrm{K\,km\,s^{-1}\,pc^2}$) following Solomon et al. (1992), via,

$$L'_{\mathrm{CO}} = 3.25 \times 10^7 \, S_{\mathrm{CO}} \Delta v \, \nu_{\mathrm{obs}}^{-2} \, D_{\mathrm{L}}^2 (1+z)^{-3}, \tag{3.1}$$

where $S_{\mathrm{CO}}\Delta v$ is the velocity-integrated line flux (in Jy $\mathrm{km\,s^{-1}}$), ν_{obs} is the observed-frame frequency of the CO transition in GHz and D_{L} is the luminosity distance in Mpc. We down-convert these line luminosities to the CO(1-0) line luminosity via the following ratios (Table 3.2). For ALPS.3, both the CO(3-2) and CO(1-0) transitions have been observed (Riechers et al., 2020). Thus, we apply the measured luminosity ratio $r_{31} = L'_{\mathrm{CO(3-2)}}/L'_{\mathrm{CO(1-0)}} = 0.79 \pm 0.21$. For ALPS.1 and 2 we have no CO(1-0) observations. Thus, we assume an excitation correction based on the measurements of $r_{21} = L'_{\mathrm{CO(2-1)}}/L'_{\mathrm{CO(1-0)}}$ for other high-redshift samples (Daddi et al., 2015; Bothwell et al., 2013; Spilker et al., 2014), and, the values inferred for the ASPECS sample (Boogaard et al., 2020).

To convert the inferred CO(1-0) line luminosities to molecular gas masses we apply CO-to-molecular gas mass conversion factors, α_{CO}, calculated via the assumed metallicities (provided in Table 3.2). We infer the metallicities (according to the Pettini and Pagel 2004 scale) from the stellar masses using the mass-metallicity calibration in Equation (12a) of Genzel et al. (2015) (taking into account both the uncertainties on the measured stellar mass and the empirical relation). We

note that for ALPS.2 the strong emission lines Hα and [N II] have been observed, yielding a slightly higher inferred metallicity than the value based on the mass-metallicity calibration (Williams et al., 2014). However, the difference is only 0.05 dex, which is lower than the typical systematic uncertainty of metallicity measurements (e.g. Kewley and Ellison, 2008). We calculate the CO-to-molecular gas mass conversion factor, $\alpha_{\rm CO}$, according to the Equation (2) of Tacconi et al. (2018). We choose these mass-metallity and $\alpha_{\rm CO}$ calibrations based on the detailed comparison of such relations presented in Appendix A.3 of Liu et al. (2019b). The final molecular gas masses quoted in Table 3.2 are the inferred $L'_{\rm CO(1-0)}$ multiplied by the metallicity-based $\alpha_{\rm CO}$.

We estimate the total dust masses in two ways; 1) from the SED fits (see Section 3.3.2) and 2) from the 1.3 mm (Band 6) flux densities. To convert the flux densities measured at 1.3 mm to dust masses we assume that the dust emission is optically thin and can be modeled by a modified blackbody of the form,

$$S_{\rm obs} = (1+z) D_L^{-2} \kappa_{\nu_{\rm rest}} M_{\rm dust} B_{\nu_{\rm rest}}(T_{\rm dust}) \tag{3.2}$$

where $\kappa_{\nu_{\rm rest}}$ is the dust mass opacity coefficient, $M_{\rm dust}$ is the dust mass, $B_{\nu_{\rm rest}}$ is the blackbody radiation spectrum and $T_{\rm dust}$ is the temperature of the dust. We assume a temperature of 25 K, as motivated in Scoville et al. (2014). We determine the opacity coefficient by relating it to a reference frequency via the power law dependency,

$$\kappa_{\nu_{\rm rest}} = \kappa_{\nu_0} (\nu_{\rm rest}/\nu_0)^{\beta}, \tag{3.3}$$

where β is the dust spectral emissivity index. We use the rest-frame 850 µm as our reference frequency, taking $\kappa_{\nu_{850-{\rm m}}} = 0.77\,{\rm g}^{-1}{\rm cm}^2$ (Draine and Lee, 1984) and $\beta = 1.8$ (e.g. Planck Collaboration et al., 2011a).

For ALPS.1 and 2, the dust masses derived from the 1.3 mm flux densities are larger than the values inferred from the SED fitting (Table 3.2), although still consistent within errors for ALPS.1. The discrepancy is the result of a combination of the assumed (or fit) temperatures and emissivity indices, which are affected by the AGN template used for ALPS.2. Unlike the single MBB model, MAGPHYS includes both a warm and cold dust component with emissivity indices of 1.5 and 2 respectively. The temperature of the two components is determined during the fit. Thus, the mass-weighted temperature is not fixed. For ALPS.2, in particular, the mass-weighted temperature of the MAGPHYS fit is greater than for the single MBB, resulting in the difference between the two values.

3.3.2 Stellar Masses and SFRs

We rely on spectral energy distribution (SED) modeling to infer the stellar masses and SFRs of our sources. As part of the UDF, our sample has been observed with a wide range of ground- and space-based observatories. To trace the extent of the stellar continuum, we rely on the HST/WFC3 F160W images from the XDF data release, described in Illingworth et al. (2013)[(1)]. Given our small sample size, and use of the HST/WFC3 F160W Band to trace the stellar continuum, we revisit the accuracy of the HST photometry in Appendix A.2.2.

We select the following sets of data for the SED analysis. For the UV-NIR photometry we use the values from the Guo et al. (2013) catalogue, which are extracted from large enough apertures to enclose the full extent of the emission for the extended sources analysed here (see Appendix A.2.2). In addition, we use the deblended *Spitzer*/MIPS 24 µm photometry from Whitaker et al. (2014) and the deblended *Herschel*/PACS 100 µm and 160 µm data from Elbaz et al. (2011). We take the maximum of the local and simulated noise levels as the uncertainties for the *Herschel* data. We also use the 1.3 mm dust continuum measurements of Dunlop et al. (2017) and González-López et al. (2019) and the 3 mm continuum limits presented in González-López et al. (2019).

[(1)] https://archive.stsci.edu/prepds/xdf/

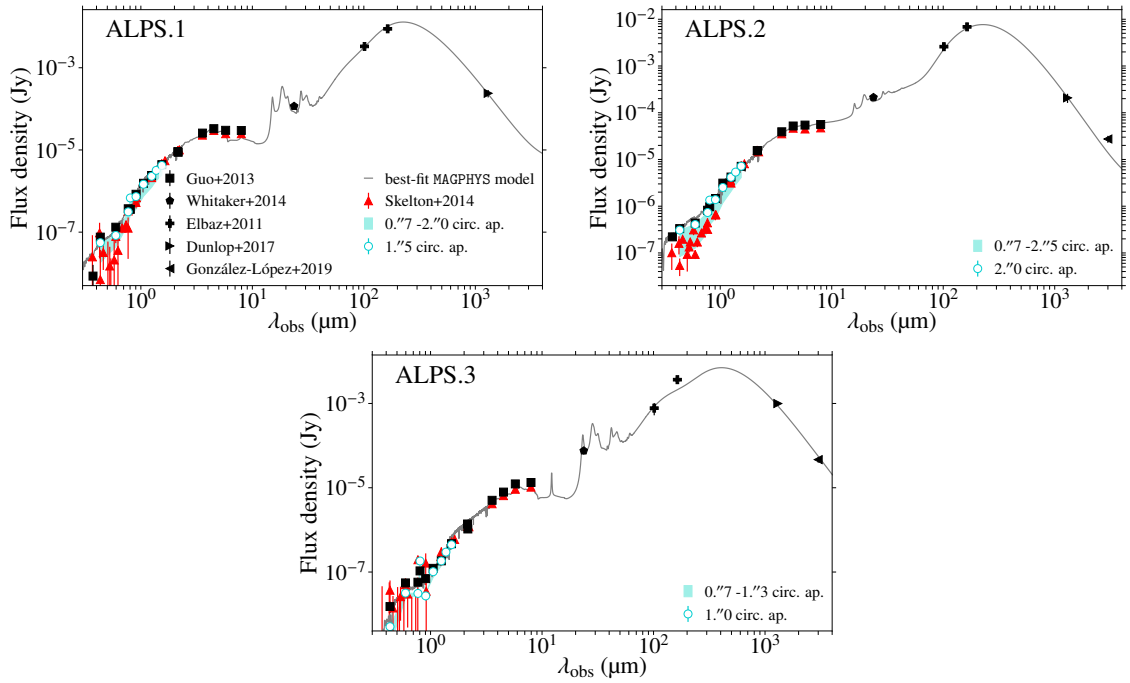

Figure 3.3: Photometry used for the SED modeling (black filled symbols) and best-fit solutions (black lines) for our three sources. The UV-IR photometry of Guo et al. (2013) (black squares) and Skelton et al. (2014) (red triangles) are also compared (see Appendix A.2.2). Compared to the Skelton et al. (2014) photometry, we find the Guo et al. (2013) HST photometry to be systematically larger for the measurements from the rest-frame UV-optical (particularly at 1.6 μm), consistent with what we measure from apertures enclosing the extent of the source emission (cyan circles representing the flux measured from the XDF images within circular apertures encompassing the full extent of source emission). This is especially true for the most extended source, ALPS.2. Also shown are the *Spitzer*, *Herschel* and ALMA continuum data used to constrain the SEDs (as decsribed in the legend).

We model the photometry using two, adapted, versions of the high-redshift extension to the SED-fitting algorithm MAGPHYS (da Cunha et al., 2008; 2015). To account for the impact of obscuration and high SFRs on the attenuation, we apply the adaptation to the high-redshift extension of the MAGPHYS code, developed by Battisti et al. (2019). We find that this adapted version significantly reduces the fitting residuals, particularly for ALPS.3 (see Appendix A.2.2). Thus, we quote the fitting parameters from this adaptation of MAGPHYS for ALPS.1 and 3 in Table 3.2. Despite the more sophisticated dust treatment, the IRAC and PACS photometry for ALPS.2 remain poorly fit by the adapted version of MAGPHYS. This is likely due to the presence of an AGN, identified from *Chandra* observations (the details of which are described in Luo et al., 2017). Thus, for ALPS.2 we apply the adapted version of MAGPHYS that accounts for a contribution by AGN to the dust heating (Chang et al., 2020). The inferred stellar mass and SFR are a factor of 2 and 1.6 times smaller, respectively, when the AGN component is considered. We note that this extension does not include the adaptations introduced by Battisti et al. (2019). We provide the parameters from the fit including ξ_{AGN}, the estimated fraction of the template AGN emission contributing to the total IR luminosity, in Table 3.2. Based on the variation in the derived stellar masses and SFRs for different sets of photometry, the inclusion/exclusion of an AGN component and the choice of applied dust attentuation curve, we adopt an uncertainty floor on the stellar masses and SFRs of $\pm \sim 0.3$ dex consistent with a factor of ~ 2 increase/decrease in stellar mass and factor of ~ 1.5 increase/decrease in SFR.

To place our sources in the context of the main sequence, at the measured redshift of each source, we apply the best-fit MS relation of Schreiber et al. (2015). We choose this MS for consistency with the HUDF and ASPECS parent samples shown in Aravena et al. (2020) (see their Figure

Table 3.2: Derived Properties

Source	ALPS.1	ALPS.2	ALPS.3
SED fitting[a]			
M_* (10^{11} $M_\odot$)	$1.9^{+1.9}_{-1.0}$	$1.1^{+2.2}_{-0.6}$	$3.0^{+3.0}_{-1.5}$
$M_{\rm dust}^{\rm SED}$ (10^8 $M_\odot$)	$1.1^{+0.3}_{-0.2}$	$1.6^{+0.1}_{-0.5}$	$7.8^{+1.2}_{-1.0}$
SFR ($M_\odot$ yr^{-1})	54^{+27}_{-13}	48^{+24}_{-12}	98^{+89}_{-25}
sSFR (Gyr^{-1})	$0.3^{+0.1}_{-0.1}$	$0.4^{+0.1}_{-0.8}$	$0.3^{+0.7}_{-0.4}$
sSFR/sSFR$_{\rm MS}$[b] (Schreiber+2015)	0.4 ± 0.4	0.4 ± 0.4	0.2 ± 0.2
$\xi_{\rm AGN}$		$0.15^{+0.04}_{-0.04}$	
Flux densities, applied ratios and derived masses			
$J_{\rm obs}$	2	2	3
$S_{\rm CO}\Delta v$ (mJy km s^{-1})	600 ± 130	560 ± 80	560 ± 70
$L'_{\rm CO(J_{obs}-(J_{obs}-1))}$ (10^{10} K km s^{-1} pc^2)	1.6 ± 0.3	1.7 ± 0.2	2.1 ± 0.3
$r_{J_{\rm obs},1}$	0.8 ± 0.2	0.8 ± 0.2	0.79 ± 0.21
$L'_{\rm CO(1-0)}$ (10^{10} K km s^{-1} pc^2)	2.0 ± 0.3	2.2 ± 0.2	2.6 ± 0.3
$\alpha_{\rm CO}$[c] ($M_\odot$/(K km s^{-1} pc^2))	3.9 ± 0.4	4.2 ± 0.4	4.1 ± 0.4
$M_{\rm mol}$ (10^{11} $M_\odot$)	0.8 ± 0.3	0.9 ± 0.3	1.1 ± 0.3
$S_{1.3\,\rm mm}$ (μJy)	240 ± 70	400 ± 100	860 ± 120
$M_{\rm dust}^{1.3\,\rm mm}$ (10^8 $M_\odot$)	2.4 ± 0.7	4.0 ± 1.0	7.6 ± 1.1
Inferred mass ratios			
$M_{\rm mol}/M_{\rm dust}^{1.3\,\rm mm}$	320 ± 150	230 ± 90	140 ± 50
$M_{\rm mol}/M_*$	0.4 ± 0.2	0.8 ± 0.5	0.4 ± 0.2

[a] For properties inferred from the SED fitting we quote the median values with uncertainties representing the 16th and 84th percentiles. For further calculations and for the analysis described in the text, we adopt an uncertainty floor of ±0.3 dex on the values of M_* and SFR (based on the systematic uncertainties).
[b] Calculated based on the Schreiber et al. (2015) best-fit main sequence. Uncertainties on the MS offset are calculated based on the systematic uncertainties in the SFRs and stellar masses and the uncertainty of the MS function.
[c] CO(1-0)-to-molecular gas conversion calculated based on the metallities inferred via the stellar mass-metallicity relation parameterised in Equation (12a) of Genzel et al. (2015) and applying Equation (2) of Tacconi et al. (2018).

6), which we also compare to in Figure 3.1. We note that the exact shape of the MS, particularly for the large stellar masses of our three galaxies, is still under debate (the functional forms of e.g. Whitaker et al., 2012; Whitaker et al., 2014; Speagle et al., 2014; Schreiber et al., 2015; Boogaard et al., 2018; Leslie et al., 2020, differ). Our sources range from having sSFRs consistent with the MS to being slightly below the MS, with specific star formation rates relative to the main sequence of

$sSFR/sSFR_{MS} = 0.2-0.4$, based on the Schreiber et al. (2015) MS. This places our three galaxies in a regime that has been scarcely sampled to date (e.g. Bolatto et al. 2015 have resolved CO observations for two, MS sources at $z \sim 2$). Moreover, based on the derived flux densities, our sources appear to have large gas mass fractions $M_{mol}/M_* = 0.4-0.8$ and gas-to-dust ratios typical of MS galaxies and SMGs, i.e. $M_{mol}/M_{dust} \sim 100-300$ (for this comparison we use the dust mass inferred from the 1.3 mm continuum).

3.4 GALAXY SIZE ANALYSIS

3.4.1 Sensitivity Comparison

Before comparing the spatial distribution of the dust-continuum and CO emission, we investigate how sensitive our ALMA data is to to the molecular gas. We estimate the minimum H_2 mass and column densities that are observable based on our 1.3 mm continuum and CO moment-0 maps, comparing values at a matched resolution given by the CO moment-0 map beam size. To estimate the CO-based H_2 mass limit per beam, we take the rms of the moment-0 maps and scale to a line luminosity limit using the α_{CO} conversion factors in Table 3.2. We account for the solid angle of the beam to derive the column density limit. For the dust-based values, we take the rms of the dust-continuum maps and scale these values to the beam size of the CO moment-0 maps. We convert the rms per beam to an inferred H_2 mass per beam by assuming a modified blackbody with the same assumptions on the temperature, emissivity index and opacity described in Section 3.3.1. We apply a gas-to-dust ratio of 200 ± 100, consistent with what we measure for our sample (Table 3.2). Based on these assumptions we derive the sensitivities in Table 3.3. Note that here we compare the values for H_2 only, whereas we consider the total molecular gas masses (which include He) in the rest of the text.

The sensitivities calculated here, multiplied by a suitable S/N, represent the minimum observable column density assuming that the total area of the beam is covered by source emission (i.e. a beam filling factor of unity). In the case of a spiral arm, the actual CO column would only fill a fraction of the beam, e.g. if a spiral arm only covers a tenth of the beam area, then the actual column density of molecular gas that our data are sensitive to is ten times what is quoted here. To detect the molecular gas at 3σ, the column densities would have to be $\sim 10^{22}\mathrm{cm}^{-2}$ (modulo the beam filling factor). For local disks, the typical column densities of the bar and spiral arms are $10^{21}-10^{22}\mathrm{cm}^{-2}$ whereas the column densities measured for the central starbursts are up to an order of magnitude higher, e.g. the column density of the nuclear region of NGC 253 is $2\times10^{23}\times\mathrm{cm}^{-2}$ (Weiß et al., 2008). This difference in column densities leads to a significant contrast between the nuclear region and brightest parts of the disks (and bar), i.e. factor of $20-50\times$ in the observed flux densities.

Based on the estimated sensitivities, our CO and dust-continuum observations appear to be sensitive to approximately the same column of molecular gas. The values estimated for the CO and continuum data are consistent within the uncertainties (based on the above assumptions) for ALPS.1 and 2, whereas for ALPS.3 the dust continuum may be marginally (up to 20%) more sensitive to the H_2 column. Comparing the CO data across our sample, the sensitivity is highest for ALPS.2. However, the continuum data of our sample have similar sensitivities, with slightly lower inferred H_2 mass and column density limits per beam for ALPS.1 and 3 versus ALPS.2. The comparison between CO and dust-based H_2 column sensitivities is based on the assumptions that the dust temperature and gas-to-dust ratio remain constant across the disk. Variations in the temperature or gas-to-dust ratio would serve to decrease the sensitivities of the dust emission, compared to CO, at larger radii.

Table 3.3: H_2 Mass and Column Sensitivities

Source	ALPS.1	ALPS.2	ALPS.3
rms values of the ...			
1.3 mm map (μJy)	15	18	14
CO moment-0 map (mJy km s^{-1})	49	20	25
H_2 mass limit per beam (10^8 $M_\odot$ $beam^{-1}$)			
Dust-based[a]	28 ± 14	34 ± 17	24 ± 12
CO-based[b]	55 ± 6	28 ± 3	48 ± 5
H_2 column density limit per beam (10^{21} cm^{-2} $beam^{-1}$)[c]			
Dust-based	2.7 ± 1.4	4.6 ± 2.3	2.9 ± 1.4
CO-based	5.3 ± 0.5	3.9 ± 0.4	5.7 ± 0.6

[a] Calculated assuming a gas-to-dust mass ratio of 200 ± 100, with the dust emission described by a MBB with $T = 25$ K, $\beta = 1.8$.
[b] Calculated based on the α_{CO} in Table 3.2.
[c] Calculated using the CO beam size in Table 3.1.
[*] The sensivity estimates are based on 1σ (i.e. applying the rms values at the top of the table).

3.4.2 Qualitative Comparison of Spatial Extents

Our aim is to quantify the sizes of the rest-frame optical, CO and dust-continuum emission. However, to aid the interpretation of our data, we begin with a qualitative comparison. In Figure 3.4, we compare the observed galaxy extents at half the peak surface brightness (solid lines) of the rest-frame optical, dust continuum and CO emission (with both the F160W and Band 6 dust continuum convolved to the resolution of the CO moment-0 maps). The F160W maps have been corrected for the offset of the HST astrometry measured by Franco et al. (2020) (for which the median offset is −96 mas in right ascension and +261 mas in declination and the additional local offsets for our sources differ from the medians by ≤ 40 mas). We list the S/N at half the peak surface brightness for the CO and 1.3 mm continuum in the bottom right corner of each panel. For ALPS.1, the CO and 1.3 mm continuum half-peak values are barely greater than 3σ. For ALPS.2, the half-peak value of the 1.3 mm emission is below 3σ. In contrast, for the 1.6 μm data, the S/N at half the peak value is at > 50 for each source.

We compare the normalized surface brightness profiles extracted along the entire major axis (see Figure 3.5). The normalized, major axis cut illustrates how the steepness of the surface brightness profiles compare and indicates a potential difference in the peak positions (for the three types of emission). We show the beam-convolved, major axis profiles because the accurate construction and interpretation of the radial profiles for the CO and 1.3 mm continuum emission was hindered by the poor S/N and resolution. To indicate how well our data are resolved, we compare the CO beam (dashed black lines) to the major axis profiles and show the 2σ level normalized to the peak flux of the CO and 1.3 mm continuum emission (dotted blue and red lines).

From Figures 3.4 and 3.5 it appears that for ALPS.1, little CO or dust-continuum emission is recovered, at > 2σ, on scales greater than the beam size. For ALPS.2, a significant fraction of CO and dust-continuum emission appears to be on scales larger than the beam size. In contrast, for ALPS.3, the dust and CO emission are centrally concentrated, with scarcely any emission apparent on scales greater than the image resolution. We quantify the fraction of flux within the beam area

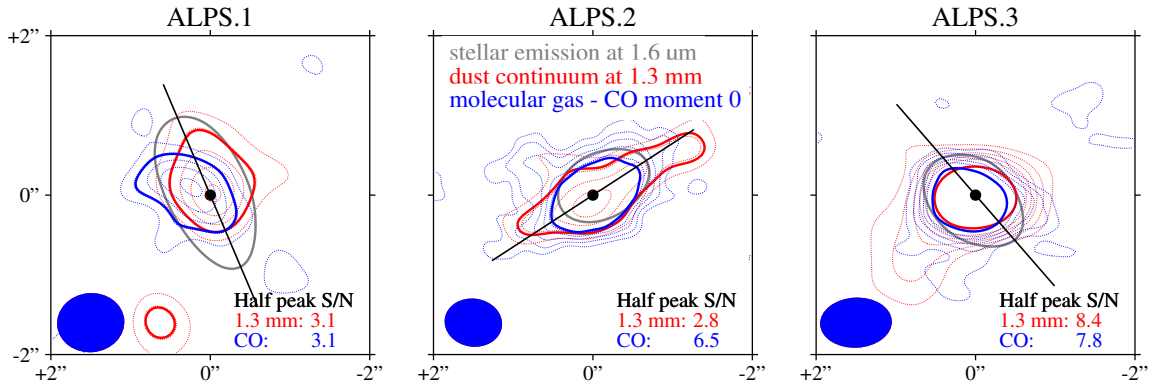

Figure 3.4: Comparison of the half-peak emission contours (solid lines) for the stellar emission at 1.6 µm (grey), the 1.3 mm dust-continuum emission (red) and the CO line emission (blue), which probes the molecular gas. Both the 1.3 mm dust continuum and HST F160W maps have been convolved to the resolution of the CO emission. Each panel shows a different source, labeled at the top. The dotted contours depict the CO (blue) and convolved 1.3 mm continuum (red) data, starting at $+2\sigma$ and increasing in steps of $+1\sigma$. The ratio of the half-peak value to the rms (half peak S/N) for both the 1.3 mm and CO data are listed on the bottom right of each panel. The black filled circle and line represent the kinematic centre and position angle used to extract the major axis profiles in the next figure. The HST astrometry has been corrected according to the offsets measured by Franco et al. (2020).

(i.e. consistent with a point source) in Section 3.4.3. The stellar-continuum emission from ALPS.1 and 3 appears to stem from a significantly larger region than the CO or dust continuum. However, for ALPS.2, the stellar emission follows a similar profile to the CO emission, with the dust continuum exhibiting a flatter, extended profile, albeit at a S/N< 3.

3.4.3 Measuring Galaxy Sizes

To quantify the source sizes, we attempt various fitting methods. For the interferometric data (i.e. the CO and dust continuum data) there are two possible approaches; fitting the maps (i.e. the image plane), or, directly fitting the visibilities (i.e. the uv-plane). For both approaches we use the axis ratios and position angles determined by van der Wel et al. (2012) from the F160W images and provided in Table 3.4, as initial estimates.

3.4.3.1 Image-plane Analysis

Before performing the image-plane analysis, we check whether our ALMA data have sufficient sensitivity and spatial resolution to estimate source sizes. To this end, we fit the emission of each source with a model point source. We check the residuals of the image-plane fit (subtracting the beam-convolved point source model from the image) and compare the point source fluxes to the measured flux densities. For ALPS.1 and 2 we recover remaining, residual structure (at $> 2\sigma$) and find that the flux densities of the point source fits are $40 \pm 20\%$ lower than our measured values. Conversely, for ALPS.3, we recover no significant residual CO or continuum emission at a spatial scale greater than that of the sythesized beams and find that the flux densities of the point source models are consistent with the measured values. Thus, for ALPS.3, we place 2σ upper limits on the half-light radii that can be measured from the moment-0 CO and dust continuum maps. Because the emission of ALPS.3 is indistinguishable from the beam, we quantify the 2σ upper limit based on the convolution of two Gaussian profiles, via,

$$FWHM^2_{\rm true} < (FWHM_{\rm beam} + 2\delta FWHM_{obs})^2 - FWHM^2_{\rm beam}, \quad (3.4)$$

where $FWHM_{\rm true}$ is the intrinsic FWHM of the galaxy, assuming a Gaussian profile, and $\delta FWHM_{\rm obs}$ is the error on measuring the FWHM based on the rms of the map. The values are

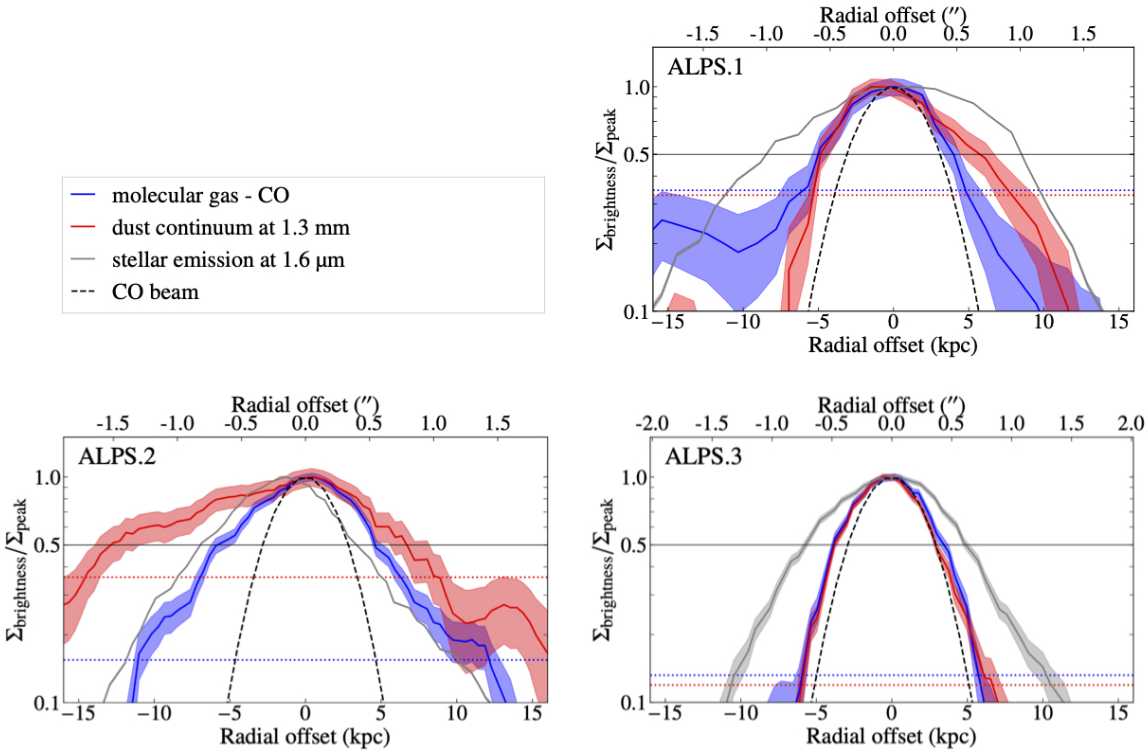

Figure 3.5: Comparison of the normalized surface brightness profiles ($\Sigma_{brightness}/\Sigma_{peak}$) of stellar emission from the F160W image (grey), 1.3 mm dust continuum (red) and CO emission, from the moment 0 map (blue) along the major axes of each source (labeled at top left of each panel). The horizontal black line of each panel indicates half the maximum surface brightness, thereby allowing the FWHM of the three profiles to be compared. The 2σ level relative to the peak surface brightness of the CO and dust-continuum emission are indicated by the blue and red dotted lines, respectively. The major axes, from which these profiles are extracted, are shown in Figure 3.4. The HST astrometry has been corrected according to the astrometric offsets provided by Franco et al. (2020).

given in Table 3.4. Although ALPS.3 is not sufficiently resolved in the CO moment-0 map, the 3D data indicates that ALPS.3 is marginally resolved, with the location of the emission shifting for different velocity channels (as indicated by the position-velocity diagram in Figure 3.6).

Having established that the CO line and 1.3 mm continuum emission of ALPS.1 and 2 are sufficiently resolved, we attempt to quantify the potential asymmetries visible in Figures 3.4 and 3.5. Following the second equation of Section 3.2 in Conselice et al. (2000), we calculate the asymmetry parameter (see also Conselice 2003). Note that a value of 0 corresponds to a galaxy that is perfectly symmetric whereas a value of 1 indicates that a galaxy is completely asymmetric. For ALPS.1, we derive asymmetry parameters of $A = 0.5 \pm 0.2$ and $A = 0.7 \pm 0.1$ for the CO and 1.3 mm continuum emission, respectively. Similarly, for ALPS.2, we derive asymmetry parameters of $A = 0.6 \pm 0.1$ and $A = 0.7 \pm 0.1$ for the CO and 1.3 mm continuum emission. Although this indicates that the observed emission is somewhat asymmetric, for both types of emission, we note that the exact noise structure and resolution heavily bias these values in ways that are challenging to quantify. Nonetheless, the values calculated here indicate that the surface brightness profiles are not well described by symmetric two-dimensional (2D) profiles.

Despite these potential asymmetries, we estimate the stellar, dust and CO half-light radii by fitting the respective maps with 2D surface brightness profiles via GALFIT (Peng et al., 2002; 2010). For each source of emission (stellar, dust and CO), we fit a $4''$ region centred on the source. We consider uniform error maps, with a constant background noise given by the rms of the full image. For the input PSFs, we supply images of 2D Gaussian profiles according to the HST PSF size and

Table 3.4: Inferred Source Sizes

Source	ALPS.1	ALPS.2	ALPS.3
Structural parameters from van der Wel et al. (2012)[a]			
$r_{1/2}^{F160W}$ (kpc)	7.46 ± 0.02	8.28 ± 0.03	4.84 ± 0.15
Sérsic index	0.48 ± 0.00	3.04 ± 0.02	0.86 ± 0.06
Position angle (degrees)	23.2 ± 0.1	302.5 ± 0.1	220.9 ± 1.1
Axis ratio	0.247 ± 0.002	0.452 ± 0.002	0.458 ± 0.013
Half-light radii measured here using GALFIT [b]			
$r_{1/2}^{F160W}$ (kpc)	7.9 ± 0.8	8.0 ± 0.8	4.9 ± 0.5
Sérsic index (F160W)	0.6 ± 0.1	2.1 ± 0.2	0.7 ± 0.1
$r_{1/2}^{CO}$ (kpc)	5.8 ± 1.7	5.5 ± 0.8	< 3.4
$r_{1/2}^{dust}$ (kpc)	3.9 ± 1.2	9.4 ± 1.4	< 1.2

[a] Used as priors for the GALFIT fitting.
[b] Measurements based on an exponential surface brightness profile.

major and minor FWHM of the synthesized beam (of the ALMA data). We allow the position and inclination angles of the best-fit models to be within ±10° of the best-fit values from van der Wel et al. (2012) and constrain the source centres to vary by ±0.″2 of the centres estimated by van der Wel et al. (2012).

We perform multiple tests to check to what extent we can recover the source sizes and Sérsic profile shapes for different intrinsic sizes, profile shapes and peak signal-to-noise values. Based on sets of simulated data at the resolution and S/N of the observations, we find that the we can accurately constrain the Sérsic index, n, of the 1.6 µm surface brightness profiles. For all three galaxies, exponential profiles ($n = 1$) provide a poor fit to the 1.6 µm emission (see also Calistro Rivera et al., 2018). In contrast to the 1.6 µm emission, the Sérsic indices cannot be accurately constrained for the dust and CO emission (based on the S/N and resolution). We therefore keep the Sérsic index as a free parameter when fitting the F160W emission but fix the Sérsic index to match an exponential profile ($n = 1$) for the CO and dust emission. This choice of exponential profile is motivated by the exponential dust-continuum profiles observed for local (e.g. Haas et al., 1998; Bianchi, 2007; Muñoz-Mateos et al., 2009; Bianchi and Xilouris, 2011) and high-redshift galaxies (Hodge et al., 2016; Barro et al., 2016; Tadaki et al., 2017b; Calistro Rivera et al., 2018; Gullberg et al., 2019). Fixing the profile shape for the CO and dust continuum has negligible impact on our conclusions as the half-light radii inferred when forcing $n = 1$ are consistent, within errors, with the values inferred when n is a free parameter. The same is not true if we fix the 1.6 µm emission to be exponential. In that case, the half-light radii measured for ALPS.1 and 2 are 20% larger and 30% smaller respectively, thanks to the presence of multiple, unobscured, stellar components, visible in the 1.6 µm emission, as well as possible contributions from dust lanes.

The uncertainties returned by GALFIT, based on the uniform error maps, underestimate the uncertainty on the fit parameters. We therefore quote uncertainties based on the distribution of best-fit values for fits to simulated maps. For the F160W emission, the error on the measured half-light radii is ≤ 10% whereas for the CO and dust-continuum emission the uncertainties (not accounting for the uncertainty of the profile shape) are ∼ 20 – 30%.

The F160W half-light radii measured here are consistent with those of van der Wel et al. (2012). The small differences in the best-fit values appear to be due to the deeper XDF data of Illingworth

et al. (2013) used here. The steepness of the stellar surface brightness profiles differs significantly for the three sources. ALPS.1 exhibits the steepest surface brightness profile, with a Sérsic index of $n \sim 0.5$, equivalent to a Gaussian profile. The unobscured stellar emission of ALPS.3 is best fit by $n \sim 0.8$ (close to the exponential profile, $n = 1$), whereas ALPS.2 exhibits the shallowest, unobscured stellar profile with $n > 2$. We note that of the sources at $1 < z < 3$ in the GOODS-South field with measured structural properties a third have profiles with $n > 2$ whereas 12% are best fit by Sérsic indices $n \lesssim 0.5$.

3.4.3.2 Uv-plane Analysis

To assess the reliability of our image-plane analysis, we also perform uv-plane source fitting using: 1) the CASA-based, UVMULTIFIT algorithm (Martí-Vidal et al., 2014) and, 2) the GILDAS-based[(2)] UV_FIT algorithm (Pety, 2005). Both algorithms fit the specified Fourier-transformed 2D surface brightness profiles, i.e. the model visibilities, to the measured visibilities by minimizing the χ^2 statistic. We correct for the fact that our sources are not at the centre of the pointings by applying the necessary phase shifts, baseline reprojections and primary beam corrections. These corrections are applied as part of the UVMULTIFIT algorithm whereas for the second approach, we corrected for the primary beam attenuation and weighting using GILDAS algorithms before merging the visibilities from the various mosaic pointings for each source. We fit both 2D elliptic Gaussian and exponential profiles but find no significant differences (< 5% in the flux and < 25% in size) between the two profiles. We refer to the exponential fits from hereon for consistency with the image-plane analysis. Additional uncertainties are introduced by the relative weighting of the low- versus high-resolution data sets, with differences of up to 40% in the inferred sizes (i.e. comparing the fits using both data sets versus the high-resolution set only).

For all three sources, we find good agreement between the fluxes fit in the uv-plane and those measured from the image plane (as described in Section 3.3.1). Without fixing any parameters, we find that the uv-based CO- and 1.3 mm size estimates for ALPS.1 and 3 are consistent, within 1σ errors, with the measurements and upper limits from the image plane, whereas for ALPS.2 (owing to the low S/N and the apparently complex morphology) the sizes fit in the uv-plane are 50 ± 30% smaller than those fit in the image-plane. However, when we fix the source centre and position angle to the results of our CO kinematic fitting (described in Section 3.5.2) during the uv fitting, we obtain half-light radii that are consistent with what we measure from the image plane. Although 20% smaller on average, we conclude that our uv- and image-plane analyses are consistent within errors for all three sources, when the source centres and position angles are fixed. Henceforth, we quote the image-plane sizes.

3.5 DYNAMICAL ANALYSIS

3.5.1 CO line kinematics

To understand the dynamical properties of our sources, we first analyse their position-velocity (pV) diagrams, shown in Figure 3.6. We create the pV maps from the 50 km s^{-1}, CO cubes using CASA's IMPV task, selecting a 0.″3 slit along the major axis, which we define using the centres and position angles fit to the CO data (see Section 3.5.2). We find clear velocity gradients for all three sources (also evident from the moment-1 maps in Figure 3.7), suggesting that the bulk of the emission stems from rotation-dominated gas disks. The maximum line-of-sight velocities are ~ 300 km s^{-1}, indicating rotation velocities of $310 - 340$ km s^{-1} (based on the inclinations inferred from the HST data).

We also assess the integrated CO spectra of our sample. The spectra from the ASPECS LP data, are shown in Figure 2 of Aravena et al. (2019) and Figure 8 of González-López et al. (2019). We also

[(2)] http://www.iram.fr/IRAMFR/GILDAS

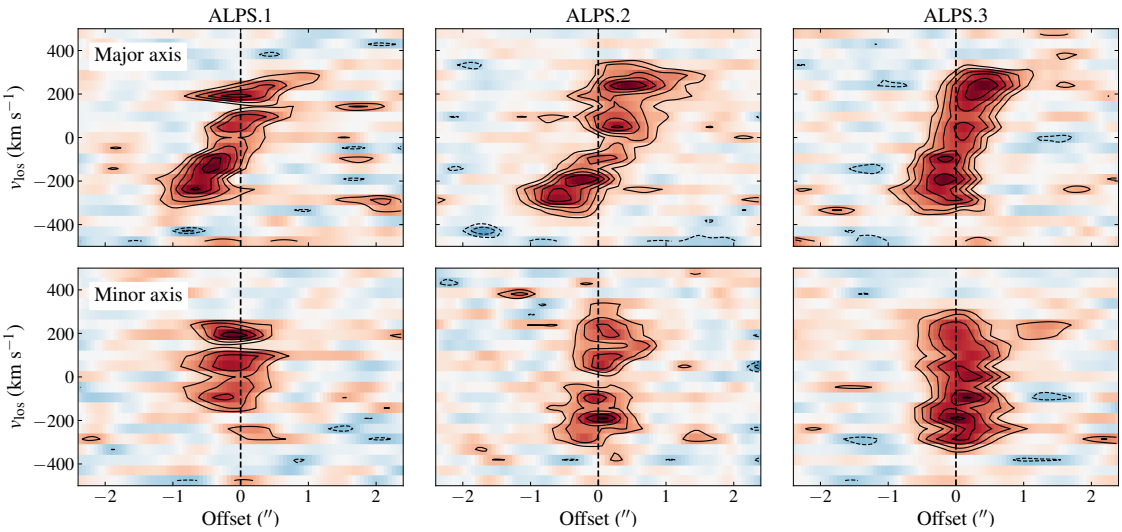

Figure 3.6: Position-velocity (pV) diagrams extracted over $\pm 500\,\mathrm{km\,s^{-1}}$ within 0.3" wide slits along the rotation axis (where the position angle is taken from the kinematic modeling of the CO data, described in Section 3.5.2) using `CASA`'s `impv`. Top row: pV diagram along along major axis. We see clear evidence of rotation in all three galaxies. Bottom row: pV diagram along minor axis. The flux density is represented by the linear, blue-to-red colorscale where white represents the zero level. Contours start at $\pm 2\sigma$ and proceed in steps of $\pm 1\sigma$.

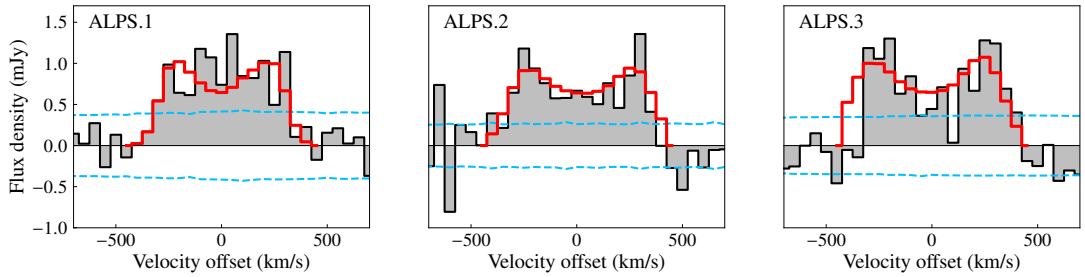

Figure 3.7: CO spectra of our sources, taken from within 1.5, 2 and 1.5 arcsecond apertures respectively for ALPS.1, 2 and 3. We compare the line profiles from the 3D convolved model of the CO emission, fit using `qubefit` (in red). The $\pm\sigma$ levels are indicated by the light blue, dahsed lines. All line profiles are inconsistent with a single Gaussian profile. The profiles for ALPS.2 and 3 are clearly double-horned, indicating that the CO emission stems from rotation-dominated disks.

provide the spectra of our three sources, based on the combined ASPECS LP and ALPS data, in Figure 3.7, comparing the line profile predicted from the dynamical modeling (described in Section 3.5.2). The observed shape of the line profile is governed by multiple effects including the inclination, velocity dispersion, total mass (related to the stellar and gas mass distributions) and steepness of the gas surface density profile (de Blok and Walter, 2014). Distinct, double-horned profiles originate from gas that is supported by rotation in a disk, and for which the rotation velocity increases sharply at small radii and flattens at larger radii. ALPS.2 and 3 both display double-horned profiles, indicating that the emission from each source stems from a rotation-dominated disk. Such profiles are commonly observed for local disk galaxies using HI, which traces the gas disk to large radii (e.g. Catinella et al., 2010).

About half of the SMGs observed at sufficient S/N exhibit double-peaked lines profiles (e.g. Birkin and et al., 2020, in prep.). Double-horned profiles are more commonly observed for massive star-forming galaxies with extended molecular gas disks (such as our sample) (e.g. Tacconi et al., 2013). The flatter-than-Gaussian profiles observed for some high-redshift galaxies are sometimes interpreted as further evidence that the gas is more turbulent than in local galaxies. However, for

Table 3.5: Inferred Dynamical Properties

Source	ALPS.1	ALPS.2	ALPS.3
Kinematic Analysis with `qubefit`			
Inclination (degrees)	76^{+10}_{-4}	60^{+4}_{-4}	69^{+6}_{-6}
$r_{1/2}^{CO}$ (kpc)	$3.7^{+0.3}_{-0.3}$	$4.6^{+0.3}_{-0.3}$	$2.6^{+0.2}_{-0.3}$
$v_{rot,max}$ (km s^{-1})	279^{+8}_{-14}	355^{+12}_{-14}	349^{+19}_{-23}
σ (km s^{-1})	57^{+11}_{-12}	73^{+13}_{-14}	77^{+10}_{-11}
$v_{rot,max}/\sigma$	4.9 ± 1.0	4.9 ± 0.9	4.5 ± 0.7
Dynamical analysis within $2\,r_{1/2}^{CO}$			
M_{dyn} (10^{11} M$_\odot$)	1.3 ± 0.2	2.7 ± 0.3	1.5 ± 0.2
M_{baryon} (10^{11} M$_\odot$)	1.9 ± 0.7	1.3 ± 0.6	2.4 ± 0.9
f_{DM}	<0.3	0.5 ± 0.2	<0.4
Dynamical analysis within $6\,r_{d}^{CO}$			
M_{dyn} (10^{11} M$_\odot$)	2.4 ± 0.3	4.8 ± 0.5	2.6 ± 0.4
M_{baryon} (10^{11} M$_\odot$)	2.6 ± 1.0	1.7 ± 0.9	3.6 ± 1.3
f_{DM}	<0.2	0.6 ± 0.2	<0.3

* The baryonic masses and hence dark matter fractions depend on the inferred α_{CO}, provided in Table 3.2.

** The quoted uncertainties are at the 1σ level whereas the upper limits are at 2σ.

many observed sources it is also possible that the observed emission stems from a small, central region that doesn't probe the maximum, rotation velocity (i.e. where the velocity curve flattens). Although we infer the velocity dispersions and maximum rotation velocities in the next section, we note here that the flat CO line profile of ALPS.1, compared to the separate peaks observed for ALPS.2 and 3, may be the result of a steeper surface density profile (i.e. as indicated by the smaller Sérsic index of the fit to the stellar emission) or the fact that the CO observations, for this source, are less sensitive to the flat part of the rotation curve.

3.5.2 Kinematic modeling

We constrain the rotation velocity and velocity dispersion of each of the three galaxies using the python-based kinematic modeling tool QUBEFIT, described in Appendix C. of Neeleman et al., 2019[3]. QUBEFIT fits a model cube to the data, convolving the model to the same spectral and spatial resolution as the data. The model is compared to the data via the χ^2 statistic, and takes into account the spatial correlation between pixels via a bootstrapping analysis. The full parameter space is sampled via the Markov Chain Monte Carlo method, thereby yielding likelihood distributions for the parameters being fit.

We model the line emission as stemming from a thin, exponential disk with only circular velocities in the plane of the disk, i.e. we do not consider any radial motions. We fit for the source centre, maximum rotational velocity, $v_{rot,max}$, velocity dispersion, σ_v and the scale length of the exponential disk, r_d. The median and $\pm 1\sigma$ values, for each galaxy, are provided in Table 3.5. We

[3] https://github.com/mneeleman/qubefit

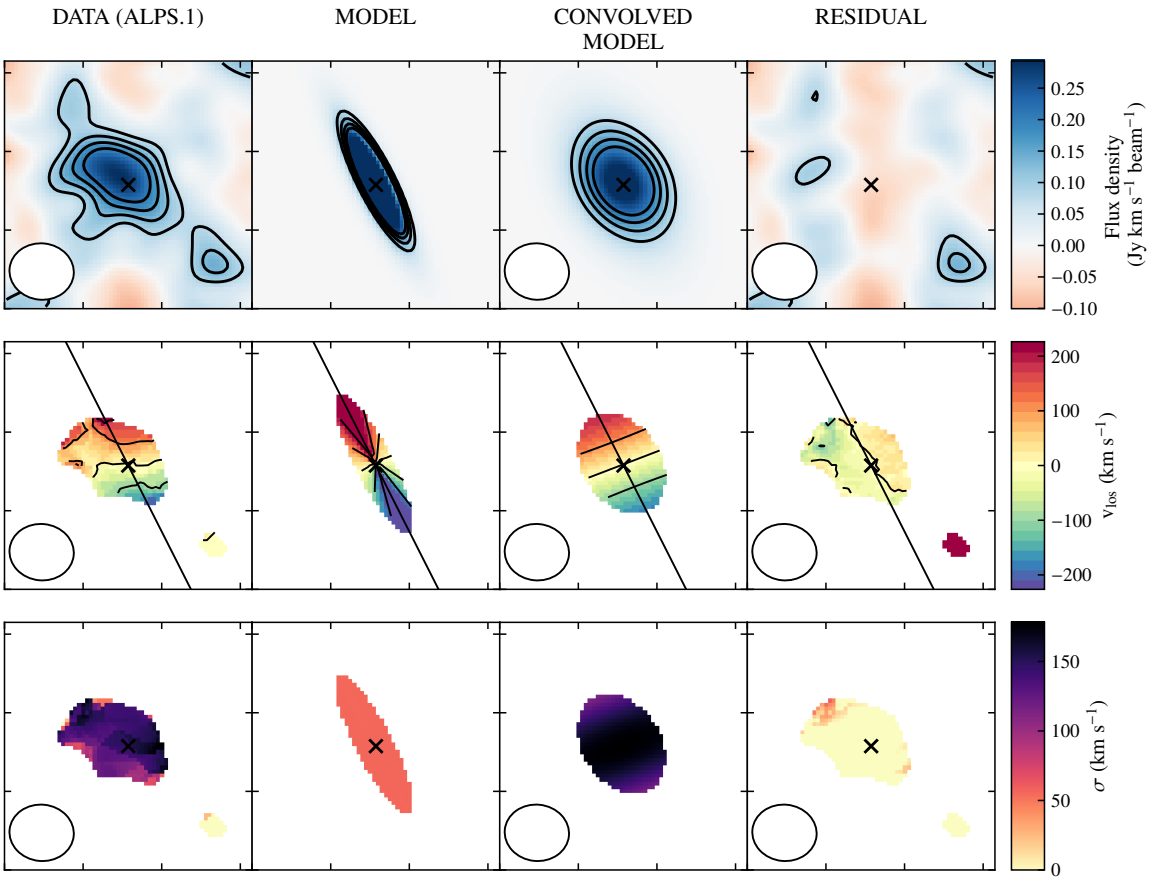
DATA (ALPS.1)
MODEL
CONVOLVED MODEL
RESIDUAL
Flux density (Jy km s^{-1} beam^{-1})
v_{los} (km s^{-1})
σ (km s^{-1})

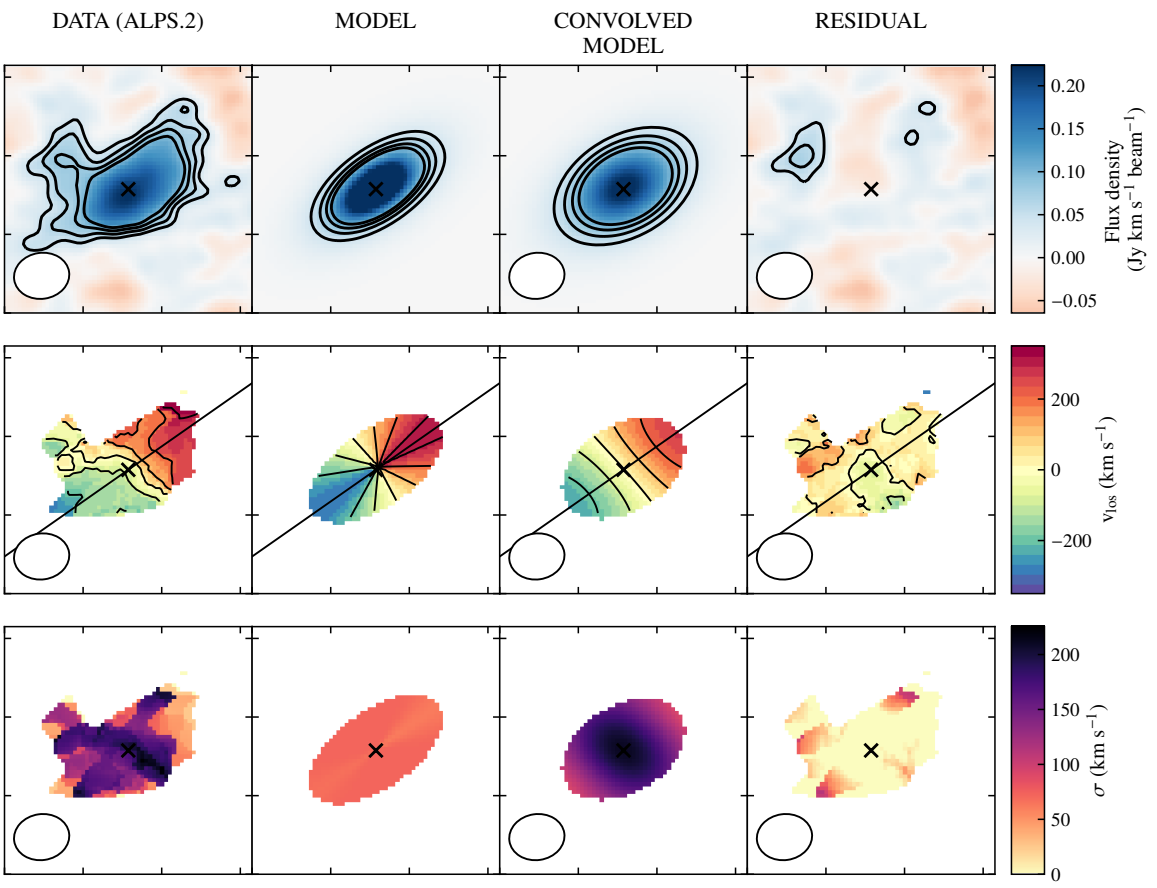
DATA (ALPS.2)
MODEL
CONVOLVED MODEL
RESIDUAL
Flux density (Jy km s^{-1} beam^{-1})
v_{los} (km s^{-1})
σ (km s^{-1})

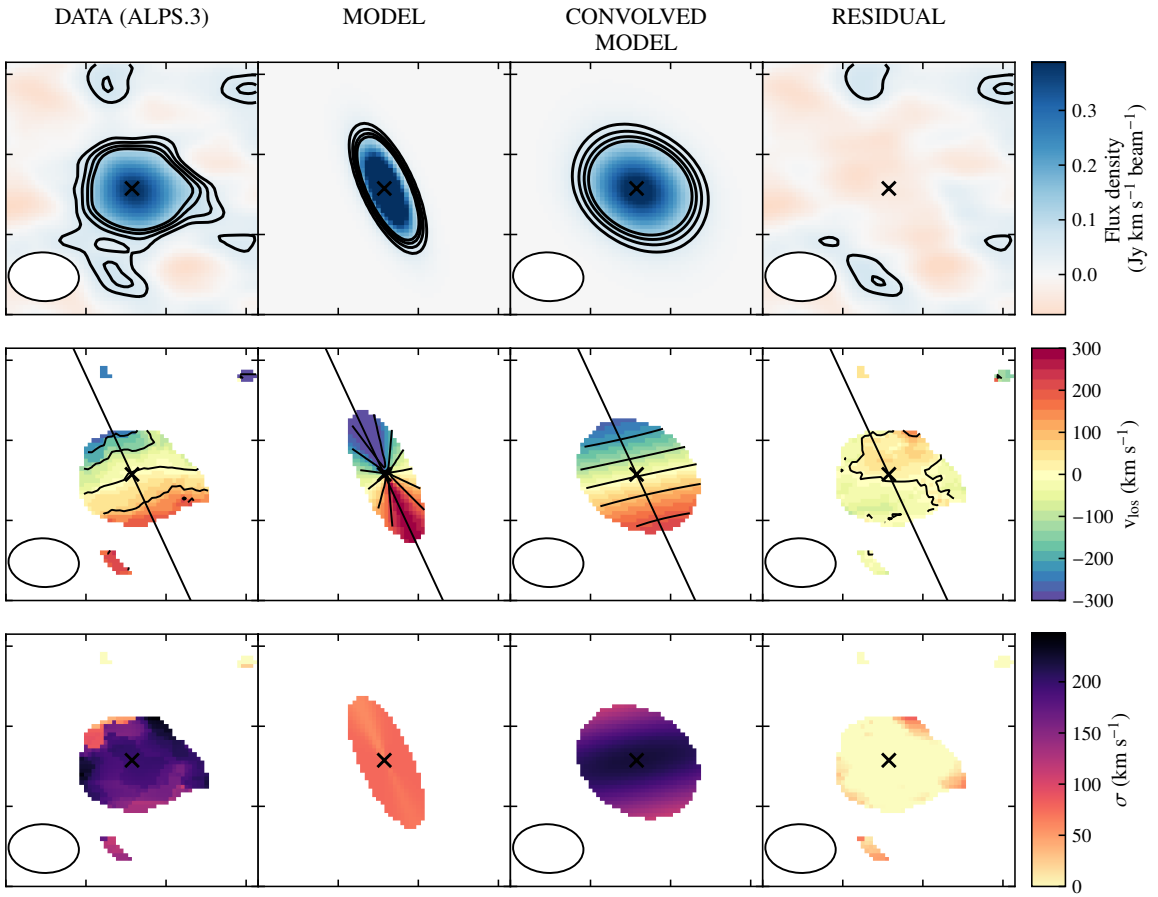

Figure 3.7: `Qubefit` models of the integrated CO flux (top row), velocity (middle row) and velocity dispersion (bottom row) of ALPS.1, 2 and 3 (labeled above data column for each). For ALPS.1 and 2 we observe CO(2-1) whereas for ALPS.3 we observe CO(3-2). From left to right: data, intrinsic model, convolved model, and residual (data - convolved model). The maps of the integrated velocity and velocity dispersion have been created using the 2σ blanking method (described in Section 3.5.2). For clarity, the maps are additionally masked at the outer 2σ contour of the integrated intensity (top row) for the respective column (data, model and convolved model). The best-fit position angles are indicated by the black lines.

choose not to place a prior on the inclination or PA as the CO emission may probe a different region than the rest-frame optical data. For the initial guesses of the inclination and position angle, we use the best-fit values of van der Wel et al. (2012), scaling the best-fit axis ratio, q, to an inclination via $\cos^2 i = q^2$. We fit the model cube to regions of 3″ diameter (larger regions resulted in poorer constraints). We note that the best-fit rotation velocities and inclination angles are highly degenerate. However, for all three galaxies we recover inclination angles consistent with those inferred based on the axis ratios fit to the *HST* data. For ALPS.3, the best-fit position angle differs by 20° from the position angle fit to the *HST* data. Forcing the position angle to match decreases the rotation velocity to a value 20 km s^{-1} lower than that quoted in Table 3.5. We caution that the inferred velocity dispersions are global estimates that include dispersions due to motion along the line-of-sight (i.e. due to motion inside a thick disk, or, motions due to warps) as well the true velocity dispersion of the gas. Thus, the dispersion inferred via QUBEFIT is an upper limit on the intrinsic gas velocity dispersion. Although we provide the estimated errors for the thin disk model in Table 3.5, we treat the dispersion values as upper limits. The CO half-light radii measured with QUBEFIT are lower than measured from the moment-0 maps with GALFIT, by at least 20%. We conclude that this is mainly due to the low S/N of the emission in individual 50 km s^{-1} channels compared to that in the map collapsed over 800 km s^{-1}.

We compare the model moment maps to those of the data in Figure 3.7. To create the moment-1 and 2 maps for the data, we implement a PYTHON-based algorithm that identifies coherant source emission, associated with a $> 3\sigma$ peak in both the spatial and spectral axis (see also Leroy et al., 2009). To do this, we expand the region around each $> 3\sigma$ peak outwards, in RA, DEC and velocity, until we reach a 2σ boundary. All pixels outside these boundaries are masked when making the moment-1 (intensity-weighted velocity) and moment-2 (intensity-weighted velocity dispersion) maps. This method produces moment maps that are more representative of the velocity fields than if we include all pixels, but some artifacts, such as the $400\,\mathrm{km\,s^{-1}}$ components for ALPS.3, still remain. The residuals of the moment 0 - 2 maps indicate a good quality of fit (see Figure 3.7) and the rotation velocity and dispersion values are consistent with the best-fit parameters inferred using the 3D modeling algorithm 3DBAROLO (Di Teodoro and Fraternali, 2015). However, for any fitting method the degeneracy between the rotation velocity and inclination is large.

Based on the data presented here, we note that single-Gaussian line profiles can severly overestimate the disk rotation. From the single Gaussian fit to the CO spectrum (of the ASPECS LP data), presented in González-López et al. (2019), the FWHM of the CO(2-1) line for ALPS.2 (ASPECS LP 3mm.05) is FWHM $= 620 \pm 60\,\mathrm{km\,s^{-1}}$. If the gas exhibits ordered motion then the maximum rotation velocity can be approximated by $v_{\rm rot} = 0.75\,\mathrm{FWHM}/\sin i$ (see e.g. Wang et al., 2013; Willott et al., 2015; Decarli et al., 2018). For ALPS.2, this results in an estimated rotation velocity of $\sim 510 \pm 50\,\mathrm{km\,s^{-1}}$, significantly larger than the value measured from the 3D modeling.

3.5.3 Dynamical Masses

Using the inferred kinematic properties, we estimate the total amount of matter within the region probed by the CO line emission,i.e. the dynamical mass, $M_{\rm dyn}$. For local galaxies, the dynamical mass is typically estimated from the circular motion, inferred from a rotation curve, and the maximum extent of the rotating disk, typically inferred from HI or stellar light profiles. In combination with measurements of the baryonic mass components (i.e. the stellar and gas mass), the dynamical mass can be applied to estimate the fraction of baryonic or dark matter within the observed region of the galaxy. Such estimates become highly uncertain for high-redshift galaxies, for which high-resolution observations of line kinematics are scarce, stellar and gas masses are highly uncertain, source sizes are challenging to constrain and the inclination is often unknown. Moreover, even for galaxies for which the emission line observations are resolved, the observations typically do not extend to the radii required to infer the dynamical mass within the entire baryonic disk.

We infer the dynamical mass of all three galaxies, assuming that the bulk of the emission can be well described by a rotating disk which appears consistent with the lines profiles, as discussed in Section 3.5.1). The correct choice of radius is somewhat arbitrary (often high-redshift studies use the rest-frame optical half-light radius or twice this value to estimate dynamical masses). Here, we estimate these values for two definitions of the maximum radius probed by the CO, twice the half-light radius $r_{\rm max} = 2r_{1/2}^{\rm CO}$ and six times the exponential scale length $r_{\rm max} = 6r_{\rm d}^{m}athrmCO$. For consistency with the inferred maximum rotation velocities, we estimate the outer radii using the half-light radii inferred using QUBEFIT (Table 3.5).

We determine the dynamical mass and total baryonic mass (stellar plus molecular gas mass) from within $r_{\rm max}$, via,

$$M_{\rm dyn}(\leq r_{\rm max}) = \frac{v_{\rm rot}^2 r_{\rm max}}{G}, \tag{3.5}$$

where $v_{\rm rot}$ is the modeled, rotation velocity and G is the gravitational constant.

Post-publication note: Eq. (3.5) is based on the assumption that the mass distribution is spherically symmetric. Although this assumption applies for the dark matter haloes that the galaxies occupy, it is likely a poor description of the distribution of the gas, with simulations suggesting that the molecular ISM settles into a thin disk by $z \sim 2$ (e.g. Pillepich et al., 2019). Some previous studies have quantified a velocity correction to account for a non-symmetric mass distribution (e.g. Binney and Tremaine, 2008), finding that Eq. (3.5) will overestimate the dynamical mass up to 30% if all of the mass is instead contained within a thin disk. However, the total mass distribution will lie somewhere between the thin disk and spherical scenario, more likely leading to an underestimate of 10-20% for the galaxies in this study. This "grain of salt" is not mentioned in the remainder of the Chapter but is worth keeping in mind in the comparison of gas and dynamical masses in Section 3.6.2.

We infer the total content of baryonic matter using the measured molecular gas and stellar masses in combination with the modeled surface brightness profiles of the CO and 1.6 µm emission, respectively. We estimate the fraction of light within $r_{\rm max}$, from the 2D model profiles, and scale the molecular gas and stellar masses by the respective fractions. We thereby assume that the 1.6 µm emission perfectly traces the stellar mass, and, that the excitation and CO-to-molecular gas mass conversion are constant over the entire galaxy disk. The dynamical and baryonic masses estimated for the three sources are provided in Table 3.5. For ALPS.2, we estimate a dynamical mass of $(2.7 \pm 0.3) \times 10^{11} {\rm M}_{\odot}$ within $2r_{1/2}^{\rm CO} \approx 9.2$ kpc, very close to the $M_{\rm dyn} \sim 2.0 \times 10^{11}\,{\rm M}_{\odot}$ inferred by Decarli et al. (2016) (from the initial 3 mm ASPECS data, based on the rest-frame optical half-light radius of 8.3 kpc).

As described in Section 3.3.2, a number of assumptions affect the inferred stellar masses. We therefore account for a factor of two uncertainty on the stellar mass (see Appendix A.2.2). The molecular gas masses are based on the assumption that the mass-metallicity relation holds for all three galaxies and that the $\alpha_{\rm CO}$ conversion factor is purely a function of the metallicity and doesn't evolve with redshift. We include the uncertainties on the metallicity estimate and $\alpha_{\rm CO}$ based on the uncertainties of the empirical relations used. We attempt to account for the uncertainty on the CO excitation. For ALPS.3 we use the measured line luminosity ratio, whereas for ALPS.1 and 2 we assume a CO(2-1)-to-CO(1-0) line ratio consistent with what has been previously measured for high-redshift sources. In addition, we assume that the ratio of ${\rm M}_{*}/L_{1.6\mu{\rm m}}$ is constant, and, that the line ratios and $\alpha_{\rm CO}$ are constant over the entire galaxy disk. Compared to other systematic uncertainties, radial variations in the applied ratios will have little impact on the derived baryonic masses and dark matter fractions. In addition to these uncertainties on the baryonic mass, the dynamical mass is heavily dependent on the inclination angle. We account for the range of inclination angles that fit the CO data in the uncertainties on the maximum rotation velocities.

Based on the dynamical and baryonic mass estimates, we estimate the dark matter fractions, $f_{\rm DM} = 1 - M_{\rm baryon}/M_{\rm dyn}$, enclosed within the two types of maximum radii chosen here. For ALPS.2, we infer dark matter fractions of up to 70% and 80% (within 1σ), within $r_{1/2}^{\rm CO}$ and $6r_{\rm d}^{\rm CO}$, respectively. We place 2σ upper limits on the dark matter fractions of ALPS.1 and 3 as the measured values are consistent with 0.

3.6 DISCUSSION

3.6.1 Comparing the Spatial Extent of CO, Dust and Stellar Emission

We have measured the spatial extent of the 1.3 mm dust-continuum, CO line and rest-frame optical emission of three star-forming galaxies at $z = 1.41, 1.55$ and 2.70. In this section, we discuss our findings and compare our results to simulations as well as previous observational studies of local and high-redshift galaxies. Although there is a wealth of high-resolution data available for

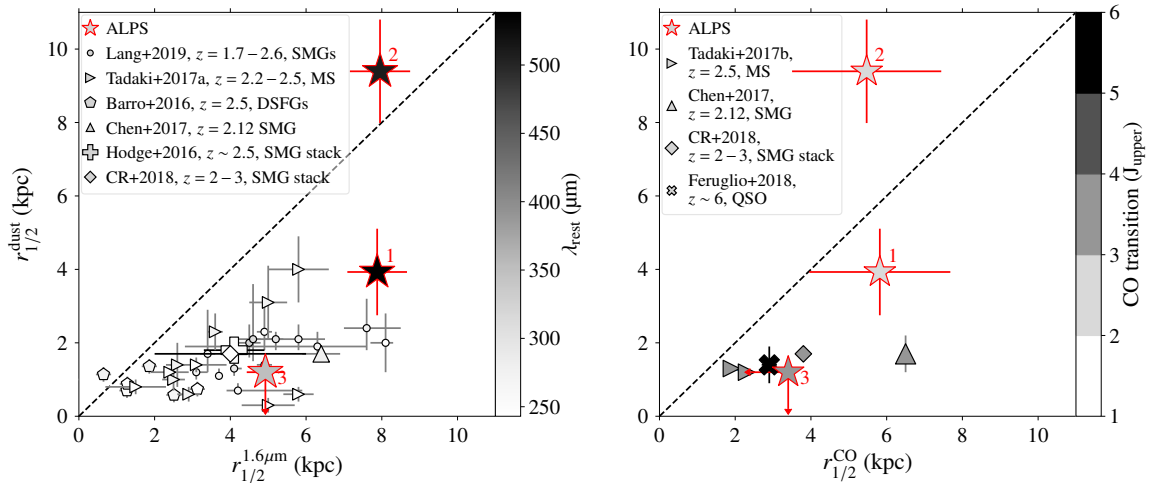

Figure 3.8: Comparison of the source sizes measured for our sample (stars) to other samples with dust-continuum size measurements (labeled in legends Barro et al., 2016; Hodge et al., 2016; Chen et al., 2017; Tadaki et al., 2017b; Tadaki et al., 2017a; Calistro Rivera et al., 2018; Feruglio et al., 2018; Lang et al., 2019). The source sizes shown here are measured from 2D maps using GALFIT (note that for the CO emission we also estimate sizes based on the 3D data as described in Section 3.5.2). Left panel: the dust half-light radii compared to the half-light radii measured from 1.6 μm emission. The greyscale of the points indicates the wavelength of the rest-frame dust-continuum emission. For most high-redshift galaxies observed to date, the dust continuum is more compact than the 1.6 μm emission. ALPS.2 is rare in that we measure equivalent dust and stellar half-light radii. Right panel: the dust half-light radii compared to the CO half-light radii. Here the greyscale indicates the upper level of the observed CO transition. As highlighted in this panel, very few high-redshift sources have the high-resolution observations of both CO and dust-continuum emission, needed to compare the relative spatial distributions.

local galaxies, few resolved observations exist of high-redshift sources that are not gravitationally lensed (summarised in Figure 3.8).

3.6.1.1 Limitations

We begin by noting that our data impose some limitations upon the methodology applied here. To estimate galaxy sizes, we fit a single disk component to all sets of data, assuming that the inferred half-light radius is representative of the entire disk. We do so because the resolution (~ 6 kpc for the CO) and sensitivity of the ALMA observations does not allow us to decompose the data into multiple components. However, stellar bulges are known to produce a steep, central rise for the rest-frame optical emission, and high central SFRs do the same for dust-continuum emission. Thus, local studies typically either decompose the stellar and continuum emission into a bulge and disk component, or omit the central few kpc when characterising the scale length of the exponential disk (e.g. Muñoz-Mateos et al., 2009; Hunt et al., 2015; Casasola et al., 2017).

3.6.1.2 CO vs Rest-frame Optical Sizes

For all three galaxies, the CO half-light radii are at least 30% smaller than the rest-frame optical half-light radii (see Table 3.4). This difference appears to be slightly larger than what has been observed for most local and high-redshift galaxies. As for our sources, Casasola et al. (2017) find that the mean scale length of the CO(2-1) and CO(1-0) surface brightness profiles for their 18, face-on local galaxies is, 20 – 60% smaller (~ 40%, on average) than the mean scale length at 0.6 μm (equivalent to the observed-frame 1.6 μm for our $z \sim 1.5$ galaxies). However, for the local galaxies in the HERA CO line Extragalactic Survey (HERACLES Leroy et al. 2009) and SINGS samples (Regan et al., 2006) the measured CO scale lengths are, on average, consistent with the scale lengths of the 3.6 μm emission, but range from half to almost twice the scale length of the stellar tracers. Similarly,

recent studies of $z = 2-3$ SMGs find equivalent CO and rest-frame optical half-light radii (Chen et al., 2017; Calistro Rivera et al., 2018).

The relative size of the CO versus rest-frame optical emission depends on the observed CO transition and rest-frame wavelength.Results from the Physics at High Angular resolution in Nearby GalaxieS (PHANGS, Schinnerer et al., 2019a) Survey as well as from HERACLES (Leroy et al., 2009) indicate that the CO(2-1) emission is co-spatial with the CO(1-0) emission. However, the ratio of the line luminosities can vary between 0.6-1.0, with brighter CO(2-1) typically found in the centers of galaxies. Brighter, or more peaked, CO emission may therefore bias our inferred measurements to smaller radii, particularly because our observations are not sensitive to gas columns below $\sim 5\times10^{21}\,\mathrm{cm^{-2}\,beam^{-1}}$. The comparison between CO and stellar disk sizes is also influenced by the observed wavelength of the stellar emission. Age gradients in the stellar population across the disk and/or increased effects of reddening in the central regions, also lead to a decline in the measured radii from the UV to NIR (e.g. Peletier et al., 1994; de Jong, 1996; Pompei and Natali, 1997; MacArthur et al., 2003; Fathi et al., 2010; Möllenhoff et al., 2006).[4] Thus, the size measured for the 1.6 µm emission is also likely to be smaller than the intrinsic size of the stellar disk.

3.6.1.3 Dust-Continuum vs Rest-frame Optical Sizes

We observe both compact and extended dust emission, amongst the three galaxies studied here. For ALPS.1 and 3, the 1.3 mm half-light radii are (50 ± 20)% and <70% of the 1.6 µm half-light radii, respectively. In contrast, the 1.3 mm half-light radius of ALPS.2 is equivalent to that at 1.6 µm.

Like the rest-frame 350 µm emission studied here, the rest-frame 240 µm (observed-frame 870 µm) dust-continuum emission of ALPS.3 is very compact. Rujopakarn et al. (2019) analyse this emission at $0\farcs03$ resolution. By modeling the source emission in the uv-plane, using two concentric, elliptical Gaussians, they find that the "extended" dust component is best described by a profile with a major axis FWHM of $\sim 3.6\pm0.1$ kpc, corresponding to a half-light radius of ~ 1.8 kpc, similar to the half-light radius measured here for the rest-frame 350 µm emission (i.e. < 1.2 kpc from the image-plane and $\sim 1.2\pm0.2$ kpc from the uv-plane analysis). Assuming that the continuum emission can be modeled by a modified blackbody with a temperature of 25 K and dust emissivity index of 1.8, the rest-frame 350 µm ASPECS LP measurement, $S = 1070\pm50$ µJy, extrapolates to a rest-frame 240 µm flux of $\sim 2890\pm120$ µJy. This is consistent with the 2780 ± 90 µJy measured by Rujopakarn et al. (2019), implying that the shorter wavelength observations have not missed a significant component of extended emission. Thus, the shorter wavelength data is further evidence that the dust component of ALPS.3 is very compact.

The spatial extent of the dust-continuum emission in ALPS.1 and 2 differs significantly, despite the two galaxies exhibiting similar rest-frame optical half-light radii and similar stellar masses and SFRs (Table 3.2). From the multi-wavelength comparison in Figure 3.2, it would appear as though the dust-continuum emission traces the bright, central stellar component visible in the 0.6 and 1.6 µm images (second and third columns from the left) for ALPS.1, with no 1.3 mm emission above our detection limit visible for the southern tail of the optical emission. Conversely, the dust emission from ALPS.2 appears to coincide with the location of the clump-like, outer disk components visible in the 0.6 and 1.6 µm images (columns 2 and 3 of Figure 3.2), but not the central, red, stellar component. We also note that an additional blue clump is apparent to the north of the UV-NIR images of ALPS.2, which is not apparent in dust-continuum emission, but it is unclear if this is a fore- or background source.

The extended dust-continuum emission of ALPS.2 differs not only from what is observed for ALPS.1 and 3, but also from other high-redshift galaxies (Figure 3.8). In most of these, the dust emission is $2-4\times$ more compact than the stellar emission, e.g. for SMGs the 870 µm half-light

[4] We also find that the stellar half-light radii of our galaxies decrease by up to 20% from the observed-frame 1.25 µm to 1.6 µm emission, e.g. the 1.25 µm half-light radius of ALPS.2 is 9.8 ± 0.9 kpc, which is 20 ± 10% larger than the 1.6 µm size.

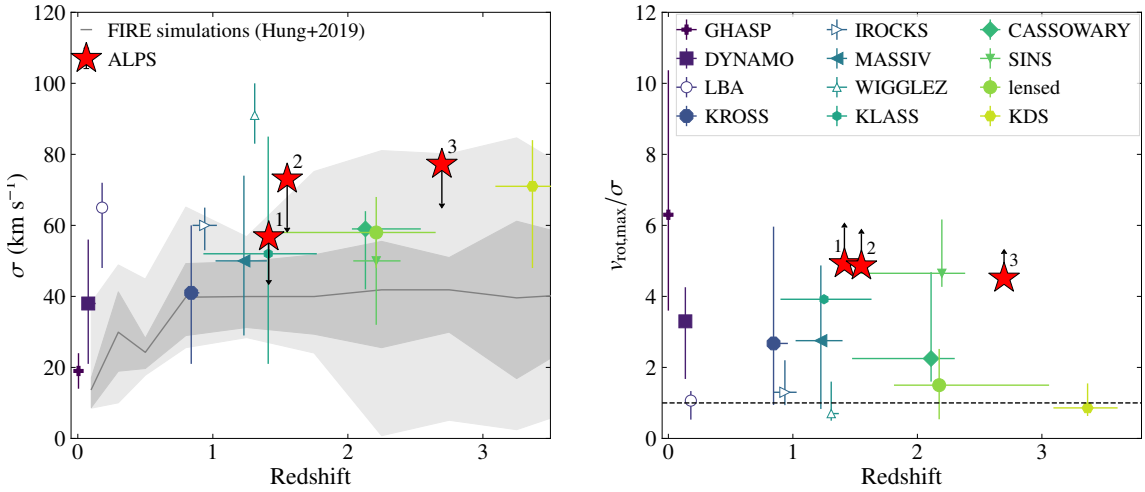

Figure 3.9: Left: Velocity dispersion as a function of redshift for star-forming galaxies. The solid grey line shows the median value for the simulated MS galaxies of Hung et al. (2019) with the dark and light grey regions enclosing 68% and 95%, respectively, of the simulated sources. The velocity dispersions of ALPS.1, 2 and 3, denoted by the red stars, are consistent with previous observations of MS galaxies. **Right:** comparison of the ratio of rotation-to-random motions for other galaxy samples. The colored symbols and errorbars in both panels indicate the median and 18th-64th percentiles of the GHASP survey (Epinat et al., 2010), DYNAMO survey (Green et al., 2014; Sweet et al., 2019), Lyman Break Analogues (LBAs in: Gonçalves et al., 2010), KROSS (Harrison et al., 2017; Johnson et al., 2018), MASSIV (Epinat et al., 2012), WiggleZ survey (Wisnioski et al., 2011), KLASS (Mason et al., 2017), CASSOWARY (Leethochawalit et al., 2016), SINS (Cresci et al., 2009), Lensed galaxies (Livermore et al., 2015) and KDS (Turner et al., 2017). The ALPS galaxies studied here have higher ratios of rotation-to-random motion than the majority of high-redshift galaxies observed to date. The velocity dispersion values for the comparison samples are provided in Table 2 of Hung et al. 2019. Observations for which the beam smearing is taken into account (for the rotation velocity) are shown as filled symbols (see Appendix A of Turner et al. 2017).

radii are typically measured to be $\lesssim 3$ kpc, whereas the 1.6 µm emission can extend to 8 kpc (Simpson et al., 2015; Hodge et al., 2015; 2019; Chen et al., 2017; Calistro Rivera et al., 2018; Lang et al., 2019; Gullberg et al., 2019). However, based on observations and radiative transfer models of local galaxies, extended dust disks with sizes comparable to the size of the stellar disk are the norm (Xilouris et al., 1999; Bianchi, 2007; Muñoz-Mateos et al., 2009; Holwerda et al., 2012). This tension can be resolved by the fact that the dust-continuum emission does not perfectly trace the bulk of the dust mass, but may be temperature-weighted and thus also sensitive to the sources of heating.

The dust-continuum emission may be very compact, if the central regions are dominated by starbursts (or AGN). Based on their FIRE simulations of high-redshift SMGs, Cochrane et al. (2019) find that the FIR continuum emission mostly stems from regions with high star formation rates, tracing both the central region as well as spiral arms. Similarly, based on Illustris TNG simulations of $1 < z < 3$ MS galaxies, Popping and et al. (2020, in prep.), find that the 1.2 mm emission best traces the regions with high rates of star formation. Moreover, both studies find that the ~ 1 mm dust half-light radii are typically smaller than the dust half-mass radii. These studies indicate that the centrally-concentrated continuum emission observed for many high-redshift galaxies has traced the high star formation rates of the central regions.

3.6.1.4 CO vs Dust-Continuum Sizes

Like the comparison to the rest-frame optical emission in the previous section, we find that the dust-continuum emission is more compact than the CO line emission from ALPS.1 and 3, but more extended than the CO emission from ALPS.2. The compact continuum emission, relative to

the CO emission, appears consistent with previous observations of unlensed high-redshift galaxies (Tadaki et al., 2017a; Chen et al., 2017; Calistro Rivera et al., 2018; Feruglio et al., 2018), as summarised in Figure 3.8.

Despite the relative differences in the extent of the CO and dust-continuum emission, the molecular gas masses inferred based on the total dust-continuum flux densities, using the empirical calibration of Scoville et al. (2014), are consistent with those measured based on the total CO emission. Thus, even though the total dust-continuum luminosity may correlate well with the CO emission (yielding the same total gas mass estimates), the dust-continuum emission is not a straightforward tracer of the extended dust disk (see also Groves et al., 2015).

In addition to the impact of dust heating, other physical effects may contribute to the difference in the extent of the CO and dust-continuum emission. Significant increases in the gas-to-dust ratio (GDR) towards the outskirts of galaxies may result in measured size differences. Although some individual galaxies exhibit evidence for an increase in the GDR with radius (e.g. Bendo et al., 2010) for most local galaxies the measured variation appears negligible (Sandstrom et al., 2013). Differences in the temperature and opacity across the disk seem likely to play a larger role, as indicated by the comparison of radiative transfer models with both the stacked CO(3-2) and dust-continuum emission in Calistro Rivera et al. (2018). We note that the dust-continuum emission of ALPS.1 and 3 appear steeper than for ALPS.2, indicating more centralised heating in these galaxies. Although the X-ray observations and SED strongly imply the presence of a central AGN in ALPS.2, there is no evidence from the UV-to-NIR images or 1.3 mm dust continuum for increased heating in the centre. Deeper, high resolution continuum observations will help to shed light on this issue.

3.6.1.5 A Plausible Explanation for Compact Dust and CO Emission

The compact dust (and CO) observations for ALPS.1 and 3 are consistent with what would be observed for galaxies hosting nuclear starbursts. To illustrate this, we use two local galaxies hosting nuclear starbursts, NGC 253 and NGC 4945, as an example (see Appendix A.2.3). Like the galaxies studied here, both of these local galaxies are heavily inclined and extended (with the 870 µm emission observed out to a radial distance of ~ 7.5 kpc). Using the 870 µm LABOCA observations of these two galaxies (Weiß et al., 2008), we create mock 1.3 mm maps with the same total flux density, resolution and S/N as the data for ALPS.1, 2 and 3 presented here.

We find that the convolved size at half the peak surface brightness of the mock 1.3 mm maps (blue contours), matches the beam of our 1.3 mm data (Figure A.6), due to the high contrast between the central, dust-continuum emission and that of the disk (up to a factor of 50 for NGC 4959). With the S/N and resolution of the data for ALPS.1 and 2, the spiral arms of NGC 253 would not be detected (at $> 3\sigma$) and only the brightest spiral of NGC4959 would be detected, making the observations appear asymmetric (similar to the 1.3 mm maps of ALPS.1 and 2 in Figure 3.2). The fact that we observe no extended structure in the 1.3 mm emission of ALPS.3 implies that the disk is less extended and/or the contrast between the nuclear and disk regions is even greater than for these two local starbursts. The comparison to these simple mock observations is consistent with the fact that our 1.3 mm observations are sensitive to a gas column of $N_{\mathrm{H}_2} \sim 10^{22}\,\mathrm{cm}^{-2}$, whereas the column densities measured for most of the spiral arms regions of NGC 253 are significantly lower.

3.6.2 Dynamical Properties

We have measured the dynamical properties of all three sources, and conclude that the gas motion of each disk is dominated by rotation. The measured velocity dispersions are consistent with the measurements from the KLASS, CASSOWARY, KROSS and SINS surveys of galaxies at $1 < z < 3$ (Mason et al., 2017; Leethochawalit et al., 2016; Johnson et al., 2018; Cresci et al., 2009) and the simulations of Hung et al. (2019) (Figure 3.9). However, the maximum rotation velocities are greater

than the majority of high-redshift galaxies in these samples. Thus, the rotation-to-random motions measured for our sample are higher than what has been been measured for most other high-redshift, star-forming galaxies (Figure 3.9) but consistent with the range of values typical of local disks (Epinat et al., 2010). It is unsurprising that the three galaxies studied here appear more rotation-dominated than most high-redshift galaxies studied to date, because our selection of extended and inclined sources favours "thin" rotating disks.

We note that ALPS.2 was also observed as part of the SINS sample (labeled GMASS 1084 in Förster Schreiber et al., 2009). Based on their Hα observations Förster Schreiber et al. (2009) measure a rotation to dispersion ratio of $v_{\rm rot}/\sigma = 4.4 \pm 2.1$, consistent with the $v_{\rm rot}/\sigma = 4.9 \pm 0.9$ derived here. However, using the intrinsic, inclination-corrected rotation curve of the best-fitting model disk they infer a lower circular velocity of $v_d = 230 \pm 38\,{\rm km\,s^{-1}}$. This lower velocity, compared to the $355 \pm 14\,{\rm km\,s^{-1}}$ measured here, is consistent with the smaller half-light radius of the Hα emission compared to that of CO (3.1 ± 1 kpc vs 4.6 ± 0.3 kpc), assuming that the rotation curve is still rising.

To compare to the literature, we inferred the dark matter fractions of our sample from within two sets of outer radii, i.e. out to twice the CO half-light radii, $2r_{1/2}$, and to six times the CO exponential scale length, $6r_{\rm d}$. For ALPS.1 and 3 the dynamical mass is of the same order as the baryonic mass, suggesting that the baryonic matter dominates at small radii. Even supposing that the molecular-to-gas mass conversion is overestimated by a factor of ~ 4 this would still be the case. In contrast, for ALPS.2, the measured dark matter fraction within $2r_{1/2}^{\rm CO(2-1)}$ is consistent with most simulations and local observations (Lelli et al., 2016; Lovell et al., 2018; Tortora et al., 2019). It is also consistent with the dark matter fractions inferred from the high-redshift observations of Molina et al. (2019) and the $0.6 < z < 2.2$ galaxies of Tiley et al. (2019). The smaller inferred dark matter fractions of ALPS.1 and 3, compared to ALPS.2, are likely related to the more centrally-concentrated molecular gas and stellar components. It is possible that these data simply do not extend far enough to measure the maximum radial velocities.

3.7 SUMMARY

We have compared ALMA and HST observations, tracing the stellar, dust and molecular gas components of three, star-forming galaxies, ALPS.1 at $z = 1.41$, ALPS.2 at $z = 1.55$ and ALPS.3 at $z = 2.70$. These galaxies were selected from the ASPECS LP, based on their bright CO and dust-continuum emission and their large, rest-frame optical sizes. Our main findings can be summarised as follows.

1. Our ALMA observations appear to trace the presence of nuclear starbursts, but are barely sensitive to extended spiral structure. For all three galaxies, the CO emission appears $\gtrsim 30\%$ more compact than the rest-frame optical emission. The 1.3 mm emission also appears more compact, by at least a factor of two, than the rest-frame optical emission of ALPS.1 and 3. In contrast, the 1.3 mm emission of ALPS.2 appears as extended as the rest-frame optical, albeit at poor S/N. The compact CO versus rest-frame optical emission implies the presence of a central, dense ISM component. Similarly, the compact 1.3 mm emission of ALPS.1 is consistent with what would be observed for an extended disk galaxy hosting a nuclear starburst, tracing a high central gas column density (and potentially also a high central star formation rate). For both the CO and 1.3 mm observations, temperature gradients would only serve to further to increase the contrast between the nuclear region and the more extended disks. Compared to ALPS.1, the more extended 1.3 mm (versus 1.6 μm) emission of ALPS.2 may imply the existence of denser spiral structure at large radii. However, higher S/N data is needed to confirm this result.

2. Our observations of ALPS.3 imply that there may exist a population of sources where the vast majority of the gas and dust is within a compact, nuclear starburst region. Both the CO and dust

continuum observations are significantly more compact than the rest-frame optical emission with no structure recovered at $\geq 3\sigma$ beyond ~ 2 kpc. For observations at the sensitivity and resolution of the 1.3 mm data for ALPS.3 we would expect to be able to observe dense spiral structure with a column density of $N_{H_2} \sim 10^{22}\,\mathrm{cm}^{-2}$ averaged over our synthesized beam, a value typical for extended local disk galaxies.

3. We investigate the dynamical properties of the three galaxies, based on our resolved observations of the CO(2-1) and CO(3-2) line emission. Our analysis indicates that the gas motion of all three galaxies is rotation-dominated. Based on the kinematic properties, we infer the dynamical masses and dark matter fractions within the region traced by the CO emission. Assuming CO-to-molecular gas conversion factors consistent with that of the Milky Way, we infer dark matter fractions of up to 0.6, consistent with simulations and observations of local galaxies with the same stellar masses.

We conclude with a note of caution. Based on our analysis, we find that measurements of the dust and CO half-light radii are still hampered by low sensitivity observations. We barely recover the extended cool dust component for one source and only observe the CO emission out to ~ 10 kpc, despite substantial time investments with ALMA. At 3σ our data are sensitive to a molecular gas column density of $10^{22}\,\mathrm{cm}^{-2}$ per beam. Thus, we miss regions of gas that are less dense than this and/or smaller than the synthesized beam. To triple the sensitivity of the observations would require a tenfold increase in the ALMA time per source, for both the CO and continuum emission. Thus, significant additional investments with ALMA are required to observe the extended gas and dust disks of high-redshift galaxies.

ACKNOWLEDGEMENTS

The analysis in the Chapter relied on the ALMA data: 2012.1.00173.S, 2016.1.00324, 2016.1.00324.L and 2017.1.00270.S. ALMA is a partnership of ESO (representing its member states), NSF (USA), and NINS (Japan), together with NRC (Canada), NSC and ASIAA (Taiwan), and KASI (Republic of Korea), in cooperation with the Republic of Chile. The Joint ALMA Observatory is operated by ESO, AUI/NRAO, and NAOJ.

The following significant contributions were made by coauthors:

- Fabian Walter, devised the project and provided scientific guidance,
- Mladen Novak, helped test the CASA scripts needed to combine the data sets and image the various combinations,
- Marcel Neeleman, created and helped use the kinematic modeling tool,
- Leindert Boogaard, pointed out additional data available on these sources,
- Axel Weiß, suggested the sensitivity analysis in Section 3.4.1,
- and Daizhong Liu, scripted the GILDAS version of the uv-plane analysis, which I performed with CASA.

Aside from the coauthors, the following people contributed:

- the anonymous referee gave prompt and constructive feedback, which improved the quality of the published article,
- Wiphu Rujopakarn shared the VLA data presented in Figure 3.2,
- Andrew Battisti described the effects of dust attenuation on SED modeling and performed some of the SED modeling with his adapted version of MAGPHYS,
- discussions with Rachel Cochrane, Arjen van der Wel, Matus Rybak and Enrico di Teodoro improved the analysis and interpretation of this work.

Thanks also to the developers of the fully-documented publicly-available codes used as part of this Chapter, i.e. Chien Peng (GALFIT), Ivan Martí-Vidal (uvmultifit) and Enrico di Teodoro (3D Barolo).

Tbd

Let's get to the details,
of the physics involved,
by simulating the clouds
that I just can't resolve.

Later, oh later...
There's data to reduce!
Simulations can wait,
while observations seduce.

A segmentation fault,
AREPO won't compile
Is it a version issue,
or am I missing a file?

Finally it is running,
four days for one cloud
Yet sometimes it stalls,
the nodes overcrowd.

What would we observe
from a distant GMC?
For that we must consider
the background intensity.

This detail now included
in the POLARIS code,
But have I run it right?
Can I trust what they showed?

"The normal state of affairs,"
said the great M Mac Low,
"is for none of it to run."
But this ruins my flow!

The endpoint is nearing,
while some issues remain.
Will the results come in time,
or will I go insane?

4

SIMULATING THE EFFECTS OF THE CMB ON [C I] AND CO LINE EMISSION AT HIGH REDSHIFT

This chapter is being prepared to be submitted to the Astrophysical Journal as M. Kaasinen, S. Glover, S. Reißl, F. Walter, E. da Cunha, P. Clark et al. "Simulating the Effects of the CMB on [C I] and CO Line Emission". The main supervisor and collaborator contributions are listed at the end of the Chapter. I performed the simulations and radiative transfer analysis, applying the tools as described but without making any changes to the codes themselves. The text is is my own, with the adoption of suggestions from my supervisors.

Abstract

Over the coming years, submillimeter facilities will increasingly be used to probe the molecular gas of galaxies beyond $z \sim 2$ via CO and [C I] lines. At these high redshifts, the excitation temperatures of the most commonly observed CO and [C I] transitions lie closer to the CMB temperature. Thus, the CMB cannot be ignored when interpreting the line emission. Previous studies have accounted for the impact of the CMB on CO line emission via models that assume virialised spheres, but this approach neglects the complex density and temperature structures of turbulent molecular gas clouds. We have therefore performed a numerical test of the impact of the CMB via AREPO simulations of giant molecular clouds from $z = 0 - 7$, including the key chemical reactions and turbulence within the molecular gas. We post-processed these simulations via the radiative transfer code POLARIS to predict the spatially-integrated line emission. In conducting this study we uncovered two issues with our simulations, which meant that we have not quantified what we set out to test. Instead, I summarise our methodology and the proof-of-concept study performed with the existing simulations.

4.1 INTRODUCTION

The molecular gas phase of the ISM plays a key role in the galactic matter cycle, hosting and providing the fuel for star formation. Constraining the amount, distribution and physical conditions within molecular gas at different cosmic epochs is therefore critical to understanding how galaxies form stars and how star formation regulates galaxy properties. However, the dominant component of the molecular ISM, H_2, barely emits at the low temperatures characteristic of star-forming gas and thus cannot be observed directly. Instead, observations of trace atomic and molecular species that emit at infared-to-submillimeter wavelengths are used to probe the bulk of the cold, molecular gas. In this wavelength regime, the Cosmic Microwave Background (CMB) may dominate the thermal energy budget. Although the temperature of the CMB is too low to play a significant role in regulating the structure and chemistry of the molecular ISM in the local Universe, it increases with redshift, thereby playing an ever more important role in regulating the emission from the molecular ISM.

The most commonly observed source of emission from the molecular gas in local galaxies is the ground transition of CO. Obtaining a molecular gas mass (or surface density) from the ob-

served CO(1-0) line luminosity requires the application of the empirically-calibrated conversion factor, $\alpha_{\rm CO}$, but $\alpha_{\rm CO}$ is far from a universal constant, varying with the metallicity, temperature and density of the gas as well as the strength of the interstellar radiation field (ISRF) and cosmic ray ionisation rate (CRIR) (e.g. Glover and Mac Low, 2011; Feldmann et al., 2012a; b; Narayanan et al., 2012). Accounting for these effects has proven challenging and it remains unclear to what extent $\alpha_{\rm CO(1-0)}$ evolves with redshift. Probing the content and distribution of molecular gas at $z > 1$ is made more challenging by the fact that CO(1-0) is shifted to a wavelength regime where it is difficult to observe. Studies of $z > 1$ galaxies therefore rely largely on observations of CO transitions with $J_{\rm upper} = 2$ or 3, which much first be down-converted to the CO(1-0) line luminosity by assuming the CO excitation, before inferring a gas mass via $\alpha_{\rm CO}$. Some of the uncertainties associated with CO may be circumvented by instead using observations of the transitions from neutral atomic carbon, C I. Although [C I] lines are typically fainter than the emission from ^{12}CO, they scale more directly with the total H_2 mass, as they are ususally optically thin and stem from a wider range of ISM conditions than ^{12}CO (e.g. Offner et al., 2014; Beuther et al., 2014; Glover et al., 2015; Glover and Clark, 2016). However, as for $\alpha_{\rm CO}$, it is still unclear to what extent the conversion between [C I] and the total molecular gas mass changes with redshift (as the CMB temperature increases).

Observations of CO and [C I] in $z >$ galaxies are (and continue to be) conducted with current (sub-)millimetre facilities, particularly the ALMA and NOEMA. Since CO transitions have frequencies of 115.27 J GHz, they are essentially observable at all redshifts with ALMA. As the highest-J transition that stems mostly from molecular clouds (rather than photodissociation regions) the CO(3-2) transition is still observable with ALMA up to $z \sim 3.1$. Likewise, the two [C I] transitions can also now be observed beyond $z \sim 2$. At 492 GHz, [C I](^{3}P$_1$ - ^{3}P$_0$) is closely separated in wavelength from CO(4-3) whereas at 809 GHz, [C I](^{3}P$_2$ - ^{3}P$_1$) has a similar frequency to CO(7-6). With the current receiver bands of ALMA, [C I](1-0) and [C I](2-1) can be targeted up to $z \sim 4.8$ and 8.5, respectively. With Bands 1 and 2 of ALMA soon becoming available, the redshift ranges at which the $J < 4$ CO and [C I] lines are observable will be extended, allowing [C I](1-0) to be probed out to $z > 10$ and CO(3-2) to be targeted up to $z \sim 8.8$.

Over the last decade, deep field surveys of $J \leq 3$ CO transitions have already helped constrain the cosmic evolution of the molecular gas density out to $z \sim 4.5$ (e.g. Decarli et al., 2019) whereas targeted CO surveys have led to the development of gas scaling relations, linking the total molecular gas masses, stellar masses, and star formation rates (SFRs) of galaxies up to $z \sim 4$ (e.g. Tacconi et al., 2018). Integrated [C I] observations have been used to probe the molecular ISM of SMGs and quasar host galaxies (QSOs) at $z \sim 2-5$ (e.g. Walter et al., 2011; Alaghband-Zadeh et al., 2013; Bothwell et al., 2017; Cañameras et al., 2018; Jin et al., 2019). Recently, integrated [C I] observations have also been conducted for a sample of typical star-forming galaxies at $z \sim 1.2$ (Valentino et al., 2018; 2020), and one compact $z \sim 2.3$ star-forming galaxy (Popping et al., 2017b). Resolved observations of CO emission are also starting to reveal the dynamics and morphology of the ISM in galaxies at $z \sim 2-4$ (e.g. Bolatto et al., 2015; Calistro Rivera et al., 2018; Rybak et al., 2019; Kaasinen et al., 2020). With integrated and resolved observation sincreasing in number and depth, it is becoming more important to accurately account for the impact of the CMB.

In the local Universe, the intrinsic excitation temperatures of the CO and [C I] line transitions lie well above the CMB temperature. Thus, this thermal background can be ignored when interpreting the line emission. However, at the high redshifts at which these lines are now routinely detected, the effects of the CMB can no longer be ignored. The local CMB temperature is $T_{\rm CMB}^{z=0} = 2.726$ K (Fixsen, 2009), whereas the bulk of the molecular gas is at ~ 20 K. But, the CMB temperature increases with redshift according to,

$$T_{\rm CMB}(z) = T_{\rm CMB}^{z=0}(1+z)\,. \tag{4.1}$$

As the CMB temperature increases so too does the minimum ISM temperature, thereby affecting the density and temperature of the molecular gas. This has two main implications for the observed

line luminosities; 1) the increased heating leads to a greater population of high rotational levels, thereby "boosting" the line luminosities, especially for higher-excitation transitions, but, 2) the emission must also observed against a stronger background (e.g. da Cunha et al., 2013b; Zhang et al., 2016; Tunnard and Greve, 2016).

The impact of the CMB on observations of CO emission has been studied by da Cunha et al. (2013b), Zhang et al. (2016), and Tunnard and Greve (2016). To predict the emission from molecular gas that is not in local thermodynamic equilibrium (LTE), these studies adopt radiative transfer models using the large velocity gradient (LVG) approximation. In their models, the CO emission is assumed to stem from radially-expanding spheres with a set, uniform H_2 density and one-component velocity gradient dv/dr. The models are based on a number of free parameters, particularly the gas kinetic temperature, H_2 number density, CO number density and velocity gradient. The sampled parameter space is reduced by setting the relative abundance of CO-to-H_2 to 8×10^{-5}. Moreover, in these studies the molecular gas is assumed to be in a virialsed spheres, which sets the velocity gradient for the chosen H_2 densities. The increase in the CMB temperature sets the minimum excitation temperature. Using the chosen parameters and $T_{\rm CMB}$, these LVG models are used to compute the line excitation temperatures and optical depths by coupling the statistical equilibrium and radiative transfer equations. From these, the velocity-averaged line fluxes and line luminosities are determined.

By comparing the intrinsic line emission at $z = 0$, with what is measured against the CMB at higher redshifts da Cunha et al., 2013b; Zhang et al., 2016; Tunnard and Greve, 2016 find that neglecting the effect of the CMB can severely bias the molecular gas masses inferred from CO emission, i.e. the inferred gas mass may be less than 20% of the actually value for a $z > 5$ galaxy when applying the typical local $\alpha_{\rm CO}$ value (da Cunha et al., 2013b). The increased background temperature may also lead to a more clumpy observed morphology (Zhang et al., 2016; Tunnard and Greve, 2016). Moreover, the CMB affects the relative strengths of the different CO transitions, thereby impacting the physical properties assumed from modelling the line ratios and excitation ladders.

Although the aforementioned studies laid the groundwork for interpreting $z \gtrsim 2$ observations of CO emission, they all assumed that the molecular gas is contained in virialised spheres. In reality, local molecular clouds appear to be dominated by supersonic turbulence (e.g. Lombardi et al., 2008; Kainulainen et al., 2009; Lada et al., 2009) and it is expected that the same is true for clouds at high redshift. As the CMB temperature increases so too will the local sound speed of the gas, decreasing the turbulent Mach number.[1] Numerical studies show that when the turbulent Mach number decreases, the density probability density function (PDF) produced by the turbulence becomes narrower (e.g. Federrath and Klessen, 2013). Thus, the increasing CMB temperature should serve to reduce the width of the density PDFs, which physically means that there are fewer and/or smaller regions of very high gas densities. Theoretically, the CMB-driven change in the density and temperature structure of the molecular gas must alter the relative amount of carbon locked up in the atomic or molecular form within different regions of the cloud, thereby also regulating the integrated line emission. Yet, these effects have not yet been modelled. It therefore remains unclear precisely how the line emission from turbulent molecular clouds is affected by the increasing CMB temperature.

In this study, we test how CO and [C I] emission is affected by the increasing CMB temperature, using simulations that account for the turbulence and chemistry within molecular clouds. We produce synthetic maps of the line emission by first simulating giant molecular clouds using the AREPO moving-mesh code (Springel, 2010a) and post-processing these simulations with the radiative transfer code POLARIS (Reissl et al., 2016). Using these synthetic observations, we quantify how the ratios between the observed CO(1-0) and [C I](1-0) line luminosities and total

[1] $\mathcal{M} = \sigma_v / c_s$ where σ_v is the volume-weighted 3D velocity dispersion and c_s is the sound speed of the gas.

H_2 masses vary as a function of redshift. This study is a *numerical experiment*, designed as a first test of the impact of the CMB of cloud structure. It is not a self-consistent simulation of molecular cloud formation, the computational expense of which would increase the run time enormously.

This Chapter is structured as follows. In Section 4.2, we outline the numerical methods used to simulate the molecular clouds and produce the synthetic emission maps. In Section 4.3 we examine how the strength and spatial distribution of the tracers varies as the background temperature increases. In Section 4.4 we discuss the implication of our findings and the limitations of our simulations.

4.2 METHODOLOGY

4.2.1 Giant Molecular Cloud Simulations

For the simulations carried out in this work, we follow the methodology of Clark et al. (2019). For clarity, we briefly outline the simulations, and any changes from Clark et al. (2019), here. We perform our simulations using the AREPO hydrodynamics code, which solves the equations of fluid flow on an unstructured mesh defined by the Voronoi tesselation of discrete points that move with the fluid in a quasi-Lagrangian way. The mesh cells can be readily refined/derefined by adding/removing mesh-generating points and the fluxes between these cells are computed via the finite-volume methodology.

AREPO is well-suited to these simulations as it captures the turbulence within the gas, while following the chemical and thermal evolution of the ISM. For our simulations, we include a magnetic field, using the treatment of ideal magnetohydrodynamics (MHD) implemented by Pakmor et al. (2011) and Pakmor and Springel (2013). The chemical network is modelled via the SGCHEM module, described in Glover and Clark (2012a), although our implementation includes a few additional improvements. We model the chemistry of hydrogen, carbon and oxygen by combining the treatment of hydrogen chemistry described in Glover and Mac Low (2007a), b with the network of CO formation and destruction from Gong et al. (2017). The latter is a modification from the simulations performed by Clark et al. (2019), who adopted the network of CO formation and destruction originally proposed by Nelson and Langer (1997). As shown in Gong et al. (2017) their improved and updated network is considerably more accurate than the Nelson and Langer (1997) network, particularly in situations where the cosmic ray ionisation rate is large. The recombination rates of the species considered in our simulations depend on the parameter $\psi = G_0 \sqrt{(T)}/n_e$ where G_0 is the UV field strength, T is the temperature and n_e the electron number density. Gong et al. (2017) calculate the grain surface recombination rates using the fitting formula provided in eq. (8) of Weingartner and Draine (2001), assuming that it is valid for all values of ψ. However, Weingartner and Draine (2001) actually state that it is only valid for $\psi > 100$. Thus, we also implement this correction.

Additional improvements over the version presented in Glover and Clark (2012a) are described in Appendix A of Clark et al. (2019) (see their Table A1 for a full list of the chemical reactions), e.g. we include the cosmic-ray induced photodissociation of CO and adopt updated rate coefficients. We do not account for the freeze-out of CO onto dust grains in our adopted chemical model as we expect this to have minimal impact on the ^{12}CO emission for two reasons; the emission is observed at a great distance from the shielded gas and the regions where freeze-out occurs are optically thick in ^{12}CO emission. The radiative heating and cooling of the gas is modeled on-the-fly in AREPO via the atomic and molecular cooling function introduced in Glover et al. (2010), updated in Glover and Clark (2012a), and imported to AREPO by Smith et al. (2014). We compute the column densities of H_2, CO and atomic carbon, via the TREECOL algorithm Clark et al. (2012a).

4.2.2 Initial Conditions

The molecular clouds that form in our simulations are the product of the collision between two clouds of initially fully atomic gas. Both clouds start with a number density of 10 cm^{-3}, have a mass of $10^4 M_\odot$ and a radius of 19 pc. For each cloud, we set an initial turbulent velocity field that follows a $P(k) \propto k^{-4}$ scaling law, includes only solenoidal forcing modes and has a velocity dispersion of 1 $km\,s^{-1}$. The clouds are set up to move directly towards each other at 3.75 $km\,s^{-1}$ along the x-axis, ensuring that they collide head-on with a combined collisional velocity of 7.5 $km\,s^{-1}$. This collision occurs along the magnetic field lines, where we have imposed a uniform field of $B_x = 3\,\mu G$.

The clouds are contained in a cubic computational domain of 190 pc^3 and are embedded in a neutral medium with a number density of 0.1cm^{-3}. Self-gravity is considered to be non-periodic whereas the MHD boundaries are periodic. Initially, the cloud centres are separated by three cloud radii (57 pc) and the cell mass is $\sim 5 \times 10^{-3}\,M_\odot$ (both in the clouds and surrounding medium). Thus, we start with $\sim$ 2 million cells in the clouds and 280 000 cells in the surrounding medium. We ensure that the thermal Jeans length is always resolved by at least 16 AREPO cells and that the volume of neighbouring cells differs by nor more than a factor of eight. The spatial resolution is a function of the local density, but remains at $\lesssim 0.1$ pc throughout the C- and CO-rich regions leading to convergence for the chemical compositions and observational properties of the cloud (see e.g. Seifried et al., 2017; Gong et al., 2018; Joshi et al., 2019).

For each redshift, we set the strength of the ISRF to the solar neighbourhood value of 1.7 in Habing (1968) units and the CRIR of neutral hydrogen to $3 \times 10^{-17}\ s^{-1}$. We also consider solar metallicity gas for all redshifts. For the initial elemental abundances of carbon and oxygen, we adopt the values given by Sembach et al. (2000). Expressed as the fractional abundance by number relative to the number of hydrogen nuclei, ξ, these values are $\xi_{C,tot} = 1.4 \times 10^{-4}$ and $\xi_{O,tot} = 3.2 \times 10^{-4}$. We take the singly ionized and neutral forms of carbon and oxygen, respectively. Although the simulations start with a cold, neutral medium, we set the initial H^+ abundance of the clouds to 0.01, in order to account for the ionisation caused by cosmic rays. This value exceeds the equilibrium value, but because the timescale for recombination is short, the gas in the clouds reach the correct ionisation fraction in < 1 Myr. The recombination also results in some cooling, however, this is soon offset by the photoelectric heating. Thus, the ionisation fraction and temperature are in equilibrium before the collision is underway.

We apply the above set-up to simulate clouds at integer spacings of redshift, from $z = 0 - 7$. Because this is a numerical test of the impact of the CMB, we only change the heating and cooling terms by setting the initial redshift of the cloud in AREPO. All other model parameters remain the same across the seven molecular clouds. We provide an example of the simulated properties of the final $z = 0$ and $z = 7$ giant molecular clouds (GMCs) in Fig. 4.1.

4.2.3 Radiative Transfer Post-Processing

We analyse our simulations at a time $t = 7.4$ Myr, shortly before the first prestellar core in the $z = 0$ simulation starts to undergo runaway gravitational collapse. To process these final snapshots, we employ the POLARIZED RADIATION SIMULATOR (POLARIS Reissl et al., 2016; Brauer et al., 2017), which is a publicly-available[(2)] radiative transfer (RT) code. POLARIS is unique in that it jointly models the physics of dust emission (Reissl et al., 2016; Reissl et al., 2018), line transfer including the Zeeman effect (Brauer et al., 2017), and synchrotron emission (Reissl et al., 2019). More importantly for our application, using POLARIS allows us to directly solve the RT equations on the AREPO Voronoi grid, without needing to interpolate first.

Using POLARIS, we map the emission from the $J = 1 \rightarrow 0$ to $J = 3 \rightarrow 2$ transitions of ^{12}CO and both transitions of [C I] for each simulated cloud. We choose this set of transitions, as these are the

[(2)] http://www1.astrophysik.uni-kiel.de/~polaris/

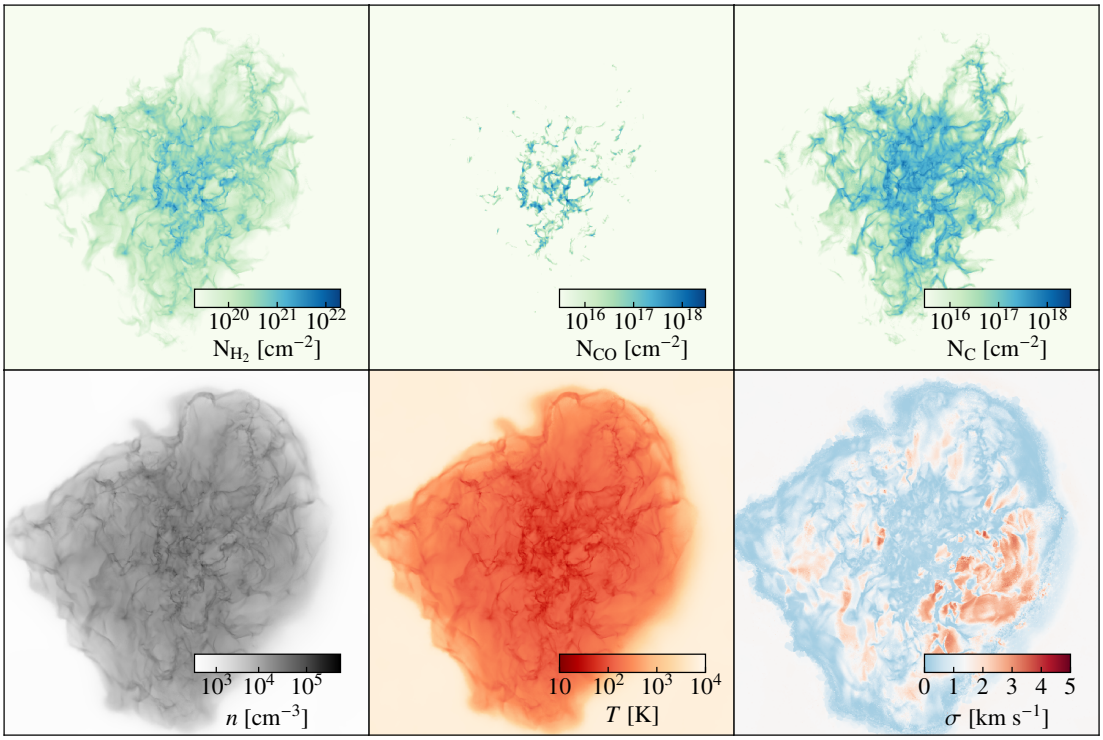

(a) $z = 0$ cloud

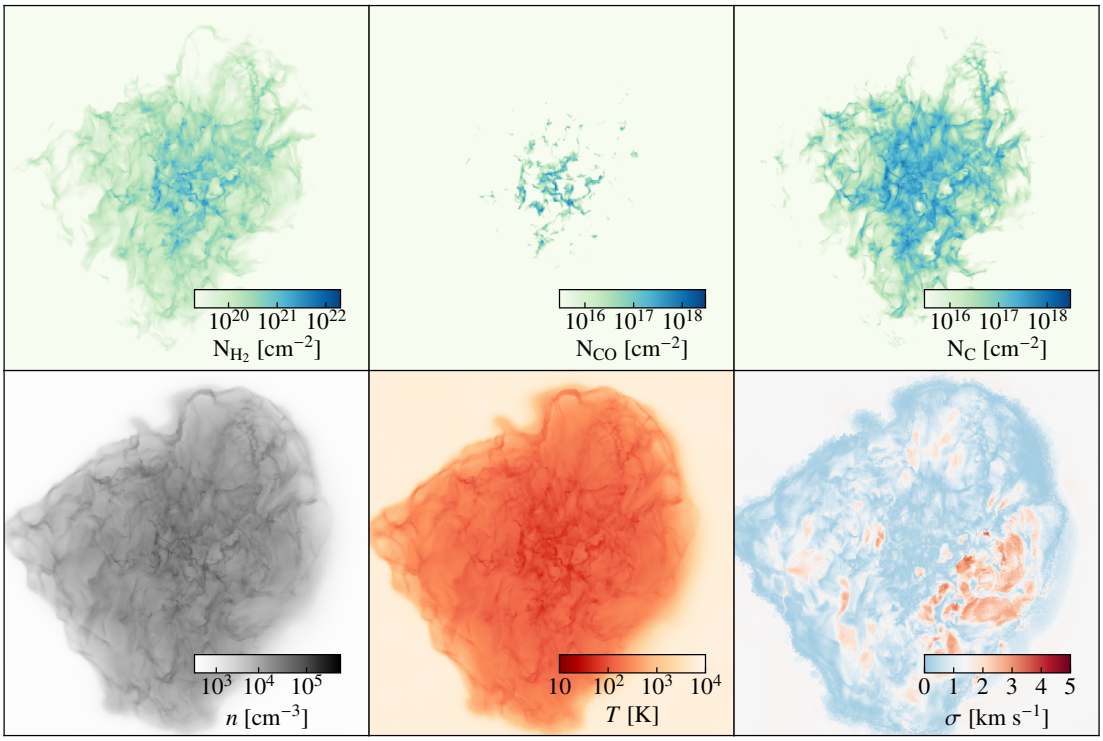

(b) $z = 7$ cloud

Figure 4.1: Physical properties of the $z = 0$ (a) and $z = 7$ (b) clouds in the 50 pc^2 region for which we perform the RT analysis. For each cloud, the panels in the top row, from left to right, show the mean H_2, CO and neutral carbon column densities along the line of sight. The panels in the bottom row, from left to right, depict the total particle number density, gas temperature and density-weighted velocity dispersion averaged along the line of sight. The $z = 7$ cloud is slightly larger and has fewer high-density and low-temperature regions than the $z = 0$ cloud. The column density of atomic carbon is significantly higher than that of CO for both clouds. We discuss this issue further in the text.

most likely to stem from dense molecular clouds rather than photodissociation regions. To compute the level populations, we apply the large velocity gradient (LVG; Sobolev, 1957) approximation, thereby assuming that the velocity variations are greater than the thermal or microturbulent velocities at a given scale. This assumption has been shown to yield accurate level populations, even beyond the limits of its applicability (Ossenkopf, 1997). For each transition, POLARIS models the mean intensity is the result of both the local transition and an external radiation field,

$$J_{\mathrm{i,j}} = (1-\beta) S_{\mathrm{i,j}} + \beta J_{\mathrm{ext}} \tag{4.2}$$

where β represents the probability for the photons to escape the grid, $S_{\mathrm{i,j}}$ is the source function of the transition and J_{ext} the external radiation field. To perform the radiative transfer, we consider the CMB to be the sole source of (external) background radiation, i.e. we ignore the interstellar radiation field. We therefore add a radiation field described by a blackbody with a temperature given by Eq. (4.1),

$$J_{\mathrm{ext}} = B_{\lambda}(T_{\mathrm{CMB}}(z)) \,. \tag{4.3}$$

The molecule/atom masses and collisional rate data need to compute the level population of CO and C I are taken from the Leiden Atomic Database (Schöier et al., 2005)[3]. We only account for collisions with H_2, because we expect that most of the CO and neutral carbon is located in gas with a high H_2 fraction.

To model the emission of each transition, we employ 200 velocity channels, covering −5 to +5 $\mathrm{km\,s^{-1}}$, resulting in a channel width of $0.05\,\mathrm{km\,s^{-1}}$. Even for cold regions, at ∼ 10 K, this is high enough to resolve the 3D thermal velocity dispersion, $\sigma_s \sim 0.3\,\mathrm{km\ s^{-1}}$, and the sound speed of gas, $c_s \sim 0.2\,\mathrm{km\ s^{-1}}$. As an input to POLARIS we subselect the central, $50\,\mathrm{pc}^3$ region of each simulated volume. This region fully encompasses the extent of the final clouds (e.g. Fig. 4.1). For the output emission maps, we sample these regions at 500 cells per side, giving a spatial resolution of $0.1\,\mathrm{pc}^2$. Our results are robust at this resolution, i.e. the predicted cloud emission does not change with a finer sampling of $0.01\,\mathrm{pc}^2$. All emission maps are created from the point of view of an observer at a distance of 5000 pc from the cloud, looking along the collision axis, i.e. the x-axis.

4.2.4 Cloud Properties

With the simulations described above, we intended to produce GMCs that were a good match for the GMCs observed in our own and other galaxies. However, analysing the properties of the resulting clouds (Figs. 4.1 and Fig. 4.2) shows that that they are actually **atypical** of local and high-redshift GMCs in that they have lower column densities and extinctions. The total hydrogen number column density of our clouds peaks at $2 \times 10^{21}\ \mathrm{cm^{-2}}$ (Fig. 4.2). Given the scaled Milky-Way-like dust treatment we have applied with AREPO,[4] this means that most of the gas in the clouds is in regions with a total extinction of $A_V = 0.5 - 1$ mag. However, both observations and simulations show that CO typically becomes abundant at $A_V = 1 - 2$ mag (Lombardi et al., 2006; Pineda et al., 2008; Glover and Clark, 2012a; Kong et al., 2015; Glover et al., 2015).

The low nuclei and dust column densities resulted in little dust- or CO self-shielding, leading to a high CO photodissociation rate. Thus, the simulated clouds have a high C I-to-CO column density ratio of ∼ 10, as shown in Fig. 4.1. This is about two orders of magnitude higher than for most local molecular clouds, which have C I/CO ratios of $\sim 0.1 - 0.3$ (e.g. Beuther et al., 2014; Papadopoulos et al., 2018). Regions with such CO-poor/C I-rich gas are expected to be typical in galaxy outskirts, molecular gas outflows or around active galactic nuclei (AGN) (e.g. Papadopoulos et al., 2018), rather than in GMCs.

[3] https://home.strw.leidenuniv.nl/~moldata/

[4] We adopt the prescription of Section 4.1 of Draine and Bertoldi (1996), which uses the average extinction curve from Bohlin et al. (1978), which has $N_H/E(B-V) = 5.8 \times 10^{21}\ \mathrm{cm^{-3}}$, and $R_V = A_V/E(B-V) = 3.1$. Thus, we assume $N_H/A_V = 1.87 \times 10^{21}\ \mathrm{cm^{-3}}$.

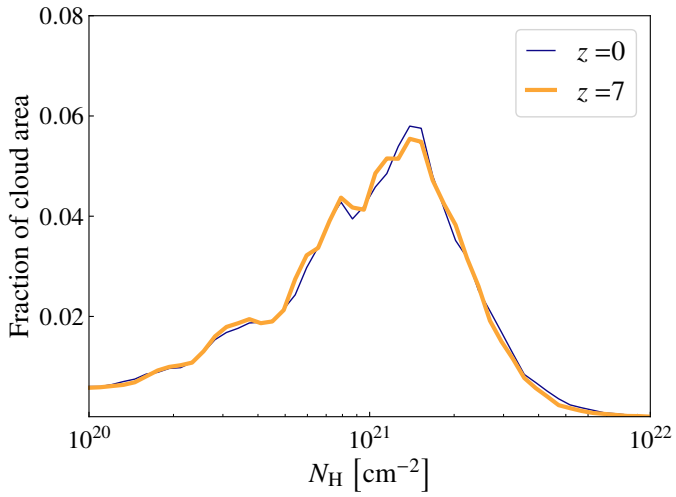

Figure 4.2: Probability density function (PDF) of the hydrogen nuclei column density, N_H, for the both the $z = 0$ and 7 clouds (purple and yellow respectively). Both PDFs peak at $N_H \sim 2 \times 10^{21}$ cm^{-2}, corresponding to an $A_V \sim 1$ mag, lower than the average for GMCs.

Unfortunately, by simulating these colliding clouds we have not ended up with the fully-evolved GMCs we set out to study. The average clouds densities are too low and the total mass of each cloud, at 2×10^4 M$_\odot$, is at least an order of magnitude lower than what is observed for local GMCs (see Section 1.1.4 of the Introduction). This issue is made worse by the fact that the masses are expected to increase with redshift, with some observation- and simulation-based studies indicating that $z \gtrsim 2$ galaxies host kpc-sized molecular "clumps" (e.g. Förster Schreiber et al., 2011; Bournaud et al., 2015; Mandelker et al., 2017; Guo et al., 2018)

The next step for this study will therefore be to utilise a different set of initial conditions, which result in a single fully-evolved GMC, with a more realistic fraction of high-density gas. To achieve this, we will likely conduct similar simulations to those of Glover et al. (2015) and Glover and Clark (2016), who simulated initially-spherical clouds, some of which had masses of 10^5 M$_\odot$. Their final clouds have a higher fraction of dense gas ($> 10^3$ cm^{-3}) with visual extinctions of > 1 mag.

For now, we have tested our analysis using the clouds simulated here. Thus, what follows is a **proof of concept**, which highlights the impact of the CMB without making realistic predictions for the conversion factors or redshift at which we longer expect to be able to detect CO or [C I] emission.

4.3 MEASURING THE IMPACT OF THE CMB

The CMB has three main effects, the magnitude of which we aim to compare here:
1. it changes the structure and relative abundances of carbon species in the clouds
2. it boosts the intrinsic line luminosities, and,
3. it becomes a stronger background against which the transitions must be observed.

To highlight the relative impact of each effect we have performed the radiative transfer on the eight clouds with the following three scenarios:

(1) only accounting for the change in the structure of the clouds, but not accounting for the enhancement to the line emission with increasing temperature, or the contrast against the CMB,

(2) accounting for both the change in structure and increase in high-excitation level populations ("line boosting"), but not the contrast against the CMB

(3) accounting for all effects, including the contrast against the CMB.

For scenario (1), we perform the RT on the simulated clouds, enforcing that $T_{\rm CMB}(z) = T_{\rm CMB}(z = 0) = 2.726$ K in Eq. (4.3) for each line and omitting the background source term. Thus, comparing the $z = 0-7$ clouds mapped in this way highlights the effect on the intrinsic emission of the CMB-driven change in the temperature and density structure and cloud composition. For scenario (2), we perform the RT on the simulated clouds for each line, accounting for the line boosting by setting the temperature to that of the CMB, Eq. (4.1). But, again we omit the CMB as a source background. Finally, for scenario (3), we perform the RT on the simulated clouds for each line, accounting for the line boosting by setting the temperature to that of the CMB, Eq. (4.1) *and* mapping this emission against the CMB.

4.3.1 Mapping CO and [C I] Emission

Figures 4.3 and 4.4 depict the velocity-integrated CO(1-0) and [C I] moment-0 maps, respectively, for the $z = 0, 3, 5$ and 7 clouds under the three scenarios described above. As expected from the low masses and column densities of the clouds, the CO(1-0) emission is faint, and is already dwarfed by the emission of the CMB at $z = 2$. However, what we had not expected to see is that a significant fraction of CO(1-0) and a small amount of [C I] is being detected in absorption at $z \geq 3$. This indicates that the CO-rich portions of the cloud are at temperatures that are colder than the background. The second law of thermodynamics dictates that this is not possible via radiative cooling, leaving only adiabatic cooling. Adiabatic cooling can explain why a small amount of CO is at temperatures below that of the CMB. Indeed, such cold regions are also known to occur within our own galaxy (e.g. in the Boomerang nebula; Sahai et al., 2017). However, only a small fraction of gas is expected to be adiabatically cooled below $T_{\rm CMB}$ at a given time. Instead, we are finding that *all* of the CO-rich gas is at these low temperatures, indicating that there is an issue with the way the overall cooling rates of the simulated clouds have been regulated.

Three main processes are expected to regulate the overall cooling rate at the temperatures and densities of the clouds: 1) fine structure cooling from C, C+ etc.; 2) CO rotational cooling; and 3) dust cooling (i.e. via the transfer of energy from gas to dust). The increasing CMB temperature will affect all three and indeed for processes (1) and (3) we already account for the CMB in AREPO. For the fine structure coolants (process 1) we solve the level populations in the optically-thin limit, because these species only have two or three levels. Here, the CMB pumping term is included when computing the level populations and the net cooling rate is calculated by subtracting the energy absorbed from the CMB per unit time from the energy emitted per unit time (as described in Section 3.1 of Glover and Jappsen, 2007).

Unlike these fine structure coolants, CO has more than three energy levels and is often optically thick. Thus, the level population equations cannot easily be solved analytically via the optically-thin assumption. Instead, we utilise a set of lookup tables computed by Neufeld and Kaufman (1993) and Neufeld et al. (1995), who used a LVG approach to compute the cooling rates from CO as a function of temperature, density and effective optical depth. However, Neufeld and Kaufman (1993) and Neufeld et al. (1995) were studying the local ISM, and thus included the local CMB temperature in their calculations. To account for the CMB temperature we would need to compute the cooling rate at $T_{\rm CMB}$ and subtract this from the cooling rate at the current gas temperature. Crucially though, the latter step had not been added to the Gong et al. (2017) network implemented in our simulations with AREPO. Thus, the implementation of CO cooling used in our simulations did not account for the increasing CMB temperature.

The fact that we neglected to include the CMB in the CO cooling was highlighted by checking the temperature vs. density phase-space diagrams in Fig. 4.5. Since CO cooling dominates over a relatively narrow range of densities, most of the temperatures in the cloud are correct (higher

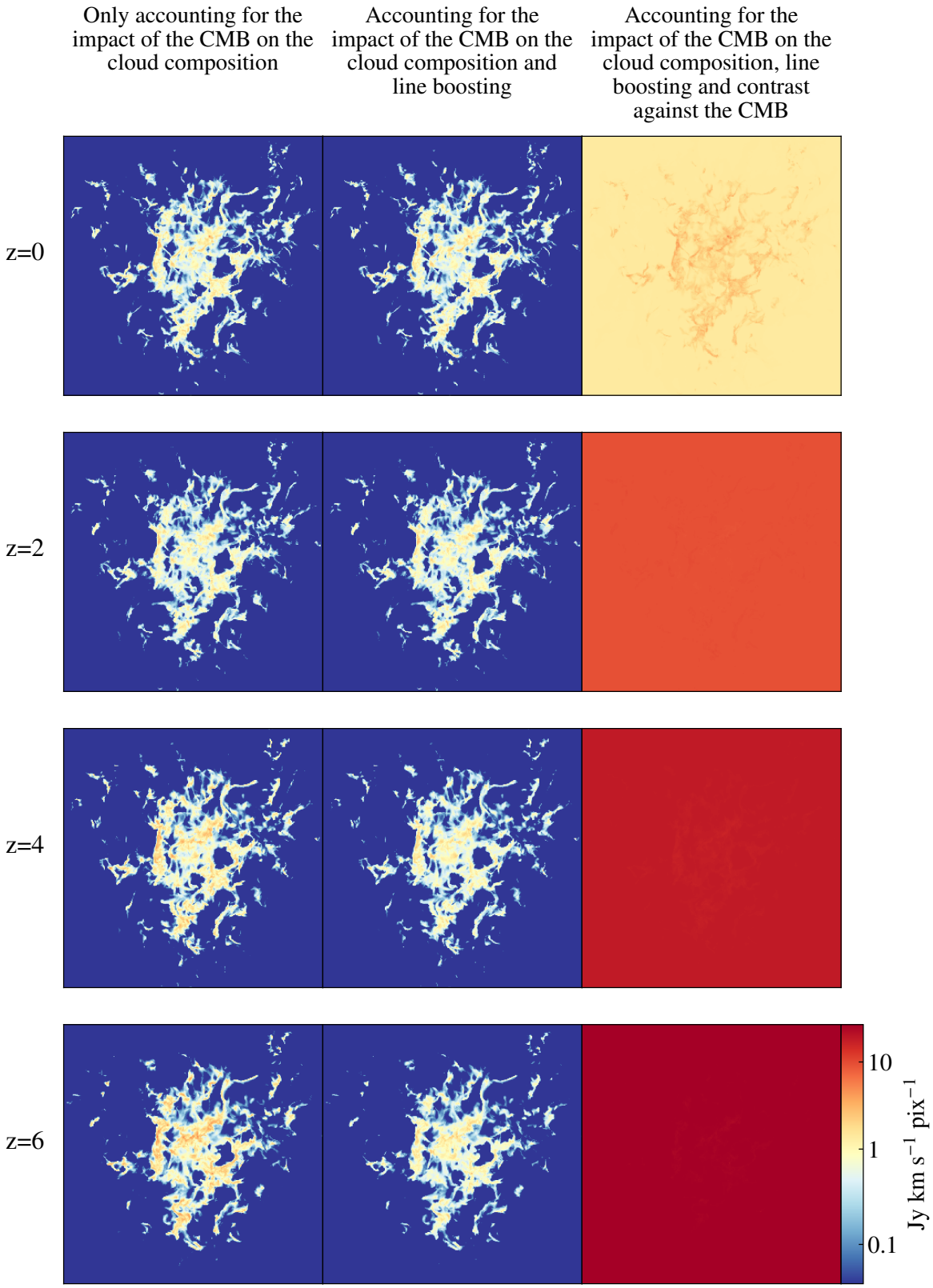

Figure 4.3: Moment 0 maps of the CO(1-0) emission accounting for the three main impacts of the CMB (labelled at top). In order for the intensities to be compared more easily, the maps depict what would be observed at 5000 pc from each cloud with the map in units of Jy km s^{-1} pix^{-1}, where each pixel is 0.1 pc^2.

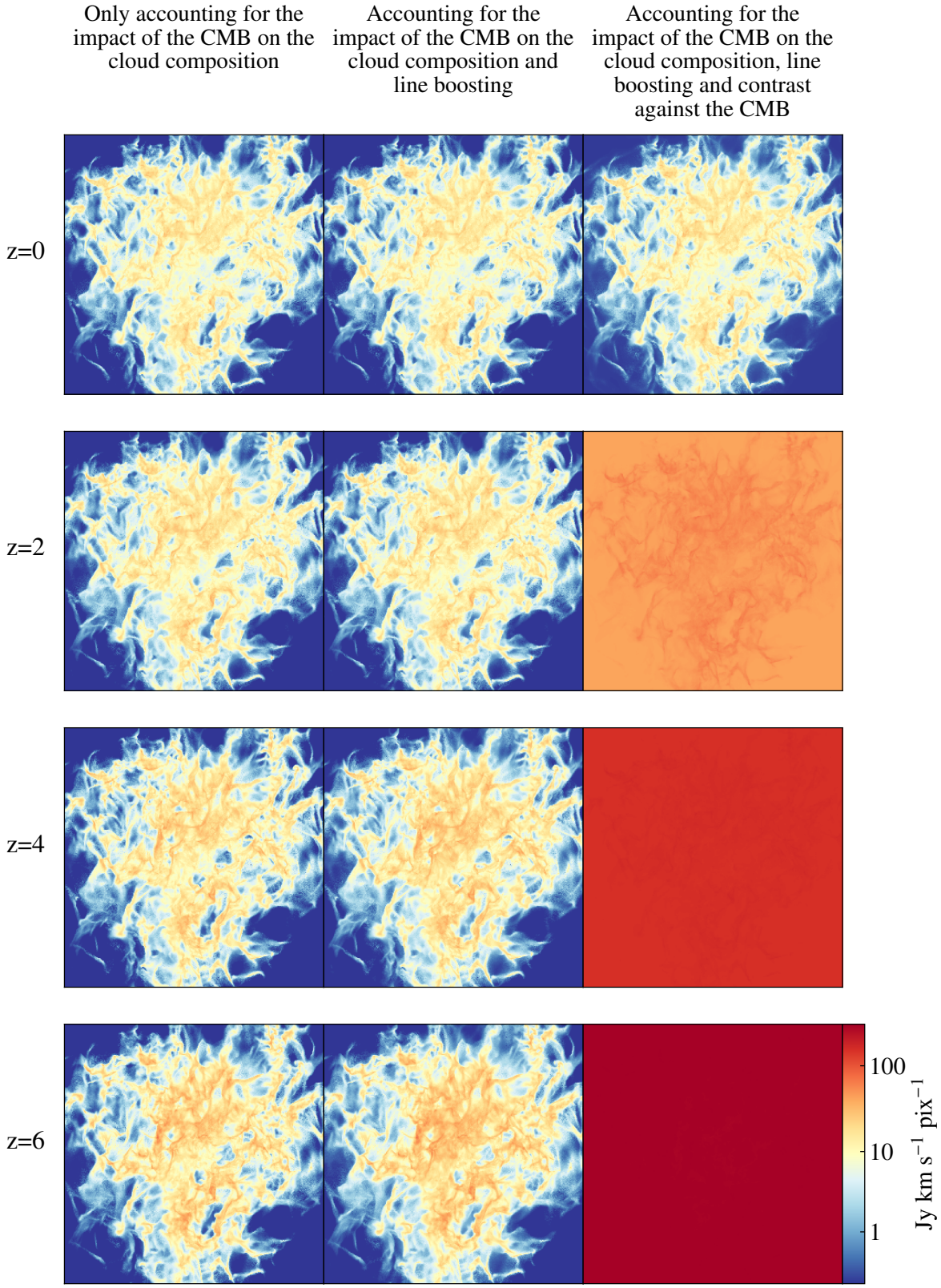

Figure 4.4: Moment 0 maps of the [C I] (1-0) emission accounting for the three main impacts of the CMB (labelled at top). In order for the intensities to be compared more easily, the maps depict what would be observed at 5000 pc from each cloud with the map in units of Jy km s^{-1} pix^{-1}, where each pixel is 0.1 pc^2.

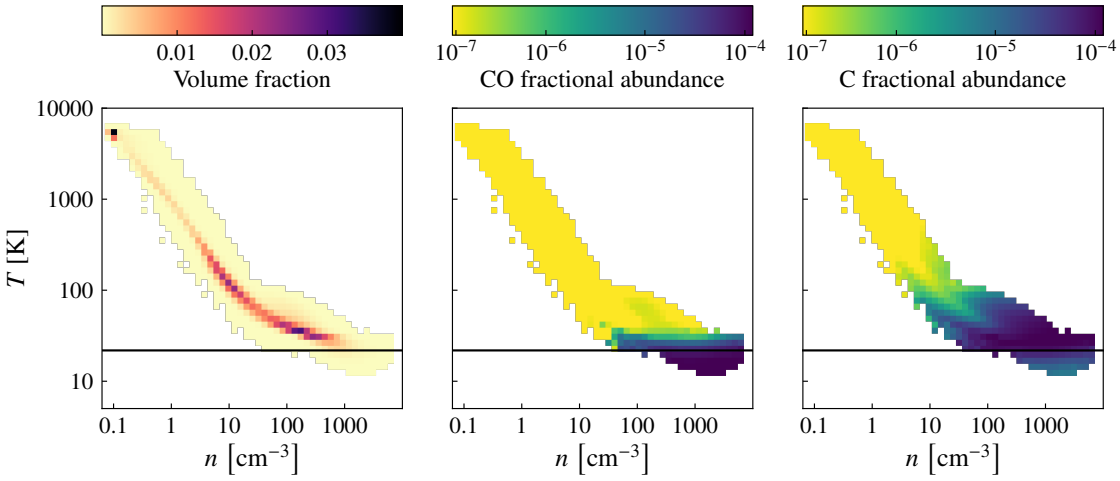

Figure 4.5: Temperature vs. density phase-space diagram for the simulated $z = 7$ cloud. The colour-coding, from left to right, depicts the volume fraction, mean fractional CO abundance and and mean fractional C abundance (by number relative to the number of hydrogen nuclei). The horizontal lines mark the CMB temperature at $z = 7$, $T_{\rm CMB} = 21.8$ K. A significant fraction of the CO is at temperatures lower than $T_{\rm CMB}(z)$, leading CO(1-0) to be mapped in absorption (Fig. 4.3). The over-cooling of CO also affects the neutral carbon, of which a large fraction is also at temperatures below $T_{\rm CMB}(z)$. Thus, a small fraction of [C I] is also mapped in absorption at $z > 5$.

than $T_{\rm CMB}(z)$). Crucially though, the temperatures that will be most strongly affected are the ones in the gas responsible for most of the CO emission, which are too low. This therefore seems to be the most likely explanation for why we see CO(1-0) in absorption rather than emission at $z > 1$. The [C I] emission is impacted less than the CO emission as the abundance of C I in the densest regions is lower (right panel, Fig. 4.5). However, a small fraction of C I, which occupies these dense regions is also at $T < T_{\rm CMB}(z)$, leading some C I to be mapped in absorption at $z \gtrsim 5$.

By analysing the post-processed maps, we have uncovered a second issue with the simulated clouds. The temperature of the CO-emitting gas is too low, as the CMB's impact on CO rotational cooling has not been taken into account. This additional caveat affects the results from here on.

Comparing the panels in the left-most column of Figures 4.3 and 4.4, highlights the impact of the warmer CMB on the temperature and density structure of the cloud. The kinetic temperature of the gas increases with $T_{\rm CMB}$, thereby resulting in brighter peaks of CO(1-0) and [C I] emission. Comparing the left and middle panels of Figures 4.3 and 4.4 shows that accounting for the impact of the CMB in regulating the level populations, via Eq. (4.2), has the effect of decreasing the CO(1-0) emission from the densest regions, whereas the [C I] emission instead increases. At the low excitation potential of the CO ground transition (5.53 K) most of the CO will already reach at least the $J = 1$ state. But as the background temperature increases, the level populations of higher J states of CO increase, which (in the case where the overall CO abundance does not change significantly) has the effect of reducing the amount of CO in the $J = 1$ state. In contrast, the excitation potential of [C I](1-0) is a lot higher than that of CO(1-0). Thus, as the background temperature increases more C atoms will reach this excited state than at lower temperatures, leading to a boost in the intrinsic line emission.

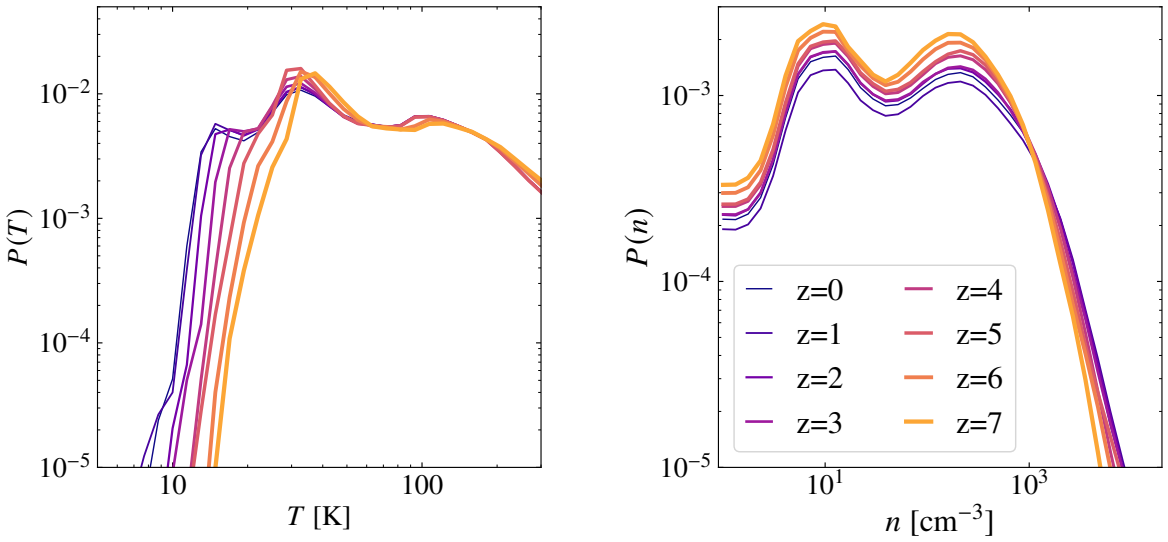

Figure 4.6: The mass-weighted temperature and density probability density functions (PDFs), left and right respectively, of the simulated $z = 0-7$ clouds (denoted by the different colours as shown in the legend). The minimum ISM temperature increases with redshift whereas and the fraction of gas at very high densities decreases as a result of increasing CMB temperature.

4.3.2 Physical Properties of the Clouds

To quantitatively compare the density and temperature structures of the clouds at different redshifts, we analyse the mass-weighted probability density functions (PDFs) of their temperature, T, and particle number density, n (Fig. 4.6). Each cloud exhibits a clear double-peaked density PDF. The peak at $\sim 10\,\mathrm{cm}^{-3}$ is at the density of the initial, purely atomic clouds, again highlighting that these clouds are *not* fully-evolved molecular clouds. The second peak, at $\sim 200\,\mathrm{cm}^{-3}$, represents the bulk of the molecular gas. Fig. 4.6 also shows that a small fraction of material in each cloud is at temperatures lower than that of the CMB, as discussed in Section 4.3.3. This is likely to be due to a combination of the fact that the CMB temperature is not included in our treatment of the CO rotational cooling and the effects of adiabatic cooling.

The CMB clearly affects the temperature and density structures of the clouds. As expected, the miminim ISM temperature is regulated by the CMB, increasing with redshift. The amount of gas at $\sim 200\,\mathrm{cm}^{-3}$ also increases with redshift. However, the increase in minimum temperature and sound speed of the gas leads to a deficit of well-shielded gas at $> 10^3\,\mathrm{cm}^{-3}$ (in Fig. 4.6). Thus, as predicted, the increasing CMB temperature reduces the width of the density PDF. Because the fraction of very high density gas decreases with redshift, the clouds become larger and the column density ratio of neutral carbon vs CO increases from $\langle N_\mathrm{C}\rangle\,/\,\langle N_\mathrm{CO}\rangle = 9.4$ to 13.5. The total column density of neutral carbon closely follows that of H_2, spanning $\langle N_\mathrm{C}\rangle\,/\,\langle N_{\mathrm{H}_2}\rangle = (3.02-3.11)\times10^{-4}$ whereas the ratio between the CO and H_2 column densities spans $\langle N_\mathrm{CO}\rangle\,/\,\langle N_{\mathrm{H}_2}\rangle = (2.2-3.3)\times10^{-5}$.

4.3.3 Comparing the Spatially-Integrated Line Emission

Our aim was to quantify the impact of the CMB on spatially-integrated line emission. To this end, we determine the total line fluxes of the clouds from the moment 0 maps produced via POLARIS as follows. First, we convert from units of Jy km s^{-1} pix^{-1} to Jy km s^{-1} sr^{-1}, dividing by the solid angle subtended by each pixel of 0.1 pc^2 for the detector distance of 5000 pc. We then calculate the

line flux from the total intensity of the moment 0 map $\Sigma I_{i,j}$ following eq. (30) of da Cunha et al. (2013a),

$$S_\nu \Delta v = \frac{\Omega_{i,j}}{(1+z)^3} \Sigma I_{i,j} \,. \tag{4.4}$$

where i, j are the pixels in the map and $\Omega_{i,j}$ is the solid angle per 0.1 pc^2 pixel at the distance of the cloud (taking into account the redshift), given by

$$\Omega_{i,j} = \frac{(1+z)^4 \, 0.1^2}{d_L^2} \,. \tag{4.5}$$

Measuring the lines fluxes in this way, from the moment 0 maps created without including the contrast against the CMB, provides estimates of the *intrinsic* line flux, $S_\nu \Delta v^{[\mathrm{intrinsic}]}$. For each transition from each simulated cloud, we estimate two intrinsic line fluxes: (1) measured from the moment 0 map produced by accounting for the change in cloud composition with increasing redshift but *not* accounting for the CMB's impact on the level populations (left-most panels of Fig. 4.3 and 4.4) and (2) measured from the moment 0 map produced by accounting for the CMB's impact on the cloud composition and level populations (middle panels of Fig. 4.3 and 4.4).

Using our synthetic observations, we can directly compare the measured vs. CMB fluxes over the area of the source. However, real observations are only sensitive to the *contrast* of the line against the CMB. Following da Cunha et al. (2013a), we calculate the contrast against the CMB, $S_\nu \Delta v^{[\mathrm{obs\ against\ CMB}]}$, by calculating the total line flux measured from the moment 0 maps produced when including the CMB as a background (the right-most panels of Fig. 4.3 and 4.4) and then subtracting the flux of the CMB integrated over the same velocity range of $\Delta v = 10\,\mathrm{km\,s^{-1}}$,

$$S_\nu \Delta v^{[\mathrm{obs.\ against\ CMB}]} = S_\nu \Delta v^{[\mathrm{obs.\ with\ CMB}]} - \Omega B_\nu \left[T_{\mathrm{CMB}}^{z=0} \right] \Delta v \tag{4.6}$$

where the observed frame CMB intensity that is relevant here is related to the rest-frame CMB intensity via,

$$B_\nu \left[T_{\mathrm{CMB}}^{z=0} \right] = \frac{B_\nu \left[T_{\mathrm{CMB}}(z) \right]}{(1+z)^3} \,. \tag{4.7}$$

This line flux contrast represents what would be measured with a velocity resolution of 10 km s^{-1}, without accounting for the effects of noise.

In Fig. 4.7, we compare the velocity-integrated values of the intrinsic line fluxes (filled circles) and those measured against the CMB (grey squares), from $z = 0 - 7$. In all cases the intrinsic line fluxes become fainter with redshift, simply because the clouds are measured at a greater distance, even if the emission observed at 5000 pc from the cloud shown in Figures 4.3 and 4.4 increases. The left upper panel, depicting the integrated CO(1-0), again highlights the absorption of CO(1-0) beyond $z \sim 2$ due to the gas temperatures being lower than $T_{\mathrm{CMB}}(z)$. However, even without this issue we would expect the impact of the CMB to start becoming more apparent at $z > 2$, at which point the CMB temperature begins to exceed the temperature corresponding to the $J = 1$ energy level (5.53 K)

Comparing the different transitions of CO in the top row highlights the effects of line boosting on the relative level populations. As the CMB temperature increases, the intrinsic CO(1-0) line flux measured with the CMB contribution to the line boosting included becomes fainter than that measured without (turquoise vs orange filled circles). In contrast, the intrinsic line emission of the CO $J = 2 - 1$ and $J = 3 - 2$ increases significantly, with the difference between the two "intrinsic" fluxes at $z = 7$ being almost an order of magnitude for the CO(3-2) emission. However, this additional line boosting is not enough to make up for the high flux density of the CMB at the frequency of the higher J transitions. Despite the intrinsic line flux of the CO(3-2) emission being a factor of

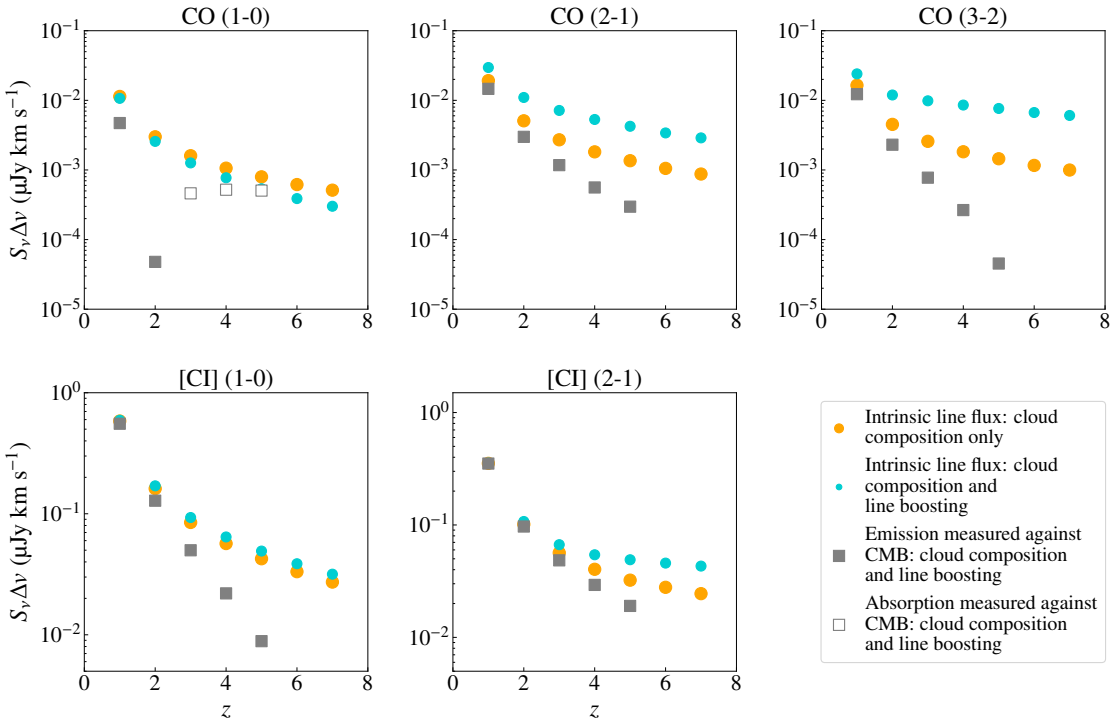

Figure 4.7: Velocity-integrated CO and [C I] line fluxes of the simulated clouds as a function of redshift. Each panel depicts three sets of values, separating the main effects of the CMB as labelled in the legend at the bottom right.

a few brighter than that of CO(2-1), the actual line flux that would be observed against the CMB is significantly lower. This is because the flux density of the CMB (over the solid angle subtended by the cloud) is higher at the observed frequency of CO(3-2) and decreases less with redshift than at the frequency of CO(2-1), i.e. from $z = 2 \rightarrow 7$ the flux density of the CMB at the observed frequency of CO(2-1) decreases from 0.196 to 0.114 μJy, whereas for CO(3-2) it decreases from 0.286 to 0.244 μJy. Thus, even the $J > 1$ lines, which are boosted by the CMB, would not be visible for this cloud beyond $z > 2$.

As for the $J > 1$ CO lines, the [C I] lines are boosted by the CMB. However, the intensity of the CMB differs significantly for the two lines. At $z = 2$ the CMB is brighter at the observed frequency of [C I](1-0) than [C I](2-1), yet at $z = 5$ the situation is reversed. This leads to the more rapidly declining CMB contrast for [C I](1-0). Conversely, the intrinsic [C I](1-0) emission is brighter than the [C I](2-1) emission at low redshift but not at high redshift. The two effects, i.e. the brighter intrinsic emission vs brighter background, balance out at $z > 5$, with neither [C I] line detected against the CMB.

4.4 DISCUSSION

4.4.1 Comparison to Results From Uniform Spherical Models

4.4.1.1 Measured vs. Intrinsic Line Fluxes

When it comes to interpreting the observed emission, what matters is how bright the measured line is relative to the intrinsic value, *i.e. what correction must be applied to the measured line flux contrast before inferring physical properties assuming the intrinsic flux?* This can be quantified by

the ratio between the velocity-integrated line flux observed against the CMB and intrinsic velocity-integrated line flux, i.e.

$$\frac{1}{\text{correction}} = \frac{S_\nu \Delta v^{[\text{obs. against CMB}]}}{S_\nu \Delta v^{[\text{intrinsic}]}} \tag{4.8}$$

We show the ratios obtained for the clouds simulated here in Fig. 4.8. Although we draw comparisons with studies based on simpler models, we remind the reader to bear in mind the two caveats highlighted in red above.

To describe the difference between our results, which are based on simulations, and those based on the modelling of uniform spheres of gas, we compare our results with those presented in da Cunha et al. (2013a), which we show again here in Fig. 4.9. We highlight their results for two different models: (left column) based on the assumption that the gas is in LTE and (right column) based on one of their non-LTE models. As described in the Introduction of this Chapter, these non-LTE models assume that the molecular gas is contained in a uniform expanding sphere, with a set H_2 number density and kinetic temperature. Since most of the H_2 in our simulations is at densities of $\lesssim 10^{3.4}$ cm^{-3}, we compare our results to their low-density model at $n_{H_2} = 10^{3.2}$ cm^{-3}. Their definition of $S_\nu \Delta v^{[\text{intrinsic}]}$ is the intrinsic emission of the cloud at $z = 0$ cloud, i.e. *not* accounting for the impact of the CMB on the level populations. Thus, the solid lines in Fig. 4.8 and in those from da Cunha et al. (2013a) (Fig. 4.9) are directly comparable.

Two quantities regulate the contrast between the CMB and CO emission (the nominator in Eq. (4.6)), the excitation temperature, T_{ex}, of the line and the line optical depth, τ_ν. This is evident from the fact that the velocity-integrated flux of the line against the CMB is given by,

$$S_\nu \Delta v^{[\text{obs. against CMB}]} = \frac{\Omega}{(1+z)^3} \left[1 - \exp\left(-\tau_\nu^{J_u}\right)\right] \left(B_\nu \left[T_{\text{ex}}^{J_u}\right] - B_\nu \left[T_{\text{CMB}}(z)\right]\right) \tag{4.9}$$

where $\tau_\nu^{J_u}$ is the optical depth of the line, J_u is the upper rotational quantum number of the CO transition and β is the escape probability, as in Eq. (4.2) (see also Eq. 31 of da Cunha et al., 2013a). The most important quantity regulating the line flux contrast is $T_{\text{ex}}^{J_u}$. By comparing our results to those of da Cunha et al. (2013a), it is apparent that the excitation temperatures vary differently with J in our simulated clouds than in these models, i.e. the impact of the CMB on the "line boosting" differs.

The non-LTE models of da Cunha et al. (2013a) (right column, Fig. 4.9) predict that as J increases, the contrast of the line flux against the CMB decreases more rapidly with redshift. This behaviour most likely results from the fact that their non-LTE model assumes that the gas is isothermal. For isothermal gas, the excitation temperature, T_{ex} is equivalent to the kinetic temperature, T_{kin} of the gas for transitions with critical densities that are lower than the gas density, whereas for transitions with higher critical densities, T_{ex} decreases with increasing J. Thus, the CMB has a greater effect with increasing J. This effect is not apparent in the LTE models of da Cunha et al. (2013a), since $T_{\text{ex}} = T_{\text{kin}}$ by construction for all transitions.

The gas in our simulated clouds is neither isothermal nor in LTE. In these clouds, the local gas density and temperature regulate both T_{ex} and the optical depth contribution of each parcel of gas along the line of sight. For optically-thick transitions, the integrated intensity of the emission from the cloud will be most sensitive to the conditions close to the surface where the optical depth $\tau_\nu \sim 1$, and thus they may be characterised by the value of T_{ex} of the gas when it approximates $\tau_\nu \sim 1$. Since the location of the $\tau_\nu \sim 1$ surface changes with each transition in these simulated clouds, the excitation temperatures vary in a different way to either the LTE or non-LTE models of da Cunha et al. (2013a). Our simulations contain a high fraction of cold CO in low-density gas, which will have a low optical depth in the $J = 2-1$ and $3-2$ transitions because these levels have small populations at low density. Thus, the $\tau \sim 1$ surface may lie in the cold, low-density gas for the $J = 1-0$ transition whereas it likely lies in warmer, denser gas in the $J = 2-1$ and $3-2$ transitions. This would result in

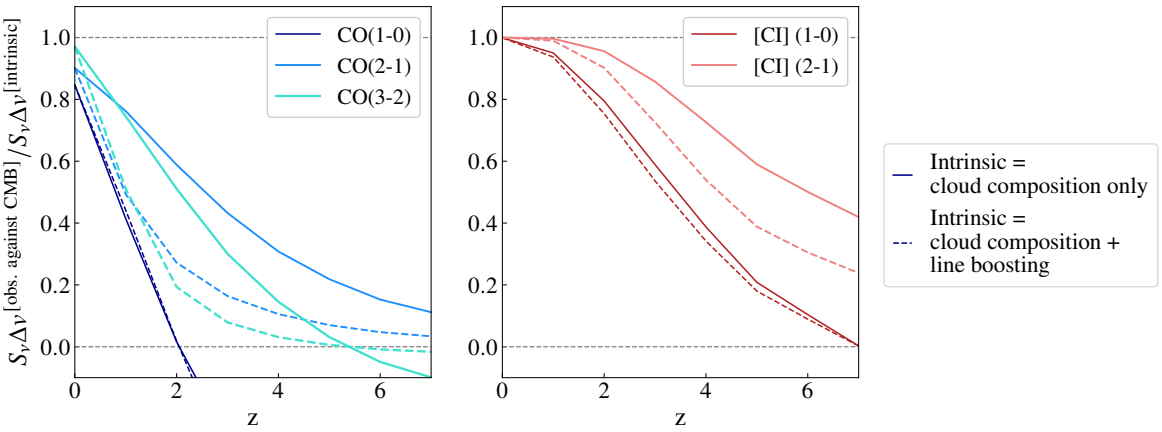

Figure 4.8: The ratio between the velocity-integrated line flux observed against the CMB and intrinsic velocity-integrated line flux of the simulated clouds as a function of redshift. We separate the effect of the CMB on the cloud composition and increase in the level populations by comparing two values of $S_\nu^{\text{[intrinsic]}}$ for each line (labelled at right) (1) considering only the effect of the CMB on the cloud structure, and (2) also including the impact of the increasing T_{CMB} on the level populations. The nominator $S_\nu \Delta v^{\text{[obs. against CMB]}}$ accounts for the CMB's impact on both the cloud composition and level populations. **Left:** Impact on the main CO lines used to trace the bulk of the cold molecular gas. **Right:** The impact on the [C I] emission.

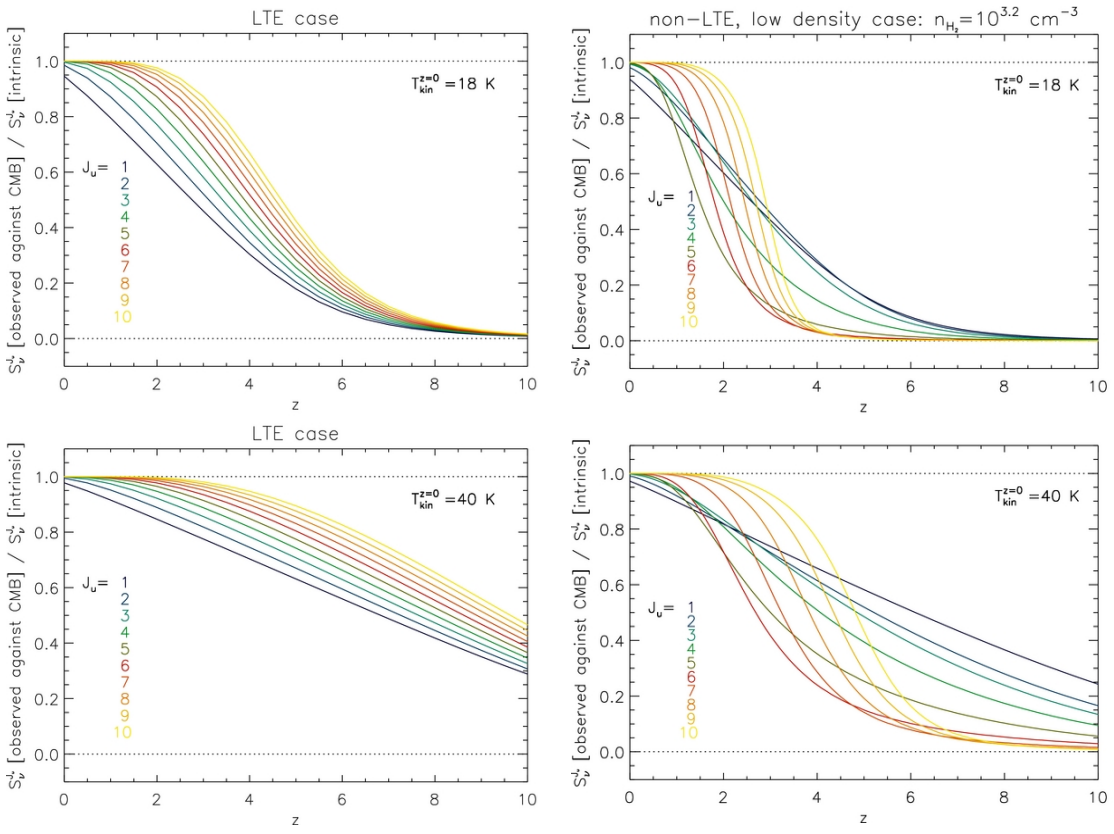

Figure 4.9: The ratio between the velocity-integrated line flux observed against the CMB and intrinsic velocity-integrated line flux for some of the model scenarios investigated in da Cunha et al. (2013a). **Left column:** Results based on models of gas in LTE. **Right column:** Results based on models of spherical, virialised and isothermal gas clouds in non-LTE, with $n_{\text{H}_2} = 10^{3.2}$ cm^{-3}. *(Taken from Figures 6 and 10 of da Cunha et al. (2013a))*

the $J = 2-1$ and $3-2$ transitions having higher excitation temperatures than the $J = 1-0$ transition, explaining why their contrasts against the CMB fall off less rapidly with redshift. In contrast, in the da Cunha et al. (2013a) models, the excitation temperature either decreases with increasing J (in their non-LTE models) or remains constant (in their LTE) models. This clear difference in behaviour demonstrates the importance for properly accounting for the density and temperature structure of the cloud when comparing the behaviour of the different transitions.

4.4.1.2 Line Luminosity to Molecular Gas Mass Conversion Factors

An important question for studies of the molecular gas content of high-redshift galaxies is by how much the CMB affects the conversion between the line luminosities and the molecular gas mass. As highlighted in the introduction, the conversion between the CO(1-0) line luminosity and molecular gas mass, $\alpha_{\rm CO(1-0)}$ depends on a range of physical properties including the strength of the ISRF, gas-phase metallicity, and, gas temperature and density. As highlighted here, the temperature and density are affected by the increase in CMB temperature with redshift. However, most observational studies, at least up to $z \sim 4$, do not correct for the CMB's impact. Instead, it is still typical to assume a Milky-Way like $\alpha_{\rm CO(1-0)}$ conversion factor for massive main-sequence galaxies up to $z \sim 4$, based on the argument that these have approximately solar metallicities. Indeed, this assumption underpins a large fraction of the measurements of the evolution of the cosmic star formation rate density, shown in Fig. 1.9.

To highlight one example, the CO observations from ASPECS are converted to molecular gas masses by assuming a Milky-Way like value of $\alpha_{\rm CO(1-0)} = 3.6\,{\rm M}_\odot\,({\rm K\,km\,s^{-1}\,pc^2})^{-1}$ (Decarli et al., 2020). Using the LTE formalism of da Cunha et al. (2013a), Decarli et al. (2020) test the possible effect of the CMB on the measured line fluxes, assuming that $T_{\rm ex} = T_{\rm kin}$ and adopting two intrinsic $z = 0$ values of $T_{\rm kin} = 20$, 40 K. Based on this, they argue that the correction for any of the observed CO lines remains at $< 20\%$ up to $z \lesssim 4$, at least for $T_{\rm kin} > 40$ K and thus they apply no correction for the CMB. However, the molecular gas is unlikely to be in LTE, nor is it at a uniform temperature.

Our aim in this study, was to account for realistic turbulence-regulated temperature and density structures, quantifying the change in the line luminosity to $\rm M_{mol}$ conversion factors with via simulations of realistic GMCs. As already highlighted, our clouds are not representative of local or high-reshifts GMCs. However, we test our analysis by quantifying the CMB's impact on the conversion factors derived for these clouds. We calculate the conversion factors via,

$$\alpha_{\rm C*} = \frac{M_{\rm mol}}{L'_{\rm C*}}, \tag{4.10}$$

where $C*$ denotes either CO(1-0) or [C I](1-0). Using Eq. (2.1), in Chapter 2, we calculate the line luminosities form the velocity-integrated line fluxes (described above). We determine the molecular gas mass of the cloud via Eq. (A.4) in Appendix A.3, multiplying by 1.36 to account for the contribution of helium. As in the previous analysis, we separate the effects on the cloud composition, increase in high-excitation level populations ("line boosting"), and contrast against the CMB by computing the line luminosities from the intrinsic line fluxes and line flux observed against the CMB.

The conversion factors calculated for our simulated clouds are shown in Fig. 4.10. Whereas the CMB's impact on the cloud composition serves to increase $\alpha_{\rm CO}$, the increase in high-excitation level populations has the opposite effect. These combined effects, however, are dwarfed by the issue of the contrast against the CMB for the simulated clouds at $z > 0$. The contrast of the CO(1-0) line against the CMB decreases sharply up to $z = 2$ for CO(1-0), as shown in Fig. 4.7, beyond which we mistakenly observe CO(1-0) in absorption. Since the clouds contain a greater amount of C I than CO, most of which is at temperaures $> T_{\rm CMB}$, the effect on $\alpha_{\rm [CI]}$, shown in Fig. 4.10, is more realistic. In this case, the line boosting effect of the CMB leads to higher intrinsic luminosities than at $z = 0$ (as discussed in Section 4.3.3) and thus leads to a decrease in the conversion factors with

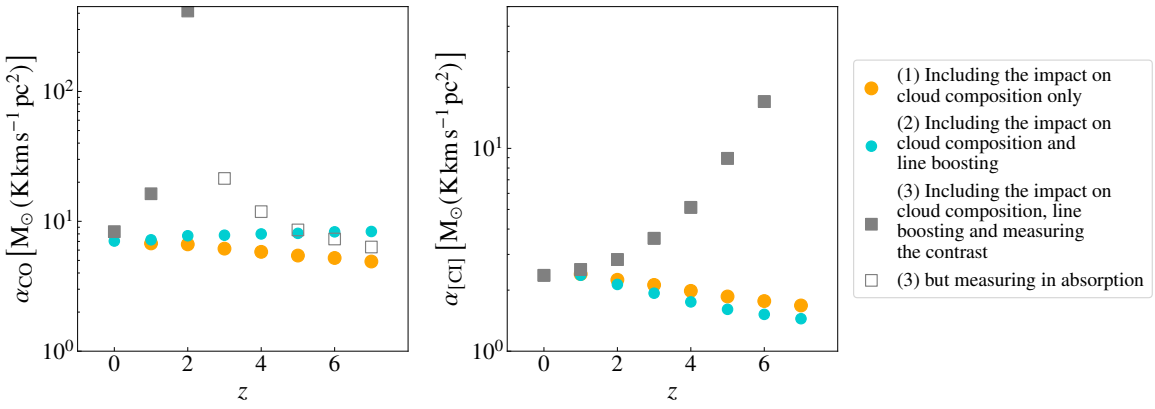

Figure 4.10: Variation of the CO(1-0) (left) and [C I](1-0) line luminosity-to-molecular gas mass conversion factors. The three main effects of the CMB are separated as labelled legend on the right.

redshift. However, the effect on the line boosting is again dwarfed by the challenge of measuring the emission against the CMB beyond $z \sim 2$.

The lack of contrast against the CMB is more severe in our study than in the studies of da Cunha et al. (2013b), Zhang et al. (2016), and Tunnard and Greve (2016) due to a combination of factors, the most important of which is the low abundance of CO in our simulated clouds. This leads to a much sharper rise in α_{CO} for our simulated clouds. Although da Cunha et al. (2013b) do not quantify how much α_{CO} is expected to vary, their computed corrections imply the following. For their models shown Fig. 4.9 the ratio between the observed and intrinsic CO(1-0) flux at $z \sim 4$ is between,

$$\frac{S_\nu \Delta v^{[\text{obs. against CMB}]}}{S_\nu \Delta v^{[\text{intrinsic}]}} = 0.3 - 0.7\,. \tag{4.11}$$

Since the line flux and line luminosity are linearly correlated, this implies that the conversion factor at $z \sim 4$ is a factor of,

$$\frac{\alpha_{CO}^{[\text{obs. against CMB}]}}{\alpha_{CO}^{[\text{intrinsic}]}} = 1.4 - 3.3 \tag{4.12}$$

higher than the local value.

Whereas da Cunha et al. (2013b) model the impact of the CMB using single lines of sight, our numerical tests are based on the assumption that much of the emission from distant galaxies stems from GMCs. In reality, galaxies contain many molecular clouds, with different properties. Tunnard and Greve (2016) attempt to account for this via a toy galaxy model with a temperature profile that falls as the inverse of the galaxy radius. They sample this profile with 10^4 molecular clouds following an exponential distribution and integrate the total emission from all clouds in the galaxy to investigate the CO excitation ladder and $\alpha_{CO(1-0)}$ conversion factor. Under these assumptions, that find that $\alpha_{CO(1-0)}$ must increase from the local value by a factor of $\sim 1.2, 1.6$ and 3.9 at $z = 2, 4$ and 8 respectively (see their Fig. 7). As in our simulations, this increase in $\alpha_{CO(1-0)}$ is driven mainly by the lack of contrast against the CMB with the line boosting playing a negligible role.

4.4.1.3 The Advantage of Atomic Carbon at Higher Redshifts

One of our aims with this study was to test whether atomic carbon would become a more easily observed tracer of the molecular gas at higher redshift than $J < 4$ CO emission, as implied by the

work of Zhang et al. (2016). In their study, they created synthetic maps of the emission from a local galaxy, NGC 628, by redshifting the emission observed at $z = 0$ using the same non-LTE, LVG radiative transfer modelling as da Cunha et al. (2013b), assuming a H_2 number density of 10^3 cm^{-3}. Their results illustrated that beyond $z \sim 4$, the [C I] lines maintain a stronger contrast against the CMB than the $J < 4$ CO lines because of the higher frequencies (see their Fig. 6) and may therefore be more viable molecular gas tracers at these redshifts.

The high C I-to-CO ratios of our simulated clouds make it difficult to draw any conclusions for real observations. However, for these clouds, we do find that a greater fraction of the intrinsic [C I](2-1) emission is recovered up to $z = 7$ than for any of the CO lines. A similar fraction of the intrinsic emission appears to be recovered up to $z \sim 4$ for the CO(3-2) and [C I](1-0) lines, although unlike the CO(3-2) emission, the [C I](1-0) can still be detected up to $z \sim 5$. The [C I](1-0) emission of our clouds also increases due to the line boosting effect, unlike the CO(1-0) emission, making a small, positive contribution to the change on $\alpha_{[CI]}$ with redshift.

4.4.2 The Effects of Galaxy Properties vs the CMB

Even if the molecular clouds simulated here had been identical to real molecular clouds at these redshifts, the *absolute* values of the derived conversion factors and line ratios could not be compared to the observed, spatially-integrated emission from high-redshift galaxies, for the following reasons.

Higher star formation rates: High-redshift galaxies have higher star formation rates (SFRs) and SFR surface densities, Σ_{SFR} than local galaxies. This affects the molecular ISM in multiple ways, increasing the ISRF strength, CRIR and also the gas densities, temperatures and line optical depths (e.g. Clark and Glover, 2015; Narayanan and Krumholz, 2014). Our simulations do not account for these effects, with the gas in all of our simulated clouds irradiated by a local ISRF and CRIR. However, the strength of the ISRF and CRIR are particularly relevant for determining the CO and [C I] excitation. Based on the numerical simulations of molecular clouds, Peñaloza et al. (2017), 2018 find that the CO(3-2)-to-CO(1-0) and CO(2-1)-to-CO(1-0) line luminosity ratios increase by up to 50% when the ISRF is increased from $1 - 100\,G_0$. The effects of star-formation regulated properties on CO excitation have also been studied by Narayanan and Krumholz (2014) using numerical simulations of high-redshift galaxies, for which they inferred the physical and chemical properties of the molecular ISM via a post-processing step. In particular, Narayanan and Krumholz (2014) investigated how the CO excitation ladders vary with Σ_{SFR}, finding that the strength of the $J > 1$ CO lines increase relative to CO(1-0) with Σ_{SFR}. They also briefly test the impact of the CMB, concluding that the CO excitation of galaxies with high Σ_{SFR} will only be marginally affected by the warmer CMB whereas for galaxies with low Σ_{SFR}, they conclude that the warmer CMB will lead to a significant increase in the CO excitation, as found for our simulated clouds. However, Narayanan and Krumholz (2014) do not predict whether the CO emission for any Σ_{SFR} would still be observed against the CMB. Thus, the combined effects of a higher Σ_{SFR} and warmer CMB have yet to be quantified.

Lower metallicities: We have enforced that the gas in all of our simulated clouds, from $z = 0 - 7$, is at solar metallicity. Yet the global metallicity of galaxies decreases with redshift. As the metallicity decreases, so too does the dust-to-gas ratio, although by exactly how much is yet unclear. With the associated reduced dust column, the shielding of CO decreases, leading to a drop in the CO column density and line luminosity for a given column of H_2 (e.g. Bell et al., 2006; Shetty et al., 2011; Feldmann et al., 2012a). At metallicities below $\sim 1/2$ the solar value the α_{CO} conversion factor increases sharply. While such low metallicities are not expected in massive star-forming galaxies at $z = 2 - 4$ (e.g. Zahid et al., 2014a), they may become more prevalent at higher redshifts.

Thus, the decreasing metallicity would only further compound the issue of the decreasing contrast against the CMB with redshift.

Averaging over cloud ensembles: Real galaxies contain ensembles of molecular clouds of different sizes and masses as well as some fraction of diffuse molecular gas. Each cloud and region of diffuse gas is exposed to different ISRFs and CRIRs, depending e.g. on the local star formation rate density. The integrated emission of these combined regions is what is observed in practice. GMCs are by far the most luminous in terms of their CO and [C I] emission and thus, to first order, the global emission will be regulated by the properties of these GMCs. The results of this Chapter already show that it is unlikely that diffuse gas or small clouds will observed against the CMB. However, is still unclear how potential variations in the cloud mass distribution will impact the galaxy-integrated emission.

For the numerical tests presented here, we removed these additional complications, assuming that the dominant component of the emission from the molecular ISM stems from molecular clouds at all redshifts and tested *only* the effects of the CMB on the line emission. To quantify the CMB's impact relative to that of the increasing star formation rate density, decreasing metallicity and variations in mass distribution of clouds with redshift will require a larger parameter study. But first, we need to refine the numerical tests attempted here.

4.4.3 Summary of Results

The results presented in this chapter suggest that the reduction in the contrast against the CMB has a larger impact on the observed CO and [C I] lines than either the CMB-driven change in structure of the cloud or the boosting of the level populations. But just how dominant this effect may be is not clear from the simulations performed here due to two issues uncovered in the late stages of this thesis. (1) the clouds that we have simulated are less dense (and less massive) than the types of structures from which we expect most of the CO and [C I] emission to stem (both at low and high redshift). This leads to less CO relative to neutral carbon for all clouds, resulting in fainter than expected CO emission. (2) The CO is at lower temperatures than the CMB in the densest regions of the simulated clouds because the CMB was not accounted for in our treatment of the CO rotational cooling. Thus, the CO(1-0) emission, which stems from the coldest regions of the clouds, is mapped in absorption at $z > 2$, rather than simply being "drowned out" by the emission of the CMB as expected. The same effect is not seen for the $J > 1$ CO lines, or [C I], lines as these stem from warmer regions on average than the CO(1-0) emission.

To achieve the goals of this study we are now making two alterations to the simulations. Firstly, we will simulate more massive molecular clouds, that reach the densities that we would expect most of the CO emission from distant galaxies to stem from. For this, we will test whether it is possible to simulate clouds of $10^6\,M_\odot$via the single-cloud setup of Glover et al. (2015) and Glover and Clark (2016). The second main modification, which has now been implmented, is to account for the CO rotational cooling in the Gong et al. (2017) chemistry network used in AREPO. However, these simulations are time-consuming to set up, perform and test. Thus, I will not end this chapter with a concise summary of findings as in the previous chapter, but will instead ask the reader to please stay tuned.

ACKNOWLEDGEMENTS

Signifiant contributions were made by coauthors via the development and testing of the code used herein and for the overview of all the physics involved. In particular:

- Simon Glover and Fabian Walter developed the idea for this study,
- Simon Glover provided guidance and physical insights throughout,
- Stefan Reißl added the CMB background radiation in POLARIS
- Paul Clark created and shared the initial conditions needed to run the simulations herein.

5

CONCLUSIONS

What's done is done.
Yet, with this thesis closing,
news doors open.

5.1 SUMMARY

This thesis capitalised on the opportunities provided by the Atacama Large Millimeter/submillimeter Array (ALMA). With its high sensitivity and resolution, ALMA has been revealing the emission from the molecular interstellar medium (ISM) of distant galaxies, thereby providing insights into the amount, distribution and properties of the gas out of which most of the stars in today's Universe formed. Yet, many assumptions need to be made in order to convert these observations into the quantities that astronomers are aiming to measure. With this thesis I tested the underlying assumptions, thereby helping to interpret current and future observations of the molecular ISM in distant galaxies.

In **Chapter 2** I investigated the reliability of 1 mm dust-continuum emission as a molecular gas tracer at $z \sim 2$. In particular, I tested an empirical calibration between the rest-frame 850 µm continuum emission (which 1 mm dust-continuum observations are converted to) and CO(1-0) luminosities (Scoville et al., 2016). This calibration was mostly based on observations of massive local galaxies and subsequently applied to measure the molecular gas masses of hundreds of $z > 1$ galaxies. However, the method had not yet been tested on these same galaxies. To this end, I analysed a unique sample of 1 mm-bright galaxies, with observations of CO(1-0) emission obtained via a large time investment with the Karl G. Jansky Very Large Array (VLA) (PI: Walter). By performing a detailed comparison of the dust and CO(1-0) derived molecular gas masses, I showed that this 1 mm calibration provided the same level of accuracy as CO(1-0) observations for massive $> 2 \times 10^{10}\,M_\odot$ star-forming galaxies at $z \sim 2$. However, this study left some open questions. *What are the average dust temperatures and dust emissivity indices of $z > 1$ galaxies? At what stellar mass and metallicity are the assumed gas-to-dust ratios no longer valid?* These questions will be addressed by combining observations at 1 mm with a fully-sampled dust spectral energy distribution (SED)s and observations of ionised gas tracers, with which the gas-phase metallicity can be diagnosed.

In **Chapter 3** I zoomed in on the molecular ISM of three $z \sim 2$ star-forming galaxies selected from the *Hubble* Ultra Deep Field (with which I opened this thesis). Over the last few years, *Hubble*'s view of this small patch of sky was complemented by the ALMA Spectroscopic Survey in the Hubble Ultra Deep Field (ASPECS). Yet, ASPECS was not designed to resolve individual galaxies. To test how dust and molecular gas were distributed in galaxies at the peak epoch of star formation, the three most extended main-sequence galaxies were selected for follow-up resolved CO observations with ALMA (PI: Walter). I analysed the distribution of the molecular gas using these CO observations in addition to the ASPECS data. To obtain matched-resolution maps

of the 1.3 mm dust-continuum emission, I combined the data from ASPECS and the survey of Dunlop et al. (2017). In addition, I used the archival *Hubble* imaging to trace the stellar emission. Using these data, I measured the half-light radii of the stellar, dust and CO emission. I found that the detected CO and dust emission were more centrally-concentrated than the stellar emission, hinting at the presence of dense, centrally-concentrated molecular ISM reservoirs, akin to those of local nuclear starbursts. For two of the galaxies, the 1.3 mm dust-continuum emission was more compact than the CO emission, indicating that long-wavelength dust-continuum emission is highly sensitive to the heating by star formation in addition to the dust column. By modelling the CO kinematics, I also showed that the gas motion in these galaxies is rotation-dominated, in contrast to what is typically found based on observations of the ionised gas in $z \sim 2$ star-forming galaxies. Despite large time investments with ALMA, the combined sensitivity and resolution of the CO and dust observations were too poor to detect regions of gas with the column densities typical of local spiral arms. Thus, significant additional time investments with ALMA (i.e. a tenfold in the integration time compared to these observations) are still required to observe the extended gas and dust disks of high-redshift galaxies.

In **Chapter 4** I delved into the molecular ISM in more detail, simulating molecular clouds from $z \sim 0-7$ in order to study the impact of the CMB on the CO and [C I] line emission of distant galaxies. To predict what would be observed of these molecular clouds against the increasingly warm CMB we post-processed the simulations with the radiative transfer code POLARIS. Unfortunately, the simulations did not result in the types of giant molecular clouds (GMCs) we set out to study, with most of the gas at lower densities than in real GMCs. I therefore presented an initial, proof-of-concept study with these simulations, analysing how the increase in the temperature of the Cosmic Microwave Background (CMB) with redshift affects the emission due to three effects: (1) changes to the cloud structure, (2) the increase in level populations and (3) the increasing background intensity against which the lines are measured. The CMB clearly affected the structure of the molecular ISM, altering the relative amount of CO and neutral carbon. However, at least for these clouds, the background emission of the CMB is a more important effect than the either change in composition of the cloud or the boosting of the level populations. This study will now be performed with more realistic simulations of massive ($> 10^5$ $M_\odot$) and higher-density molecular clouds.

5.2 FUTURE OUTLOOK

The studies conducted as part of this thesis paved the way for future studies of the molecular ISM, posing new questions and highlighting the limits of existing observations. To conclude, I will summarise some of the most fundamental questions that remain open and how these can be addressed with state-of-the art modelling tools and observational facilities.

5.2.1 The Distribution and Kinematics of Molecular Gas

One of the major science goals driving the development of ALMA has been to map the distribution of molecular gas in $z > 1$ galaxies. Yet, despite ALMA having been in operation for almost a decade, the resolution of molecular gas observations at $z > 1$, including those analysed in Chapter 3, remains significantly poorer than that of the stellar emission. Thus, many key questions remain unanswered, including: *What were the main sites of star formation in galaxies at the peak epoch of star formation; nuclear starbursts, kpc-sized clumps, or spiral arms and bars, as seen locally? And, what was the temperature, density and kinetic energy content of the gas out of which stars were forming?*

Answering these key questions requires high-resolution observations of the emission from components of the molecular ISM that scale directly with the total molecular gas column. As high-

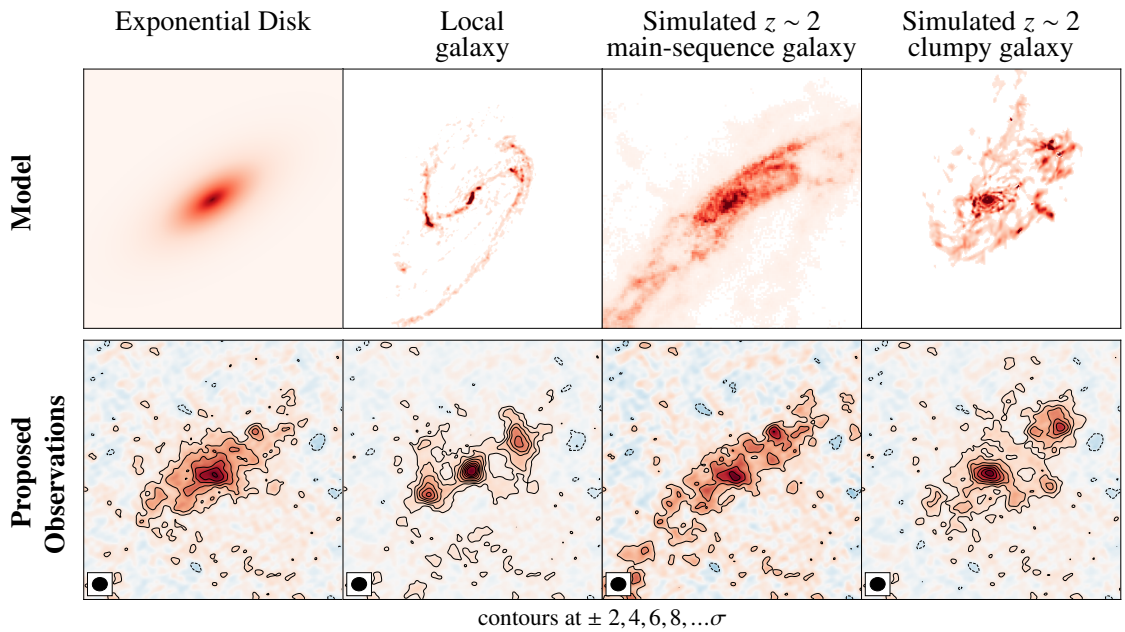

Figure 5.1: Input model galaxies (top row) and simulated CO(2-1) moment 0 maps (bottom row), assuming an intergration time of 26 hours in the C43-8 configuration in addition to the C43-5 observations presented in Chapter 3. The addition of the C43-8 observations, would enable the molecular gas distribution in this $z = 1.6$ galaxy to be constrained. *(Figure produced for a Cycle 8 ALMA proposal of which I am PI.)*

lighted in Section 1.2, the most time-efficient molecular gas tracers at $z > 1$ are long-wavelength (rest-frame $300 - 800\,\mu$m) dust-continuum emission and the emission from CO transitions with rotational quantum numbers, $J > 1$. However, the results presented in Chapter 3 of this thesis, along with the prior observational studies discussed therein, indicate that dust emission does *not* directly trace the *distribution* of molecular gas. Instead, dust-continuum emission closely follows the high central star formation rates. These findings have now been further supported by simulations. By post-processing the simulated $z > 1$ main-sequence galaxies from IllustrisTNG with the radiative transfer code SKIRT, Popping et al. (2021, including MK) showed that the synthetic $850\,\mu$m continuum emission is more compact than the inferred molecular gas component, instead directly correlating with the star formation rate surface density. Thus, dust-continuum emission seems to be a poor probe of the distribution of molecular gas, particularly in the outer disk. To constrain the distribution of molecular gas at $z > 1$ will therefore require high-resolution observations of low-J CO transitions. Not only do these map the distribution of molecular gas, they will also provide crucial insights into the gas kinematics, which cannot be addressed with continuum measurements.

If high-resolution mapping of molecular gas at $z > 1$ was such an obvious science case for ALMA, why has it not yet been done? Again, we come back to the little matter of observing time. As discussed in Section 1.3, ALMA has the technical capability to resolve the low-J CO emission from galaxies at $z \sim 2$ at scales down to ~ 350 pc. But, in practice, these observations are extremely time consuming ($t_{\rm int} > 100$ h per galaxy). Thus, a compromise must be reached in terms of the sample size, selection and resolution. Over the last 10 years, heavy compromises have been made at both ends. Low-J CO emission has been "resolved" at scales of only $5-9$ kpc for a handful of $z > 1$ main-sequence galaxies, including those presented in Chapter 3. At such low resolutions it is impossible to distinguish between a clumpy or spiral/barred molecular gas structure, let alone constrain the gas velocity dispersion and probe the effects of turbulence vs self-gravity. CO emission has also been mapped at $\lesssim 1$ kpc for handful of more extreme objects, e.g. the submillimeter-bright $z \sim 4$ galaxy, GN20 (Fig. 1.10 Hodge et al., 2015) and the lensed dusty $z \sim 3$ galaxy, SDP.81 (Rybak et al., 2020). However, these galaxies are far from the norm at their respective redshifts.

Multiple scenarios have been proposed for how and where molecular gas settles in $z > 1$ galaxies, based on observations of local galaxies and simulations of high-redshift galaxies. Locally, star formation and molecular gas have been mapped down to scales of < 100 pc (e.g. Schinnerer et al., 2019b), revealing that the molecular ISM is mostly contained in spiral structures within thin disks. Yet, some local nuclear starbursts harbour large, centrally-concentrated molecular gas reservoirs (Weiß et al., 2008). Based on the results presented in Chapter 3, this "nuclear starburst" scenario may also be more typical of $z \sim 2$ star-forming galaxies. However, some observation- and simulation-based studies instead find evidence that $z \gtrsim 2$ galaxies contain giant kpc-sized gas clumps (e.g. Förster Schreiber et al., 2011; Bournaud et al., 2015; Mandelker et al., 2017; Guo et al., 2018). Yet other cosmological simulations appear to find that the gas has mostly settled into more regular thin disks by $z \sim 2$ (Pillepich et al., 2019). Although current $z > 1$ observations of molecular gas are unable to distinguish between these different scenarios, the higher gas masses measured for $z > 1$ galaxies imply that the molecular gas must either be far denser than at $z = 0$, or distributed in larger structures.

To illustrate that ALMA can (and hopefully will) be used to differentiate between the proposed molecular gas morphologies, I have created mock observations of the velocity-integrated CO(2-1) emission, assuming four different molecular gas morphologies (Figure 5.1). For this exercise, I assume that the model galaxies have the same molecular gas content as measured for ALPS.2, in Chapter 3, i.e. each model image is scaled such that the total CO(2-1) flux density matches the measured value. I then simulated the ALMA observations using CASA's SIMOBSERVE task and imaging and cleaned the observed emission as I would the real data with the TCLEAN task. I have assumed that for each resolution element of $0\farcs1$, the linewidth is spread over 100 km s^{-1}, which is the upper limit calculated from the existing CO data. Thus, the mock moment 0 maps in the bottom row represent the *worst-case* scenario. For these mock observations, I have assumed a total observation time of 26 hours in the C43-8 configuration (which has a maximum baseline of 8.5 km) in addition to the existing C43-5 observations. Supplementing the existing data with the more extended configuration observations would make it possible to distinguish between the proposed centrally-concentrated gas reservoirs, multiple large distinct "clumps" or more regular spiral/barred structures.

These velocity-integrated maps, however, only illustrate the two-dimensional information that can be extracted from resolved CO observations. With the extended-configuration CO observations, it is also possible to trace the molecular gas kinematics and thereby investigate the impact of chaotic vs ordered gas motion. Velocity dispersions of $10 - 20$ km s^{-1} are typically measured for local galaxies, based on observations of neutral hydrogen and CO (e.g. Ianjamasimanana et al., 2012; Caldú-Primo et al., 2013; Mogotsi et al., 2016; Marasco et al., 2019; Sun et al., 2020), but it is unclear to what extent this changes with the higher molecular gas fraction of galaxies at $z > 1$. Velocity dispersions have only been inferred for a handful of unlensed $z > 1$ galaxies based on CO observations, i.e. the main-sequence galaxies studied by (Bolatto et al., 2015) and the galaxies studied in Chapter 3. However, the spatial (and spectral) resolution of these observations is too poor to disentangle the chaotic motions from the inclination and scale height of the gas disk. Thus, these dispersion measurements only provide upper limits of ~ 60 km s^{-1}.

Observations of the *ionised* gas in $z \sim 2$ galaxies have yielded velocity dispersions of $\gtrsim 50$ km s^{-1} (e.g. Cresci et al., 2009; Wisnioski et al., 2011; Epinat et al., 2012; Leethochawalit et al., 2016; Harrison et al., 2017; Turner et al., 2017; Johnson et al., 2018; Mason et al., 2017; Sweet et al., 2019). However, most of these measurements are similarly affected by low resolution. Moreover, using ionised gas tracers may overestimate the intrinsic gas velocity dispersion, as ionised gas is likely to be more sensitive to energetic events, such as such as winds and outflows, than CO. These differences between ionised and molecular gas dispersions have rarely been quantified at high redshift, although in a recent study comparing the kinematics inferred from [O II] and CO for the lensed $z \sim 1$, star-forming galaxy dubbed the "Cosmic Snake", Girard et al. (2019) found evidence that the

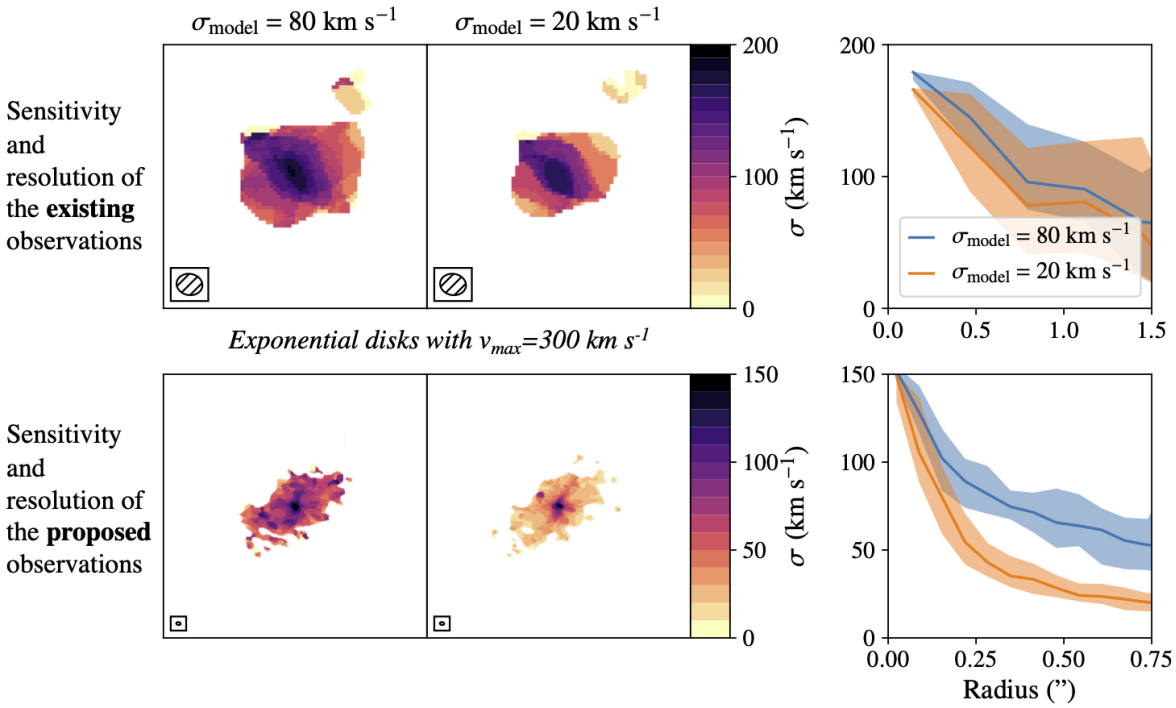

Figure 5.2: Comparison of the intensity-weighted velocity dispersion maps and radial profiles for an exponential gas disk with an intrinsic maximum rotation velocity of 300 km s^{-1} and velocity dispersions of 80 km s^{-1} vs. 20 km s^{-1}. Whereas the existing observations cannot distinguish between the two scenarios, observations taken at a resolution of 0.″1 and a sensitivity of ~ 0.05 mJy beam^{-1} per 100 km s^{-1} would. *(Figure produced for a Cycle 8 ALMA proposal of which I am PI.)*

molecular gas disk may be smaller and thinner than the ionised gas disk. Unfortunately, simulations have not helped to clear up this picture. Cosmological simulations typically predict velocity dispersions of ~ 50 – 100 km s^{-1} for the *warm* gas component of massive $z \sim 2$ galaxies (Pillepich et al., 2019), but there are no reliable predictions for the molecular gas dispersions due to the difficulty of simulating molecular gas at sufficient resolution (see Section 1.4.1).

The current observation- and simulation-based limitations pose a significant challenge for understanding the competing effects of turbulence and self-gravity in regulating star formation at $z > 1$. One of the key aims of molecular gas studies over the coming years will be to accurately measure the velocity dispersion and thereby distinguish between dense and thin gas disks and more "puffed-up" galaxies with turbulence-dominated gas. To illustrate that such observational tests can start to be conducted with ALMA, I have again used the galaxy, ALPS.2, from Chapter 3 as a test case. I have assumed that the gas is indeed distributed in an exponential disk with the CO(2-1) half-light radius and maximum rotation velocity measured from the existing observations. I then modelled this exponential CO(2-1) disk at the same resolution and signal-to-noise as the data herein for disks of two very different velocity dispersions: a low value of 20 km s^{-1}, similar to what is measured for local galaxies, and 80 km s^{-1}, the upper limit measured for ALPS.2. The mock moment-2 maps for these two scenarios are shown in the top row of Fig. 5.2, with the velocity dispersion profile predicted from these on the right. As claimed in Chapter 3, the existing observations cannot distinguish between velocity dispersions of 20 and 80 km s^{-1}. However, at a resolution of 0.″1 and a signal-to-noise ratio (S/N) of at least 3 per 20 km s^{-1} channel it *is* possible to distinguish between these two, very different, velocity dispersions, as shown in the bottom row of Fig. 5.2. These kinds of tests are now starting to be requested with ALMA, and perhaps the future reader of this thesis is already lucky enough to know the results.

Accurately interpreting future resolved molecular ISM studies at $z > 1$, will require realistic synthetic maps of the emission from the molecular ISM of entire galaxies. However, most pub-

lished galaxy simulations lack the resolution and/or molecular chemistry needed to accurately model both the molecular ISM and star formation at $z \gtrsim 2$ and thereby produce reliable comparisons. Recent advances in computing and modelling have finally made it possible to simulate entire galaxies, including the molecular chemistry. For example, Tress et al. (2020) used AREPO to simulate the molecular gas and star formation in an interacting M51-like galaxy. Their simulations reach sub-parsec resolution while tracking the non-equilibrium chemistry of the molecular ISM and self-consistently accounting for the formation of stars from this medium. Such simulations could now also be performed for isolated $z \gtrsim 2$ galaxies, the only difference compared to Tress et al. (2020) being the choice of initial conditions. For these, one could either select a galaxy from a cosmological simulation and resimulate it at the high resolution needed to follow the molecular gas, or, set up a disk with values of the halo, disk and bulge mass informed by observations and cosmological simulations.

Although such isolated-galaxy simulations are useful tests for individual galaxies, predictions of the distribution and kinematics of molecular gas in many galaxies (spanning a range of redshifts and global properties) will require combining models of H_2, either on-the-fly or in post-processing, with hydrodynamic simulations (e.g. as in Christensen et al., 2012; Kuhlen et al., 2012; Diemer et al., 2018). In order for this approach to yield accurate results, the effects of turbulence in the molecular ISM need to be accounted for. Over the last few years, a few models of H_2 have been developed that include a phenomenological description of the turbulent molecular ISM, informed by cloud-scale numerical studies and observations of local GMCs. For example, the model of Tomassetti et al. (2015), calculates the non-equilibrium abundance of molecular hydrogen from hydrodynamical simulations via two main assumptions: 1) motivated by observations of local GMCs', the sub-grid clumps follow a lognormal (mass-weighted) probability density function (PDF) and 2) the unresolved gas follows the gas temperature-density relation determined from the numerical simulations of Glover and Mac Low (2007b). In this model, the calculated local density of molecular hydrogen is then directly linked to the local star formation rate. Compared to models that only compute the equilibrium abundance of H_2, this type of non-equilibrium model better reproduces the stellar abundance and gas reservoirs of high-redshift galaxies. By combining cosmological simulations and these, more accurate H_2 models, it will become possible to make realistic predictions of the impact of the CMB on the clumpiness and distribution of molecular gas at high redshift.

5.2.2 The Temperature and Density of the Molecular ISM

Constraining the distribution and kinematics of the bulk of the cold, molecular ISM, as described above, is only part of completing our understanding of how and where stars form. To understand how star formation is regulated at $z > 1$, it is also critical to measure the gas density, gas and dust temperature and strength of the interstellar radiation field (ISRF). Based on the last decade of infrared (IR) and submillimeter observations, it is already expected that these conditions are very different in $z > 1$ star-forming galaxies than in local galaxies. For example, the combination of higher molecular gas fractions *and* smaller sizes (i.e. half-light radii) measured for $z > 1$ star-forming galaxies imply that the radiation pressure and/or molecular gas density are higher, on average, than in local star-forming galaxies. Yet, these effects are only just starting to be quantified in a galaxy-averaged sense at $z > 1$ (e.g. Harrington et al., 2021).

To probe physical conditions such as the gas density, gas and dust temperature and strength of the ISRF, requires observations of a set of gas and dust tracers. The brightest line emission typically stems from CO, thus CO rotational transitions are some of the most accessible diagnostics. The relative strengths of CO transitions are governed by multiple physical properties, especially the gas density, temperature and optical depth distributions (as described in Chapter 4). Hence, CO transitions alone cannot be used to constrain the gas temperatures. However, unlike for CO, the

two atomic carbon (C I) lines are usually optically thin, and thus the ratio of the [C I] (2-1) and [C I] (1-0) lines is particularly sensitive to the gas temperature. By jointly modelling observations of both [C I] and multiple CO transitions it is therefore possible to infer the kinetic temperature and desnity of the gas. To additionally model the dust properties (and thereby build up a complete description of the molecular ISM) requires a well-sampled dust SED, covering both the peak of the dust emission and the long-wavelength tail (e.g. Fig. 5.4). Unfortunately, obtaining high-resolution observations of the dust SEDs and CO plus [C I] excitation ladders at $z > 1$, remains out of reach, even with ALMA. Thus, there are two main options for now:

(i) only resolving a subset of the brightest CO lines and dust-continuum emission for one lensed and/or bright star-forming galaxy at a time, and,

(ii) gathering *spatially-integrated* dust-continuum, CO line and C I line observations for samples of star-forming galaxies to infer the *average* ISM conditions per galaxy.

Regarding option (i), the ratios of some mid-to-low-J CO lines are particularly sensitive to the gas density and strength of the ISRF (e.g. the CO(5-4) and CO(2-1) ratio used in Liu et al., 2021). Like the mid-J CO emission, dust-continuum emission is sensitive to the source of heating. Thus, comparing resolved maps of mid-J and/or dust continuum emission to maps of low-J emission can reveal the star formation rate surface density and existence of active galactic nuclei (AGN) in these galaxies. Indeed, brighter, more centrally-concentrated mid-J emission is observed in low-redshift galaxies with high central SFRs (Saito et al., 2017). Similarly, the heating of the ISM by AGN may enhance the emission from higher-J transitions and/or suppress the emission from CO(2-1) (Rosario et al., 2019; Kawamuro et al., 2020). Brighter high-J CO and dust emission has also been predicted for the large gas clumps that form in some simulations of $z > 1$ galaxies, as these appear to contain a significant warm and dense ISM component (Bournaud et al., 2015). Other simulations indicate that, at least for main-sequence galaxies, this warm and dense component is mainly confined to the highly star-forming centres (Popping et al., 2021). Higher resolution comparisons are therefore needed to test whether the putative nuclear or clumpy molecular gas reservoirs are warmer and/or denser than the rest of the molecular ISM.

Option (ii) will be critical to measure the molecular ISM conditions for samples large enough to perform statistical studies linking the gas depletion times, specific star formations rates, and galaxy sizes to the average temperature and density of the molecular gas. For these studies, it will be crucial to have a theoretical framework that can account for the fact that the molecular gas is turbulent and not in local thermodynamic equilibrium (LTE). Recently, non-LTE, radiative transfer models have been developed, which self-consistently account for the emission from dust as well as the main observable molecular and atomic chemical species within the turbulent molecular ISM (Harrington et al., 2021; Liu et al., 2021). Both these turbulence-regulated models represent the integrated molecular ISM using a single gas component, described by a turbulence-driven lognormal gas density distribution. The CO and [C I] line fluxes are then modelled by solving the radiative transfer equations with the large velocity gradient (LVG) assumption for different gas volume densities, species abundances, etc. These density-PDF models enable a more accurate interpretaion of the relative line strengths and dust SEDs than the previous single- or double-component models.

Although the modelling framework is now in place, what is still missing is a sample of unlensed $z > 1$ star-forming galaxies with the full set of dust, CO and [C I] observations. One of the main limitations of existing $z > 1$ galaxy samples is the lack of CO(1-0) observations, but the sample studied in Chapter 2 is a rare exception. In November 2020, we additionally obtained high S/N CO(3-2) measurements for this sample through a 30 hour NOEMA program of which I was PI (e.g. Fig. 5.4). I will use these data to test the $L'_{CO(3-2)}/L'_{CO(1-0)}$ ratio that is typically assumed for $z \sim 2$ galaxies in order to infer molecular gas masses. This sample now presents the opportunity to efficiently

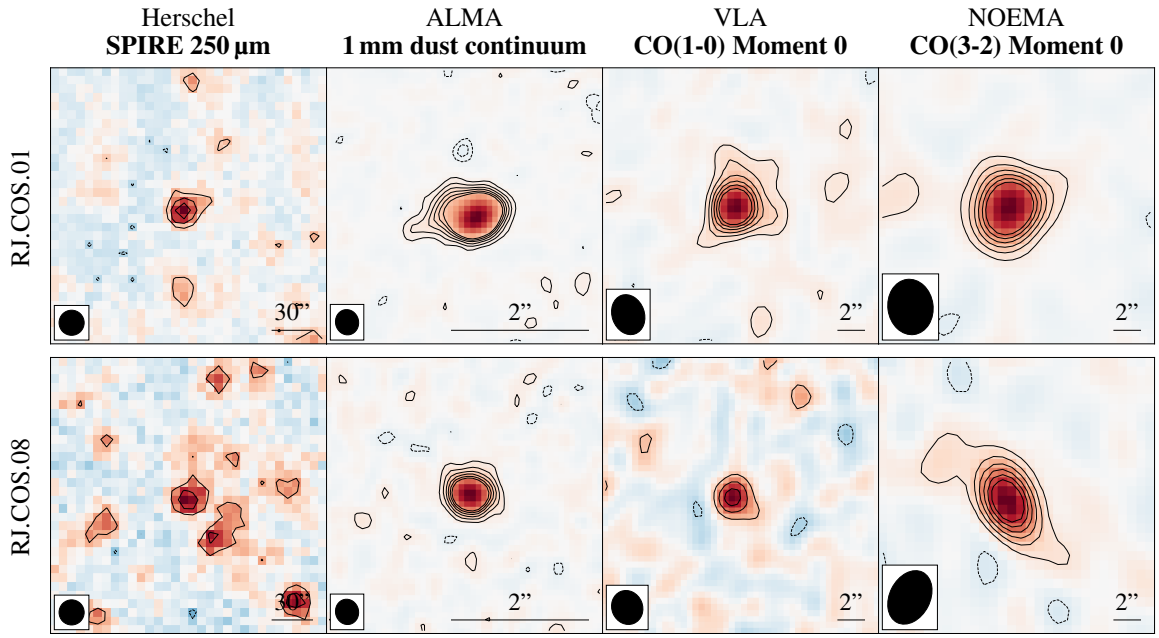

Figure 5.3: Example of the dust and CO observations already obtained for eight of the galaxies studied in Chapter 2. The additional CO(3-2) observations stem from a NOEMA program, of which I was PI. This sample is unique in that it is the largest sample of unlensed galaxies at $z \sim 2$ with such high S/N observations of both CO(1-0) and CO(3-2). It therefore presents the unique opportunity to model the molecular ISM details. *(Figure produced for a Cycle 8 ALMA proposal of which I am PI.)*

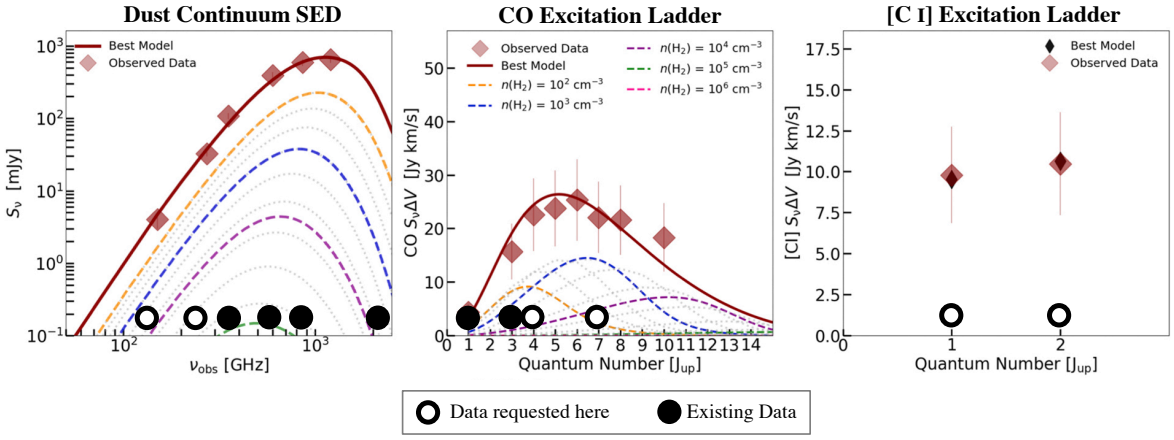

Figure 5.4: Example of the modelling that can be performed with a well-sampled dust SED, CO excitation ladder and [C I] excitation ladder. The example shows the measurements and turbulence modeling conducted by Harrington et al. (2021) for a $z = 2.4$ lensed, Planck-selected starburst galaxy (adapted from their Fig. 4). The black points indicate the data that has already been obtained for a subsample of eight galaxies studied in Chapter 2. The open circles indicate the additional data needed to model the gas and dust temperatures, gas densities and ISRF strengths. *(Figure produced for a Cycle 8 ALMA proposal of which I am PI.)*

observe the higher-J CO, [C I] and long-wavelength dust-continuum emission with ALMA,[(1)] enabling the average molecular ISM conditions to be accurately modelled (Fig. 5.4).

In Chapter 2 I investigated a commonly-applied method of deriving molecular gas masses from 1 mm dust-continuum observations (developed by Scoville et al., 2016), finding broad agreement between the CO(1-0)- and 1 mm-derived gas masses. However, the lack of longer wavelength continuum measurements left the dust temperature unconstrained. With the addition of 1.1 mm

[(1)] with only two frequency tunings per galaxy

and 2 mm continuum measurements it would be possible to accurately measure both the mass- and luminosity-weighted dust temperatures, breaking the degeneracy between the dust temperature and the dust emissivity index, β. Conducting these kinds of dust temperature measurements for star-forming galaxies with a range of measured star formation efficiencies, i.e. SFR/M_{mol}, will be an important test of how the increased star formation activity affects the ISM properties.

In addition, the subsample of galaxies from Chapter 2 with high S/N measurements of CO(1-0) and CO(3-2) presents the unique opporunity to cross-calibrate all $z \sim 2$ molecular gas tracers (i.e. the 1 mm continuum, $J > 1$ CO and [C I] line emission) against the local standard, CO(1-0). Over the last few years [C I] has increasingly garnered attention as a potentially more reliable molecular gas tracer than $J > 1$ CO emission (e.g. Valentino et al., 2018). Unlike CO, [C I] is optically thin and traces the surfaces of molecular clouds in a range of environments (Weiß et al., 2005; Offner et al., 2014; Glover et al., 2015). However, [C I] has not yet been calibrated as a molecular gas tracer at $z > 1.5$. Indeed, of the ten $z \sim 2$ SFGs with [C I] observations, only one is unlensed (Popping et al., 2017b). Future observations of [C I] emission will be crucial to probe the total mass and average temperature of molecular gas in galaxies up to the Epoch of Reionisation.

5.2.3 A Bright Future for Molecular ISM Studies

The observational facilities and modelling used to study the molecular ISM of high-redshift galaxies are actively being improved, providing the potential for new insights in the decade to come. Current submillimeter-to-radio wavelength facilities continue to be upgraded and expanded, and even more facilities are being proposed. The resolution and wavelength windows of thse facilities are highlighted in Fig. 5.5.

The planned developments of ALMA will further increase its sensitivity, frequency coverage, bandwidth and angular resolution. Of particular relevance for high-redshift studies are the installment of the long-wavelength receiver bands. The Band 1 receivers, covering the wavelength range between 6 and 8.5 mm, are planned to be installed by the end of 2022 (Carpenter et al., 2020) whereas the Band 2 receivers, covering the wavelength range between 3.3 and 4.5 mm are expected to be operational starting 2024 (Yagoubov et al., 2020). Together, these receivers will enable observations of the CO(1-0) emission to be conducted for galaxies up to $z = 2$, bypassing the uncertain excitation corrections that existing studies rely upon. Moreover, Band 1 will enable observations of [C I](1-0) emission to be conducted for galaxies in the Epoch of Reisonisation, providing robust measurements of their molecular gas masses. In addition, the planned broadening of ALMA's receiver bandwidth will greatly increase the efficiency of spectral scan surveys as well as the continuum sensitivity, reducing the time required for blind/deep-field surveys of molecular gas and dust. The large spectral line surveys conducted so far with ALMA are therefore only the beginning, with the additional improvements enabling a greater range of redshifts, larger area and a larger range of molecular ISM tracers to be probed via future large programs.

Submillimeter interferometry is also receiving an upgrade in the Northern Hemisphere. The eleventh antenna of the NOrthern Extended Millimeter Array (NOEMA) will soon be completed, with the twelfth expected in 2022. These antennas will lead to a $\sim 10\%$ increase in sensitivity and a factor of four reduction in the minimum beam size. More importantly, by adding 11(12) more baselines the additional antennas will increase the dynamical range and image fidelity[(2)] enabling more high-resolution studies of distant galaxies.

Together, these sub-/millimeter interferometers will be used over the coming decade for additional spectral scan surveys, multi-line and multi-band continuum studies, and high-resolution gas and dust observations. These will provide tighter constraints on the cosmic molecular gas density and gas scaling relations, the *conditions* within the molecular ISM, and the distribution and kinematics of the molecular ISM. Additionally, single-dish telescopes, especially the IRAM 30 m

[(2)] The image fidelity how well the image represents the real source distribution.

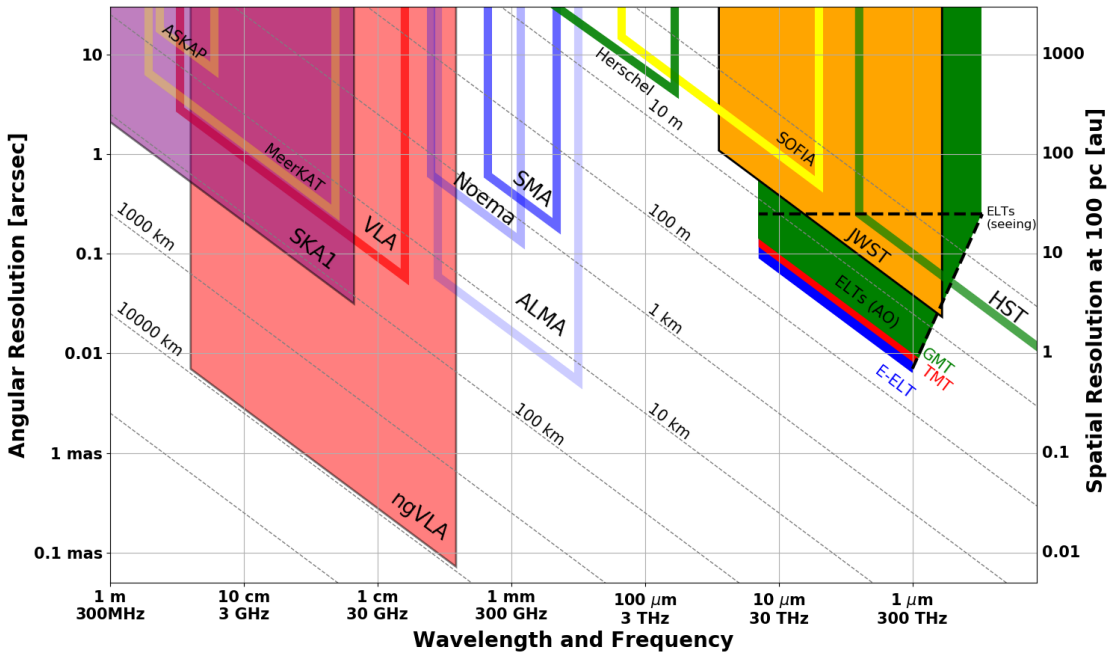

Figure 5.5: The achievable angular resolutions, across the electromagnetic spectrum, for the most impactful existing and future astronomical facilities for studies of distant galaxies. *(Figure taken from the Summary of ngVLA Science Goals, available at* `https://ngvla.nrao.edu/page/about`*)*

and Green Bank Telescope, will continue to enable surveys of spatially-integrated line and continuum emission, identifying targets for follow-up studies with ALMA and NOEMA.

One exciting future facility for studies of the molecular ISM, which is still pending funding,[(3)] is the next generation VLA (ngVLA). As shown in Fig. 5.5, the ngVLA is envisioned to achieve a tenfold increase in sensitivity over the VLA, operate at wavelengths of 2.5 mm to 25 cm and have 30 times longer baselines than the VLA (achieving milliarcsecond resolution) (McKinnon et al., 2019). The ngVLA would therefore be capable of resolving the cold molecular gas of $z > 1$ galaxies, via CO(1-0) emission. Moreover, the proposed design would achieve higher resolutions and probe fainter galaxies than what is possible with ALMA, leading to more accurate constraints on the dynamics, distribution and properties of the molecular ISM in distant galaxies (Casey et al., 2018a; Dale and ngVLA Key Science Goal 3 Team, 2020). The high proposed bandwidth, in combination with the high sensitivity, will also make it the most suitable facility for large cosmic volume surveys of molecular gas via CO and [C I] transitions and even the dense molecular gas tracers, HCN and HCO+ (Riechers et al., 2017).

In addition to detailed studies of the molecular ISM, completing our understanding of how the baryonic matter cycle is regulated by and within galaxies will require complementary views of their stellar populations, dust properties, metal content, neutral hydrogen reservoirs, AGN properties and more. These will be facilitated by a range of upcoming optical-to-radio wavelength facilities. In particular, the *James Webb Space Telescope* (JWST) and Extremely Large Telescope (ELT) will help resolve the build-up of dust and metals as well as the stellar populations and AGN of distant galaxies. Moreover, one of the fundamental blind spots in our picture of distant galaxies, their neutral hydrogen reservoirs, will be filled in by the Square Kilometer Array (SKA). Together with the expanded sub-/millimeter facilities, these new observatories provide the spatial resolution, sensitivity and wavelength coverage needed for the next leap forward in our understanding of star formation and galaxy evolution.

[(3)] The ngVLA has already received mention in the Astro2020 decadal report. This, in addition to the funding forseen for astronomy in the Commerce, Justice, Science, and Related Agencies (CJS) 2021 Appropriations Bill mean that the ngVLA is one of the most likely future facilities to receive funding from the US government.

A

APPENDIX

A.1 THE DATA USED IN CHAPTER 2

I provide the visual representation of the data for the galaxies in Chapter 2 here. Figure A.1, shows all 16 observed VLA spectra, extracted at the source position. The spectral line fits, described in Section 2.2.2, are shown in Figure A.2 and the dust continuum and CO(1-0) emission maps of our final sample of CO-detected sources are shown in Figure A.3. The SED fits, described in Sections 2.3.2.2 and 2.3.3.1, are shown along with the photometric measurements on which they are based in Figure A.4.

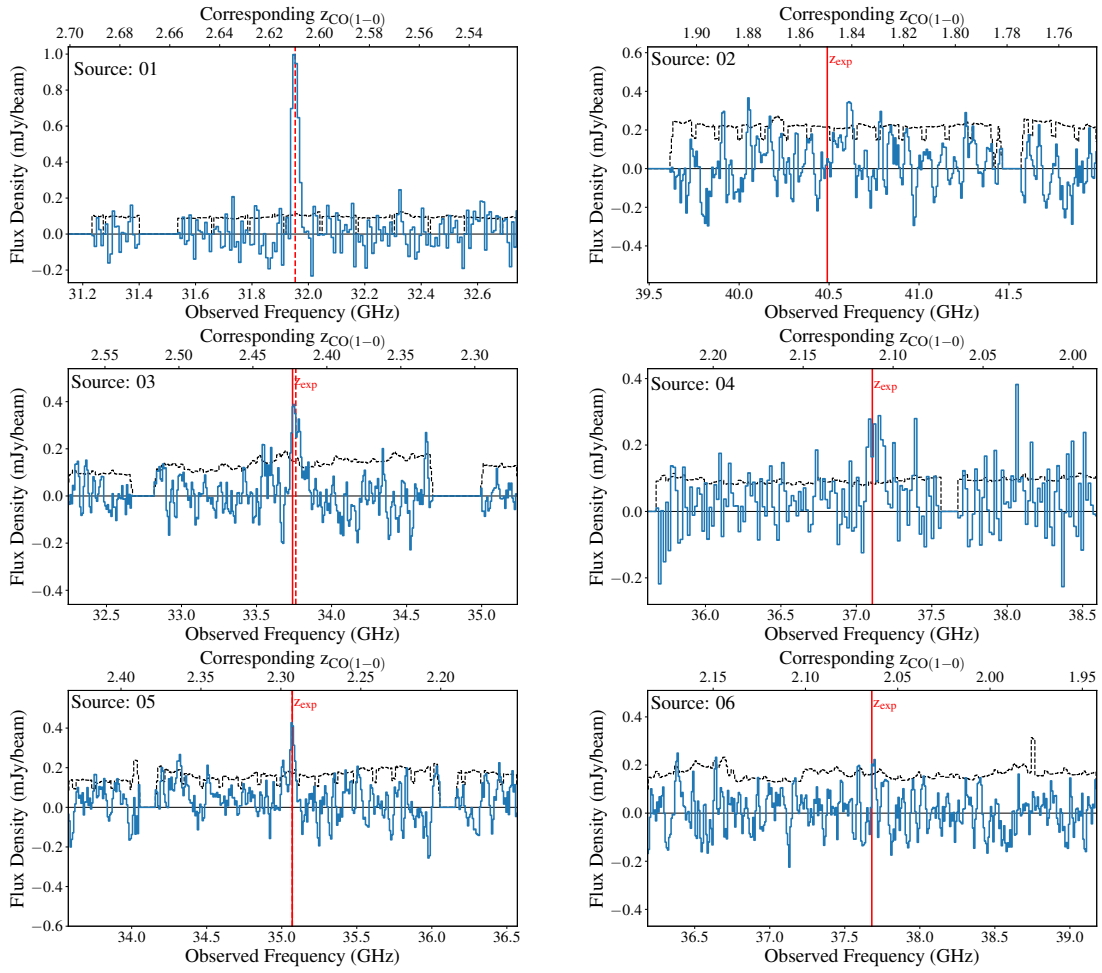

Figure A.1: VLA source spectra extracted at the expected source position. The catalogued redshift, used to design the observations, is indicated by the solid, red, vertical line and is labelled as z_{exp}. For cases where the CO(1-0)-derived redshift differed from this expected redshift, the CO(1-0)-derived redshift is shown by a dashed, red, vertical line.

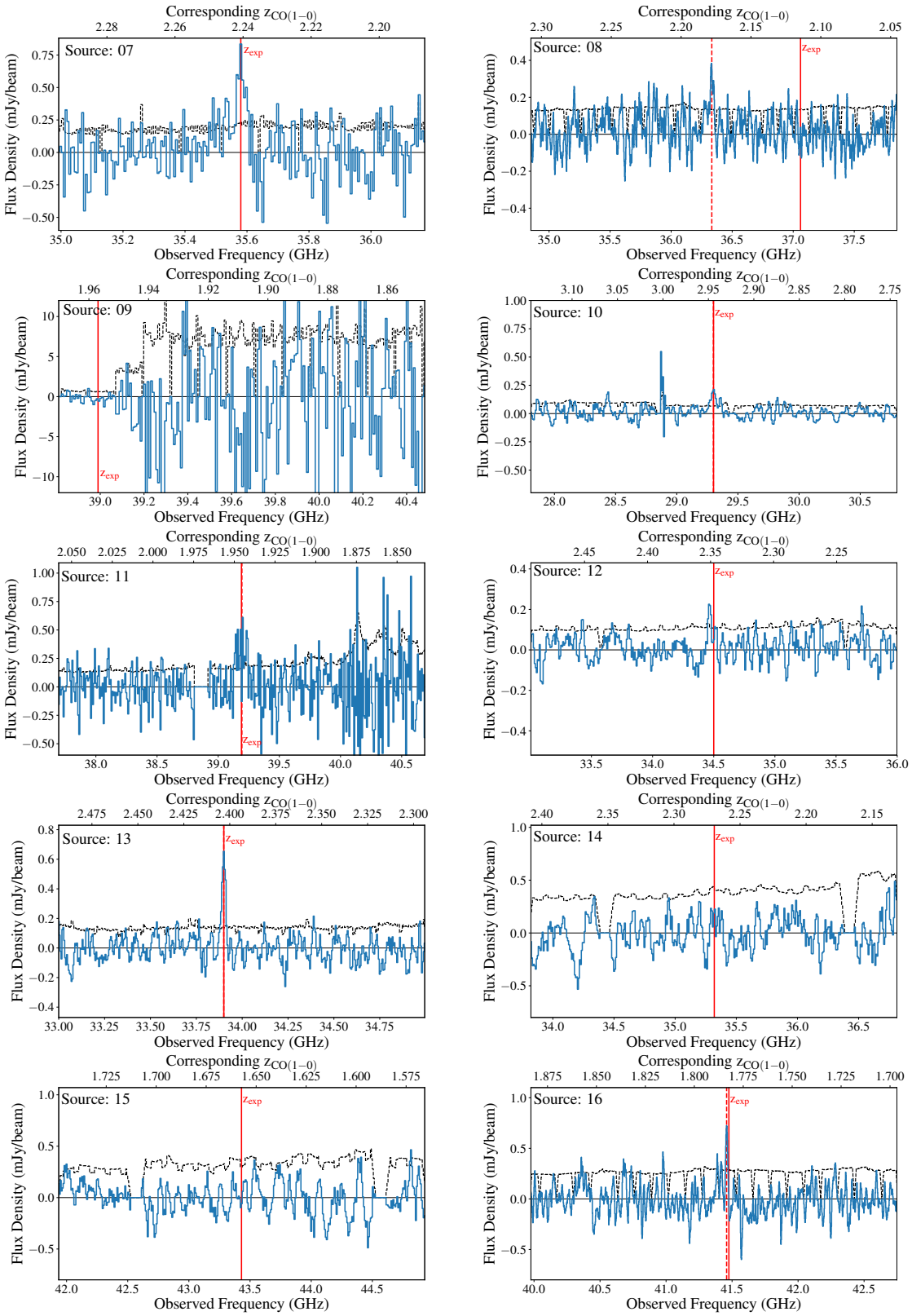

Figure A.1: continued

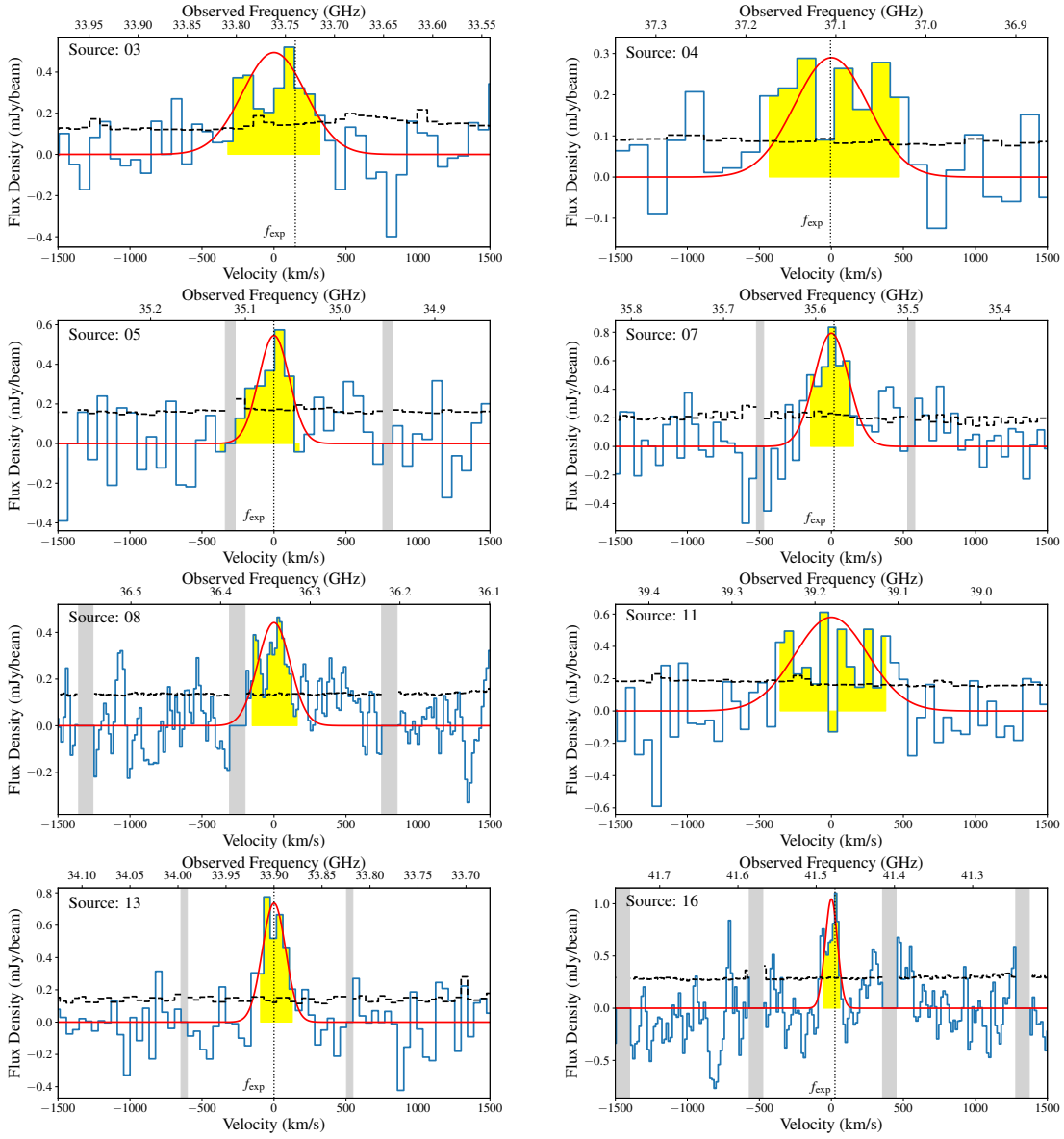

Figure A.2: Spectra of the CO(1-0)-detected sources (blue). The Gaussian line fits are shown for comparison (red) with the spectral region used to create the integrated maps in Figure A.3 shaded in yellow (1.2 FWHM for all sources apart from 4 and 5). Flagged channels, not used for the line fits, are shaded in grey. The root-mean-square noise per channel is indicated by the black, dashed histogram.

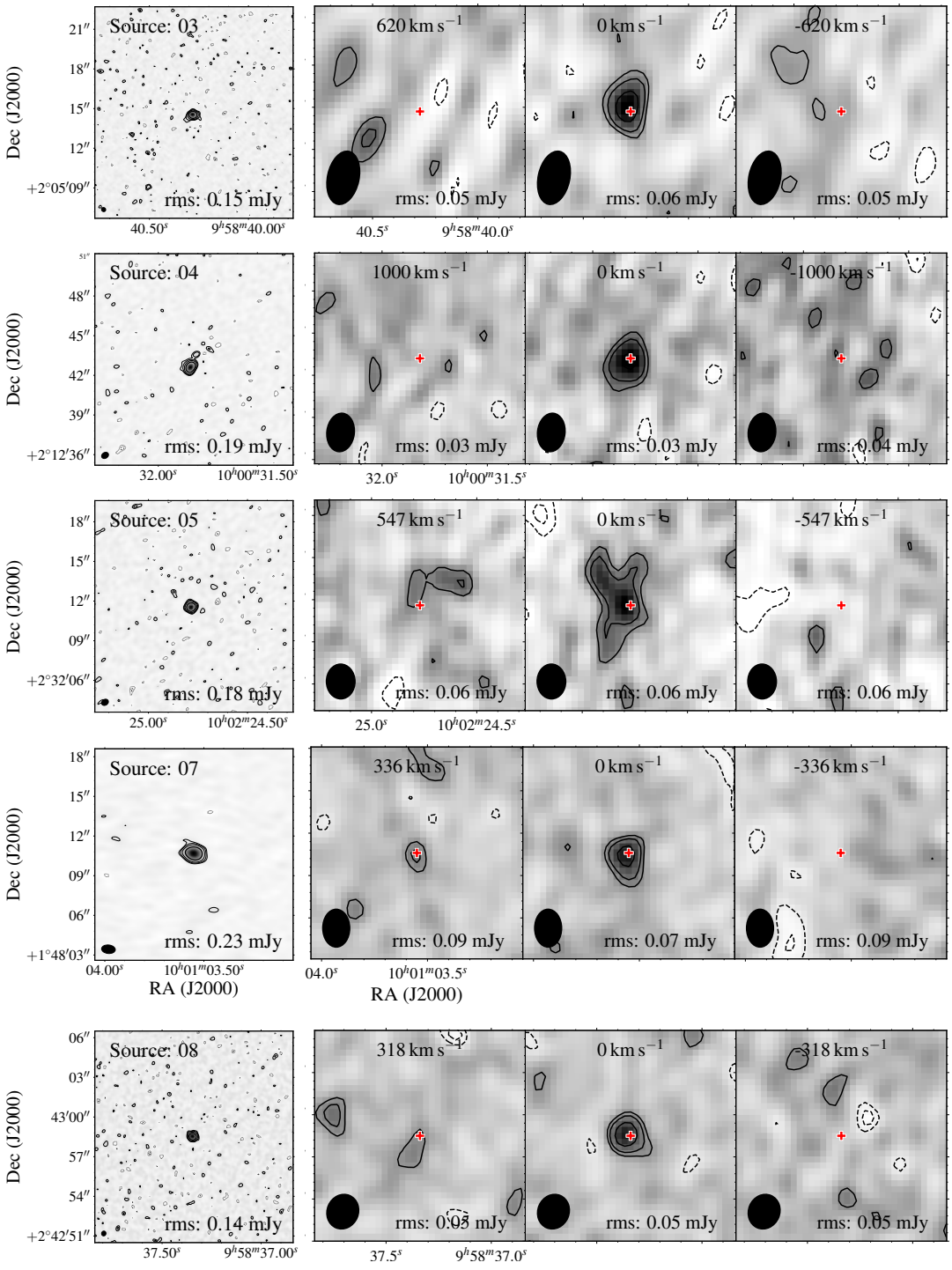

Figure A.3: Comparison of the ALMA dust continuum (left map) and integrated VLA CO(1-0) maps for sources with CO(1-0) detections. The source number is labeled at the top left of the left hand panel in each row. The rms value is given in the bottom right corner of each map. Left column: ALMA observations at 343.5 GHz. Contours are shown for $\pm 2, 3, 5$ and 10σ (dashed contours for negative values). Right columns: Channel maps around the measured (expected) CO(1-0) line. For each source, the central panel of the VLA channel map represents the moment zero map and is centred at the central velocity of the CO spectrum. The velocity width of the integrated maps is chosen to encompass the full source emission (1.2×FWHM of the CO(1-0) line for sources other than 4 and 5). Contours are shown for $\pm 2, 3$ and 5σ (dashed contours for negative values). The red cross indicates the expected position of the source, at which the CO spectrum was extracted. The colour shading indicates the flux density in mJy/beam.

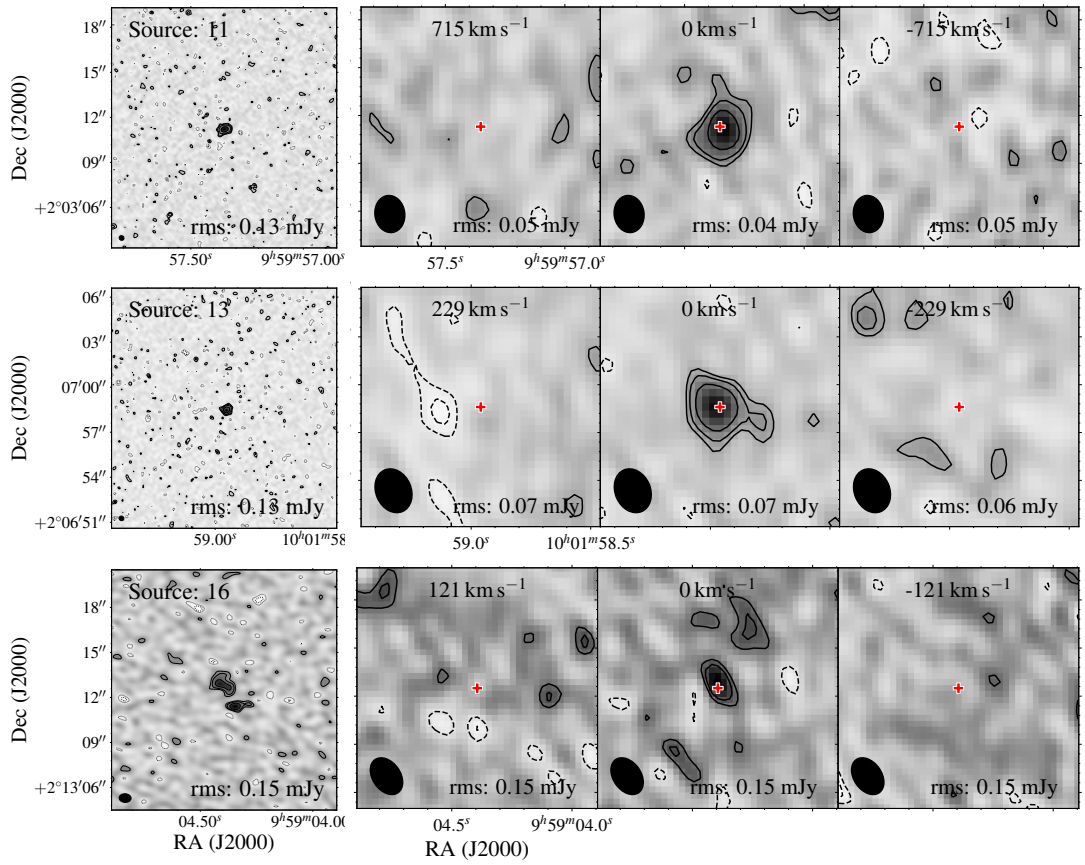

Figure A.3: continued

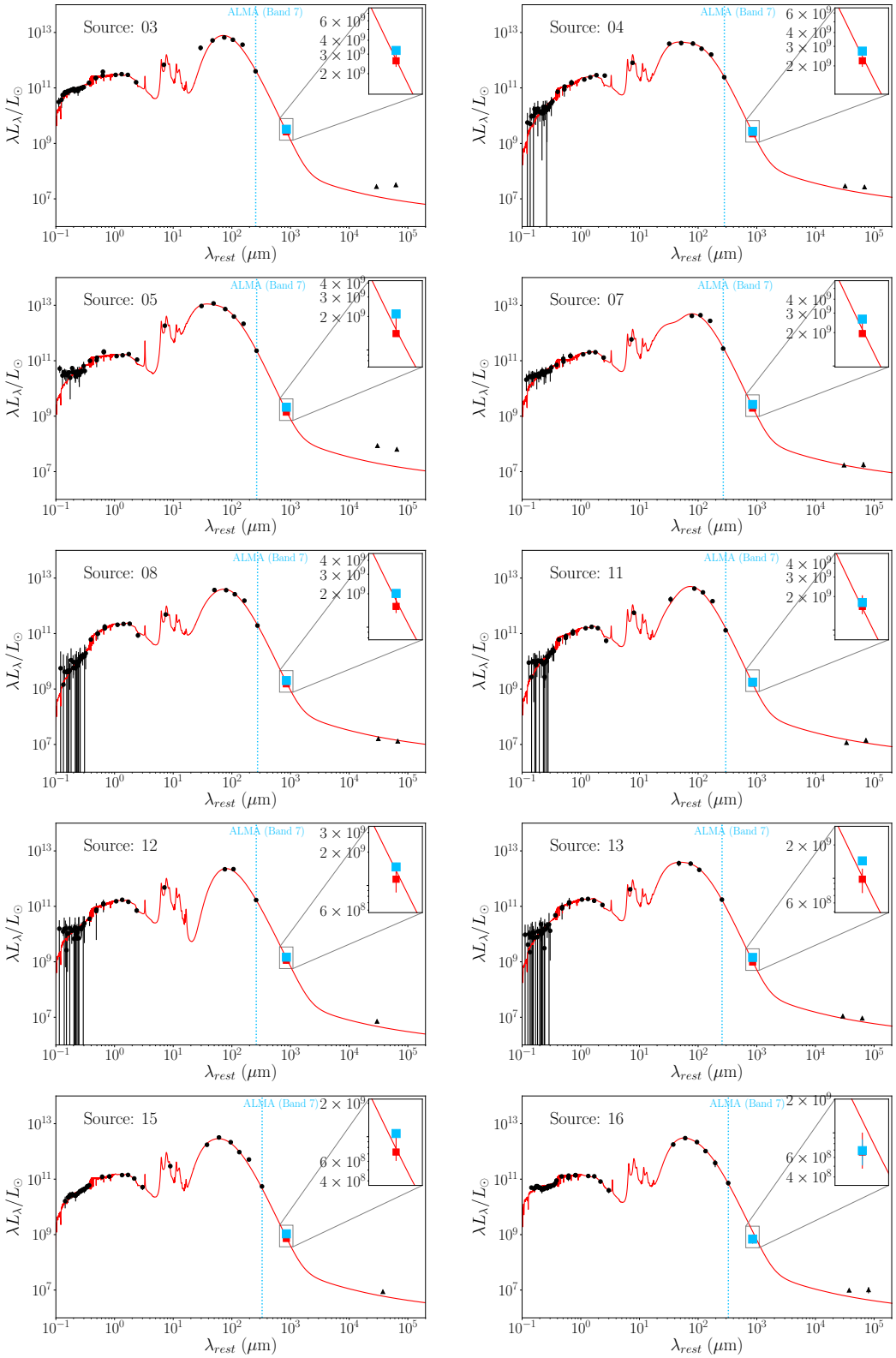

Figure A.4: Rest-frame SEDs of the CO(1-0)-detected galaxies. The inset focuses on the portion of the rest-frame spectrum around 850μm, comparing the single-band (blue) and SED-derived (red) $L_{850\mu\mathrm{m,rest}}$, where the single-band derived value is calculated from Equation (2.5). Note that the best-fit SED and value of $L_{850\mu\mathrm{m,rest}}$ shown are based on the standard MAGPHYS assumptions of $\beta = 1.5$ and 2.0 for the warm and cold components, respectively, with the temperature of the cold dust component as a free parameter. The black filled circles represent the photometry used to fit the SEDs whereas the black triangles show the radio fluxes, which were not used to fit the SEDs.

A.2 DETAILS RELATED TO CHAPTER 3

The use of "we" in the following subsections denotes that this work was published along with Chapter 3.

A.2.1 Additional target

Along with ALPS.3, we observe an additional galaxy at an angular separation of 7.″56. The additional source is labeled 3mm.09, in the 3 mm ASPECS Large Programme González-López et al. (2019) and UDF1 in the the 1.3 mm programme of Dunlop et al. (2017). The galaxy is classified as an AGN, based on the X-Ray observations of Luo et al. (2017) and has a molecular gas to stellar mass fraction around unity (Boogaard et al., 2019). We show the *Hubble Space Telescope* (HST) data along with our ALMA observations and the 5 cm continuum in Figure A.5. Resolved observations of this source, at 870 µm, are presented and discussed in Rujopakarn et al. (2019). They also model the HST H160 emission, which they find is best-fit by the combination of a bright, point source and fainter Sérsic component with a half-light radius of 3.16 ± 0.17 kpc (potentially representing the AGN and disk, respectively). The centroid of the 870 µm emission (Rujopakarn et al., 2019) and the 1.3 mm data presented here, is co-located with the AGN/point source. We find no evidence for resolved CO or 1.3 mm continuum emission for this source, nor do we find any evidence for rotation based on the channel maps or position-velocity diagrams.

The CO data for this source shows both the compact region observed in the 1.3 mm dust continuum as well as an additional CO emitting region to the north, detected at $\gtrsim 3\sigma$. The northern region may be an additional CO emitter, which matches the position of the MUSE absorption line at the same redshift (presented and discussed in Figure 2 and Appendix A of Boogaard et al., 2019). This additional or adjoined source exhibits a red core in the HST images but is barely apparent in the rest-frame UV images and is not observed in the 870 µm data of Rujopakarn et al. (2019).

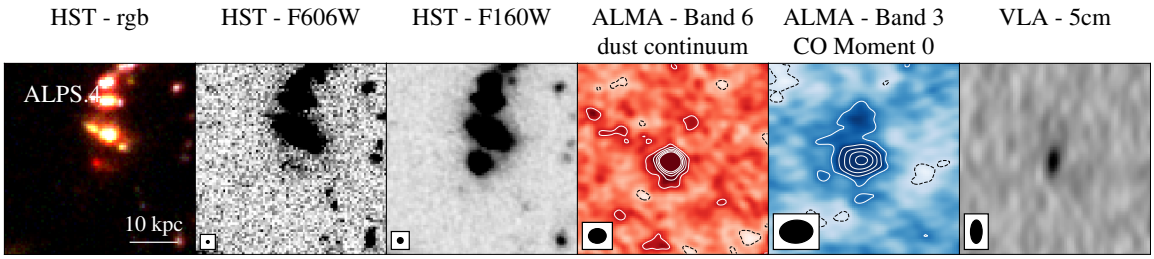

Figure A.5: Multiwavelength data for the additional source, ASPECS LP 3mm.09, observed with ALPS.3. The dust-continuum and CO emission are unresolved and the source appears compact in the rest-frame optical (columns 1-3). Each panel depicts a 5" × 5" region centred on the HST-defined centre of the source. Columns, from left to right: HST 435/775/105 color composite, HST/F606W, HST/F160W, Band 6 (1.3 mm) dust continuum (combined ASPECS and Dunlop et al. (2017) data), CO moment 0 map (from the combined ASPECS and ALPS data) and VLA - 5 cm continuum flux. The contours for the Band 6 dust continuum and CO moment 0 start at $\pm 2\sigma$ and change in steps of 2σ. Dashed black (solid white) lines show negative (positive) contours.

A.2.2 SED Analysis

To model the SEDs, we relied on the accuracy of the measured photometry. Two catalogues of photometry are available for the HUDF, spanning from the UV to the mid-IR (*Spitzer* IRAC), those of Guo et al. (2013) and the 3D-HST catalogue described in Skelton et al. (2014). The HST fluxes from the two HUDF catalogues vary significantly across different bands for our sources. Although

both Guo et al. (2013) and Skelton et al. (2014) extract fluxes from HST images matched to the source-detection image (the HST F160W Band for our sources), their chosen aperture sizes differ. Skelton et al. (2014) extract the source flux from circular apertures of 0."7 diameter whereas Guo et al. (2013) infer the total flux from the isophotal area (i.e. the detection footprint in the F160W image), The sources investigated in Chapter 3 exhibit extended rest-frame optical emission, with F160W half-light radii of $0\farcs6 - 0\farcs98$ (see Table 3.2). Thus, the 3D-HST measurements underestimate the flux of our sources, especially at shorter wavelengths (in the UV). We therefore choose to use the HST and *Spitzer*/IRAC photometry from the Guo et al. (2013) catalogue, which are consistent with the fluxes inferred from the XDF images using circular apertures enclosing our sources (cyan shaded regions and circles in Figure 3.3). For ALPS.1 and 2 the stellar masses inferred based on the Guo et al. (2013) catalogue are factor of 1.5 times lower than inferred from the Skelton et al. (2014) catalogue whereas the SFRs are 1.5 times greater. Conversely, for ALPS.3 the Guo et al. (2013) photometry results in a stellar mass 1.5 times greater and SFR 1.5 times smaller than when using the Skelton et al. (2014) photometry.

To model the SEDs use the MAGPHYS algorithm. MAGPHYS simulates the stellar emission of a galaxy using population sythesis models, based on a variety of star formation histories, and links the stellar energy absorbed and scattered by dust grains to the energy of the thermal emission. As discussed in Buat et al. (2019) and Battisti et al. (2019), the assumptions used to link the stellar and dust emission, such as a simple star formation history (SFH) and dust attenuation recipe, can significantly bias the derived parameters. Attenuation curves vary between galaxies (e.g. Salmon et al., 2016; Salim et al., 2018; Buat et al., 2018) and flatten when the amount of obscuration or SFR increase (e.g. Jonsson et al., 2010; Chevallard et al., 2013; Roebuck et al., 2019).

In this work we have adopted two, adapted versions of the MAGPHYS algorithm as the fits using the standard high-redshift MAGPHYS algorithm left significant residuals. We apply the version of Battisti et al. (2019) to ALPS.1 and 3. This adapted version includes a star formation history that both rises linearly at early ages and then declines exponentially (where before it was an exponentially declining function), has broader priors on the range of optical dust depths and equilibrium dust temperatures (to reflect high-redshift observations, particularly of sub-mm galaxies), includes a prescription for absorption by the intergalactic medium and includes an additional component in the attenuation curve for the diffuse ISM to characterize the attenuation due to the 2175 Å feature.

We test the extent to which the inferred stellar masses and SFRs depend on different photometric bands. Based on the omission of different bands, we find that the peak of the near-infrared emission is particularly important in the stellar mass fits, i.e. the SED fits are highly sensitive to the IRAC photometry, particularly for ALPS.3. For ALPS.1, 2 and 3, respectively, omitting the IRAC photometry resulted in an inferred median stellar masses of ~ 1.5, ~ 3 and ~ 5 times smaller than the median values inferred when using the full set of photometry.

Multiple assumptions systematically bias the inferred stellar masses and SFRs, including the choice of aperture size for the HST photometry (which change the inferred stellar masses by a factor of 1.5 - 2), our reliance on the accuracy of photometry at the peak of the stellar continuum emission (which change the inferred stellar masses by a factor of 1.5 - 5), the inclusion of an unconstrained AGN component (which change the inferred stellar masses by a factor of ~ 2 for $\xi_{\rm AGN} \sim 0.15$) and the applied dust attenuation curve (which also changes the inferred stellar masses by factor of $\sim 1.5 - 2$). Based on these systematics we adopt an uncertainty floor of ± 0.3 dex on the stellar masses and SFRs inferred here.

A.2.3 Local Starbursts

To place the measured sizes for our data in context, we create mock 1.3 mm maps of two local galaxies that harbour nuclear starbursts, NGC 253 and NGC 4945. We use the 870 µm LABOCA

maps from Weiß et al. (2008), smooth these to the resolution of the Band 6 data, scale the flux to match the total flux density of each of our sources and add the same level of noise as for our data (smoothed to the beam). We thereby assume that the distribution of the rest-frame 870 µm matches that of the rest-frame 540, 509 and 350 µm emission, respectively, for ALPS.1, 2 and 3. The results are shown in Figure A.6. The mock observations are barely resolved, with the observed size at half the peak surface brightness (blue contours) matching the 1.3 mm beam size. Only a portion of the brightest spiral arms appear to be recovered at $> 3\sigma$.

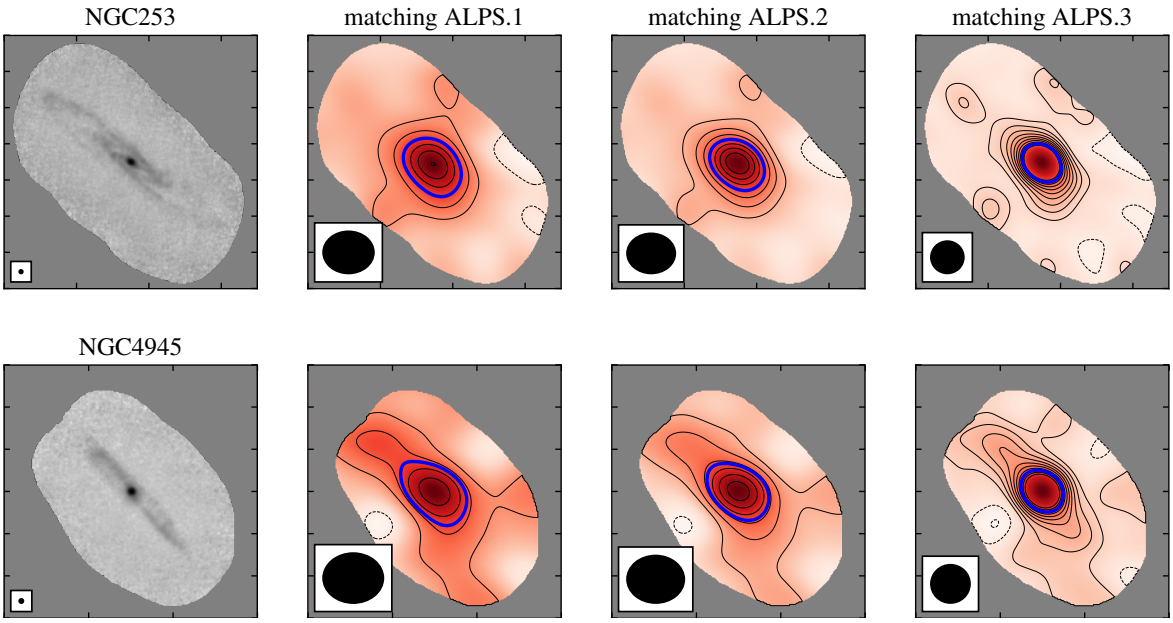

Figure A.6: Mock observations of the local starburst galaxies, NGC 253 and NGC 4945, matching the total dust mass (i.e. measured flux) to the sources observed here. Left column: original Laboca observations. Second to fourth column: mock 1.3 mm observations matching the rms and total flux density of ALPS.1, 2 and 3 respectively. Contours start at $\pm 2\sigma$ and go in steps of 2σ. Solid (dashed) lines show positive (negative) contours. The half-peak emission contours are shown in blue.

A.3 CONVERTING BETWEEN CO(1-0)-TO-H_2 CONVERSION FACTORS

Both $X_{\rm CO}$ and $\alpha_{\rm CO}$ can be referred to as the CO-to-H_2 conversion factor but the two are valid at different spatial scales. $X_{\rm CO}$ converts between the velocity-integrated CO(1-0) intensity averaged over the projected area of a molecular cloud, $W_{CO(1-0)}$ (in K km s^{-1}), and the H_2 column density $N_{\rm H_2}$ (in cm^{-2}),

$$X_{\rm CO} = \frac{N_{\rm H_2}}{W_{CO(1-0)}}\,. \tag{A.1}$$

In contrast, $\alpha_{\rm CO}$ converts between the total molecular gas mass $M_{\rm mol}$ and the integrated CO(1-0) line luminosity,

$$M_{\rm mol} = \alpha_{\rm CO} L'_{\rm CO(1-0)}\,. \tag{A.2}$$

Thus, $\alpha_{\rm CO}$ is simply the result of integrating over the emitting area and correcting the mass contribution of heavier elements mixed in with H_2 as follows.

Suppose the source is at a distance, D, and subtends a solid angle Ω. The CO luminosity of the source, in units of K km s^{-1} pc^2 is,

$$L'_{CO(1-0)} = D^2 W_{\rm CO(1-0)} \Omega \tag{A.3}$$

where D is the distance in pc. The molecular gas mass (in $M_\odot$) of the source is given by,

$$M_{\rm H_2} = \frac{A N_{\rm H_2} m_{\rm H_2}}{M_\odot} \tag{A.4}$$

where $m_{\rm H_2}$ is the mass of a hydrogen molecule, A is the area of the source in cm^{-2} and $N_{\rm H_2}$ is the mean H_2 column density.

The area can be defined as,

$$A = D^2 \Omega \left(\frac{pc}{cm}\right)^2 \tag{A.5}$$

Thus the mass of the source becomes,

$$M_{\rm H_2} = \frac{D^2 \Omega N_{\rm H_2} m_{\rm H_2}}{M_\odot} \left(\frac{pc}{cm}\right)^2 \tag{A.6}$$

Rearranging,

$$D^2 \Omega = \frac{M_{\rm H_2} M_\odot}{N_{\rm H_2} m_{\rm H_2}} \left(\frac{cm}{pc}\right)^2 \tag{A.7}$$

and hence

$$L'_{CO(1-0)} = \frac{W_{\rm CO(1-0)}}{N_{\rm H_2}} \frac{M_{\rm H_2} M_\odot}{m_{\rm H_2}} \left(\frac{cm}{pc}\right)^2 \tag{A.8}$$

Rearranging for $\alpha_{\rm CO}$,

$$\alpha_{\rm CO}^{-1} = \frac{L'_{CO(1-0)}}{m_{\rm H_2}} \tag{A.9}$$

$$= \frac{(W_{\rm CO(1-0)}}{N_{\rm H_2}} \frac{M_\odot}{m_{\rm H_2}} \left(\frac{cm}{pc}\right)^2 \tag{A.10}$$

Evaluating,

$$\frac{M_\odot}{m_{\rm H_2}} \left(\frac{cm}{pc}\right)^2 \approx 6.3 \times 10^{19} \tag{A.11}$$

Thus,

$$X_{\rm CO} = 6.3 \times 10^{19} \alpha_{\rm CO} \tag{A.12}$$

But, **this only accounts for the mass of the $\mathbf{H}_2$**. To account for the mass of helium (other heavy elements can be ignored), then this needs to corrected for an additional factor of 1.36. Folding this into the conversion between $X_{\rm CO}$ and $\alpha_{\rm CO}$, results in,

$$X_{\rm CO} = 4.65 \times 10^{19} \alpha_{\rm CO}\,. \tag{A.13}$$

PUBLICATIONS

The following is a complete list of publications that I have contributed to. The publications marked with a filled black star (★) make up the Chapters of this thesis. The publications marked by filled squares (■) are ones that I contributed to during my doctoral research and are related to the work presented herein.

AS LEAD AUTHOR:

★ **M. Kaasinen**, F. Walter, M. Novak, I. Smail, L. Boogaard, E. da Cunha, A. Weiß, D. Liu, R. Decarli, G. Popping, T. Díaz-Santos, P. Cortés, M. Aravena, P. van der Werf, D. A. Riechers, H. Inami, J. A. Hodge, H.-W. Rix, P. Cox.
A Comparison of the Stellar, CO and Dust-Continuum Emission from Three, Star-Forming HUDF Galaxies at $z \sim 2$
The Astrophysical Journal (2020), vol. 889, p. 37

★ **M. Kaasinen**, N. Scoville, F. Walter, E. da Cunha, G. Popping, R. Pavesi, B. Darvish, C. Casey, D. A. Riechers, S. Glover.
The Molecular Gas Reservoirs of z∼2 Galaxies: A Comparison of CO(1-0) and Dust-based Molecular Gas Masses
The Astrophysical Journal (2019), vol. 880, 15

- **M. Kaasinen**, L. J. Kewley, F. Bian, B. Groves, D. Kashino, J. Silverman, J. Kartaltepe.
The ionization parameter of star-forming galaxies evolves with the specific star formation rate
MNRAS (2018) vol. 477, p. 5568

- **M. Kaasinen**, F. Bian, B. Groves, L. J. Kewley, A. Gupta.
The COSMOS [OII] Survey: Evolution of Electron Density with Star Formation rate
MNRAS (2017), vol. 465, p. 3220

AS CONTRIBUTING AUTHOR:

■ M. Neeleman, M. Novak, B. P. Venemans, F. Walter, R. Decarli, **M. Kaasinen**, J.-T. Schindler, E. Bañados, C. L. Carilli, A. B. Drake, X. Fan, H.-W. Rix
The Kinematics of $z \sim 6$ Quasar Host Galaxies
The Astrophysical Journal (2021), accepted. (arXiv:2102.05679)

■ G. Popping, A. Pillepich, G. Calistro Rivera, S. Schulz, L. Hernquist, **M. Kaasinen**, F. Marinacci, D. Nelson, M. Vogelsberger.
The dust-continuum size of TNG50 galaxies at $z = 1-5$: a comparison with the distribution of stellar light, stars, dust and H_2
The Astrophysical Journal (2021), accepted. (arXiv:2101.12218)

■ M. Novak, B. P. Venemans, F. Walter, M. Neeleman, **M. Kaasinen**, L. Liang, R. Feldmann, E. Bañados, C. Carilli, R. Decarli, A. Drake, X. Fan, E. P. Farina, C. Mazzucchelli, R. Wang.
No evidence for [C II] halos or high-velocity outflows in $z \sim 6$ quasar host galaxies
The Astrophysical Journal (2020), vol. 904, p. 131

■ B. P. Venemans, F. Walter, M. Neeleman, M. Novak, J. Otter, R. Decarli, E. Bañados, A. Drake, E. P. Farina, **M. Kaasinen**, C. Mazzucchelli, C. Carilli, X. Fan, H.-W. Rix, R. Wang.

Kiloparsec-scale ALMA Imaging of [CII] and Dust continuum Emission of 27 Quasar Host Galaxies at $z \sim 6$
The Astrophysical Journal (2020), vol. 904, p. 130

■ V. Marian, K. Jahnke, I. Andika, E. Bañados, V. N. Bennert, S. Cohen, B. Husemann, **M. Kaasinen**, A. M. Koekemoer, M. Mechtley, M. Onoue, JT. Schindler, M. Schramm, A. Schulze, J. D. Silverman, I. Smirnova-Pinchukova, A. van der Wel, C. Villforth, R. A. Windhorst.
A significant excess in the major merger rate for AGNs with the highest Eddington ratios at $z < 0.2$
The Astrophysical Journal (2020), vol. 904, p. 79

■ H. Inami, R. Decarli, F. Walter, A. Weiß, C. Carilli, M. Aravena, L. Boogaard, J. González-López, G. Popping, E. da Cunha, F. Bauer, P. Cox, E. Daddi, T. Díaz-Santos, I. Smail, **M. Kaasinen**, D. A. Riechers, J. Wagg, P. van der Werf.
The ALMA Spectroscopic Survey in the HUDF: A Constant Molecular-to-Stellar Mass Ratio at Stellar Masses of $\log(M_*/M_\odot) < 10$, revealed by a CO Emission Stacking Analysis of z 1.5 Star-Forming Galaxies
The Astrophysical Journal (2020), vol. 902, p. 113

■ L. A. Boogaard, P. van der Werf, A. Weiß, G. Popping, R. Decarli, F. Walter, M. Aravena, R. Bouwens, D. A. Riechers, J. González-López, I. Smail, C. Carilli, **M. Kaasinen**, P. Cox, T. Díaz-Santos, P. Cortés, J. Wagg.
The ALMA Spectroscopic Survey in the HUDF: CO Excitation and Atomic Carbon in Star Forming Galaxies at $z = 1 - 3$
The Astrophysical Journal (2020), vol. 902, p. 109

• K. Jahnke, C. Fendt, M. Fouesneau, I. Georgiev, T. Herbst, **M. Kaasinen**, D. Kossakowski, J. Rybizki, M. Schlecker, G. Seidel, T. Henning, L. Kreidberg, H.-W. Rix.
An astronomical institute's perspective on meeting the challenges of the climate crisis
Nature Astronomy (2020), vol. 4, p. 812

■ D. A. Riechers, L. A. Boogaard, R. Decarli, J. González-López, I. Smail, F. Walter, M. Aravena, C. Carilli, P. Cortés, P. Cox, T. Díaz-Santos, J. A. Hodge, H. Inami, R. J. Ivison, **M. Kaasinen**, J. Wagg, A. Weiß, P. van der Werf.
VLA-ALMA Spectroscopic Survey in the Hubble Ultra Deep Field (VLASPECS): Total Cold Gas Masses and CO Line Ratios for $z = 2 - 3$ Main-sequence Galaxies
The Astrophysical Journal (2020), vol. 696, p. 21

• A. Acharyya, L. J. Kewley, J. Rigby, M. Bayliss, F. Bian, D. Nicholls, C. Federrath, **M. Kaasinen**, M. Florian, G. A. Blanc.
Rest-frame UV and optical emission line diagnostics of ionized gas properties: a test case in a star-forming knot of a lensed galaxy at $z \sim 1.7$
MNRAS (2019), vol. 488, p. 5862

• E. J. Hampton, A. M. Medling, B. Groves, L. J. Kewley, M. Dopita, R. Davies, I.-T. Ho, **M. Kaasinen**, S. Leslie, R. Sharp, S. M. Sweet, A. D. Thomas, J. Allen, J. Bland-Hawthorn, S. Brough, J. J. Bryant, S. Croom, M. Goodwin, A. Green, I. S. Konstantantopoulos, J. Lawrence, Á. R. López-Sánchez, N. P. F. Lorente, R. McElroy, M. S. Owers, S. N. Richards, P. Shastri
Using an artificial neural network to classify multicomponent emission lines with integral field spectroscopy from SAMI and S7
MNRAS (2019), vol. 488, p. 5862

BIBLIOGRAPHY

Aihara, H., Prieto, C. A., An, D., et al. (2011). In: *The Astrophysical Journal Supplement Series* 193.2, p. 29.

Alaghband-Zadeh, S., Chapman, S. C., Swinbank, A. M., et al. (2013). In: *MNRAS* 435.2, pp. 1493–1510.

Albertsson, T., Semenov, D. A., Vasyunin, A. I., Henning, T., and Herbst, E. (2013). In: *The Astrophysical Journal Supplement Series* 207.2, p. 27.

Apostolovski, Y., Aravena, M., Anguita, T., et al. (2019). In: *A&A* 628, A23, A23.

Aravena, M., Hodge, J. A., Wagg, J., et al. (2014). In: *MNRAS* 442, pp. 558–564.

Aravena, M., Boogaard, L., Gónzalez-López, J., et al. (2020). In: *arXiv e-prints*, arXiv:2006.04284, arXiv:2006.04284.

Aravena, M., Decarli, R., Gónzalez-López, J., et al. (2019). In: *ApJ* 882.2, 136, p. 136.

Arnouts, S., Cristiani, S., Moscardini, L., et al. (1999). In: *MNRAS* 310, pp. 540–556.

Baars, J. W. M., Hooghoudt, B. G., Mezger, P. G., and de Jonge, M. J. (1987). In: *A&A* 175.1-2, pp. 319–326.

Barro, G., Kriek, M., Pérez-González, P. G., et al. (2016). In: *ApJL* 827.2, L32, p. L32.

Battisti, A. J., da Cunha, E., Grasha, K., et al. (2019). In: *ApJ* 882.1, 61, p. 61.

Behroozi, P. S., Wechsler, R. H., and Conroy, C. (2013). In: *The Astrophysical Journal* 770.1, p. 57.

Bell, T. A., Roueff, E., Viti, S., and Williams, D. A. (2006). In: *MNRAS* 371.4, pp. 1865–1872.

Bendo, G. J., Wilson, C. D., Warren, B. E., et al. (2010). In: *MNRAS* 402.3, pp. 1409–1425.

Béthermin, M., Greve, T. R., De Breuck, C., et al. (2018). In: *A&A* 620, A115, A115.

Beuther, H., Ragan, S. E., Ossenkopf, V., et al. (2014). In: *A&A* 571, A53, A53.

Bianchi, S. (2007). In: *A&A* 471.3, pp. 765–773.

Bianchi, S., De Vis, P., Viaene, S., et al. (2018). In: *A&A* 620, A112, A112.

Bianchi, S. and Xilouris, E. M. (2011). In: *A&A* 531, L11, p. L11.

Bigiel, F., Leroy, A., Walter, F., et al. (2008). In: *AJ* 136, pp. 2846–2871.

Bigiel, F., Leroy, A. K., Walter, F., et al. (2011). In: *ApJL* 730, L13, p. L13.

Binney, J. and Tremaine, S. (2008).

Birkin, J. and et al. (2020, in prep.). In:

Bischetti, M., Feruglio, C., Piconcelli, E., et al. (2021). In: *A&A* 645, A33, A33.

Blain, A. W., Smail, I., Ivison, R. J., Kneib, J. .-P., and Frayer, D. T. (2002). In: *PhR* 369.2, pp. 111–176.

Bohlin, R. C., Savage, B. D., and Drake, J. F. (1978). In: *ApJ* 224, pp. 132–142.

Bolatto, A. D., Warren, S. R., Leroy, A. K., et al. (2015). In: *ApJ* 809, 175, p. 175.

Bolatto, A. D., Wolfire, M., and Leroy, A. K. (2013). In: *ARA&A* 51, pp. 207–268.

Boogaard, L. A., Brinchmann, J., Bouché, N., et al. (2018). In: *A&A* 619, A27, A27.

Boogaard, L. A., Decarli, R., González-López, J., et al. (2019). In: *ApJ* 882.2, 140, p. 140.

Boogaard, L. A., van der Werf, P., Weiss, A., et al. (2020). In: *ApJ* 902.2, 109, p. 109.

Borchert, E. M. A., Walch, S., Seifried, D., et al. (2021). In: *arXiv e-prints*, arXiv:2102.00778, arXiv:2102.00778.

Bothwell, M. S., Aguirre, J. E., Aravena, M., et al. (2017). In: *MNRAS* 466.3, pp. 2825–2841.

Bothwell, M. S., Smail, I., Chapman, S. C., et al. (2013). In: *MNRAS* 429.4, pp. 3047–3067.

Bournaud, F., Daddi, E., Weiß, A., et al. (2015). In: *A&A* 575, A56, A56.

Bourne, N., Dunne, L., Bendo, G. J., et al. (2013). In: *MNRAS* 436, pp. 479–502.

Bouwens, R., González-López, J., Aravena, M., et al. (2020). In: *The Astrophysical Journal* 902.2, p. 112.

Brand, J. and Wouterloot, J. G. A. (1995). In: *A&A* 303, p. 851.
Brauer, R., Wolf, S., Reissl, S., and Ober, F. (2017). In: *A&A* 601, A90, A90.
Bromm, V. and Larson, R. B. (2004). In: *ARA&A* 42.1, pp. 79–118.
Bryant, P. M. and Scoville, N. Z. (1996). In: *ApJ* 457, p. 678.
Bryant, P. M. and Scoville, N. Z. (1999). In: *AJ* 117.6, pp. 2632–2655.
Buat, V., Boquien, M., Małek, K., et al. (2018). In: *A&A* 619, A135, A135.
Buat, V., Ciesla, L., Boquien, M., Małek, K., and Burgarella, D. (2019). In: *A&A* 632, A79, A79.
Caldú-Primo, A., Schruba, A., Walter, F., et al. (2013). In: *AJ* 146.6, 150, p. 150.
Calistro Rivera, G., Hodge, J. A., Smail, I., et al. (2018). In: *ApJ* 863, 56, p. 56.
Camps, P. and Baes, M. (2015). In: *Astronomy and Computing* 9, pp. 20–33.
Cañameras, R., Yang, C., Nesvadba, N. P. H., et al. (2018). In: *A&A* 620, A61, A61.
Carilli, C. L. and Walter, F. (2013). In: *ARA&A* 51, pp. 105–161.
Carlstrom, J. E., Ade, P. A. R., Aird, K. A., et al. (2011). In: *PASP* 123.903, p. 568.
Carpenter, J., Iono, D., Kemper, F., and Wootten, A. (2020). In: *arXiv e-prints*, arXiv:2001.11076, arXiv:2001.11076.
Casasola, V., Cassarà, L. P., Bianchi, S., et al. (2017). In: *A&A* 605, A18, A18.
Casey, C. M., Narayanan, D., Carilli, C., et al. (2018a). In: *Science with a Next Generation Very Large Array*. Ed. by E. Murphy. Vol. 517. Astronomical Society of the Pacific Conference Series, p. 629.
Casey, C. M., Narayanan, D., and Cooray, A. (2014). In: *PhR* 541.2, pp. 45–161.
Casey, C. M., Zavala, J. A., Spilker, J., et al. (2018b). In: *ApJ* 862.1, 77, p. 77.
Casoli, F., Combes, F., and Gerin, M. (1984). In: *A&A* 133, pp. 99–109.
Catinella, B., Schiminovich, D., Kauffmann, G., et al. (2010). In: *MNRAS* 403.2, pp. 683–708.
Chabrier, G. (2003). In: *PASP* 115, pp. 763–795.
Chang, Y.-Y., Le Floc'h, E., Juneau, S., et al. (2020). In: *ApJ* 888.1, 44, p. 44.
Chen, C.-C., Hodge, J. A., Smail, I., et al. (2017). In: *ApJ* 846, 108, p. 108.
Chevallard, J., Charlot, S., Wandelt, B., and Wild, V. (2013). In: *MNRAS* 432.3, pp. 2061–2091.
Christensen, C., Quinn, T., Governato, F., et al. (2012). In: *MNRAS* 425.4, pp. 3058–3076.
Clark, P. C. and Glover, S. C. O. (2015). In: *MNRAS* 452.2, pp. 2057–2070.
Clark, P. C., Glover, S. C. O., and Klessen, R. S. (2012a). In: *MNRAS* 420.1, pp. 745–756.
Clark, P. C., Glover, S. C. O., Klessen, R. S., and Bonnell, I. A. (2012b). In: *MNRAS* 424.4, pp. 2599–2613.
Clark, P. C., Glover, S. C. O., Ragan, S. E., and Duarte-Cabral, A. (2019). In: *MNRAS* 486.4, pp. 4622–4637.
Clements, D. L., Dunne, L., and Eales, S. (2010). In: *MNRAS* 403, pp. 274–286.
Cochrane, R. K., Hayward, C. C., Anglés-Alcázar, D., et al. (2019). In: *MNRAS* 488.2, pp. 1779–1789.
Colombo, D., Hughes, A., Schinnerer, E., et al. (2014). In: *ApJ* 784.1, 3, p. 3.
Conselice, C. J. (2003). In: *ApJS* 147.1, pp. 1–28.
Conselice, C. J., Bershady, M. A., and Jangren, A. (2000). In: *ApJ* 529.2, pp. 886–910.
Cresci, G., Hicks, E. K. S., Genzel, R., et al. (2009). In: *ApJ* 697.1, pp. 115–132.
da Cunha, E., Charlot, S., and Elbaz, D. (2008). In: *MNRAS* 388, pp. 1595–1617.
da Cunha, E., Groves, B., Walter, F., et al. (2013a). In: *ApJ* 766, 13, p. 13.
da Cunha, E., Walter, F., Decarli, R., et al. (2013b). In: *ApJ* 765, 9, p. 9.
da Cunha, E., Walter, F., Smail, I. R., et al. (2015). In: *ApJ* 806, 110, p. 110.
Daddi, E., Bournaud, F., Walter, F., et al. (2010a). In: *ApJ* 713, pp. 686–707.
Daddi, E., Dannerbauer, H., Liu, D., et al. (2015). In: *A&A* 577, A46, A46.
Daddi, E., Dickinson, M., Morrison, G., et al. (2007). In: *ApJ* 670, pp. 156–172.
Daddi, E., Elbaz, D., Walter, F., et al. (2010b). In: *ApJL* 714, pp. L118–L122.
Dale, D. and ngVLA Key Science Goal 3 Team (2020). In: *American Astronomical Society Meeting Abstracts #235*. Vol. 235. American Astronomical Society Meeting Abstracts, p. 364.18.
Dame, T. M., Elmegreen, B. G., Cohen, R. S., and Thaddeus, P. (1986). In: *ApJ* 305, p. 892.

Dame, T. M., Hartmann, D., and Thaddeus, P. (2001). In: *ApJ* 547.2, pp. 792–813.
Darvish, B., Scoville, N. Z., Martin, C., et al. (2018). In: *ApJ* 860, 111, p. 111.
de Blok, W. J. G. and Walter, F. (2014). In: *AJ* 147.5, 96, p. 96.
De Breuck, C., Williams, R. J., Swinbank, M., et al. (2014). In: *A&A* 565, A59, A59.
de Jong, R. S. (1996). In: *A&A* 313, pp. 377–395.
Decarli, R., Smail, I., Walter, F., et al. (2014). In: *ApJ* 780.2, 115, p. 115.
Decarli, R., Walter, F., Aravena, M., et al. (2016). In: *ApJ* 833, 70, p. 70.
Decarli, R., Aravena, M., Boogaard, L., et al. (2020). In: *ApJ* 902.2, 110, p. 110.
Decarli, R., Walter, F., Gónzalez-López, J., et al. (2019). In: *ApJ* 882.2, 138, p. 138.
Decarli, R., Walter, F., Venemans, B. P., et al. (2018). In: *ApJ* 854.2, 97, p. 97.
Dekel, A. and Birnboim, Y. (2006). In: *MNRAS* 368.1, pp. 2–20.
Dessauges-Zavadsky, M., Zamojski, M., Schaerer, D., et al. (2015). In: *A&A* 577, A50, A50.
Di Teodoro, E. M. and Fraternali, F. (2015). In: *MNRAS* 451.3, pp. 3021–3033.
Diemer, B., Stevens, A. R. H., Forbes, J. C., et al. (2018). In: *The Astrophysical Journal Supplement Series* 238.2, p. 33.
Dong, C., Spilker, J. S., Gonzalez, A. H., et al. (2019). In: *ApJ* 873.1, 50, p. 50.
Downes, D. and Solomon, P. M. (1998). In: *ApJ* 507.2, pp. 615–654.
Downes, D., Solomon, P. M., and Radford, S. J. E. (1993). In: *ApJL* 414, p. L13.
Draine, B. T. (2003). In: *ApJ* 598.2, pp. 1017–1025.
Draine, B. T. and Bertoldi, F. (1996). In: *ApJ* 468, p. 269.
Draine, B. T. and Lee, H. M. (1984). In: *ApJ* 285, p. 89.
Draine, B. T. (2011).
Dudzevičiūtė, U., Smail, I., Swinbank, A. M., et al. (2020). In: *MNRAS* 494.3, pp. 3828–3860.
Dullemond, C. P., Juhasz, A., Pohl, A., et al. (2012).
Dunlop, J. S., McLure, R. J., Biggs, A. D., et al. (2017). In: *MNRAS* 466, pp. 861–883.
Dunne, L., Eales, S., Edmunds, M., et al. (2000). In: *MNRAS* 315.1, pp. 115–139.
Eales, S., Smith, M. W. L., Auld, R., et al. (2012). In: *ApJ* 761, 168, p. 168.
Elbaz, D., Dickinson, M., Hwang, H. S., et al. (2011). In: *A&A* 533, A119, A119.
Elmegreen, B. G. (2007). In: *ApJ* 668.2, pp. 1064–1082.
Emonts, B. H. C., Feain, I., Röttgering, H. J. A., et al. (2013). In: *MNRAS* 430.4, pp. 3465–3471.
Epinat, B., Amram, P., Balkowski, C., and Marcelin, M. (2010). In: *MNRAS* 401.4, pp. 2113–2147.
Epinat, B., Tasca, L., Amram, P., et al. (2012). In: *A&A* 539, A92, A92.
Evans Neal J., I., Dunham, M. M., Jørgensen, J. K., et al. (2009). In: *ApJS* 181.2, pp. 321–350.
Ezawa, H., Kawabe, R., Kohno, K., and Yamamoto, S. (2004). In: *Ground-based Telescopes*. Ed. by J. Oschmann Jacobus M. Vol. 5489. Society of Photo-Optical Instrumentation Engineers (SPIE) Conference Series, pp. 763–772.
Fathi, K., Allen, M., Boch, T., Hatziminaoglou, E., and Peletier, R. F. (2010). In: *MNRAS* 406.3, pp. 1595–1608.
Federrath, C. and Klessen, R. S. (2013). In: *ApJ* 763.1, 51, p. 51.
Feldmann, R., Gnedin, N. Y., and Kravtsov, A. V. (2012a). In: *ApJ* 747.2, 124, p. 124.
– (2012b). In: *ApJ* 758.2, 127, p. 127.
Ferriére, K. M. (2001). In: *Reviews of Modern Physics* 73.4, pp. 1031–1066.
Feruglio, C., Fiore, F., Carniani, S., et al. (2018). In: *A&A* 619, A39, A39.
Fixsen, D. J. (2009). In: *ApJ* 707.2, pp. 916–920.
Förster Schreiber, N. M., Genzel, R., Bouché, N., et al. (2009). In: *ApJ* 706.2, pp. 1364–1428.
Förster Schreiber, N. M., Shapley, A. E., Genzel, R., et al. (2011). In: *ApJ* 739.1, 45, p. 45.
Franco, M., Elbaz, D., Zhou, L., et al. (2020). In: *arXiv e-prints*, arXiv:2005.03040, arXiv:2005.03040.
Frater, R. H., Brooks, J. W., and Whiteoak, J. B. (1992). In: *Journal of Electrical and Electronics Engineering Australia* 12.2, pp. 103–112.
Frayer, D. T., Ivison, R. J., Scoville, N. Z., et al. (1998). In: *ApJL* 506.1, pp. L7–L10.

Freundlich, J., Combes, F., Tacconi, L. J., et al. (2019). In: *A&A* 622, A105, A105.
Galliano, F., Galametz, M., and Jones, A. P. (2018). In: *ARA&A* 56, pp. 673–713.
Gao, Y. and Solomon, P. M. (2004). In: *ApJ* 606.1, pp. 271–290.
Genzel, R., Tacconi, L. J., Gracia-Carpio, J., et al. (2010). In: *MNRAS* 407, pp. 2091–2108.
Genzel, R., Tacconi, L. J., Lutz, D., et al. (2015). In: *ApJ* 800, 20, p. 20.
Giavalisco, M., Ferguson, H. C., Koekemoer, A. M., et al. (2004). In: *ApJL* 600.2, pp. L93–L98.
Girard, M., Dessauges-Zavadsky, M., Combes, F., et al. (2019). In: *A&A* 631, A91, A91.
Glover, S. C. O., Federrath, C., Mac Low, M. .-M., and Klessen, R. S. (2010). In: *MNRAS* 404.1, pp. 2–29.
Glover, S. C. O. and Jappsen, A. .-K. (2007). In: *ApJ* 666.1, pp. 1–19.
Glover, S. C. O. and Mac Low, M. .-M. (2011). In: *MNRAS* 412.1, pp. 337–350.
Glover, S. C. O. (2003). In: *ApJ* 584.1, pp. 331–338.
Glover, S. C. O. and Clark, P. C. (2012a). In: *MNRAS* 421.1, pp. 116–131.
– (2012b). In: *MNRAS* 421.1, pp. 9–19.
– (2012c). In: *MNRAS* 426.1, pp. 377–388.
– (2016). In: *MNRAS* 456.4, pp. 3596–3609.
Glover, S. C. O., Clark, P. C., Micic, M., and Molina, F. (2015). In: *MNRAS* 448.2, pp. 1607–1627.
Glover, S. C. O. and Mac Low, M.-M. (2007a). In: *ApJS* 169.2, pp. 239–268.
– (2007b). In: *ApJ* 659.2, pp. 1317–1337.
Goldsmith, P. F., Heyer, M., Narayanan, G., et al. (2008). In: *ApJ* 680.1, pp. 428–445.
Gonçalves, T. S., Basu-Zych, A., Overzier, R., et al. (2010). In: *ApJ* 724.2, pp. 1373–1388.
Gong, M., Ostriker, E. C., and Kim, C.-G. (2018). In: *ApJ* 858.1, 16, p. 16.
Gong, M., Ostriker, E. C., and Wolfire, M. G. (2017). In: *ApJ* 843.1, 38, p. 38.
González-López, J., Decarli, R., Pavesi, R., et al. (2019). In: *ApJ* 882.2, 139, p. 139.
González-López, J., Novak, M., Decarli, R., et al. (2020). In: *arXiv e-prints*, arXiv:2002.07199, arXiv:2002.07199.
Green, A. W., Glazebrook, K., McGregor, P. J., et al. (2014). In: *MNRAS* 437.2, pp. 1070–1095.
Grenier, I. A., Casandjian, J.-M., and Terrier, R. (2005). In: *Science* 307.5713, pp. 1292–1295.
Greve, T. R., Bertoldi, F., Smail, I., et al. (2005). In: *MNRAS* 359.3, pp. 1165–1183.
Griffin, M. J., Abergel, A., Abreu, A., et al. (2010). In: *A&A* 518, L3, p. L3.
Groves, B. A., Schinnerer, E., Leroy, A., et al. (2015). In: *ApJ* 799, 96, p. 96.
Guilloteau, S., Delannoy, J., Downes, D., et al. (1992). In: *A&A* 262, p. 624.
Gullberg, B., Smail, I., Swinbank, A. M., et al. (2019). In: *MNRAS* 490.4, pp. 4956–4974.
Guo, Y., Ferguson, H. C., Giavalisco, M., et al. (2013). In: *ApJS* 207.2, 24, p. 24.
Guo, Y., Rafelski, M., Bell, E. F., et al. (2018). In: *ApJ* 853.2, 108, p. 108.
Güsten, R., Nyman, L. Å., Schilke, P., et al. (2006). In: *A&A* 454.2, pp. L13–L16.
Haas, M., Lemke, D., Stickel, M., et al. (1998). In: *A&A* 338, pp. L33–L36.
Habing, H. J. (1968). In: *BAN* 19, p. 421.
Hamanowicz, A. (2020). PhD thesis. Fakultät für Physik der, Ludwig–Maximilians–Universität, München.
Harrington, K. C., Yun, M. S., Magnelli, B., et al. (2018). In: *MNRAS* 474, pp. 3866–3874.
Harrington, K. C., Weiss, A., Yun, M. S., et al. (2021). In: *ApJ* 908.1, 95, p. 95.
Harris, A. I., Baker, A. J., Zonak, S. G., et al. (2010). In: *ApJ* 723, pp. 1139–1149.
Harrison, C. M., Johnson, H. L., Swinbank, A. M., et al. (2017). In: *MNRAS* 467.2, pp. 1965–1983.
Hartwig, T., Clark, P. C., Glover, S. C. O., Klessen, R. S., and Sasaki, M. (2015). In: *ApJ* 799.2, 114, p. 114.
Haworth, T. J., Glover, S. C. O., Koepferl, C. M., Bisbas, T. G., and Dale, J. E. (2018). In: *NewAR* 82, pp. 1–58.
Heiderman, A., Evans Neal J., I., Allen, L. E., Huard, T., and Heyer, M. (2010). In: *ApJ* 723.2, pp. 1019–1037.

Heyer, M. H., Carpenter, J. M., and Snell, R. L. (2001). In: *ApJ* 551.2, pp. 852–866.
Ho, P. T. P., Moran, J. M., and Lo, K. Y. (2004). In: *ApJL* 616.1, pp. L1–L6.
Hodge, J. A., Carilli, C. L., Walter, F., Daddi, E., and Riechers, D. (2013). In: *ApJ* 776.1, 22, p. 22.
Hodge, J. A., Carilli, C. L., Walter, F., et al. (2012). In: *ApJ* 760.1, 11, p. 11.
Hodge, J. A. and da Cunha, E. (2020). In: *Royal Society Open Science* 7.12, 200556, p. 200556.
Hodge, J. A., Riechers, D., Decarli, R., et al. (2015). In: *ApJL* 798, L18, p. L18.
Hodge, J. A., Smail, I., Walter, F., et al. (2019). In: *ApJ* 876.2, 130, p. 130.
Hodge, J. A., Swinbank, A. M., Simpson, J. M., et al. (2016). In: *ApJ* 833.1, 103, p. 103.
Holwerda, B. W., Bianchi, S., Böker, T., et al. (2012). In: *A&A* 541, L5, p. L5.
Hughes, A., Meidt, S. E., Colombo, D., et al. (2013). In: *ApJ* 779.1, 46, p. 46.
Hughes, T. M., Ibar, E., Villanueva, V., et al. (2017). In: *MNRAS* 468, pp. L103–L107.
Hung, C.-L., Hayward, C. C., Yuan, T., et al. (2019). In: *MNRAS* 482.4, pp. 5125–5137.
Hunt, L. K., Draine, B. T., Bianchi, S., et al. (2015). In: *A&A* 576, A33, A33.
Huynh, M. T., Emonts, B. H. C., Kimball, A. E., et al. (2017). In: *MNRAS* 467.1, pp. 1222–1230.
Ianjamasimanana, R., de Blok, W. J. G., Walter, F., and Heald, G. H. (2012). In: *AJ* 144.4, 96, p. 96.
Ilbert, O., Arnouts, S., McCracken, H. J., et al. (2006). In: *Astronomy & Astrophysics* 457.3, pp. 841–856.
Illingworth, G. D., Magee, D., Oesch, P. A., et al. (2013). In: *ApJS* 209.1, 6, p. 6.
Inami, H., Decarli, R., Walter, F., et al. (2020). In: *ApJ* 902.2, 113, p. 113.
Iono, D., Wilson, C. D., Yun, M. S., et al. (2009). In: *ApJ* 695, pp. 1537–1549.
Ivison, R. J., Papadopoulos, P. P., Smail, I., et al. (2011). In: *MNRAS* 412, pp. 1913–1925.
Jin, S., Daddi, E., Magdis, G. E., et al. (2019). In: *ApJ* 887.2, 144, p. 144.
Johnson, H. L., Harrison, C. M., Swinbank, A. M., et al. (2018). In: *MNRAS* 474.4, pp. 5076–5104.
Jonsson, P., Groves, B. A., and Cox, T. J. (2010). In: *MNRAS* 403.1, pp. 17–44.
Joshi, P. R., Walch, S., Seifried, D., et al. (2019). In: *MNRAS* 484.2, pp. 1735–1755.
Kaasinen, M., Scoville, N., Walter, F., et al. (2019). In: *ApJ* 880.1, 15, p. 15.
Kaasinen, M., Walter, F., Novak, M., et al. (2020). In: *ApJ* 899.1, 37, p. 37.
Kainulainen, J., Beuther, H., Henning, T., and Plume, R. (2009). In: *A&A* 508.3, pp. L35–L38.
Kawamura, A., Mizuno, Y., Minamidani, T., et al. (2009). In: *The Astrophysical Journal Supplement Series* 184.1, pp. 1–17.
Kawamuro, T., Izumi, T., Onishi, K., et al. (2020). In: *ApJ* 895.2, 135, p. 135.
Kennicutt Robert C., J. (1989). In: *ApJ* 344, p. 685.
Kennicutt Jr., R. C. (1998). In: *ARA&A* 36, pp. 189–232.
Kennicutt, R. C. and Evans, N. J. (2012). In: *ARA&A* 50, pp. 531–608.
Kereš, D., Katz, N., Weinberg, D. H., and Davé, R. (2005). In: *MNRAS* 363.1, pp. 2–28.
Keto, E. and Caselli, P. (2008). In: *ApJ* 683.1, pp. 238–247.
– (2010). In: *MNRAS* 402.3, pp. 1625–1634.
Kewley, L. J. and Ellison, S. L. (2008). In: *ApJ* 681.2, pp. 1183–1204.
Klessen, R. S. and Glover, S. C. O. (2016). In: *Saas-Fee Advanced Course* 43, p. 85.
Klitsch, A., Zwaan, M. A., Péroux, C., et al. (2019a). In: *MNRAS* 482.1, pp. L65–L69.
Klitsch, A., Péroux, C., Zwaan, M. A., et al. (2019b). In: *MNRAS* 490.1, pp. 1220–1230.
Koepferl, C. M. and Robitaille, T. P. (2017). In: *ApJ* 849.1, 3, p. 3.
Kong, S., Lada, C. J., Lada, E. A., et al. (2015). In: *ApJ* 805.1, 58, p. 58.
Krumholz, M. R. (2014). In: *MNRAS* 437.2, pp. 1662–1680.
Krumholz, M. R., Leroy, A. K., and McKee, C. F. (2011). In: *ApJ* 731.1, 25, p. 25.
Krumholz, M. R. and McKee, C. F. (2005). In: *ApJ* 630.1, pp. 250–268.
Krumholz, M. R., McKee, C. F., and Tumlinson, J. (2009). In: *ApJ* 699.1, pp. 850–856.
Kuhlen, M., Krumholz, M. R., Madau, P., Smith, B. D., and Wise, J. (2012). In: *ApJ* 749.1, 36, p. 36.
Lada, C. J., Forbrich, J., Lombardi, M., and Alves, J. F. (2012). In: *ApJ* 745.2, 190, p. 190.
Lada, C. J., Lombardi, M., and Alves, J. F. (2009). In: *ApJ* 703.1, pp. 52–59.

Lada, C. J., Lombardi, M., and Alves, J. F. (2010). In: *ApJ* 724.1, pp. 687–693.
Lagos, C. d. P., da Cunha, E., Robotham, A. S. G., et al. (2020). In: *MNRAS* 499.2, pp. 1948–1971.
Laigle, C., McCracken, H. J., Ilbert, O., et al. (2016). In: *ApJS* 224, 24, p. 24.
Lang, P., Schinnerer, E., Smail, I., et al. (2019). In: *ApJ* 879.1, 54, p. 54.
Lee, N., Sanders, D. B., Casey, C. M., et al. (2013). In: *ApJ* 778, 131, p. 131.
Lee, N., Sanders, D. B., Casey, C. M., et al. (2015). In: *ApJ* 801, 80, p. 80.
Leethochawalit, N., Jones, T. A., Ellis, R. S., et al. (2016). In: *ApJ* 820.2, 84, p. 84.
Lelli, F., McGaugh, S. S., and Schombert, J. M. (2016). In: *AJ* 152.6, 157, p. 157.
Leroy, A., Schinnerer, E., Hughes, A., et al. (2021). In: *American Astronomical Society Meeting Abstracts*. Vol. 53. American Astronomical Society Meeting Abstracts, p. 208.03.
Leroy, A. K., Walter, F., Brinks, E., et al. (2008). In: *AJ* 136, pp. 2782–2845.
Leroy, A. K., Bolatto, A., Gordon, K., et al. (2011). In: *ApJ* 737.1, 12, p. 12.
Leroy, A. K., Walter, F., Bigiel, F., et al. (2009). In: *AJ* 137.6, pp. 4670–4696.
Leroy, A. K., Walter, F., Sandstrom, K., et al. (2013). In: *AJ* 146.2, 19, p. 19.
Leslie, S. K., Schinnerer, E., Liu, D., et al. (2020). In: *ApJ* 899.1, 58, p. 58.
Liang, L., Feldmann, R., Faucher-Giguère, C.-A., et al. (2018). In: *MNRAS*.
Liang, L., Feldmann, R., Kereš, D., et al. (2019). In: *MNRAS* 489.1, pp. 1397–1422.
Lilly, S. J., Le Fèvre, O., Renzini, A., et al. (2007). In: *ApJS* 172.1, pp. 70–85.
Liu, D., Daddi, E., Schinnerer, E., et al. (2021). In: *ApJ* 909.1, 56, p. 56.
Liu, D., Lang, P., Magnelli, B., et al. (2019a). In: *ApJS* 244.2, 40, p. 40.
Liu, D., Schinnerer, E., Groves, B., et al. (2019b). In: *ApJ* 887.2, 235, p. 235.
Livermore, R. C., Jones, T. A., Richard, J., et al. (2015). In: *MNRAS* 450.2, pp. 1812–1835.
Lombardi, M., Alves, J., and Lada, C. J. (2006). In: *A&A* 454.3, pp. 781–796.
Lombardi, M., Lada, C. J., and Alves, J. (2008). In: *A&A* 489.1, pp. 143–156.
Lonsdale, C. J., Farrah, D., and Smith, H. E. (2006). In: *Astrophysics Update 2*. Ed. by J. W. Mason, p. 285.
Lovell, M. R., Pillepich, A., Genel, S., et al. (2018). In: *MNRAS* 481.2, pp. 1950–1975.
Luo, B., Brandt, W. N., Xue, Y. Q., et al. (2017). In: *ApJS* 228.1, 2, p. 2.
Lutz, D., Poglitsch, A., Altieri, B., et al. (2011). In: *A&A* 532, A90, A90.
MacArthur, L. A., Courteau, S., and Holtzman, J. A. (2003). In: *ApJ* 582.2, pp. 689–722.
Madau, P. and Dickinson, M. (2014). In: *ARA&A* 52, pp. 415–486.
Magnani, L., Blitz, L., and Mundy, L. (1985). In: *ApJ* 295, pp. 402–421.
Magrini, L., Bianchi, S., Corbelli, E., et al. (2011). In: *A&A* 535, A13, A13.
Mandelker, N., Dekel, A., Ceverino, D., et al. (2017). In: *MNRAS* 464.1, pp. 635–665.
Mao, R.-Q., Schulz, A., Henkel, C., et al. (2010). In: *ApJ* 724, pp. 1336–1356.
Marasco, A., Fraternali, F., Heald, G., et al. (2019). In: *A&A* 631, A50, A50.
Martí-Vidal, I., Vlemmings, W. H. T., Muller, S., and Casey, S. (2014). In: *A&A* 563, A136, A136.
Mason, C. A., Treu, T., Fontana, A., et al. (2017). In: *ApJ* 838.1, 14, p. 14.
McElroy, D., Walsh, C., Markwick, A. J., et al. (2013). In: *A&A* 550, A36, A36.
McKinnon, M., Beasley, A., Murphy, E., et al. (2019). In: *Bulletin of the American Astronomical Society*. Vol. 51, p. 81.
McMullin, J. P., Waters, B., Schiebel, D., Young, W., and Golap, K. (2007). In: *Astronomical Data Analysis Software and Systems XVI ASP Conference Series, Vol. 376, proceedings of the conference held 15-18 October 2006 in Tucson, Arizona, USA. Edited by Richard A. Shaw, Frank Hill and David J. Bell., p.127*. Ed. by R. A. Shaw, F. Hill, and D. J. Bell. Vol. 376. Astronomical Society of the Pacific Conference Series, p. 127.
Meidt, S. E., Hughes, A., Dobbs, C. L., et al. (2015). In: *ApJ* 806.1, 72, p. 72.
Meier, D. S. and Turner, J. L. (2004). In: *AJ* 127.4, pp. 2069–2084.
Meier, D. S., Turner, J. L., and Hurt, R. L. (2008). In: *ApJ* 675.1, pp. 281–302.
Miettinen, O., Delvecchio, I., Smolčić, V., et al. (2017). In: *A&A* 606, A17, A17.

Mo, H., van den Bosch, F. C., and White, S. (2010).
Mogotsi, K. M., de Blok, W. J. G., Caldú-Primo, A., et al. (2016). In: *AJ* 151.1, 15, p. 15.
Molina, J., Ibar, E., Smail, I., et al. (2019). In: *MNRAS* 487.4, pp. 4856–4869.
Möllenhoff, C., Popescu, C. C., and Tuffs, R. J. (2006). In: *A&A* 456.3, pp. 941–952.
Muñoz-Mateos, J. C., Gil de Paz, A., Boissier, S., et al. (2009). In: *ApJ* 701.2, pp. 1965–1991.
Narayanan, D. and Hopkins, P. F. (2013). In: *MNRAS* 433.2, pp. 1223–1229.
Narayanan, D. and Krumholz, M. R. (2014). In: *MNRAS* 442.2, pp. 1411–1428.
Narayanan, D., Krumholz, M. R., Ostriker, E. C., and Hernquist, L. (2012). In: *MNRAS* 421.4, pp. 3127–3146.
Neeleman, M., Bañados, E., Walter, F., et al. (2019). In: *ApJ* 882.1, 10, p. 10.
Nelson, E. J., Tadaki, K.-i., Tacconi, L. J., et al. (2019). In: *ApJ* 870.2, 130, p. 130.
Nelson, R. P. and Langer, W. D. (1997). In: *The Astrophysical Journal* 482.2, pp. 796–826.
Neri, R., Genzel, R., Ivison, R. J., et al. (2003). In: *ApJL* 597.2, pp. L113–L116.
Neufeld, D. A. and Kaufman, M. J. (1993). In: *ApJ* 418, p. 263.
Neufeld, D. A., Lepp, S., and Melnick, G. J. (1995). In: *ApJS* 100, p. 132.
Noeske, K. G., Weiner, B. J., Faber, S. M., et al. (2007). In: *ApJL* 660.1, pp. L43–L46.
Novak, M., Smolčić, V., Delhaize, J., et al. (2017). In: *A&A* 602, A5, A5.
Novak, M., Bañados, E., Decarli, R., et al. (2019). In: *ApJ* 881.1, 63, p. 63.
Offner, S. S. R., Bisbas, T. G., Bell, T. A., and Viti, S. (2014). In: *MNRAS* 440, pp. L81–L85.
Oka, T., Hasegawa, T., Hayashi, M., Handa, T., and Sakamoto, S. (1998). In: *ApJ* 493.2, pp. 730–761.
Oka, T., Hasegawa, T., Sato, F., Tsuboi, M., and Miyazaki, A. (2001). In: *PASJ* 53.5, pp. 787–791.
Ossenkopf, V. (1997). In: *NewA* 2.4, pp. 365–385.
– (2002). In: *A&A* 391, pp. 295–315.
Ostriker, E. C. and Shetty, R. (2011). In: *ApJ* 731.1, 41, p. 41.
Oteo, I., Zhang, Z.-Y., Yang, C., et al. (2017a). In: *ApJ* 850, 170, p. 170.
Oteo, I., Zwaan, M. A., Ivison, R. J., Smail, I., and Biggs, A. D. (2016). In: *ApJ* 822.1, 36, p. 36.
– (2017b). In: *ApJ* 837.2, 182, p. 182.
Pakmor, R. and Springel, V. (2013). In: *MNRAS* 432.1, pp. 176–193.
Pakmor, R., Bauer, A., and Springel, V. (2011). In: *MNRAS* 418.2, pp. 1392–1401.
Pan, Z., Peng, Y., Zheng, X., Wang, J., and Kong, X. (2019). In: *The Astrophysical Journal* 885.1, p. L14.
Papadopoulos, P. P., van der Werf, P. P., Xilouris, E. M., et al. (2012a). In: *MNRAS* 426, pp. 2601–2629.
Papadopoulos, P. P., Bisbas, T. G., and Zhang, Z.-Y. (2018). In: *MNRAS* 478.2, pp. 1716–1725.
Papadopoulos, P. P., van der Werf, P., Xilouris, E., Isaak, K. G., and Gao, Y. (2012b). In: *ApJ* 751.1, 10, p. 10.
Pavesi, R., Sharon, C. E., Riechers, D. A., et al. (2018). In: *ApJ* 864, 49, p. 49.
Peletier, R. F., Valentijn, E. A., Moorwood, A. F. M., and Freudling, W. (1994). In: *A&AS* 108, pp. 621–641.
Peñaloza, C. H., Clark, P. C., Glover, S. C. O., and Klessen, R. S. (2018). In: *MNRAS* 475.2, pp. 1508–1520.
Peñaloza, C. H., Clark, P. C., Glover, S. C. O., Shetty, R., and Klessen, R. S. (2017). In: *MNRAS* 465.2, pp. 2277–2285.
Peng, C. Y., Ho, L. C., Impey, C. D., and Rix, H.-W. (2002). In: *AJ* 124.1, pp. 266–293.
– (2010). In: *AJ* 139.6, pp. 2097–2129.
Perley, R. A., Chandler, C. J., Butler, B. J., and Wrobel, J. M. (2011). In: *ApJL* 739.1, L1, p. L1.
Pettini, M. and Pagel, B. E. J. (2004). In: *MNRAS* 348.3, pp. L59–L63.
Pety, J. (2005). In: *SF2A-2005: Semaine de l'Astrophysique Francaise*. Ed. by F. Casoli, T. Contini, J. M. Hameury, and L. Pagani, p. 721.
Pety, J., Schinnerer, E., Leroy, A. K., et al. (2013). In: *ApJ* 779.1, 43, p. 43.
Pillepich, A., Nelson, D., Springel, V., et al. (2019). In: *MNRAS* 490.3, pp. 3196–3233.
Pillepich, A., Springel, V., Nelson, D., et al. (2018). In: *MNRAS* 473.3, pp. 4077–4106.

Pineda, J. E., Caselli, P., and Goodman, A. A. (2008). In: *ApJ* 679.1, pp. 481–496.
Planck Collaboration, Abergel, A., Ade, P. A. R., et al. (2011a). In: *A&A* 536, A21, A21.
Planck Collaboration, Ade, P. A. R., Aghanim, N., et al. (2011b). In: *A&A* 536, A19, A19.
Pompei, E. and Natali, G. (1997). In: *A&AS* 124, pp. 129–141.
Popping, G., Somerville, R. S., and Galametz, M. (2017a). In: *MNRAS* 471, pp. 3152–3185.
Popping, G., Decarli, R., Man, A. W. S., et al. (2017b). In: *A&A* 602, A11, A11.
Popping, G. and et al. (2020, in prep.). In:
Popping, G., Pillepich, A., Calistro Rivera, G., et al. (2021). In: *arXiv e-prints*, arXiv:2101.12218, arXiv:2101.12218.
Popping, G., Somerville, R. S., and Trager, S. C. (2014). In: *MNRAS* 442.3, pp. 2398–2418.
Privon, G. C., Narayanan, D., and Davé, R. (2018). In: *ArXiv e-prints*.
Rahman, N., Bolatto, A. D., Xue, R., et al. (2012). In: *ApJ* 745.2, 183, p. 183.
Raymond, A. W., Palumbo, D., Paine, S. N., et al. (2021). In: *arXiv e-prints*, arXiv:2102.05482, arXiv:2102.05482.
Regan, M. W., Thornley, M. D., Vogel, S. N., et al. (2006). In: *ApJ* 652.2, pp. 1112–1121.
Reissl, S., Wolf, S., and Brauer, R. (2016). In: *A&A* 593, A87, A87.
Reissl, S., Brauer, R., Klessen, R. S., and Pellegrini, E. W. (2019). In: *ApJ* 885.1, 15, p. 15.
Reissl, S., Stutz, A. M., Brauer, R., et al. (2018). In: *MNRAS* 481.2, pp. 2507–2522.
Rémy-Ruyer, A., Madden, S. C., Galliano, F., et al. (2014). In: *A&A* 563, A31, A31.
Riechers, D. A., Carilli, C. L., Maddalena, R. J., et al. (2011). In: *ApJL* 739, L32, p. L32.
Riechers, D. A., Carilli, C. L., Walter, F., and Momjian, E. (2010). In: *ApJL* 724, pp. L153–L157.
Riechers, D. A., Boogaard, L. A., Decarli, R., et al. (2020). In: *The Astrophysical Journal* 896.2, p. L21.
Riechers, D. A., Carilli, C. L., Casey, C., et al. (2017). In: *American Astronomical Society Meeting Abstracts #229*. Vol. 229. American Astronomical Society Meeting Abstracts, p. 348.12.
Riechers, D. A., Nayyeri, H., Burgarella, D., et al. (2021). In: *ApJ* 907.2, 62, p. 62.
Riechers, D. A., Pavesi, R., Sharon, C. E., et al. (2019). In: *ApJ* 872.1, 7, p. 7.
Robson, I., Holland, W. S., and Friberg, P. (2017). In: *Royal Society Open Science* 4.9, 170754, p. 170754.
Roebuck, E., Sajina, A., Hayward, C. C., et al. (2019). In: *ApJ* 881.1, 18, p. 18.
Rosario, D. J., Togi, A., Burtscher, L., et al. (2019). In: *ApJL* 875.2, L8, p. L8.
Rujopakarn, W., Daddi, E., Rieke, G. H., et al. (2019). In: *ApJ* 882.2, 107, p. 107.
Rybak, M., Calistro Rivera, G., Hodge, J. A., et al. (2019). In: *ApJ* 876.2, 112, p. 112.
Rybak, M., Hodge, J. A., Vegetti, S., et al. (2020). In: *MNRAS* 494.4, pp. 5542–5567.
Sahai, R., Vlemmings, W. H. T., and Nyman, L. .-Å. (2017). In: *ApJ* 841.2, 110, p. 110.
Saintonge, A., Kauffmann, G., Wang, J., et al. (2011). In: *MNRAS* 415.1, pp. 61–76.
Saito, T., Iono, D., Xu, C. K., et al. (2017). In: *ApJ* 835.2, 174, p. 174.
Salim, S., Boquien, M., and Lee, J. C. (2018). In: *ApJ* 859.1, 11, p. 11.
Salmi, F., Daddi, E., Elbaz, D., et al. (2012). In: *ApJL* 754.1, L14, p. L14.
Salmon, B., Papovich, C., Long, J., et al. (2016). In: *ApJ* 827.1, 20, p. 20.
Sanders, R. L., Shapley, A. E., Jones, T., et al. (2020). In: *arXiv e-prints*, arXiv:2009.07292, arXiv:2009.07292.
Sandstrom, K. M., Leroy, A. K., Walter, F., et al. (2013). In: *ApJ* 777, 5, p. 5.
Schaye, J., Dalla Vecchia, C., Booth, C. M., et al. (2010). In: *MNRAS* 402.3, pp. 1536–1560.
Schinnerer, E., Groves, B., Sargent, M. T., et al. (2016). In: *ApJ* 833, 112, p. 112.
Schinnerer, E., Leroy, A., Blanc, G., et al. (2019a). In: *The Messenger* 177, pp. 36–41.
Schinnerer, E., Hughes, A., Leroy, A., et al. (2019b). In: *ApJ* 887.1, 49, p. 49.
Schmidt, M. (1959). In: *ApJ* 129, p. 243.
Schöier, F. L., van der Tak, F. F. S., van Dishoeck, E. F., and Black, J. H. (2005). In: *A&A* 432.1, pp. 369–379.
Schreiber, C., Elbaz, D., Pannella, M., et al. (2016). In: *A&A* 589, A35, A35.

Schreiber, C., Pannella, M., Elbaz, D., et al. (2015). In: *A&A* 575, A74, A74.
Schruba, A., Leroy, A. K., Walter, F., and HERACLES Team (2012). In: *American Astronomical Society Meeting Abstracts #219*. Vol. 219. American Astronomical Society Meeting Abstracts, p. 346.02.
Scoville, N., Aussel, H., Sheth, K., et al. (2014). In: *ApJ* 783, 84, p. 84.
Scoville, N., Lee, N., Vanden Bout, P., et al. (2017). In: *ApJ* 837, 150, p. 150.
Scoville, N., Sheth, K., Aussel, H., et al. (2016). In: *ApJ* 820, 83, p. 83.
Scoville, N. Z. (2012).
Scoville, N. Z., Yun, M. S., Clemens, D. P., Sanders, D. B., and Waller, W. H. (1987). In: *ApJS* 63, pp. 821–915.
Seifried, D., Walch, S., Girichidis, P., et al. (2017). In: *MNRAS* 472.4, pp. 4797–4818.
Sembach, K. R., Howk, J. C., Ryans, R. S. I., and Keenan, F. P. (2000). In: *ApJ* 528.1, pp. 310–324.
Sharon, C. E., Riechers, D. A., Hodge, J., et al. (2016). In: *ApJ* 827, 18, p. 18.
Shetty, R., Glover, S. C., Dullemond, C. P., and Klessen, R. S. (2011). In: *MNRAS* 412.3, pp. 1686–1700.
Simpson, J. M., Smail, I., Swinbank, A. M., et al. (2015). In: *ApJ* 799.1, 81, p. 81.
Skelton, R. E., Whitaker, K. E., Momcheva, I. G., et al. (2014). In: *ApJS* 214.2, 24, p. 24.
Smith, R. J., Glover, S. C. O., Clark, P. C., Klessen, R. S., and Springel, V. (2014). In: *MNRAS* 441.2, pp. 1628–1645.
Sobolev, V. V. (1957). In: *Soviet Ast.* 1, p. 678.
Solomon, P. M., Downes, D., and Radford, S. J. E. (1992). In: *ApJL* 398, pp. L29–L32.
Solomon, P. M., Rivolo, A. R., Barrett, J., and Yahil, A. (1987). In: *ApJ* 319, pp. 730–741.
Speagle, J. S., Steinhardt, C. L., Capak, P. L., and Silverman, J. D. (2014). In: *ApJS* 214, 15, p. 15.
Spilker, J. S., Marrone, D. P., Aguirre, J. E., et al. (2014). In: *ApJ* 785.2, 149, p. 149.
Springel, V. (2010a). In: *MNRAS* 401.2, pp. 791–851.
– (2010b). In: *ARA&A* 48, pp. 391–430.
Stach, S. M., Dudzevičiūtė, U., Smail, I., et al. (2019). In: *MNRAS* 487.4, pp. 4648–4668.
Strong, A. W. and Mattox, J. R. (1996). In: *A&A* 308, pp. L21–L24.
Sun, J., Leroy, A. K., Schinnerer, E., et al. (2020). In: *ApJL* 901.1, L8, p. L8.
Sweet, S. M., Fisher, D. B., Savorgnan, G., et al. (2019). In: *MNRAS* 485.4, pp. 5700–5714.
Swinbank, A. M., Papadopoulos, P. P., Cox, P., et al. (2011). In: *ApJ* 742.1, 11, p. 11.
Swinbank, A. M., Simpson, J. M., Smail, I., et al. (2014). In: *MNRAS* 438.2, pp. 1267–1287.
Swinbank, A. M., Smail, I., Longmore, S., et al. (2010). In: *Nature* 464.7289, pp. 733–736.
Tacconi, L. J., Genzel, R., Neri, R., et al. (2010). In: *Nature* 463, pp. 781–784.
Tacconi, L. J., Genzel, R., Saintonge, A., et al. (2018). In: *ApJ* 853, 179, p. 179.
Tacconi, L. J., Genzel, R., Smail, I., et al. (2008). In: *The Astrophysical Journal* 680.1, pp. 246–262.
Tacconi, L. J., Neri, R., Genzel, R., et al. (2013). In: *ApJ* 768, 74, p. 74.
Tadaki, K.-i., Kodama, T., Nelson, E. J., et al. (2017a). In: *ApJL* 841, L25, p. L25.
Tadaki, K.-i., Genzel, R., Kodama, T., et al. (2017b). In: *ApJ* 834.2, 135, p. 135.
Teyssier, R. (2015). In: *ARA&A* 53, pp. 325–364.
Thompson, A. R., Clark, B. G., Wade, C. M., and Napier, P. J. (1980). In: *ApJS* 44, pp. 151–167.
Tielens, A. G. G. M. (2005).
Tiley, A. L., Swinbank, A. M., Harrison, C. M., et al. (2019). In: *MNRAS* 485.1, pp. 934–960.
Togi, A. and Smith, J. D. T. (2016). In: *ApJ* 830.1, 18, p. 18.
Tomassetti, M., Porciani, C., Romano-Díaz, E., and Ludlow, A. D. (2015). In: *MNRAS* 446.4, pp. 3330–3345.
Torrey, P., Vogelsberger, M., Marinacci, F., et al. (2019). In: *MNRAS* 484.4, pp. 5587–5607.
Tortora, C., Posti, L., Koopmans, L. V. E., and Napolitano, N. R. (2019). In: *MNRAS* 489.4, pp. 5483–5493.
Tress, R. G., Smith, R. J., Sormani, M. C., et al. (2020). In: *MNRAS* 492.2, pp. 2973–2995.
Tunnard, R. and Greve, T. R. (2016). In: *ApJ* 819.2, 161, p. 161.

Tunnard, R. and Greve, T. R. (2017). In: *ApJ* 849.1, 37, p. 37.
Turner, O. J., Cirasuolo, M., Harrison, C. M., et al. (2017). In: *MNRAS* 471.2, pp. 1280–1320.
Uzgil, B. D., Carilli, C., Lidz, A., et al. (2019). In: *ApJ* 887.1, 37, p. 37.
Valentino, F., Magdis, G. E., Daddi, E., et al. (2018). In: *ApJ* 869.1, 27, p. 27.
Valentino, F., Magdis, G. E., Daddi, E., et al. (2020). In: *ApJ* 890.1, 24, p. 24.
Vallini, L., Pallottini, A., Ferrara, A., et al. (2018). In: *MNRAS* 473.1, pp. 271–285.
van de Voort, F., Schaye, J., Booth, C. M., Haas, M. R., and Dalla Vecchia, C. (2011). In: *MNRAS* 414.3, pp. 2458–2478.
van der Wel, A., Bell, E. F., Häussler, B., et al. (2012). In: *ApJS* 203.2, 24, p. 24.
Varsavsky, C. M. (1966). In: *SSRv* 5.3, pp. 419–434.
Venemans, B. P., Walter, F., Decarli, R., et al. (2017). In: *ApJ* 845.2, 154, p. 154.
Vogelsberger, M., Genel, S., Sijacki, D., et al. (2013). In: *MNRAS* 436.4, pp. 3031–3067.
Walch, S., Girichidis, P., Naab, T., et al. (2015). In: *MNRAS* 454.1, pp. 238–268.
Walter, F., Weiß, A., Downes, D., Decarli, R., and Henkel, C. (2011). In: *ApJ* 730.1, 18, p. 18.
Walter, F., Carilli, C., Neeleman, M., et al. (2020). In: *ApJ* 902.2, 111, p. 111.
Walter, F., Decarli, R., Aravena, M., et al. (2016). In: *ApJ* 833.1, 67, p. 67.
Wang, F., Wang, R., Fan, X., et al. (2019). In: *ApJ* 880.1, 2, p. 2.
Wang, R., Wagg, J., Carilli, C. L., et al. (2013). In: *ApJ* 773.1, 44, p. 44.
Weingartner, J. C. and Draine, B. T. (2001). In: *ApJ* 553.2, pp. 581–594.
Weiß, A., Downes, D., Henkel, C., and Walter, F. (2005). In: *A&A* 429, pp. L25–L28.
Weiß, A., Kovács, A., Güsten, R., et al. (2008). In: *A&A* 490.1, pp. 77–86.
Whitaker, K. E., Franx, M., Leja, J., et al. (2014). In: *ApJ* 795, 104, p. 104.
Whitaker, K. E., van Dokkum, P. G., Brammer, G., and Franx, M. (2012). In: *ApJL* 754.2, L29, p. L29.
Williams, C. C., Labbe, I., Spilker, J., et al. (2019). In: *ApJ* 884.2, 154, p. 154.
Williams, R. J., Maiolino, R., Santini, P., et al. (2014). In: *MNRAS* 443.4, pp. 3780–3794.
Williams, R. E., Blacker, B., Dickinson, M., et al. (1996). In: *AJ* 112, p. 1335.
Willott, C. J., Bergeron, J., and Omont, A. (2015). In: *ApJ* 801.2, 123, p. 123.
Wisnioski, E., Glazebrook, K., Blake, C., et al. (2011). In: *MNRAS* 417.4, pp. 2601–2623.
Wolfire, M. G., Hollenbach, D., and McKee, C. F. (2010). In: *ApJ* 716.2, pp. 1191–1207.
Wong, T. and Blitz, L. (2002). In: *ApJ* 569, pp. 157–183.
Wootten, A. and Thompson, A. R. (2009). In: *IEEE Proceedings* 97, pp. 1463–1471.
Xilouris, E. M., Byun, Y. I., Kylafis, N. D., Paleologou, E. V., and Papamastorakis, J. (1999). In: *A&A* 344, pp. 868–878.
Yagoubov, P., Mroczkowski, T., Belitsky, V., et al. (2020). In: *A&A* 634, A46, A46.
Younger, J. D., Fazio, G. G., Wilner, D. J., et al. (2008). In: *ApJ* 688.1, pp. 59–66.
Yun, M. S. and Carilli, C. L. (2002). In: *ApJ* 568, pp. 88–98.
Zahid, H. J., Dima, G. I., Kudritzki, R.-P., et al. (2014a). In: *ApJ* 791, 130, p. 130.
Zahid, H. J., Kashino, D., Silverman, J. D., et al. (2014b). In: *ApJ* 792, 75, p. 75.
Zhang, Z.-Y., Papadopoulos, P. P., Ivison, R. J., et al. (2016). In: *Royal Society Open Science* 3.6, 160025, p. 160025.

Back cover image: Figure created by the author to illustrate the capabilities of ALMA.

Resolving Molecular Gas at the Peak Epoch of Star Formation: Examples of what star-forming galaxies with different molecular gas morphologies but the same high molecular gas content will look like with future observations of CO emission.
(Figure described in Chapter 5)

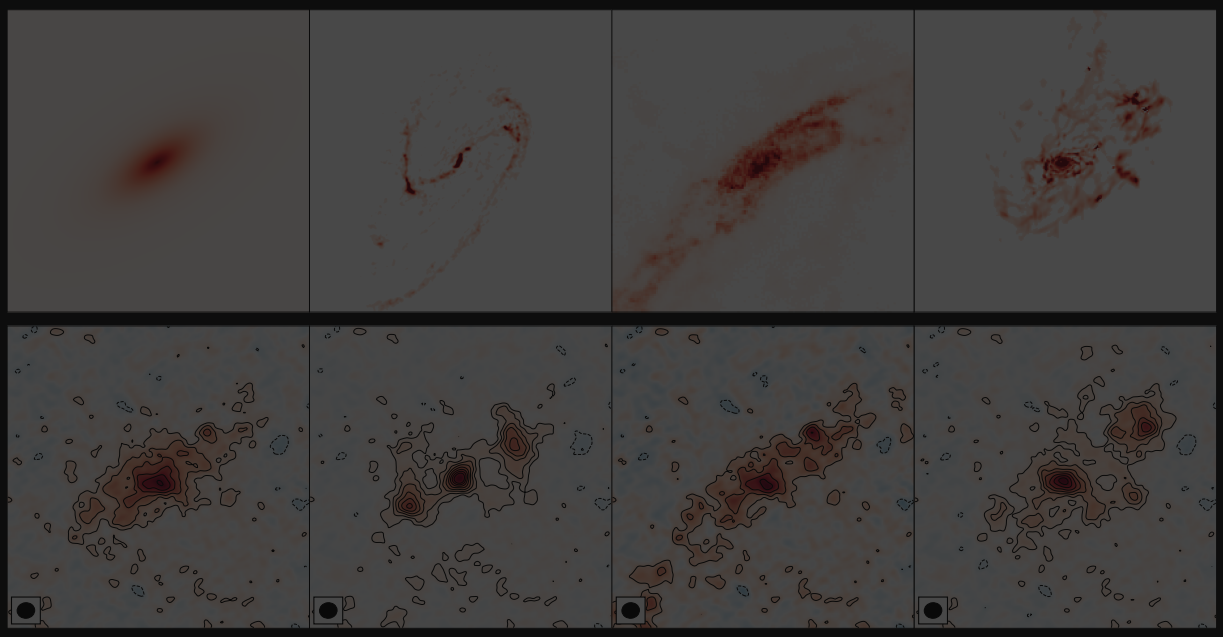

One of the key processes regulating the structure and composition of galaxies, and the Universe as a whole, is the formation of stars. Nearly a decade ago, astronomy had reached a concensus on how much mass went into forming stars, at least from 12 billion years ago to the present day. Distant galaxies (observed as they were many billions of years ago) formed stars far more rapidly than do nearby galaxies (observed as they were fairly recently), with the result that about half the stars in today's Universe had already been formed nine billion years ago. Despite this fundamental insight, astronomy still missed a key piece of puzzle, a description of the matter out of which stars form, *the molecular interstellar medium*. This limitation was removed in the last decade with advances in sub-/millimeter interferometry, leading to a wealth of studies of the molecular interstellar medium in distant galaxies. It therefore became critical to test how the physical properties of the molecular interstellar medium affected the observed emission. This thesis presents three in-depth studies of what can be learned from observations of the molecular interstellar medium in distant galaxies, thereby laying some of the groundwork for interpreting current and future observations of distant galaxies with sub-/millimeter facilities.